SIMULATION OF COMPRESSIBLE FLOW IN TUNNEL SYSTEMS INDUCED BY TRAINS TRAVELING AT HIGH SPEED

THÈSE N° 1806 (1998)

PRÉSENTÉE AU DÉPARTEMENT DE GÉNIE MÉCANIQUE

ÉCOLE POLYTECHNIQUE FÉDÉRALE DE LAUSANNE

POUR L'OBTENTION DU GRADE DE DOCTEUR ÈS SCIENCES TECHNIQUES

PAR

Alexander RUDOLF
Diplom-Ingenieur, Universität Fridericiana, Karlsruhe, Allemagne
de nationalité allemande

acceptée sur proposition du jury:

Prof. P. Monkewitz, directeur de thèse
Prof. M. Jufer, rapporteur
Prof. A. Vardy, rapporteur
M. A. Weatherill, rapporteur

Lausanne, EPFL
1998

ACKNOWLEDGMENTS

Ahead of all I would like to express my sincere appreciation to Prof. P.A. Monkewitz, who assigned me the task to work on an interesting and immediately useful aspect of the project Swissmetro, who ensured a period of clear and stable conditions for my professional environment and who has always been an open thesis advisor with helpful, encouraging and humorous comments.

Prof. A. Vardy was a tremendously kind support, particularly concerning the validation of NUMSTA. The code profited a lot from the exchange in several telephone calls and faxes during the final part of the thesis work.

I also was very happy to meet another author of outstanding publications. This allowed me to associate some more scientific papers to a pleasant personality: Professor Roe was in Lausanne where we met for Pizza as well as professionally. The discussion about the new numerical scheme he proposed is at this moment ongoing.

Many thanks to Prof. M. Deville (Michel), Dr. Drotz, Dr. B. Khobalatte and Dr. Y. Marx who helped me to find my way into numerics. Prof. A. Bottaro (Alex) was a great organizer for the DEA classes.

The financial support of the Swiss Confederation for the entire time of my assistantship is gratefully acknowledged. I thank the german Friedrich-Naumann-Foundation for liberal politics for the financial and immaterial support during my studies and in the beginning of my Ph.D. It has been an inspiring environment for the studies.

I would also like to thank the representatives of Swissmetro for including me as a foreigner into the primarily Swiss project, in particular Dr. A. Turi and M. A. Weatherill. The two trips with the 'Association des Amis de Swissmetro' to the Transrapid and the Eurotunnel were welcomed platforms for discussion and are nice remembrances.

I appreciate the members of the 'jury de thèse' to have accepted this task and to have given useful advice throughout the thesis.

The EPFL and the IMHEF generously covered education and work related costs for displacement and telecommunication, highlights being an introductory course about fluid dynamics at the VKI in Bruxelles, the DEA classes in Lyon and Lausanne and the participation at the 9th ISAVVT in Aosta. The atmosphere at the IMHEF/LMF, an open interaction between professors, assistants and students of different origins, the exceptional computer equipment and the social evenings contributed to a pleasant and productive professional background.

Other Ph.D. students and assistants at the EPFL have been kindly available, in particular C. Petrescu, F. Blom, T. Tefy, E. Magère and Ingemar Persson. Thanks also for the excellent work of our system administrator Florence Hagen, who exchanges old Apples against new PCs and for the exchange with O. Guignard who chose me as his advisor for semester and diploma work.

I want to underline the importance of a supportive private environment. My wife Christina now knows more about tunnel aerodynamics than every other entomologist before her and she has been a remarkable support during the last years. To my family, in particular my parents, my brother and my grandparents, I express my most sincere gratitude to their ongoing loyalty.

I am especially delighted that the time here, which was dominated by one task, allowed me to make friends from various countries with whom I passed many very joyful moments in a beautiful part of Europe.

ABSTRACT

This work is concerned with the development, the validation and the application of a new computer tool with the name NUMSTA (NUMerical Simulation of Tunnel Aerodynamics). This program allows the efficient and precise simulation of a multitude of configurations involving vehicles in tunnel systems.

NUMSTA is based on a 1D formulation of the conservative Euler equations for flow in a tube with time and space variable cross-section. Mass transfer, friction and heat transfer are considered in additional source terms following the idea of the 'distributed loss model'. The conservation equations are discretized in a finite volume approach using a numerical scheme based on the 2nd order TVD scheme of Roe.

The dynamical mesh generator implemented in NUMSTA ensures a minimum number of refined points around geometrical discontinuities and decomposes the domain into parts with coarse and with fine grid spacing. In fine parts, a small time step is required and in coarse parts large time steps can be applied. This is the origin of efficient computations which is necessary if complex configurations shall be simulated with a large number of parameter variations.

NUMSTA is successfully validated with several steady inviscid and viscous analytical cases as well as with unsteady inviscid analytical cases, by the comparison with two computer codes based on the methods of characteristics for realistic cases and by comparison with experimental results. For high-friction cases NUMSTA shows markedly different results than the established code THERMOTUN/4. A detailed analysis shows errors in the MoC code and concludes that cases with high-flow velocities and important source term contributions can, at present, better be computed with a finite volume method.

Typical compressible flow phenomena for various train/tunnel configurations are discussed by means of examples and the applicability of NUMSTA on complex tunnel networks involving several vehicles, cross-vents, air shafts and perforated walls is demonstrated.

VERSION ABRÉGÉE

Ce travail concerne le développement, la validation et l'application d'un nouvel outil informatique qui porte le nom de NUMSTA pour 'NUMerical Simulation of Tunnel Aerodynamics'. Ce logiciel permet une simulation efficace et précise d'une multitude de configurations avec des véhicules dans des réseaux de tunnels.

NUMSTA est basé sur la formulation unidimensionelle conservative des équations d'Euler pour l'écoulement dans un tuyau de section variable en temps et en espace. Transfert de masse, frottement et transfert d'énergie sont considérés en termes de sources suivant l'idée des 'pertes distribuées'. Les équations de conservation sont discrétisées sur la base du schéma numérique du $2^{\text{ième}}$ ordre TVD de Roe dans une approche des volumes finis.

Le générateur de maillage dynamique implémenté dans NUMSTA assure un raffinement autour d'une discontinuité géométrique; il décompose ainsi le domaine en des parts avec un maillage grossier et d'autres avec un maillage fin. Dans les parts raffinées on doit appliquer un pas de temps petit alors que dans les zones grossières on peut admettre un pas de temps grand. Cela permet des calculs efficaces, ce qui est d'importance pour des configurations complexes et un grand nombre de variations de paramètres.

NUMSTA est validé avec succès en comparant ses résultats avec des cas où une solution analytique existe. Cela comprend des cas stationnaires sans et avec frottement et des cas instationnaire sans frottement. En plus, NUMSTA est comparé avec les solutions de deux logiciels classiques pour des cas réalistes et avec des résultats expérimentaux. NUMSTA produit des résultats sensiblement différents de ceux du logiciel THERMOTUN/4 pour les cas où les vitesses de l'écoulement et les termes de frottement sont dominants. Une analyse detaillée montre les erreurs de la méthode des caractéristiques. L'analyse montre que, pour l'instant, des configurations avec des vitesses d'écoulement élevées et des termes de source importantes peuvent mieux être calculé avec une méthode basée sur des volumes finis.

À l'aide de certains exemples, des phénomènes typiques pour les écoulements compressibles sont montrés et l'applicabilité de NUMSTA pour des réseaux de tunnels avec plusieurs véhicules, rameaux d'anti-pistonnement, des puits et des parois perforées est démontrée.

ZUSAMMENFASSUNG

Die hier vorliegende Arbeit umfaßt die Entwicklung, die Validierung und die Anwendung eines neuartigen Computerprogramms mit dem Namen NUMSTA, was für 'NUMerical Simulation of Tunnel Aerodynamics' steht. Es erlaubt eine effiziente und präzise Simulation einer Vielzahl von Anordnungen von Fahrzeugen in einem Tunnelsystem.

Das physikalische Modell, auf dem NUMSTA basiert, ist das System der konservativen Form der 1D Euler Gleichungen für die Strömung in einem Rohr mit räumlich und zeitlich veränderlichem Querschnitt. Massenübertragung, Reibungseffekte und Wärmeübertragung werden durch zusätzliche Quellenterme gemäß des Modells der 'verteilten Verluste' berücksichtigt. Das System der Erhaltungsgleichungen wird mit einem numerischem Schema, das auf dem Schema von Roe (2. Ordnung, TVD) basiert, in einem finite Volumen Ansatz diskretisiert.

Der dynamische Netz Generator, der in NUMSTA programmiert ist, stellt sicher, daß eine minimale Anzahl von feinen Netzabständen in der Umgebung von geometrischen Unstetigkeiten angeordnet wird. Er teilt somit die Berechnungsdomäne in Zonen mit groben oder feinen Netzabständen auf. In verfeinerten Zonen muß ein kleiner Zeitschritt angewendet werden, wohingegen die groben Abstände einen großen lokalen Zeitschritt zulassen. Dies ist der Ursprung für effiziente Programmläufe, die notwendig zur Simulation von komplexen Anordnungen unter Variation einer Vielzahl von Parametern sind.

Die Ergebnisse von NUMSTA werden in der vorliegenden Arbeit erfolgreich bestätigt, indem sie zunächst mit mehreren analytischen Lösungen verglichen werden. Dies umfaßt sowohl zeitunabhängige reibungsfreie und reibungsbehaftete als auch zeitabhängige reibungsfreie Strömungen. Außerdem wurde NUMSTA mit klassischen Simulationsprogrammen, die auf der Charakteristikenmethode basieren, und mit experimentellen Ergebnissen anhand von realistischen Fällen verglichen. Ein Ergebnis war, daß für Fälle, in denen Reibung sehr dominant ist, NUMSTA ein deutlich anderes Verhalten zeigt als das etablierte Programm THERMO-TUN/4. Eine detaillierte Analyse zeigt Fehler der Charakteristikenmethode auf und kommt zu dem Schluß, daß Fälle mit hohen Strömungsgeschwindigkeiten und bedeutenden Beiträgen der Quellenterme z.Z. besser mit einer finite Volumen Methode berechnet werden kann.

Anhand von Beispielen werden typische kompressible Strömungsphänomene diskutiert und die Anwendbarkeit von NUMSTA auf komplexe Tunnel-Netzwerke mit mehreren Fahrzeugen, Querverbindungen, Ventilationsschächten und perforierten Wänden wird demonstriert.

APPENDIX

LIST OF SYMBOLS AND ABBREVIATIONS

Latin symbols

symbol	**explanation**	**unit**
A	cross sectional area	m^2
a	speed of sound	m/s
a^*	critical speed of sound or speed of sound for flow with sonic speed	m/s
c	wave velocity	m/s
C_f	friction coefficient or dimensionless surface shear stress defined as $C_f = \frac{\tau_s}{\rho(u^2/2)}$	-
C_f^*	incompressible friction coefficient	-
CFL	Courant-Friedrich-Levy number defined as $CFL = \lvert\lambda_{max}\rvert\frac{\Delta t}{\Delta x}$	-
c_p	specific heat at constant pressure	J/(kg K)
c_v	specific heat at constant volume	J/(kg K)
d	diameter	m
E_t	total internal energy in control volume	J
e	specific internal energy	J/kg
e_t	total specific internal energy defined as $e_t = e + \frac{u^2}{2}$	J/kg
F	force	N
$\underline{F}, \underline{G}$	numerical flux vectors with 3 components	[kg/(s m^2), N/m^2, W/m^2]
f	force per unit length	N/m
f	friction factor or dimensionless pressure drop for internal flow defined as $f = \left(-\frac{\partial p}{\partial x}\right)\frac{D}{\rho(u^2/2)}$	-

f^*	incompressible friction factor	-
$\underset{\sim}{f}, \underset{\sim}{g}$	physical flux vectors with 3 components	[kg/(s m^2), N/m^2, W/m^2]
G_∞, G_1	global errors calculated with infinity-norm and the 1-norm as defined in subsection 6.2	-
h	specific enthalpy defined as $$h = e + \frac{p}{\rho}$$	J/kg
h_t	total specific internal energy defined as $$h_t = h + \frac{u^2}{2}$$	J/kg
h	height of a flow channel	m
J	index for a special discrete x-position, Jacobian	-
j	index for discrete x-position	-
k	wall roughness	mm
k_s	equivalent sand grain roughness	mm
$\bar{\bar{L}}$	left handed eigenvector with respect to the conservative variables	-
l	length	m
La	Laval number or critical Mach number defined as $$La = \frac{u}{a^*}$$	-
M	momentum in control volume	kg m/s
m	mass contained in control volume	kg
$\dot{m}$	mass flow	kg/s
N	highest index for discrete space position	-
n	index for discrete time level	-
$\underline{n}$	external normal vector with unit length	-
P	perimeter	m
P	power	W
p	pressure	Pa
Pr	Prandtl number	-
q	time rate of heat transfer per unit length	W/m

R	individual gas constant	J/(kg K)
R	radius of control volume	m
$\bar{\bar{R}}$	matrix of right handed eigenvectors with respect to the conservative variables	-
r	space coordinate	m
r	auxiliary variable for the scheme of Roe	-
$\underset{\sim}{r}$	right handed eigenvector	-
Re	Reynolds number	-
S	surface of a control volume	m^2
$\underline{S}$	source term vector	[kg/(s m), N/m, W/m]
$\underset{\sim}{S}_a$	vector of additional source terms	[kg/(s m), N/m, W/m]
s	specific entropy	J/(kg K)
sp	vehicle speed	km/h
St	Stanton number	-
T	temperature	K
TI	time level for big time steps	s
ti	time level for small time step	s
$\underset{\sim}{u}$	vector of conservative flow values	[kg/m^3, kg/(s m^2), J/m^3]
$\underline{v}$	2D flow velocity vector	m/s
$\dot{w}$	time rate of work on surface	W/m^2
$\underset{\sim}{w}$	characteristic flow values	-
$U_\perp$, U_r	vertical, radial velocity component of the moving wall	m/s
u, u_r	horizontal, radial component of air velocity in tunnel fixed coordinate system	m/s
V	volume of a control volume	m^3
v	air velocity in vehicle fixed coordinate system, vertical air velocity in cross-vents, transverse air velocity in perforations	m/s
x, y	space coordinates	m

Greek symbols

α	heat transfer coefficient	W/m^2
α	inlet angle for perforated walls	-
β	blockage ratio, i.e. ratio of maximum vehicle cross-section over free tunnel cross-section	-
χ	adimensional mass flow, second type	-
ε	fraction of cross-sections	-
Φ	limiter function	-
γ	perforation ratio	m^2/m
φ	local inclination of wall	-
κ	isentropic exponent	-
$\bar{\bar{\Lambda}}$	diagonal matrix of eigenvalues	m/s
λ	eigenvalue	m/s
μ	contraction ratio (in subsection 5.3.2)	-
μ	dynamic viscosity	kg/(s m)
θ	adimensional mass flow, first type	-
ρ	density	kg/m^3
σ	sign of the wave speed	-
ζ	pressure loss coefficient	-
ω	slope indicator	-

Head indices

0, 1, 2	indices for distinction of different source term vectors
a	additional source term
n	discrete time level

Foot indices

a	ambient state
b	vehicle back
c	critical
e	end
eq	equivalent
f	friction, fine grid, foot value
fr	vehicle front
ga	gallery
L	left
l	index associated to wave number
n	nose
p	pressure, perforation
R	right
r	radial
s	start
sh	ventilation shaft
t	total
tl	tail
tu	tunnel (coarse grid)
v	vehicle
w	wall
1	additional source term for the continuity equation
2	additional source term for the momentum equation
3	additional source term for the energy equation

Remark:

If several indices are required, they are frequently grouped without separating delimiter.

Diacritical marks

$\underline{x}$	vector
$\bar{\bar{X}}$	tensor
$\bar{x}$	spatial average
x'	Roe's average (in section 3.3)
x', x''	values in the vehicle frame of reference
$\hat{x}$	estimate
$\overset{\frown}{x}$	exact solution
$\dot{x}$	time derivative
x^*	critical value, i.e. flow value at sonic speed

1D, 2D, 3D	one, two, three dimensional
BRR	British Rail Research
CFF/SBB	Chemin de Fer Féderaux Suisse / Schweizerische Bundesbahnen
CPU	central processing unit
CSM	Classic Swissmetro
DB	Deutsche Bahn AG
ETHZ	Eidgenössische Technische Hochschule in Zürich
EPFL	Ecole Polytechnique Fédérale de Lausanne
FCT	flux correction term, i.e. a term containing additional information and yielding a scheme of higher order
GDF	gas dynamical functions, i.e. functions of the *La* number only
ISAVVT	International Symposium of Aerodynamics and Ventilation in Vehicle Tunnels
IMHEF	Institut des Machines Hydrauliques et de Mécanique des Fluides
JNR	Japanese National Railway Company
LHS	left handed side (of an equation)
MoC	method of characteristics
RHS	right handed side (of an equation)
RTRI	Railway Technical Research Institute (Japan)
SNCF	Societé Nationale des Chemin de Fer (France)
TGV	Train à Grande Vitesse
TSM	TurboSwissmetro
TVD	total variation diminishing, i.e. oscillation avoiding property of a numerical scheme
b.c.	boundary condition

1 INTRODUCTION

About one century after the first train line opened between Manchester and Liverpool, high speed trains were realized in the first half of the century in Germany. In record runs, electrical trains from Siemens and from AEG reached in 1903 already 200km/h and 210km/h, respectively. But is was not until 1936 that high speed trains served regularly between Berlin and Hamburg where electrical engines operated with 205km/h and aerodynamically paneled steam engines with 200km/h [80]. These trains were realized to expose the vain glory of dictatorship rather than to provide an economically viable means of transportation. They disappeared in the drawers of history when reality overruled megalomania. During the following two decades, trains were not faster than in the beginning of the century.

With the fast increasing traffic demand, first plans for high speed ground transportation were developed in the 50s by the Japanese National Railways (JNR) and roughly 10 years later by the French National Railway Company (SNCF) [79] and then the Western German railways (DB).

The Shinkansen project started in 1956, construction of the Tokaido line was begun in 1959 and test runs were started in 1962 on the Kamonomiya test line. In october 1964, regular service was opened between Tokio and Osaka with train speed of up to 250km/h.

The first prototype of the 'Train à Grande Vitesse', the TGV 001, was built with helicopter turbines. It started testing in 1970 with peak velocities of 320km/h breaking up-to-date speed records. Before entering regular service, the oil crisis of 1972 rendered the system unprofitable. Powered by electricity, the first TGV line was built between Paris and Lyon in the late 70's and revenue service was opened in 1981, when the TGV marked the speed record with 380km/h. The streamlined, bright orange trains became well known and marked a blatant success of the SNCF. Since 1981 new generations of the TGV and new lines have been realized in France. Based on the TGV technology, relatives have been developed, i.e. the Eurostar and the Thalys. The world speed record was pushed to 515km/h in may 1990.

Impelled by the high acceptance of the TGV, the DB altered existing plans for new lines with a speed of around 200km/h and planned from then on a very high speed train system reaching up to 350km/h. The train was finished until 1985 and became the star for the 150th anniversary of the German railways under the name Inter City Experimental (ICE) or later ICE-V. A train speed of up to 350km/h was reached at that time. Regular service was started in 1991 under the name Inter City Express (ICE). Since then two new versions, ICE1 and ICE2 were put in service.

Other classical high speed train projects followed, notably in Belgium, Italy, Spain, the UK and the scandinavian peninsula. The technology became a profitable export product of the respective countries. Competitive offers were presented to countries interested in buying high speed ground transportation systems, such as the USA and South Korea. Currently, existing high speed lines are extended and new lines are planned especially for eastern Europe.

The speed of classical rail systems is limited by maintenance costs, security considerations and comfort criteria. Magnetic levitation and guidance systems eliminate the wear associated with the wheel / rail contact. Furthermore, these systems allow higher speeds of the order of 500km/h with reasonable energy consumption and high passenger comfort. Currently, MAGLEV trains are about to be built, tested and studied in Germany, Japan and in Switzerland.

In Germany, a research project was initiated in 1969 with the aim to study the technical options to cope with the increasing traffic load by means of MAGLEV vehicles. In the same year, a first prototype, the Transrapid 01, was presented. Various configurations have been examined on short test tracks with up to 2.4 km length since the early 70s. Construction of a looped test track with 31.5 km in the 'Test- und Versuchsanlage' (TVE) in Lathen was begun in 1980 and completed in 1987. Since then, full speed continuous tests can be realized. The Transrapid 07 is in test since 1988 and held for long the world speed record for manned MAGLEV vehicles with 450km/h. It represents a technically feasible system. The German parliament decided in may 1996 to realize a Transrapid system between Hamburg and Berlin. The beginning of construction is scheduled for late 1998 and the system shall be in regular service in 2005.

In Japan, research on MAGLEV systems has begun at the Railway Technical Research Institute (RTRI) of the JNR in the early 70s. First test runs were undertaken in July 1977 on the 7 km Miyazaki test track. Also here, various manned configurations have been tested since. The highest speed with a manned vehicle reached so far is 411km/h with the MLU002N. In september 1996, the Yamanashi test center was opened with the aim to realize a MAGLEV system in 1999. The Yamanashi test center consists of a test track with a length of 42.8 km with 87% in tunnels, which shall later be integrated in the service network.

It is a somewhat historic coincidence that the RTRI announces the same day this text was written (28 Nov 1997) that a manned vehicle of type MLX01 beat the existing speed record with 503km/h. The fasted speed reported in the sequel is 550km/h reached at 24 Dec 1997. As can be seen, progress is on the way and competition is high in this very modern branch of transport technology.

The Swiss approach for a modern high speed ground transportation system is the project Swissmetro. The special topographical situation of the alpine country does not allow to built classical high speed trains or MAGLEV systems since they require large curve radii. Besides, the political acceptance of such technical installations with its impact on the environment is likely to be critical.

1.1 Swissmetro

The idea of a means of transportation linking the most important Swiss towns came to Rodolphe Nieth at the beginning of the 70s when he was an engineer at the Swiss Federal Railways (CFF). Such a metro needs to combine short travel time, high frequency of service, competitive costs and a high safety level. The idea of a Swiss metro, the Swissmetro project, started to take form in the beginning of the eighties among professors and scientists of the Swiss Federal Institute of Technology in Lausanne (EPFL).

Financial support for a preliminary study of the Swissmetro system came later from the Swiss Confederation. Research credits for the universities were granted. Industry companies supported the study by engineering manpower. The aim was to study the technical feasibility of the project in depth. Between 1989 and 1992, the efforts of researchers, scientists and engineers from some 30 companies were coordinated at the EPFL, resulting in a first lay-out of the system. The technical feasibility of the system was shown in broad terms and areas requiring additional investigation in the next phase of the project were defined [45].

The results of the preliminary study persuaded the initiators of the project to act in order to obtain a license to build and to operate a pilot-line of the SWISSMETRO. The company Swissmetro SA was therefore established in 1993 with shareholders drawn from individuals supporting the project, small engineering offices, enterprises having been active in the preliminary study, banks and larger electromechanical industries, both from within and outside of Switzerland. The goals of Swissmetro SA are [63]:

- to coordinate all the activities with the aim of obtaining the license from the federal authorities for a pilot line,
- to secure the financing of the main study for the years 1994 - 1998 and

- to promote the project in Switzerland and abroad both politically and commercially.

Swissmetro is based on four complementary technologies:

1. the entirely underground infrastructure consisting of a twin-bore tunnel of around 5.5 meter diameter which, when closed and sealed, enables the creation of a
2. partial vacuum in the tubes, hence reducing the air density. A service pressure in the order of one tenth of the atmosphere reduces the power requirement of the vehicles so that a speed of 400 - 500km/h can be attained at blockage ratios (ratio of train and tunnel cross-sections) of about $\beta = 0.4 - 0.5$.
3. Contact free guidance and magnetic levitation (MAGLEV) assure motion without mechanical friction and
4. linear electric motors are an efficient means for propulsion.

None of the four technologies is new per se. Underground urban transportation systems were created since the end of last century, commercial airplane technology deals successfully with partial vacuum and MAGLEV as well as linear electric motors are beyond prototype phase both in Germany and in Japan. What is new on SWISSMETRO is the combination of these four technologies in one system.

Questions arise in many technical and various other fields. The organizational structure of the project Swissmetro reflects these various domains in different work and research groups. Technical groups cover the fields electromechanics, mechanics, security and civil engineering. Other groups are concerned with management, infrastructure, operation, economy or public relations.

For preliminary design purposes of this particular project, an in depth investigation of aerodynamic issues is essential since many vital parameters depend on the aerodynamic phenomena induced by the movement of the trains. As an example the distribution of pressure and temperature be mentioned. It defines the forces on the vehicle and other system components which influence material and methods chosen to cope with the pressures and temperatures arising during normal and emergency operation. It also defines the power required to overcome the aerodynamic drag. This value is important for the dimensioning of the electromechanical components and defines to a high degree the operation costs.

Initially, it was thought that aerodynamic problems could be mastered if only the service pressure in the tunnels is reduced to values between 0.08 bar and 0.3 bar. It is true that an important aerodynamic system parameter, the Reynolds number, decreases linearly with the pressure and with it the vehicle drag and also pressure fluctuations. It is, however, a wrong idea that this solves the aerodynamic problems associated with the train movement in a tunnel. A reduced service pressure only reduces aerodynamic problems, but a partial vacuum evokes other problems such as the conservation of this partial vacuum, the re-establishment of atmospheric pressure in case of emergency, maintenance labor in the tunnels, effects of the low pressure on the installations and security questions.

1.2 Tunnel Aerodynamics

Train and tunnel aerodynamics have evolved together with increasing train speeds. As indicated above, the japanese Yamanashi test line requires 87% tunnels in the hilly area between Tokio and Nagoya on the foot of Mt. Fuji. New installations of the TGV and ICE require also a high percentage of tunnels and detailed examination of aerodynamic phenomena becomes increasingly important both for passenger comfort and for the train movement itself.

Important parameters for the description of a train / tunnel configuration are the blockage ratio

β, defined as the ratio of maximal vehicle cross-section over free tunnel cross-section, the vehicle speed sp and, for closed systems, the initial pressure level p_0.

Characteristic for the train movement through open tunnels are the tunnel entry, the train encounter, the passage at geometrical discontinuities, the interaction with reflected waves and the tunnel exit. For closed systems, such as the Swissmetro, entry and exit do not exist. The open tunnel ends are here replaced by walls.

When a train enters a tunnel or accelerates from within a tunnel, a pressure wave is generated in front of the train and an expansion wave is generated behind the vehicle tail. The pressure difference between both vehicle ends generates important flow velocities in the annular gap around the vehicle and eventually, particularly for high blockage ratios, the flow may attain sonic speed. Thus, the flow can no longer be described with steady and incompressible models. Compressibility effects become important and a coupled unsteady treatment of the near and the far field flow is required.

For passenger comfort, an important criterion is the time rate of pressure change at a given location. For the Swiss project 'Rail 2000' the limit for this value has been set to 1.5kPa/4s for a single train in a tunnel and to 3.5kPa/4s for a train encounter [29]. These values have been determined in collaboration between the DB and BRR.

For the train movement it is important to know the unsteady forces acting on the train. They determine the vehicle drag and the stability of the vehicle movement. The vehicle drag and with it the required aerodynamic power to overcome this drag can be predicted with 1D models. The deformation of a structure under the influence of a flow field is examined in the field of aeroelasticity or fluid structure interaction [3]. This is a classical discipline which currently experiences an elevated interest with the rapid growth of computer performance. For trains, aeroelastic effects may occur when the pressure changes rapidly on the sides of the train contributing to destabilize its linear movement.

The aerodynamic vehicle drag is composed of two contributions: the friction and the pressure drag. The pressure difference between the front and the back of the vehicle is responsible for the pressure drag which exceeds the friction drag for high blockage ratios.

It is the task of tunnel aerodynamics to describe the fluid flow induced by trains in a tunnel system and to propose configurations satisfying comfort and other technical constraints. As origin of the vehicle drag the pressure difference between both vehicle ends can be identified. It is therefore of particular interest to examine installations which allow flow to pass by the train, thereby reducing this pressure difference. Passive and active installations are imaginable. Passive installations do not require additional energy, whereas active installations do.

Tunnel aerodynamic examinations require detailed simulations of the unsteady compressible flow in the entire tunnel network. Being confronted with typical lengths of several 10 km, the power of modern computers is not yet sufficient to model the flow in 3D. This problem can be bypassed considering that in most of the domain, particularly along continuous tunnel parts, the flow is sufficiently well described with 1D models. Local 3D effects can be considered by empirical coefficients obtained either from detailed local numerical simulations or from experiments.

A very early contribution to tunnel aerodynamics came in 1927 from Tollmien [64], a student of L. Prandtl, who examined the drag and the pressure distribution for train entry and train encounter using a natural grid based on a prediction of the streamlines.

There is a significant amount of literature published in the past 3 decades based on 1D simulations and corrective models. The conference proceedings of the "International Symposium on

Aerodynamics and Ventilation in Vehicle Tunnels" (ISAVVT) (see for example [93]), a triennial meeting held since 1973 in various European locations, give a good account of the up-to-date developments. Other relevant conferences in the field are the 'International Conference on Pressure Surges', the 'World Congress on Railway Research' and the 'International Conference on unsteady flow and fluid transients'.

Stimulated by the first plans for the Channel Tunnel, a first approach for a numerical solution of problems related to tunnel aerodynamics have been proposed in the year 1969 by D.A. Henson [43] in his Ph.D. thesis at Leeds University. Henson performed then together with J.A.Fox work for BRR. W.A. Woods and R.G. Gawthorpe were confronted with similar problems in [75] in 1972. A.E. Vardy, likewise from Leeds, presented in 1973 together with Fox a paper about the generation and alleviation of pressure transients caused by high speed trains at the 1^{st} ISAVVT in Canterbury. For the same occasion, Woods and C.W. Pope published an article examining the action of the tunnel entry wave [76]. The above named british scientists are in the sequel authors of a large number of articles treating various problems related to tunnel aerodynamics. An interesting method can also be found in the article [62] by C.R. Strom, where the unsteady computation of the far field is coupled with the steady or unsteady solution for the near field by the method of characteristics.

An account of tube vehicle movement is not complete without mentioning A. G. Hammitt (see [40], [41]) who gave interesting solutions for a coupled near and far field flow. His contributions represented at the time state-of-the-art but have been since been superseded by more recent publications in the field. Because of their classical character, Hammitt's texts are useful to become familiar with the problems involved and the possible solution techniques.

A second phase begins at the end of the 70s marked by many contributions from the before mentioned authors, from researchers around by H. Sockel [59] at the Technical University of Vienna as well as from japanese research groups at the RTRI of the JNR [51].

Early contributions from Sockel date back to 1972 [58]. Studies at the TU of Vienna carried over multiple aspects related to the train movement in tunnels. The researchers at the RTRI were mainly interested in environmental aspects of tunnel aerodynamics. An example is the micro-pressure-wave generated at the tunnel exit by an incident steep pressure wave which discomforts inhabitants of nearby houses.

A major role in the aerodynamic examinations of the project Eurotunnel can be attributed to Mott Mac Donald and WS Atkins, two british consultancies. Publications involving D. Henson and WMS Bradbury (see for example [27], [44]) give account of aerodynamic considerations in this exceptional project.

The solution procedures of all the authors mentioned so far is based on the method of characteristics (MoC) which has been first described in [18]. A complete and representative account for this method applied on tunnel aerodynamics is given in [61]. The method requires to trace all geometrical and flow discontinuities, such as the train ends, the shocks or contact discontinuities. Every possible interaction of discontinuities has to be modeled separately. This requires a rather complex solution algorithm, which gives in fact very good results. This has been proven over the decades by a series of comparisons with small and full scale experiments. Several improvements of the models employed in the 1D codes have been discussed in various conference contributions since.

Independently but parallel to the developments for the Swissmetro, a group around A. Baron at the 'Polytecnico de Milano' (Italy) studies aerodynamic phenomena due to train movement in a tunnel with a different approach based on a finite volume discretization of the domain [25].

Several reduced scale experimental installations for the generation and the study of pressure wave with or without moving parts have been realized. They can be localized at the JPL of the Caltech [30], at the University of Dundee, UK [31], at BRR in Derby, UK [54], in Japan [46], at the TU in Vienna [52], at the SNCF in France [37] and recently also at the NLR in the Netherlands [74] sustained the theoretical developments in that field over the decades. \

The aerodynamic research group of the Swissmetro project intends also to construct an experimental installation with a guided and continuously propelled model under the name 'High Speed Train Aerodynamic Rig (HISTAR)' [28]. A reduced 'shock-tube' installation has been realized so far.

1.3 Aims of the present work, NUMSTA

Starting with the task to predict compressible flow phenomena for the Swissmetro and to estimate the power requirement for this system, a computer program with the acronym NUMSTA for "NUMerical Simulation of Tunnel Aerodynamics" has been developed.

It follows a different approach than the previous workers. For high vehicle speeds and high blockage ratios the classical method of characteristics fails, whereas NUMSTA continues to deliver reliable results. This demonstrates that calculations for modern high-speed train systems can only be performed with the new method.

In NUMSTA the domain is dynamically separated in coarse and fine parts. This allows to use a big time step for the coarse parts and requires a small time step only in the fine parts. Each part is updated with an explicit upwind scheme based on a finite volume discretization. This conceptually easier approach yields a reliable, versatile and efficient computational tool for problems related to tunnel aerodynamics. Because of the models and the numerical method used, the treatment of flow discontinuities is readily included. This allows simulations of a wealth of complex vehicle/tunnel configurations including friction, heat transfer and correctional source terms with reasonable CPU time requirement.

In the present work, the models and the solution algorithm implemented in NUMSTA are explained. The basic equations of tunnel aerodynamics in the tunnel and the vehicle frame of reference are derived. The code is validated with cases where analytical solutions exist and by comparison with other numerical codes and experimental data. Its usefulness for preliminary design purposes is demonstrated. Aerodynamic phenomena induced by the high-speed train movement in a tunnel system such as Swissmetro are explained and results for sample configurations are given.

Further, two for the project Swissmetro important subjects are developed: the repressurization and an alternative to the classical train/tunnel system, the TurboSwissmetro.

In this work, engineering aspects of the preliminary design for Swissmetro are intentionally not discussed in detail. They are subject of separate technical reports. Equally, the influence of certain parameters on the vehicle movement is not discussed in detail for all examples.

2 THE GOVERNING EQUATIONS

The large calculation domain requires models which are simple enough to provide the required computational performance and yet to give results with sufficient precision. The problem to be described is in fact 3D, time dependent, turbulent, viscous and compressible. A full scale numerical simulation for this problem is, at present, not feasible, even with modern codes adapted to vector or parallel machines.

A 2D calculation for a 3D geometry evokes the question of the relation between the numerical model and the reality, even if an axisymmetric coordinate system in used.

Therefore, the problem has to be considered as quasi 1D, time dependent and compressible Friction and heat transfer must be considered as well. The 1D form of the Navier-Stokes equations can not account for the shear layer. The flow must therefore be modeled based on the Euler form of the conservation equations with additional source terms accounting for friction and heat transfer. In order to facilitate the procedure of adding source terms for discrete positions, the problem is treated entirely in a tunnel fixed coordinate system. The moving trains can be considered by a time and space dependent cross-section.

Friction and purely 3D flow effects are included by empirical models as external forces. This method is known as the 'distributed loss model' [15, p. 81]. Its idea is to distribute the forces applied on a control volume equally on fluid particles in it. For friction effects, empirical coefficients relating the average flow velocity to a friction force can be formulated. Losses due to the distortion of the flow in a branchment, for instance, can also be considered this way.

The definition of these empirical coefficients is a critical point in the construction of the numerical models. Standard coefficients to be found in text books are mostly given under simplifying assumptions, such as a general geometry or for steady flow. Coefficients that display local 3D flow effects for a 1D computation can be obtained from a more precise local numerical simulation or from experiments.

2.1 The derivation of the Euler equations for flow in a tube with spatio-temporally varying cross-section

For tunnel aerodynamics, the system of conservation equations for 1D flow in a tube with time and space dependent cross-section, henceforth called area function, is required. The flow can be described either relative to a tunnel fixed coordinate system or relative to the moving and accelerated vehicle frame of reference.

The system of Euler differential equations for a tube with a time and space dependent area function can be derived from the integral form of the conservation equations. The theorems of Leibniz and Gauß will be used in the sequel. With Leibniz' theorem the time derivative over a volume integral can be transformed into a volume integral of a time derivative plus a flow across the control surface. Under the condition that the resulting integrands are differentiable, Gauß' theorem transforms surface integrals of vectors to volume integrals according to

$$\int_S (\underline{v} \cdot \underline{n}) dS = \int_V (\nabla \cdot \underline{v}) dV . \tag{2.1}$$

A similar expression allows to transform surface integrals of scalars into volume integrals as

$$\int_S u \underline{n} dS = \int_V (\underline{\nabla} u) dV . \tag{2.2}$$

The flow values will be considered for the derivation as being differentiable, that means flow discontinuities, such as shocks or contact surfaces are not allowed. However, these flow discontinuities can still be computed since the numerical scheme applied on these conservation equations assumes a piecewise constant distribution of flow values within each computational cell. Flow discontinuities will thus only be resolved over several mesh cells depending on the accuracy of the discretization.

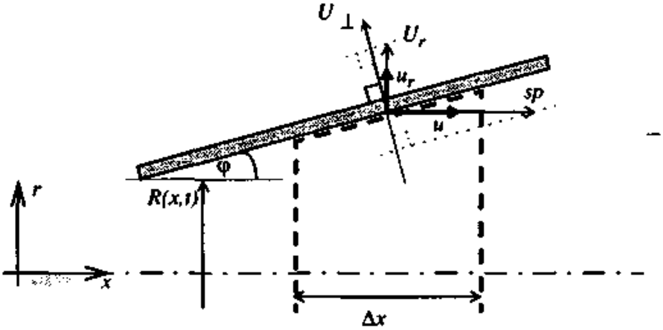

Figure 2.1 Instantaneous picture of an axisymmetric control volume with a wall surface part moving in *x*- and *r*- direction

For the derivation of the governing equations, the nomenclature introduced by Figure 2.1 is used. The velocity vector with its two components be represented by

$$\underset{\sim}{v} = \begin{pmatrix} u \\ u_r \end{pmatrix}, \tag{2.3}$$

the horizontal movement of the wall be marked with *sp*, which is from now on used for the vehicle speed, the radius and the cross-section of the control volume be denoted with $R(x,t)$ and $A(x,t)$, respectively, and φ is the local wall angle.

2.1.1 The continuity equation

The general form of the continuity equation for an arbitrary control volume in vectorial form is given by

$$\frac{dm}{dt} = \int\limits_V \frac{\partial\rho}{\partial t} dV + \int\limits_S \rho(\underset{\sim}{v} \cdot \underline{n}) dS = 0 \ . \tag{2.4}$$

Applying eq. (2.4) to the control volume in Figure 2.1 and transforming the surface integral to a volume integral, the equation of mass conservation in cylindrical coordinates for axisymmetric flow is

$$\int_V \left[\frac{\partial \rho}{\partial t} + \frac{\partial}{\partial x}(\rho u) + \frac{1}{r}\frac{\partial}{\partial r}(r\rho u_r)\right] dV = 0 \tag{2.5}$$

Substituting $dV = 2\pi r dr dx$ it follows

$$2\pi \int_0^{\Delta x}\int_0^{R(x,t)} \left[\frac{\partial \rho}{\partial t} + \frac{\partial}{\partial x}(\rho u) + \frac{1}{r}\frac{\partial}{\partial r}(r\rho u_r)\right] r dr dx = 0 . \tag{2.6}$$

In the quasi 1D case, ρ and u are taken as the average values over the cross-section. Then, the first two terms in the integral are constant over r and eq. (2.6) becomes

$$\int_0^{\Delta x} \left\{ A(x,t)\left[\frac{\partial \rho}{\partial t} + \frac{\partial}{\partial x}(\rho u)\right] + 2\pi r \rho u_r \Big|_0^{R(x,t)} \right\} dx = 0 . \tag{2.7}$$

The second primitive in eq. (2.7) needs further discussion.

- If A=$A(x)$, the radial component of the air velocity u_r is given by the wall streamline

$$R = R(x) \Rightarrow \frac{u_r}{u}\bigg|_R = \frac{dR}{dx} . \tag{2.8 a}$$

It follows immediately $u_r\big|_R = u\big|_R \frac{dR}{dx}$. (2.8 b)

Using the identity $A = \pi R^2$ the conservation equation (2.7) yields

$$\text{for } A=A(x): \boxed{A\frac{\partial \rho}{\partial t} + \frac{\partial}{\partial x}(A\rho u) = 0} \tag{2.9}$$

- If A=$A(x,t)$, the radial component of the air velocity u_r is defined by the condition that the normal velocity of the wall is equal to the normal air velocity at the wall:

$$U_\perp = u_\perp \text{ or} \tag{2.10 a}$$

$$U_r \cos\varphi - sp\sin\varphi = u_r\big|_R \cos\varphi - u\big|_R \sin\varphi . \tag{2.10 b}$$

Considering that $\frac{\partial R}{\partial x} = \tan\varphi$ it follows

$$u_r\big|_R = u\big|_R \frac{\partial R}{\partial x} + U_r - sp\frac{\partial R}{\partial x} . \tag{2.10 c}$$

The conservation equation (2.7) yields then

$$A\frac{\partial \rho}{\partial t} + \frac{\partial}{\partial x}(\rho A u) = \rho\left(sp\frac{\partial A}{\partial x} - 2\pi R U_r\right) . \tag{2.11}$$

This expression is valid for a wall moving horizontally with *sp* and independently in radial direction with U_r. In tunnel aerodynamics, it is only the vehicle displacement which changes the cross-section, thus

$$U_r = 0 \text{ and } \left(sp\frac{\partial A}{\partial x}\right)_{t\,=\,\text{const.}} = -\left(\frac{\partial A}{\partial t}\right)_{x\,=\,\text{const.}} . \qquad (2.12)$$

Eq. (2.11) can therefore be transformed into

$$\text{for } A=A(x,t){:}\ \boxed{\frac{\partial}{\partial t}(A\rho) + \frac{\partial}{\partial x}(A\rho u) = 0} \qquad (2.13)$$

Note that the thermodynamic flow values and the velocity component *u* have been set constant over the corresponding surfaces of the control volume. The sum of the integrands in eq. (2.7) can be set to zero since it is continuously differentiable and the integral over *dx* is zero for an arbitrary Δx.

2.1.2 The momentum equation

The general form of the momentum equation for an arbitrary control volume in vectorial form is given by

$$\frac{dM}{dt} = \int_V \frac{\partial}{\partial t}(\rho\underline{u})dV + \int_S \rho\underline{u}(\underline{v}\cdot\underline{n})dS = \int_S \underline{f}_S dS . \qquad (2.14)$$

The forces on the surface shall for the present purpose be restricted to the pressure force, thus

$$\underline{f}_S = -p\underline{n} \qquad (2.15)$$

viscous forces will be included in the considerations later. Using relation (2.2), the right hand surface integral can be transformed according to

$$-\int_S p\underline{n}dS = \int_V \underline{\nabla}p dV . \qquad (2.16)$$

After transforming the left hand surface integral to a volume integral according to Gauß' theorem and applying eq. (2.14) to the control volume in Figure 2.1, the *x*-component of the momentum equation in cylindric coordinates for axisymmetric flow becomes

$$x{:}\ \int_V \left[\frac{\partial}{\partial t}(\rho u) + \frac{\partial}{\partial x}(\rho u^2 + p) + \frac{1}{r}\frac{\partial}{\partial r}(r\rho u u_r)\right]dV = 0 . \qquad (2.17)$$

Following the same arguments as for the continuity equation, the 1D momentum equation in conservative variables yields

- for $A=A(x)$ with u_r given by eq. (2.8 b)

$$\text{for } A=A(x){:}\ \boxed{A\frac{\partial}{\partial t}(\rho u) + \frac{\partial}{\partial x}[A(\rho u^2 + p)] = p\frac{dA}{dx}} \qquad (2.18)$$

- for $A=A(x,t)$ with u_r given by eq. (2.10 c) and under the condition (2.12)

$$\text{for } A=A(x,t){:}\quad \boxed{\frac{\partial}{\partial t}(A\rho u)+\frac{\partial}{\partial x}[A(\rho u^2+p)] = p\frac{\partial A}{\partial x}} \tag{2.19}$$

2.1.3 The energy equation

The general form of the energy equation for an arbitrary control volume in vectorial form is given by

$$\frac{dE_t}{dt} = \int_V \frac{\partial}{\partial t}(\rho e_t)dV + \int_S \rho e_t(\underset{\sim}{v}\cdot\underset{\sim}{n})dS = \int_S \dot{w}_S dS \tag{2.20}$$

where the total energy is defined as $e_t = e+\frac{u^2}{2}$.

As before, the right handed side shall here be restricted to the time rate of work due to the pressure forces, thus

$$\dot{w}_S = -p(\underset{\sim}{v}\cdot\underset{\sim}{n}) . \tag{2.21}$$

Friction and heat transfer will be considered at a later stage as additional source terms. Using Gauß' theorem for the surface integrals, eq. (2.20) can be transformed to

$$\int_V \left[\frac{\partial}{\partial t}(\rho e_t)+\frac{\partial}{\partial x}(\rho u e_t)+\frac{1}{r}\frac{\partial}{\partial r}(r\rho e_t u_r)\right]dV = -\int_V \left(\frac{\partial}{\partial x}(pu)+\frac{1}{r}\frac{\partial}{\partial r}rpu_r\right)dV . \tag{2.22}$$

Applying eq. (2.22) to the control volume in Figure 2.1 and following the same argumentation as before, the 1D energy equation reads

- for $A=A(x)$ with u_r given by eq. (2.8 b)

$$\text{for } A=A(x){:}\quad \boxed{A\frac{\partial}{\partial t}(\rho e_t)+\frac{\partial}{\partial x}(A\rho u h_t) = 0} \tag{2.23}$$

- in the case of $A=A(x,t)$, using u_r given by eq. (2.10 c)

$$\text{for } A=A(x,t){:}\quad \boxed{\frac{\partial}{\partial t}(A\rho e_t)+\frac{\partial}{\partial x}(A\rho u h_t) = -p\frac{\partial A}{\partial t}} . \tag{2.24}$$

2.2 The governing equations for tunnel aerodynamics including friction, heat and mass transfer

The governing equations for the treatment of problems related to tunnel aerodynamics are composed of the 1D Euler equations, accounting for the frictionless flow in a tube with time and space variable area function and additional source terms, i.e. corrective terms accounting for local 3D effects.

2.2.1 Conservation equations in the tunnel frame of reference

The system of 1D conservation equations for the flow in a tube with spatially and temporally varying cross-section is now defined. It can be summarized and presented in vectorial form as:

$$\frac{\partial}{\partial t}(A\underset{\sim}{u}) + \frac{\partial}{\partial x}(A\underset{\sim}{f}) = \underset{\sim}{S}^0 + \underset{\sim}{S}^1 + \underset{\sim}{S}^a \text{ ,where} \tag{2.25}$$

$$\underset{\sim}{u} = \begin{pmatrix} \rho \\ \rho u \\ \rho e_t \end{pmatrix}, \underset{\sim}{f} = \begin{pmatrix} \rho u \\ \rho u^2 + p \\ \rho u h_t \end{pmatrix} \tag{2.25 a}$$

$$\underset{\sim}{S}^0 = \begin{pmatrix} 0 \\ p \\ 0 \end{pmatrix}\frac{\partial A}{\partial x} \text{ and } \underset{\sim}{S}^1 = \begin{pmatrix} 0 \\ 0 \\ -p \end{pmatrix}\frac{\partial A}{\partial t} \tag{2.25 b}$$

Remarks:

- The area change is only due to the horizontal vehicle movement. No additional radial wall movement is allowed.
- For an only space dependent area function, $A = A(x)$, the term $\underset{\sim}{S}^1 = 0$.
- In the case of constant cross-section, A=const., the terms $\underset{\sim}{S}^0 = \underset{\sim}{S}^1 = 0$ and equation (2.25) can be divided by the area function A.
- The term $\underset{\sim}{S}^a$ stands for additional source terms due to friction, heat and mass transfer or pressure losses due to particular geometries. This term will be discussed in section 5.

2.2.2 Conservation equations in the vehicle frame of reference

Eq. (2.25) is transformed in the vehicle frame of reference by the variable transformation

$$t' = t \text{ and } x' = x - x_v \ . \tag{2.26}$$

The symbol x_v stands for the actual position of the origin of the primed system as indicated in Figure 2.2. The total differential of a function $h(x, t)$ defined relative to the tunnel fixed system is

$$dh = \frac{\partial h}{\partial t}dt + \frac{\partial h}{\partial x}dx \ . \tag{2.27}$$

The relation between the partial derivatives relative to the unprimed and the primed system follows as

$$\frac{\partial}{\partial t'} = \frac{\partial}{\partial t} + \dot{x}_v \frac{\partial}{\partial x} \text{ and } \frac{\partial}{\partial x'} = \frac{\partial}{\partial x}\,, \tag{2.28}$$

where $\dot{x}_v = \left(\frac{\partial x}{\partial t'}\right)_{x' = \text{const.}}$ is the actual speed of the primed system, i.e. the vehicle speed *sp*.

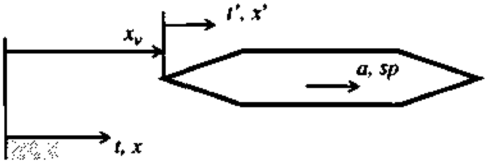

Figure 2.2 Unprimed tunnel fixed and primed vehicle fixed coordinate system

With this preparation, the system of 1D conservation equations in the vehicle fixed coordinate system is

$$A\frac{\partial}{\partial t'}\underset{\sim}{u} + \frac{\partial}{\partial x'}A\underset{\sim}{f} = \underset{\sim}{S}^{0'} + \underset{\sim}{S}^{1'} + \underset{\sim}{S}^{2'} + \underset{\sim}{S}^{a}\text{, where} \tag{2.29}$$

$$\underset{\sim}{u} = \begin{pmatrix} \rho \\ \rho u \\ \rho e_t \end{pmatrix},\ \underset{\sim}{f} = \begin{pmatrix} \rho u \\ \rho u^2 + p \\ \rho u h_t \end{pmatrix} \tag{2.29 a}$$

$$\underset{\sim}{S}^{0'} = \begin{pmatrix} 0 \\ p \\ 0 \end{pmatrix}\frac{dA}{dx'},\ \underset{\sim}{S}^{1'} = \begin{pmatrix} 0 \\ 0 \\ p \end{pmatrix} sp\frac{dA}{dx'} \text{ and } \underset{\sim}{S}^{2'} = sp\frac{\partial}{\partial x'}(A\underset{\sim}{u}) \tag{2.29 b}$$

Remarks:

- In the primed coordinate system, the area function is only space dependent $A = A(x')$, thus the term $\underset{\sim}{S}^{0'}$ is identical to $\underset{\sim}{S}^{0}$.
- The term $\underset{\sim}{S}^{1'}$ is identical to $\underset{\sim}{S}^{1}$ (see eq. (2.12)).
- The term $\underset{\sim}{S}^{2'}$ accounts for the flux due to the relative movement of the control surfaces.
- The air velocity *u* is still taken relative to the tunnel frame of reference. It is related to the air velocity *v* relative to the vehicle frame of reference by

$$v = u - sp\ . \tag{2.30}$$

- The source term $\underset{\sim}{S}^{a}$ contains the same elements as in eq. (2.25), i.e. it contains the source terms as they appear for an observer in the tunnel frame of reference.

After lengthy algebra involving the use of the first line for the derivation of the second and the use of the first and the second line for the derivation of the third line, system (2.29) can be written with the air velocity in the vehicle frame of reference as

$$A\frac{\partial}{\partial t'}\underline{u}' + \frac{\partial}{\partial x'}A\underline{f}' = \underline{S}^{0'} + \underline{S}^{1''} + \underline{S}^{2''} + \underline{S}^{a}\text{, where} \tag{2.31}$$

$$\underline{u}' = \begin{pmatrix} \rho \\ \rho v \\ \rho e'_t \end{pmatrix}, \underline{f}' = \begin{pmatrix} \rho v \\ \rho v^2 + p \\ \rho v h'_t \end{pmatrix}, \tag{2.31 a}$$

$$e_t' = c_v T + \frac{v^2}{2}, h_t' = c_p T + \frac{v^2}{2} \tag{2.31 b}$$

$$\underset{\sim}{S}^{0'} = \begin{pmatrix} 0 \\ p \\ 0 \end{pmatrix}\frac{dA}{dx'}, \underset{\sim}{S}^{1''} = sp\begin{pmatrix} 0 \\ -S_1^a \\ \frac{sp}{2}S_1^a - S_2^a \end{pmatrix} \text{ and } \underset{\sim}{S}^{2''} = -\begin{pmatrix} 0 \\ A\rho \\ A\rho v \end{pmatrix}\dot{s}p \tag{2.31 c}$$

For constant vehicle speed ($\underset{\sim}{S}^{2''} = 0$), eq. (2.31) takes almost the same form as the conservation equations in the tunnel fixed coordinate system (2.25) if *u* is replaced by *v*. As formal difference remain the source terms for the momentum and the energy equation, which account for the change of the reference system. If the additional source term $\underline{S}^a$ is combined with the term $\underset{\sim}{S}^{1''}$, a new additional source term $\underline{S}^{a'}$ in the vehicle frame of reference is obtained. This term accounts for the fact that relative to an observer traveling with the vehicle the pressure and the friction force originating at the vehicle surface are stationary but forces originating at the tunnel wall move with the negative vehicle speed and require an additional source term in the energy equation.

For tunnel aerodynamics, equations in the three forms (2.25), (2.29) and (2.31) are useful for various problems. Attention must be paid to a change of the reference system since the source terms do not follow intuitively.

2.2.3 Constitutive equations

For tunnel aerodynamics, air can be considered as a perfect gas (ideal gas with constant specific heats) because its specific heat c_p varies in the temperature interval T=[200 K, 1000 K] by only approximately 8% [1, p.424]. This range is barely used for flow phenomena in tunnel aerodynamics and thus the assumption of air as perfect gas is widely used.

The equation of state for ideal gases,

$$\boxed{p = \rho R T}, \tag{2.32}$$

delivers the yet missing constitutive relation to solve for the 4 unknowns ρ, u, T and p.

The constant caloric values are related by

$$\kappa = \frac{c_p}{c_v} \tag{2.33}$$

$$c_p = R + c_v \tag{2.34}$$

The gas considered here is dry air in its normal composition as given for example in [1, p. 207]. The caloric values used in NUMSTA summarized in Table 2.1. Other authors may use slightly different values which are based on a different assumption of the air composition.

For ideal gases, changes of internal energy and enthalpy can be expressed by

$$de = c_v dT \text{ and } dh = c_p dT . \tag{2.35}$$

For isentropic change of state the following useful relations can be derived from the definition of the entropy:

$$p\rho^{-\kappa} = \text{const.}, T\rho^{1-\kappa} = \text{const. and } p^{1-\kappa}T^{\kappa} = \text{const.} \tag{2.36}$$

Table 2.1 Caloric values used in the present simulation

symbol	explanation	value
c_p	specific heat at constant pressure	1005.7 J / (kg K)
R	individual gas constant	290.0 J / (kg K)
c_v	specific heat at constant volume	715.7 J / (kg K)
κ	isentropic exponent	1.4052

2.2.4 Mathematical nature of the Euler equations

The Euler equations describe a purely convective flow problem. Convective fluxes appear with first order derivative, whereas diffusive fluxes are indicated by second order derivatives. These terms, describing the viscous effects, have been replaced here by source terms which are functions of the conservative variables only. Thus, the system (2.25) is hyperbolic.

This physical consideration for the nature of the Euler equations can be sustained by showing that the propagation directions of waves or characteristics are real and distinct.

The Jacobian matrix for the conservative variables is determined by

$$\bar{\bar{J}} = \frac{\partial}{\partial \bar{u}} \bar{f} . \tag{2.37}$$

It reads [16, p.144]

$$\bar{\bar{J}} = \begin{bmatrix} 0 & 1 & 0 \\ (\kappa-3)\frac{u^2}{2} & (3-\kappa)u & \kappa-1 \\ ((\kappa-1)u^3-\kappa u e_t) & \left(\kappa e_t - 3\frac{\kappa-1}{2}u^2\right) & \kappa u \end{bmatrix} . \tag{2.38}$$

The right handed eigenvectors resulting from $\bar{\bar{J}}\bar{\bar{R}} = \bar{\bar{R}}\bar{\bar{\Lambda}}$ are given in the columns of the expression [16, p. 160]

$$\bar{\bar{R}} = \begin{bmatrix} 1 & 1 & 1 \\ u & u+a & u-a \\ \frac{u^2}{2} & (h_t+ua) & (h_t-ua) \end{bmatrix} \tag{2.39}$$

and the left handed eigenvectors defined according to $\bar{\bar{L}}\bar{\bar{J}} = \bar{\bar{\Lambda}}\bar{\bar{L}}$ form the lines of

$$\bar{\bar{L}} = \bar{\bar{R}}^{-1} = \begin{bmatrix} \left(1-\frac{\kappa-1}{2a^2}u^2\right) & \frac{\kappa-1}{a^2}u & -\frac{\kappa-1}{a^2} \\ \left(\frac{\kappa-1}{2}u^2-ua\right) & a-(\kappa-1)u & \kappa-1 \\ -\left(\frac{\kappa-1}{2}u^2+ua\right) & a+(\kappa-1)u & -(\kappa-1) \end{bmatrix} \tag{2.40}$$

The Jacobian $\bar{\bar{J}}$ can be diagonalized by

$$\bar{\bar{\Lambda}} = \bar{\bar{L}}\bar{\bar{J}}\bar{\bar{R}} = \begin{bmatrix} u & 0 & 0 \\ 0 & u+a & 0 \\ 0 & 0 & u-a \end{bmatrix} = \begin{bmatrix} \lambda_1 & 0 & 0 \\ 0 & \lambda_2 & 0 \\ 0 & 0 & \lambda_3 \end{bmatrix}. \qquad (2.41)$$

The eigenvalues λ_1, λ_2 and λ_3 are real and distinct, thus the Euler equations are of hyperbolic type.

The domain of dependence of the hyperbolic problem is limited by the two characteristics with extreme propagation speeds, λ_2 and λ_3. The particle trajectory λ_1 is within these lines. Figure 2.3 shows the domain of dependence and of influence of a point P which is in the space-time domain to be computed. The graph shows that every point in the computational domain depends on the initial conditions $u(x, 0)$ and potentially also on the boundary conditions $u(x_s, t)$ and $u(x_e, t)$. For the problem to be well posed it has to be formulated as an initial-boundary value problem.

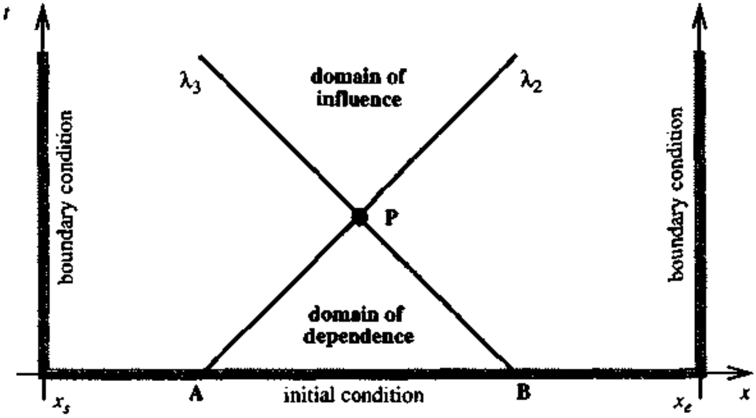

Figure 2.3 Domain of dependence and of influence of a point P in the domain

2.3 Summary of chapter 2

In this chapter, the system of the 1D Euler equations for flow in a tube with spatio-temporally varying cross-section in the tunnel frame of reference are derived. They are summarized in eq. (2.25). A coordinate transformation yields the system of 1D conservation equations in the vehicle frame of reference, once written with air velocities relative to the tunnel (eq. (2.29)) and once written with air velocities relative to the vehicle (eq. (2.31)).

Mass, momentum and energy exchange have been introduced by an additional source term $\underset{\sim}{S}_a$.

This term has not been discussed here; its detailed discussion is subject of chapter 5.

The system of Euler equations is hyperbolic, which restricts the choice of the numerical method and gives information about the required initial and boundary conditions.

3 CHOICE OF THE NUMERICAL SOLVER

The discretization of the Euler equations implemented in NUMSTA has been chosen after evaluating the performance of several numerical solvers with a test case. With respect to the domain of application of the computer program, which involves the simulation of wave generation and interaction of shocks in a tunnel system, the solvers were tested with the Riemann problem, the non-linear inviscid wave propagation in a shock tube.

3.1 A short classification of numerical schemes

Early discretization methods for the Euler equations evolved in the early 50's [15, II, p. 125 ff]. Important contributions followed the development of computer technology. A major stream of innovative publications can be observed between the end of the 70's until the mid-80's.

SPACE-CENTERED SCHEMES are based on purely mathematical continuations of the Taylor expansion. Important types combine space and time integration (e.g. Lax-Friedrich, Lax-Wendroff). Methods with separate spatial and temporal discretization allow for variable accuracy in the two directions (e.g. Beam & Warming, Jameson).

UPWIND SCHEMES introduce physical properties of the flow into the discretized form of the Euler equations. Flux vector splitting schemes are based on the directional discretization of the flux derivatives (e.g. Steger and Warming, van Leer). Riemann solvers or Gudonov type schemes are based on the non-linear local solution of the conservation equations for discontinuous neighboring states (see section 3.3).

Phenotypes of both groups of schemes appear in explicit and implicit formulations.

Both classes of numerical methods for the Euler equations produce relatively good results in smooth regions of the flow; however, in regions with strong gradients or shocks, second order schemes produce oscillations. This is predicted by Gudonov's theorem: "A linear, monotonicity preserving method is at most first order accurate" [17, p. 174]. Attempts were made to deal with this fundamental limitation by the concept of artificial viscosity. However, it is difficult to determine the appropriate viscosity coefficient to reduce oscillations without smearing sharp gradients.

Rather than reducing oscillations once they are created, TOTAL VARIATION DIMINISHING (TVD) methods avoid oscillations before they occur. The idea is here to detect the creation of a new extremum by the solver and to control this situation with a non-linear limiter function, which makes the scheme TVD under certain conditions for the limiter function. Monotonicity is a stronger criterion than TVD but the latter is sufficient to avoid the creation of overshoots at discontinuities.

Methods which are at least 2^{nd} order accurate on smooth solutions and which give well-resolved, non-oscillatory discontinuities are called HIGH RESOLUTION METHODS.

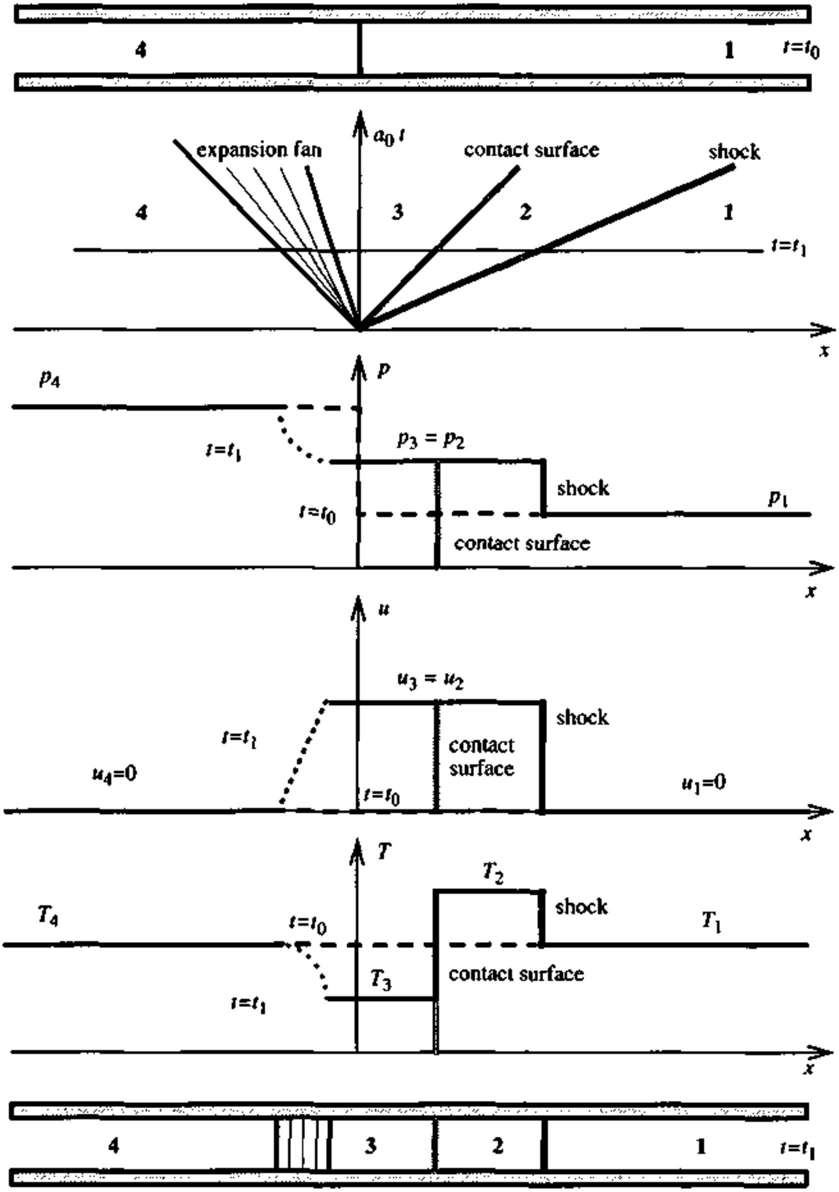

Figure 3.1 Distribution of flow values in an inviscid shock tube: sketch of pressure, velocity and temperature distribution at two different times with indication of shock, expansion fan and contact surface

3.2 Comparison of numerical solvers for the shock tube problem

An analytical solution for the flow induced in a shock tube after releasing gas instantaneously from the high pressure reservoir into a region of low pressure can be given if friction is neglected. The solution for this classical problem can be found in standard text books of fluid dynamics such as [8, p.374 ff.].

After gas is released from the high pressure reservoir, a shock is propagating into the low pressure zone and an expansion wave moves into the high pressure reservoir. Gas initially in the high pressure reservoir remains separated from gas initially in the low pressure reservoir by the contact surface.

This process and a qualitative distribution of flow values are sketched in Figure 3.1. In the following development, indices according to this figure are used. Table 3.1 shows the initial values used for this test case. As test fluid air was chosen with the caloric values given in Table 2.1. A shock generated with a pressure ratio of 10 can be considered a strong shock. This parameter combination allows to see if the solver is robust or if numerical oscillations cause an early 'explosion' of the solver, even though the CFL condition is fulfilled.

3.2.1 Theory of non linear wave propagation and shock relations

For the analytical solution of the inviscid shock tube problem, the following assumptions are made:

- the flow is 1-D,
- the flow is adiabatic and without friction, thus isentropic except for the shock,
- the gases in both reservoirs are chemically identical,
- the gas can be considered a perfect gas (ideal gas with constant c_p and c_v).

The exact solution for the flow values away from the shock can be found with the theory of nonlinear wave propagation. The Euler equations in non-conservative form for the above assumptions write:

$$\frac{\partial \rho}{\partial t} + u\frac{\partial \rho}{\partial x} + \rho\frac{\partial u}{\partial x} = 0 \tag{3.1 a}$$

$$\frac{\partial u}{\partial t} + u\frac{\partial u}{\partial x} + \frac{1}{\rho}\frac{\partial p}{\partial x} = 0 \tag{3.1 b}$$

$$\frac{\partial s}{\partial t} + u\frac{\partial s}{\partial x} = 0 \tag{3.1 c}$$

The system (3.1) can be transformed to:

$$\frac{2}{\kappa - 1}\left(\frac{\partial a}{\partial t} + u\frac{\partial a}{\partial x}\right) + a\frac{\partial u}{\partial x} = 0 \tag{3.2 a}$$

$$\frac{\partial u}{\partial t} + u\frac{\partial u}{\partial x} + \frac{2}{\kappa - 1}a\frac{\partial a}{\partial x} = 0 \tag{3.2 b}$$

Adding or substracting (3.2 b) and (3.2 a) the directions for the characteristics and the expressions for the Riemann invariants follow:

$$\left(\frac{\partial}{\partial t}+(u\pm a)\frac{\partial}{\partial x}\right)\left(u\pm\frac{2}{\kappa-1}a\right) = 0\ . \tag{3.3}$$

Equation (3.3) can be interpreted as a material derivative of the second term with respect to the characteristic directions C^+ and C^-

$$\left(\frac{\partial x}{\partial t}\right)_{C^\pm} = u\pm a \tag{3.4}$$

and the Riemann invariants are given by the second term in (3.3) as

$$\text{along } C^{\pm}\text{: } u\pm\frac{2}{\kappa-1}a = \text{const.} \tag{3.5}$$

The third direction along which information propagates is the particle trajectory

$$\text{along } C^0\text{: } \frac{\partial x}{\partial t} = u\ , \tag{3.6}$$

along which the condition of isentropic flow (3.1 c) applies, which yields with the definition of the entropy

$$pa^{-\frac{2\kappa}{\kappa-1}} = \text{const.}\ . \tag{3.7}$$

Note that the directions of the wave propagation are locally defined, i.e. they are in general curved lines.

Across the shock, the assumption of isentropic flow is no longer valid. The jump conditions can be derived from the integral form of the conservation equations for a control volume relating an entry state '1' with an exit state '2':

$$\rho_1 u_1 = \rho_2 u_2\ , \tag{3.8}$$

$$\rho_1 u_1^2+p_1 = \rho_2 u_2^2+p_2 \text{ and} \tag{3.9}$$

$$h_1+\frac{u_1^2}{2} = h_2+\frac{u_2^2}{2}\ . \tag{3.10}$$

Equations (3.8) - (3.10) can be solved for the state '2'. Two solutions are possible, identity of state '1' and '2' and the jump conditions given as

$$\frac{u_2}{u_1} = \frac{\rho_1}{\rho_2} = 1-\frac{2}{\kappa+1}\left(1-\frac{1}{M^2}\right), \tag{3.11}$$

$$\frac{p_2}{p_1} = 1+\frac{2\kappa}{\kappa+1}(M^2-1) \text{ and} \tag{3.12}$$

$$\frac{T_2}{T_1} = \frac{a_2^2}{a_1^2} = \left[1+\frac{2\kappa}{\kappa+1}(M^2-1)\right]\left[1-\frac{2\kappa}{\kappa+1}\left(1-\frac{1}{M^2}\right)\right]. \tag{3.13}$$

3.2.2 Analytical solution of the shock tube problem

If the above relations are applied to the shock tube problem with indices as given in Figure 3.1, it is found that the trajectory of the particles which were initially at the separation surface forms a contact surface, across which pressure and air velocity are constant but the temperature jumps, thus:

$$p_1 = p_3 \tag{3.14}$$

$$u_2 = u_3. \tag{3.15}$$

With the shock speed u_s, the shock Mach number be defined as $M_s = \frac{u_s}{a_1}$. In the case T_4=T_1 the shock Mach number is related to the initial values for pressure and density in the high and low pressure reservoir with the following relation

$$\frac{p_4}{p_1} = \frac{\rho_4}{\rho_1} = \left[1+\frac{2\kappa}{\kappa+1}(M_s^2-1)\right]\left[1-\frac{\kappa-1}{\kappa+1}\frac{M_s^2-1}{M_s}\right]^{-\frac{2\kappa}{\kappa-1}}. \tag{3.16}$$

The pressure jump across the shock is

$$\frac{p_2}{p_1} = 1+\frac{2\kappa}{\kappa+1}(M_s^2-1) \tag{3.17}$$

and the air velocity behind the shock is given by

$$u_2 = \frac{2}{\kappa+1}\frac{M_s^2-1}{M_s}a_1. \tag{3.18}$$

The temperature jump across the normal shock is related to the increase of the speed of sound and the shock Mach number by

$$\frac{T_2}{T_1} = \frac{a_2^2}{a_1^2} = \left[1+\frac{2\kappa}{\kappa+1}(M_s^2-1)\right]\left[1-\frac{2}{\kappa+1}\left(1-\frac{1}{M_s^2}\right)\right]. \tag{3.19}$$

The missing value T_3 results from the Riemann invariant across the expansion fan. It reads:

$$\frac{2}{\kappa-1}a_4 = u_3+\frac{2}{\kappa-1}a_3, \tag{3.20}$$

which can now be solved for a_3 and T_3 follows immediately with

$$a_3^2 = \kappa R T_3 \ . \tag{3.21}$$

The analytical results for the flow values in the different regions of an example are displayed in Table 3.1.

Table 3.1 Initial conditions and analytical results for the shock tube problem

	value in zone			
symbol	1	2	3	4
p [Pa]	10000	28461.3		100000
u [m/s]	0	282.70		0
T [K]	293.15	409.47	204.27	293.15
ρ [kg/m^3]	0.117628	0.239679	0.480449	1.176284

The shock Mach number is here M_s=1.6062 and the shock speed is u_s=555.16 m/s. The shock speed being constant, the shock position at different times is:

$$x_s = x_{s0} + u_s t \tag{3.22}$$

with x_{s0} as the initial position of the separation surface.

The exact solution for the flow values across the expansion fan result from applying the conservation equations in their form (3.2) with boundary conditions given by the confining ξ-characteristics. Substituting x and t by $z = \frac{x}{t}$ equations (3.2) write

$$\frac{2}{\kappa-1}(u-z)a' + au' = 0 \tag{3.23 a}$$

$$u'(u-z) + \frac{2}{\kappa-1}aa' = 0, \tag{3.23 b}$$

where the prime denotes a derivative to z only.

Solutions of the form $u = A_1 + A_2 z$ and $a = B_1 + B_2 z$ are sought with boundary conditions given by the characteristic line C$^-$ bordering to the zone 4 $u_4 = 0$ and a_4. The result is

$$\frac{u}{a_4} = \frac{2}{\kappa+1}\left(1 + \frac{x}{a_4 t}\right) \tag{3.24 a}$$

$$\sqrt{\frac{T}{T_4}} = \frac{a}{a_4} = \frac{2}{\kappa+1}\left(1 - \frac{\kappa-1}{2}\frac{x}{a_4 t}\right). \qquad (3.24\text{ b})$$

Isentropic flow across the expansion fan according to equation (3.7) gives the corresponding pressure as

$$\frac{p}{p_4} = \left(\frac{a}{a_4}\right)^{\frac{2\kappa}{\kappa-1}}. \qquad (3.24\text{ c})$$

The result shows that u and a are constant along lines with z=const. These are the characteristic lines of the C^--family in the expansion fan. This can be shown by applying the Riemann invariants from a point A on a C^--characteric to a point B on the same C^--characteric with a priori unknown path. Since the characteristics of the C^+-family connect A and B to the initial state in zone 4, the flow values u and a have to be equal in A and in B. Thus, the C^--characteristics are straight lines in the expansion fan. This is not the case for the family of C^+-characteristics, which change their slope from zone 4 to zone 3 gradually.

3.2.3 Numerical Solution of the shock tube problem

The test case requires the following initial conditions:

$$\begin{pmatrix}\rho\\ u\\ T\end{pmatrix} = \begin{cases}(\rho_4, u_4, T_4)^T, x \le 0\\ (\rho_1, u_1, T_1)^T, x > 0\end{cases} \qquad (3.25)$$

with the values as given in Table 3.1. The simulation domain and time were chosen such that no wave reflections at the ends occur. The mesh width was chosen to $\Delta x = 0.1\,\mathrm{m}$ and the time step was $\Delta t = 0.1\,\mathrm{ms}$. This arbitrary choice yields a CFL number of $CFL \approx 0.69$ which is inferior to the stability criterion. The initial shock position is actually $\widehat{x_{s0}} = 0$. In order to account for the discrete nature of numerical solvers, the initial shock position has been shifted by

$$x_{s0} = \frac{p_4 - p_2}{p_4 - p_1}\Delta x \approx 0.0795m\ . \qquad (3.26)$$

In order to visualize the fit of the numerical with the exact analytical solution, the shock tube problem was solved for $t \le 6$ ms. Figure 3.2 and Figure 3.3 show the result with the 1st order FDS solver of Roe and the 2nd order TVD solver of Roe, respectively.

The graphs show the exact analytical solution (solid line without markers) and the numerical solution (solid line with circles at the position of each data point) at the times t=2 ms, t=4 ms and t=6 ms.

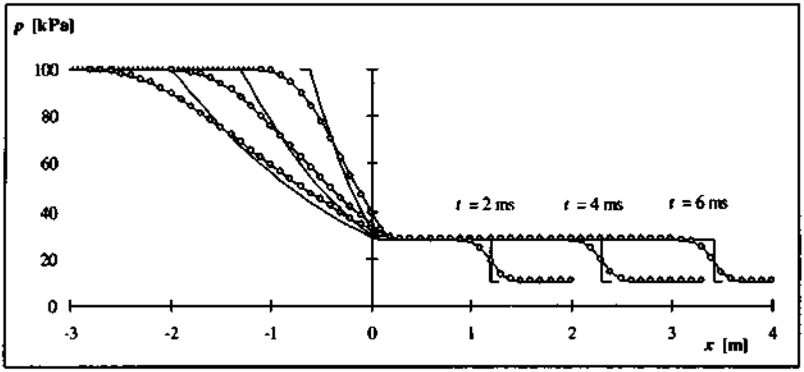

Figure 3.2 Solution of the shock tube problem, Roe's 1^{st} order FDS solver versus exact analytical solution

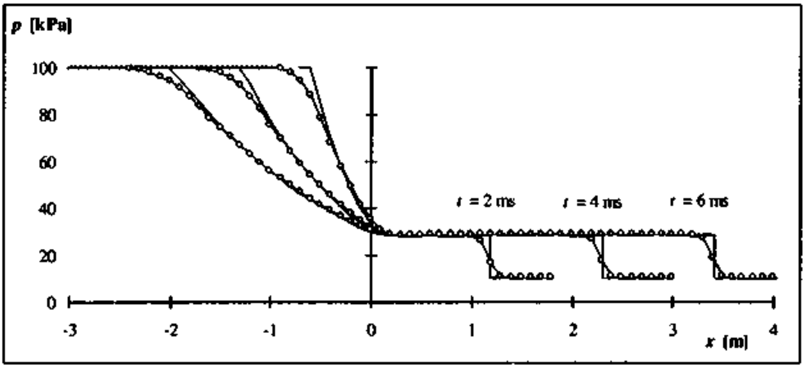

Figure 3.3 Solution of the shock tube problem, 2^{nd} order TVD Roe solver versus exact analytical solution

Both solvers show no oscillations around the flow discontinuities. The 2^{nd} order solver resolves the shock better than the 1^{st} order solver. The fit of the numerical solution with the analytical result is quite good over a wide range. The pressure plateau behind the shock (zone 2) shows a relative error of some 0.02%. Deviations from the exact solution occur around the shock position and at the end of the expansion fan. The starting point of the expansion fan remains stationary as is the case for the sonic problem. The shock is smeared over 6-7 and 4-5 mesh points for the 1^{st} and 2^{nd} order solver, respectively.

The behavior of these non-oscillatory solvers can be compared with a classical space centered solver. A calculation of a shock tube problem was performed with the 2nd order Mac Cormack scheme. In this case, a solution for the pressure ratio 10 and the same CFL number as before could not be obtained. The solver's oscillatory nature causes an early 'explosion' of the numerical results. In order to demonstrate the typical oscillatory behavior of this solver predicted by Gudonovs theorem, results for a pressure ratio of 2 are given in Figure 3.4.

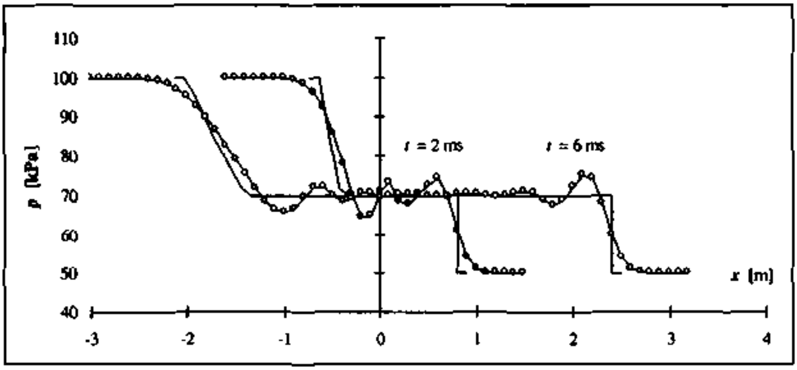

Figure 3.4 Solution of the shock tube problem with a pressure ratio of 2, 2nd order Mac Cormack solver versus exact analytical solution

For a better characterization of the 2nd order solver by Roe, the dissipative behavior for a high number of time steps has been examined. The Figs. 3.5 a-c show the shock form after 1000, 3000 and 5000 time steps. The mesh width and the time step were the same as in the case before. The initial corrected shock position was here $x_{s0} = 500.0795\text{m}$.

The graphs show that the shock is smeared constantly over 5 mesh points. This value has already been found after t=2 ms. Thus, the shock dilatation is constant over time. The numerical dissipation of the solver is therefore low. The shock position is well in agreement with the analytical finding suggesting a shift of $u_s = 555.16\text{m/s} \Rightarrow u_s \cdot 0.2\text{s} = 111.032\text{m}$ between two images (see Figure 3.5).

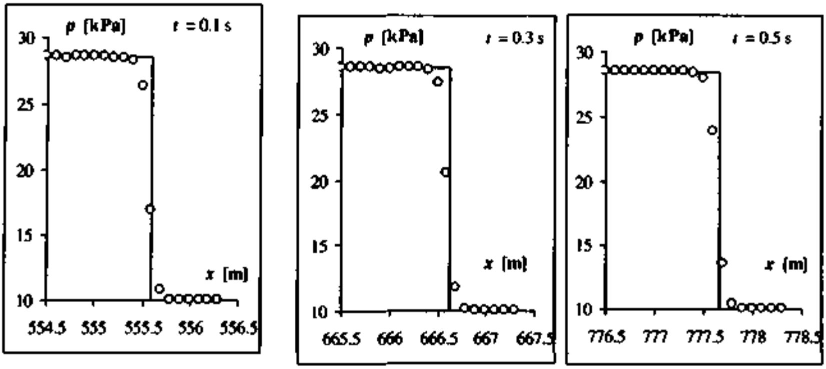

Figure 3.5 Shock shapes after 1000, 3000 and 5000 time steps obtained with the 2nd order TVD solver of Roe with minmod limiter

In the preceding considerations, it has been shown that the solver of Roe delivers for the Riemann problem a solution with low numerical dissipation and exact values in smooth regions of the flow. Its extraordinary behavior for the treatment of flow discontinuities and the absence of oscillations make it a perfect candidate for the solution of flows for which the creation and the interaction of strong pressure waves or shock waves are characteristic.

The 2nd order solver of Roe differs from the 1st order solver of Roe only by an additional flux correction term (FCT), which is computationally relatively inexpensive; the solution, however, improves considerably. The TVD nature of this solver allows further to adjust the limiter function to the kind of problem treated. Here, the minmod limiter has been chosen. This limiter function produces relatively smooth solutions, which are well behaved at shocks and give a good fit for wave type solutions. The explicit solver can be implemented in a compact form. It shows high computational performance and can be vectorized.

Based on these considerations, the 2nd order TVD solver of Roe has been chosen as the numerical solver for the Euler equations in NUMSTA.

3.3 The numerical algorithm implemented in NUMSTA

Two groups of Riemann solvers can be distinguished. EXACT RIEMANN SOLVERS find the exact analytical solution of the Riemann problem for a cell on the basis of approximated flow values over the cell (e.g. Gudonov, Glimm). APPROXIMATE RIEMANN SOLVERS or Flux Difference Splitting (FDS) schemes update the flow values in the cell with the difference of entering and exiting fluxes across the cell interfaces and find therefore an approximate solution. These fluxes are computed exactly based on the approximate flow values on both sides of the corresponding cell interface (e.g. Roe, Osher, Harten). For a first order scheme, the approximation employed is a constant flow value within the cell. Higher order schemes can be formulated with a non-constant distribution of flow values within the cell or with corrective higher order fluxes.

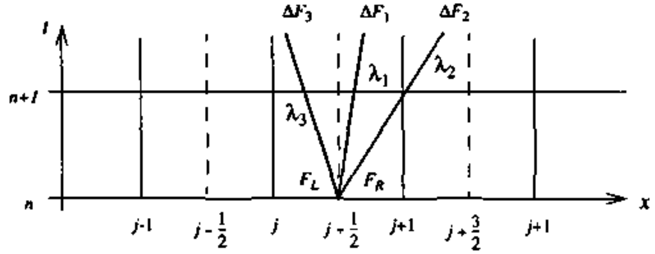

Figure 3.6 Waves and associated flux differences originating at a cell interface

A domain can be discretized into cells with cell 'centers' and cell interfaces according to Figure 3.6. The cell 'centers' are indexed with $0, \ldots, j, \ldots, N$ and the cell interfaces have the indices $\frac{1}{2}, \ldots, j+\frac{1}{2}, N-\frac{1}{2}$. Both the cell width and the time step may vary in space and in time. The cell 'centers' are the mesh points; they may not coincide with the geometrical cell center. Their position has to be considered in the interpolation of the flow values at the cell interfaces.

In the following subsections, the Roe solver and the additional terms required for tunnel aerodynamics are developed step by step. Convergence of the scheme is discussed in chapter 6.

3.3.1 The classical 1st order scheme of Roe for the Euler equations

The system of Euler equations for constant cross-section is given by eq. (2.25) as

$$\frac{\partial}{\partial t}\underset{\sim}{u} + \frac{\partial}{\partial x}\underset{\sim}{f} = 0 \ . \tag{3.27}$$

Roe's solver [20] can be derived by transforming the flux term in eq. (3.27) into its wave contributions.

With the definition of the Jacobian in eq. (2.37) it follows

$$\frac{\partial}{\partial t}\underset{\sim}{u} + \bar{\bar{J}}\frac{\partial}{\partial x}\underset{\sim}{u} = 0 \ , \tag{3.28}$$

then with relation (2.41)

$$\frac{\partial}{\partial t}\underset{\sim}{u} + \bar{\bar{R}}\bar{\bar{\Lambda}}\bar{\bar{L}}\frac{\partial}{\partial x}\underset{\sim}{u} = 0 \ . \tag{3.29}$$

Defining the characteristic variables as $\partial\underset{\sim}{w} = \bar{\bar{L}}\partial\underset{\sim}{u}$, eq. (3.29) transforms into

$$\frac{\partial}{\partial t}\underset{\sim}{u} + \bar{\bar{R}}\bar{\bar{\Lambda}}\frac{\partial}{\partial x}\underset{\sim}{w} = 0 \ . \tag{3.30}$$

Taking advantage of the diagonal form of the eigenvalue matrix, this expression can be written to yield

$$\frac{\partial}{\partial t}\underline{u} = -\sum_{l=1}^{3} \underline{r}_l \lambda_l \frac{\partial w_l}{\partial x} = -\frac{\partial}{\partial x}\underline{f} . \tag{3.31}$$

After this preparation, eq. (3.31) can now be discretized in a finite volume approach integrating both in space and in time using the notation introduced in Figure 3.6

$$u_j^{n+1} - u_j^n = -\left(\frac{\Delta t}{\Delta x}\right)_j^n \left(\underline{F}^n_{j+\frac{1}{2}} - \underline{F}^n_{j-\frac{1}{2}}\right) \tag{3.32}$$

where $\Delta x_j = x_{j+\frac{1}{2}} - x_{j-\frac{1}{2}}$ and the numerical fluxes at the cell interfaces $j+\frac{1}{2}$ and $j-\frac{1}{2}$ can be formulated with the flux difference due the left or right traveling waves as:

$$\underline{F}_{j+\frac{1}{2}} = \underline{F}_L + \sum_{\lambda_i < 0} (\underline{r}_i'\lambda_i'\Delta w_i')_{j+\frac{1}{2}} \text{ or } \underline{F}_{j+\frac{1}{2}} = \underline{F}_R - \sum_{\lambda_i > 0} (\underline{r}_i'\lambda_i'\Delta w_i')_{j+\frac{1}{2}} \tag{3.33}$$

where the indices L and R stand for discontinuous flow values left and right of the cell interface and the prime indicates a special average. This average assigns flow values to the waves originating at the cell interface as a function of the flow values $\underline{u}_L$ and $\underline{u}_R$. Roe proposed to derive the average as to satisfy the condition

$$\sum_i \underline{r}_i'\lambda_i'\Delta w_i' = \underline{F}_R - \underline{F}_L . \tag{3.34}$$

The expressions for the eigenvalues and the right handed eigenvectors have been given in section 2.2.4. The discretized expressions for the characteristic variables or the wave strength is given by

$$\Delta w_1' = \frac{1}{a'^2}(a'^2\Delta\rho - \Delta p) \qquad \text{for } \lambda_1' = u' , \tag{3.35 a}$$

$$\Delta w_2' = \frac{1}{2a'^2}(\Delta p + \rho' a' \Delta u) \qquad \text{for } \lambda_2' = u' + a' \text{ and} \tag{3.35 b}$$

$$\Delta w_3' = \frac{1}{2a'^2}(\Delta p - \rho' a' \Delta u) \qquad \text{for } \lambda_3' = u' - a' ., \tag{3.35 c}$$

where $\Delta\rho = \rho_R - \rho_L$, $\Delta p = p_R - p_L$ and $\Delta u = u_R - u_L$.

Roe's average follows as:

$$\rho' = \sqrt{\rho_L \rho_R} , \tag{3.36 a}$$

$$u' = \frac{r u_L + u_R}{r+1}\ , \tag{3.36 b}$$

$$h_t' = \frac{r h_{t,L} + h_{t,R}}{r+1} \text{ and} \tag{3.36 c}$$

$$a'^2 = (\kappa - 1)\left(h_t' - \frac{u'^2}{2}\right) \tag{3.36 d}$$

with the auxiliary variable $r = \sqrt{\rho_L/\rho_R}$.

The computational procedure can now be described:

1. Compute the auxiliary variable r.
2. Compute Roe's average according to system (3.36).
3. Compute the wave strengths according to system (3.35).
4. Compute the fluxes across the cell interface according to eq. (3.33).
5. Update the conservative flow values according to eq. (3.32).

In the case of the 1st order scheme the flow values are constant within a cell. Eq. (3.33) can then be used to determine the flux differences for the cell interfaces by

$$\underset{\sim}{F}_{j+\frac{1}{2}} - \underset{\sim}{F}_j = \sum_{\lambda_i < 0} (\underset{\sim}{r}_i'\lambda_i'\Delta w_i')_{j+\frac{1}{2}} \text{ and} \tag{3.37 a}$$

$$\underset{\sim}{F}_{j-\frac{1}{2}} - \underset{\sim}{F}_j = -\sum_{\lambda_i > 0} (\underset{\sim}{r}_i'\lambda_i'\Delta w_i')_{j-\frac{1}{2}}\ . \tag{3.37 b}$$

The waves originating from the Riemann problem at the cell interface and the resulting flux differences are illustrated in Figure 3.6. It follows for the discretization in eq. (3.32)

$$\underset{\sim}{F}^n_{j+\frac{1}{2}} - \underset{\sim}{F}^n_{j-\frac{1}{2}} = \sum_{\lambda_i < 0} (\underset{\sim}{r}_i'\lambda_i'\Delta w_i')_{j+\frac{1}{2}} + \sum_{\lambda_i > 0} (\underset{\sim}{r}_i'\lambda_i'\Delta w_i')_{j-\frac{1}{2}}\ , \tag{3.37 c}$$

which means that the flux differences are split into wave contributions and only those components are added to a cell which are associated to an entering wave.

3.3.2 Extension to 1D flow in tubes with spatially varying cross-section

The Euler equations for flow in a tube with space varying cross-section are (see eq. (2.25))

$$A\frac{\partial}{\partial t}\underset{\sim}{u} + \frac{\partial}{\partial x}A\underset{\sim}{f} = \begin{pmatrix}0\\ p\\ 0\end{pmatrix}\frac{dA}{dx}\ . \tag{3.38}$$

In [21] Roe extends his classical numerical scheme to the form of the Euler equations given in eq. (3.38). The only necessary change relative to the procedure described above is that the expressions for the characteristic variables (3.35) have to be replaced by

$$\Delta w_1' = \frac{1}{a'^2}(a'^2\Delta\rho - \Delta p) \tag{3.39 a}$$

$$\Delta w_2' = \frac{1}{2a'^2}\left(\Delta p + \rho' a' \Delta u + \frac{\rho' u' a'^2 \Delta A}{(u' + a')A}\right) \tag{3.39 b}$$

$$\Delta w_3' = \frac{1}{2a'^2}\left(\Delta p - \rho' a' \Delta u + \frac{\rho' u' a'^2 \Delta A}{(u' - a')A}\right) \tag{3.39 c}$$

where $A = A_{j+\frac{1}{2}}$ and $\Delta A = A_R - A_L$ with which the numerical flux differences in eq. (3.37) for this case are obtained.

3.3.3 Extension to a 2nd order TVD scheme

In the same article [21], Roe extends this classical 1st order FDS scheme to a 2nd order TVD scheme. The numerical flux terms in eq. (3.33) are corrected by a 2nd order TVD flux according to

$$\underset{\sim}{F}{}^{2nd}_{j+\frac{1}{2}} = \underset{\sim}{F}_{j+\frac{1}{2}} + \frac{1}{2}\sum_l \left[\Phi(\omega_l')(\sigma_l' - \nu_l')(\underset{\sim}{r}_l' \lambda_l' \Delta w_l')\right]_{j+\frac{1}{2}} , \tag{3.40}$$

where

$$\sigma_l' = \operatorname{sgn}(\lambda_l') , \tag{3.41}$$

$$\nu_l' = \begin{cases} \lambda_l'\left(\dfrac{\Delta t}{\Delta x}\right)_R & \text{for } \lambda'_l > 0 \\ \lambda_l'\left(\dfrac{\Delta t}{\Delta x}\right)_L & \text{for } \lambda'_l < 0 \end{cases} \quad \text{(local CFL number)} \tag{3.42}$$

and the limiter function $\Phi(\omega)$ must be within the TVD region. Classical are symmetric limiter functions, e.g. van Leer, Albada, minmod, Superbee or asymmetric limiter functions, e.g. Chakravarthy and Osher [16, p. 536 ff.]. For the implementation, the symmetry property may be used with advantage.

The definition of the slope indicator ω is, according to Roe [21, p. 356], not critical. The following definition according to [17, p. 191] has been chosen for the present implementation:

$$\omega_l = \frac{(\underset{-}{r}_l \Delta w_l)_{j+\frac{1}{2}-\sigma_l'}}{(\underset{-}{r}_l \Delta w_l)_{j+\frac{1}{2}}} \tag{3.43}$$

in which the right handed eigenvector has to be taken componentwise. This expression is computationally cheap to obtain since its terms had to be computed for the fluxes before.

3.3.4 Consideration of spatio-temporally varying cross-section

The Euler equations for flow in a tube with time and space varying cross-section under the constraints explained in chapter 2 write (see eq. (2.25))

$$\frac{\partial}{\partial t}A\underline{u}+\frac{\partial}{\partial x}A\underline{f} = \begin{pmatrix}0\\p\\0\end{pmatrix}\frac{\partial A}{\partial x}+\begin{pmatrix}0\\0\\-p\end{pmatrix}\frac{\partial A}{\partial t} \tag{3.44}$$

A corresponding numerical procedure based on the 2^{nd} order scheme of Roe could not be found in the literature. A time integration scheme has therefore been developed for the present purpose. The discretization follows the subsequent argumentation. In a finite volume approach, eq. (3.44) is integrated for each cell temporally and spatially.

$$\int_0^{\Delta t}\int_0^{\Delta x}\frac{\partial}{\partial t}A\underline{u}\,dx\,dt+\int_0^{\Delta t}\int_0^{\Delta x}\left[\frac{\partial}{\partial x}A\underline{f}-\begin{pmatrix}0\\p\\0\end{pmatrix}\frac{\partial A}{\partial x}\right]dx\,dt = \int_0^{\Delta t}\int_0^{\Delta x}\begin{pmatrix}0\\0\\-p\end{pmatrix}\frac{\partial A}{\partial t}\,dx\,dt \tag{3.45}$$

Assuming that the area and the flow values are constant within each cell and that the cell width remains constant in time, eqn. (3.45) can be integrated in space yielding

$$\Delta x\int_0^{\Delta t}\frac{\partial}{\partial t}A\underline{u}\,dt+\int_0^{\Delta t}\left(A\underline{g}_{j+\frac{1}{2}}-A\underline{g}_{j-\frac{1}{2}}\right)dt = \Delta x\int_0^{\Delta t}\begin{pmatrix}0\\0\\-p\end{pmatrix}\frac{\partial A}{\partial t}\,dt\ , \tag{3.46}$$

in which $A\underline{g}_{j\pm\frac{1}{2}}$ represents the analytical flux terms due to the expression $\frac{\partial}{\partial x}A\underline{f}-\begin{pmatrix}0\\p\\0\end{pmatrix}\frac{\partial A}{\partial x}$ at the right or left interface, respectively. A time variable cell width can be considered at time level n in a preliminary step yielding the level $n0$ as explained in subsection 3.3.6.

Performing the time integration for the left handed terms, eq. (3.46) can be written with numerical fluxes as

$$(A\underline{u})_j^{n+1}-(A\underline{u})_j^{n0}+\frac{\Delta t}{\Delta x}\left(A\underline{G}_{j+\frac{1}{2}}-A\underline{G}_{j-\frac{1}{2}}\right)^{\bar{n}} = \int_{A^n}^{A^{n+1}}\begin{pmatrix}0\\0\\-p\end{pmatrix}dA\ , \tag{3.47}$$

where $\bar{n}$ designates a for now unknown intermediate time level satisfying the average property of integrals which is associated with an area between A^n and A^{n+1}. In this form, the scheme of Roe for only space varying cross-section can be applied on the left hand side. The term on the right hand side accounts for the work due to the time variation of the cross-section. It can be calculated analytically.

Possible time integration algorithms are discussed in subsection 3.3.5. A particular integration algorithm was chosen following a performance analysis. A possible variation of the cell width is considered in a preliminary step 0 yielding the flow values at level $n0$. This is discussed in subsection 3.3.6.

step 1:

Compute the flow values for an intermediate level $n1$ by adding the source terms due to the area change according to

$$A_j^{n+1}(\underline{u}_j^{n1} - \underline{u}_j^{n0}) = \int_{A_j^n}^{A_j^{n+1}} \begin{pmatrix} 0 \\ 0 \\ -p \end{pmatrix}_j dA - \underline{u}_j^{n0}(A_j^{n+1} - A_j^n) . \tag{3.48}$$

The integral considers an isentropic change of state in order to avoid systematic overprediction or underprediction of the pressure for expansion or compression, respectively. The isentropic pressure change in a closed control volume with constant width can be expressed according to relations (2.36) as

$$p = p^{n0}\left(\frac{A^n}{A}\right)^{\kappa} \tag{3.49}$$

and the integral follows as

$$-\int_{A^n}^{A^{n+1}} p dA = \frac{1}{\kappa - 1} p^{n0} A^n \left[\left(\frac{A^n}{A^{n+1}}\right)^{\kappa - 1} - 1\right] \tag{3.50}$$

This step corresponds to a change of state in the cells when considered as closed control volumes. In NUMSTA, the area change is entirely caused by the vehicle displacement. The algorithm described here allows to superpose the area change contributions of different vehicles at one space position as well as to determine the transient power requirement of each of these vehicles individually.

step 2:

Evaluate the additional source terms at time level $n1$ and add them to $\underline{u}_j^{n1}$ according to

$$A^{n+1}(\underline{u}_j^{n2} - \underline{u}_j^{n1}) = (\Delta t)_j^n (\underline{S}^a)_j^{n1} . \tag{3.51}$$

step 3:

Apply the 2nd order TVD scheme of Roe as described previously on the flow values at the intermediate level $n2$ with the space varying cross-section function A^{n+1}.

$$\underline{u}_j^{n+1} - \underline{u}_j^{n2} = -\frac{(\Delta t)_j^n}{(\Delta x)_j^n}\left(\underline{F}_{j+\frac{1}{2}}^{2nd} - \underline{F}_{j-\frac{1}{2}}^{2nd}\right)^{n2} . \tag{3.52}$$

Physically, this step corresponds to opening suddenly the previously deformed control volumes with source terms added in order to allow for flow across cell interfaces.

3.3.5 Discussion of the time integration algorithm

There is a multitude of possibilities of how to include the RHS into the numerical scheme and how to choose the intermediate time level $\bar{n}$ at which the fluxes are evaluated. Figure 3.7 graphically represents three different time integration schemes with special consideration of the sequence. In all three cases, the change of the mesh width is considered first yielding the state n_0.

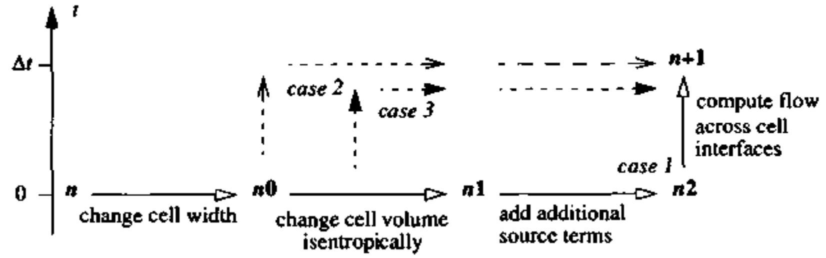

Figure 3.7 Options for time integration schemes

case 1:

This time integration scheme has been implemented in NUMSTA. It is indicated with a solid line and the triangular arrowheads. A horizontal line connects the states n and $n0$, in which the change of the cell width is considered. Another horizontal line connects $n0$ to $n1$, where the cell values are adapted isentropically as if only the cell volume changed. A horizontal line indicates the change from state $n1$ to state $n2$ where the additional source terms are added. The vertical line finally considers the fluxes across cell interfaces which are computed based on the new area distribution yielding state $n+1$.

case2:

The open arrows describe an algorithm in which the flux terms are evaluated before the area change term and the additional source terms are added.

case 3:

In the third case, half the area change is considered over half a time step yielding $\bar{n}$. Then, the flux terms are evaluated. The work due to the second half of the area change and the additional source terms are added in a final step. This method is computationally more costly.

At which moment in the time integration scheme the additional source terms are added is not essential, however the sequence of adding the work due to area change and the evaluation of the flux terms has a noticeable influence on the distribution of flow values around a vehicle, especially for low vehicle speeds. This is illustrated in Figure 3.8. The graphs shows the pressure distribution around a vehicle without considering friction. Ideally, the pressure distribution should follow Bernoulli's equation. The numerical result gives too high pressures in the compression zone when the work due to area change is added after evaluating the fluxes (case 1). If one adds the area change term first and evaluates then the fluxes (case 2) the opposite is observed. Case 3 gives results in between. Further improvement of this behavior can be expected from a higher order time integration scheme.

However, a further improvement on the cost of increased CPU time requirement is not necessary. Consider that Figure 3.8 refers to a very low vehicle speed of *sp*=1 m/s. The error in the nose and tail region amounts only to 0.25 Pa. In front, alongside and behind the vehicle the pressure is again correctly represented. At higher vehicle speeds, the flux terms increase relative to the area change terms and the incorrect representation of the flow values in the nose and the tail region becomes insignificant. This can be seen in Figure 3.9 which shows the pressure distribution around a vehicle moving with *sp*=100m/s. The fluxes are so considerable that the sequence in the time integration scheme is of small importance. It can nonetheless still be detected on the slightly unsymmetrical pressure distribution around the vehicle. An unsymmetrical pressure distribution accounts for a non-zero drag. It can be observed that case 3 gives indeed a very symmetric pressure distribution. For case 1 the pressures in the nose (tail) region are slightly too low (too high) resulting in a resulting driving force. The opposite can be observed for case 2.

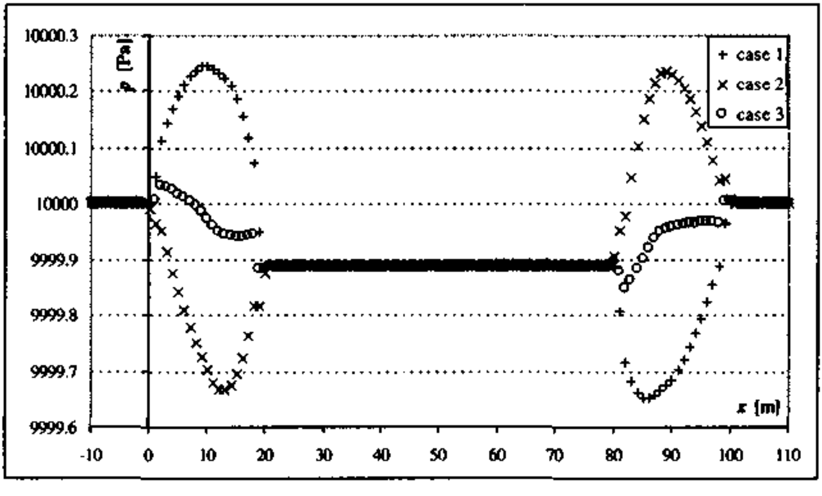

Figure 3.8 Effect of different time integration schemes on the steady pressure distribution around a very slow moving vehicle (*sp*=1 m/s) for the inviscid test case

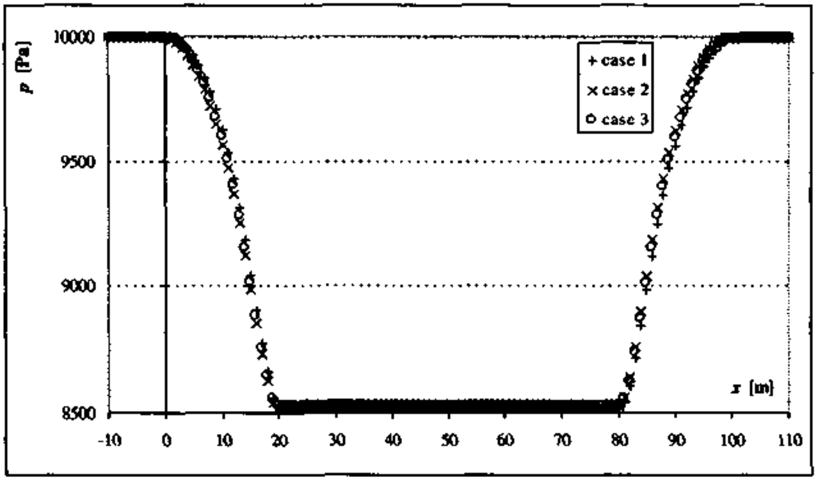

Figure 3.9 Effect of different time integration schemes on the steady pressure distribution around a fast moving vehicle (*sp*=100 m/s) for the inviscid test case

It is nonetheless case 1 which gives the best results for the power requirement as shown in Figure 3.10. It shows a power curve for the phase of initial acceleration (t = [0,1s]) and then for the period of movement with constant speed. The power value reaches a maximum at the end of the acceleration phase and tends then slowly to a constant.

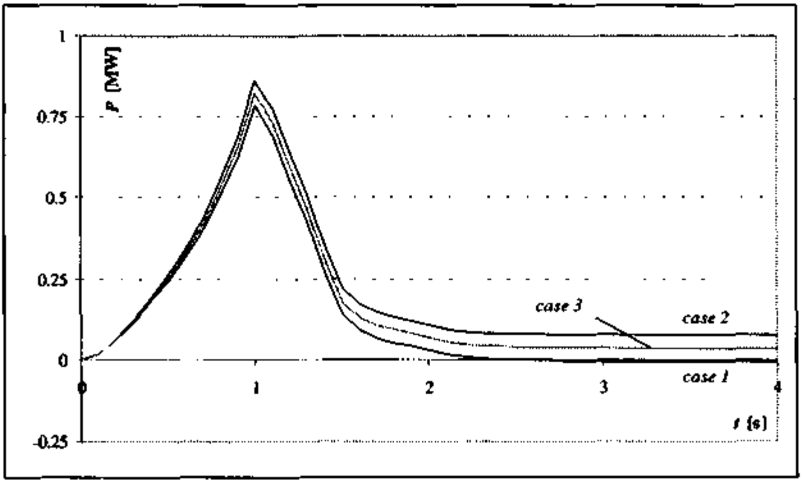

Figure 3.10 Influence of the different time integration scheme on the power requirement for a fast moving vehicle (*sp*=100 m/s) for the inviscid test case

3.3.6 Variation of the cell width

The dynamic mesh refinement (see chapter 4) requires to expand or compress cells, as is the case for fluid-structure interaction problems. The flow values on the new mesh are found based on the distribution on the old mesh satisfying mass, momentum and energy conservation with piecewise constant data. In NUMSTA, cells change only in regions with constant area.

For the sequel it is useful to define the cell width of cell j as

$$\Delta x_j = x_{j+\frac{1}{2}} - x_{j-\frac{1}{2}}, \tag{3.53}$$

the position of the cell interfaces by the arithmetic average between the positions of the cell centers

$$x_{j+\frac{1}{2}} = \frac{1}{2}(x_j + x_{j+1}) \tag{3.54}$$

and the change of the cell width as the difference between the old and the new cell interface.

$$\Delta\Delta x_j = x^{n0}_{j-\frac{1}{2}} - x^{n}_{j-\frac{1}{2}} \tag{3.55}$$

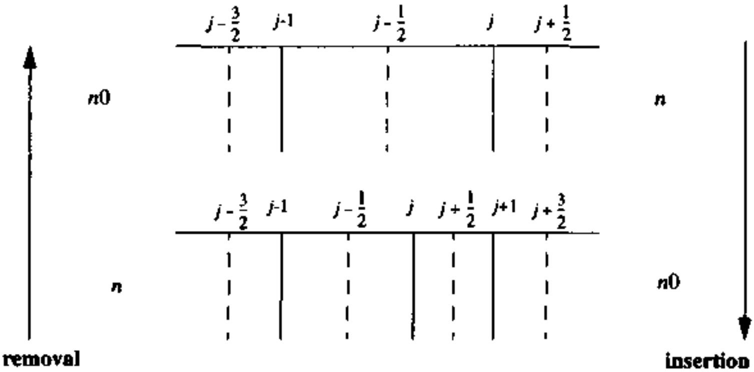

Figure 3.11 Removal (insertion) of a cell and subsequent expansion (compression) of the neighboring cells

step 0:

Removal (expansion) of cells:

Considering three cells from which one, the cell with the index j, is removed (see Figure 3.11, left side). The cell interfaces of the two neighboring cells (index j and j+1 at time level n) change.

This translates into the following equation for cell *j*-1

$$\underset{\sim}{u}^{n0}_{j-1}\Delta x^{n0}_{j-1} = \underset{\sim}{u}^{n}_{j-1}\Delta x^{n}_{j-1} + \underset{\sim}{u}^{n}_{j}\Delta\Delta x_j \tag{3.56}$$

and the corresponding expression for the cell with the index *j* at the time level *n*0 is

$$\underset{\sim}{u}^{n0}_{j}\Delta x^{n0}_{j} = \underset{\sim}{u}^{n}_{j}(\Delta x^{n}_{j} - \Delta\Delta x_j) + \underset{\sim}{u}^{n}_{j+1}\Delta x^{n}_{j+1} . \tag{3.57}$$

Insertion (compression) of cells:

Considering two cells in between which a new one is placed (see Figure 3.11, right side). The flow values in the new cell with the index *j* are found with

$$\underset{\sim}{u}^{n0}_{j}\Delta x^{n0}_{j} = \underset{\sim}{u}^{n}_{j-1}\Delta\Delta x_j + \underset{\sim}{u}^{n}_{j}\left(x^{n0}_{j+\frac{1}{2}} - x^{n}_{j-\frac{1}{2}}\right) \tag{3.58}$$

and the average flow values in the left and right cell remain unaltered since the new cell is entirely contained in the corresponding old cell.

3.3.7 Hancock's method

In a private conversation with P. Roe [23] another 2$^{\text{nd}}$ order time integration algorithm was discussed. He proposed Hancock's method [22] which is based on a linear reconstruction of the flow values according to the MUSCL approach in a first step according to

$$\text{step 1: } u^n_j(x) = \bar{u}^n_j + (x - \bar{x}_j)g^n_j$$

Then, by evaluating the Jacobian with the cell average values the cell interface values can be recalculated for a local evolution over half a time step as

$$\text{step 2: } u_j^{n+\frac{1}{2}}(x) = \bar{u}^n_j + (x - \bar{x}_j)g^n_j - \frac{\Delta t}{2}(Jg^n_j - S^n_j) .$$

With this preparation, the regular Riemann problem can be solved at each interface. This can formally be written as

$$\text{step 3: } u^{n+1}_j = u^n_j - \frac{\Delta t}{\Delta x_j}\left(F^{n+\frac{1}{2}}_{j+\frac{1}{2}} - F^{n+\frac{1}{2}}_{j-\frac{1}{2}}\right) + \Delta t S_j^{n+\frac{1}{2}} .$$

The scheme was implemented and tested. It was found that the results for the inviscid case were less satisfying than with the algorithm proposed above.

3.4 Summary of chapter 3

The topic of this chapter is to choose a numerical solver for the governing equations of tunnel aerodynamics. It starts with a short classification of numerical schemes. The performance of different schemes is discussed on the example of the shock tube problem, for which the analytical solution exists. The oscillatory nature of the 2nd order scheme of MacCormack is highlighted. The 1st order and the 2nd order TVD scheme by Roe resolve discontinuities smoothly; besides, both allow a relatively inexpensive implementation. It is for these reasons, that the numerical algorithm applied in NUMSTA is based on the 2nd order TVD scheme by Roe.

This scheme and its extension to flow in a tube with spatially varying cross-section is recalled. It is then extended to cope with spatio-temporally varying cross-sections. Different time integration methods are discussed. The finally chosen numerical algorithm for the discretization of the conservation equations consists of four steps, which are executed sequentially.

4 THE DYNAMICAL DISCRETIZATION OF THE DOMAIN

A first version of NUMSTA has been developed for simulations of the Swissmetro system. It was restricted to tunnels with constant cross-section. Because, for each vehicle, the equations were solved in the vehicle frame of reference, the passage of vehicles at cross-vents or at other vehicles was difficult to implement. This first version has nonetheless been useful in the starting phase of the main study and it allowed to define the requirements of a second, more versatile program.

In the present, second version of NUMSTA, the conservation equations are solved entirely in a tunnel fixed system. Changes in the tunnel cross-section and multiple vehicles crossing in the same tunnel are allowed. Geometrical discontinuities are again treated with local grid refinements in order to avoid numerical instabilities. Several alternatives of how to implement the dynamic adaptation of the refinement zones to the moving vehicles efficiently have been explored. The choice was based on low storage requirement and high computational speed.

The most desirable feature from a purely fluid dynamic point of view is a mesh adapting dynamically to the gradients of the flow values. However, this is computationally very expensive since the entire domain has to be re-meshed in each timestep and new cell values must be interpolated. Besides, it would require a time step fulfilling the CFL condition for the smallest cell.

For tunnel aerodynamics, the zones of highest gradients are approximately known: they are in vicinity of the geometrical discontinuities. There are stationary geometrical discontinuities, e.g. cross-vents and changes of the tunnel diameter, and unsteady geometrical discontinuities, which are associated only with the vehicles.

A continuous mesh with refinements adapting to the actual position of the vehicles has thus been chosen. For simplicity and without considerable loss of performance, only two basic distances are used in the initial generation of the mesh: coarse in the tunnel (Δx_{tu}) and fine around geometrical discontinuities (Δx_f). The two different mesh widths account for the typical scales of the problem: The vehicle has a length in the order of some l_v=100 m. This is much shorter than the length of a tunnel, which is in the order of some l_{tu}=10 km. The typical length scales are thus different by a factor of 100.

The domain is subdivided into fine and coarse tunnel parts and zones. The dynamical mesh generator adapts their position dynamically to the instantaneous position of the geometrical discontinuities.

Fine parts have cell widths between Δx_{tu} and Δx_f, limited to multiples of Δx_f. Coherent intervals with constant fine mesh spacing are in the sequel called refined zones. There are steady refined zones for stationary geometrical discontinuities and unsteady refined zones which move with a vehicle. Refined zones are entirely contained in fine parts. Fine parts have at least one refined zone.

Coarse parts have a uniform cell width of Δx_{tu}, again chosen as a multiple of Δx_f. Coherent intervals with constant coarse mesh spacing are called coarse zones. Coarse zones can be spread across part borders.

The computational efforts required to redefine the parts are more than compensated by the speed-up gained from the two time-step method.

The distinction between 'parts' and 'zone' is necessary because pointer arrays are required to contain the actual position of both. In coarse parts, a coarse time step is allowed, whereas fine parts require a small time step in order to fulfill the stability criterion. The position of coherent steady or unsteady refined zones must be known in order to decide which point can be repositioned with a vehicle movement.

The dynamical mesh generator is a central part of NUMSTA contributing to reasonable computation time and high precision. Its function is explained in the sequel and its validation can be found in the appendix A2.

4.1 The domain decomposition

A typical configuration for NUMSTA is a tunnel system with cross-vents and vehicles as sketched in Figure 4.1. It shows the decomposition of the domain into parts with partially refined mesh (fine part) and with uniform coarse mesh spacing (coarse part).

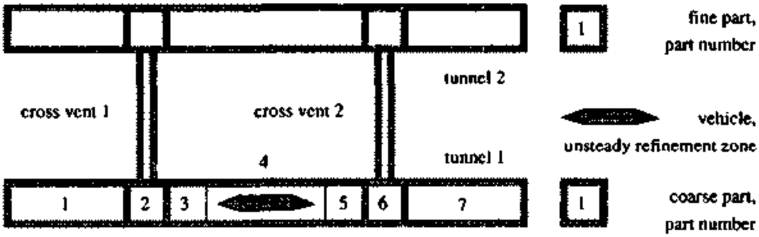

Figure 4.1 Dynamical domain decomposition

Refined zones exist where geometrical discontinuities have the tendency to render the numerical solution unstable, e.g.

- around the nose and the tail of vehicles or around the entire vehicle if the creation of a coarse zone along the vehicle is not possible or not desired,
- in intervals with strongly varying tunnel diameter,
- around the inlets of cross-vents and
- at the ends of the tunnels.

The remainder, i.e. long intervals with constant or slowly varying cross-section, are modeled with coarse grid spacing. Vehicles change their position and with it the position of the geometrical discontinuity. Steady and unsteady refined zones are therefore distinguished. Steady refined zones have a constant position in space. Examples are: cross-vents, changes of tunnel cross-section, tunnel ends. Unsteady refined zones change their position during the simulation. They are associated with the only moving parts of the system, the vehicles. However, it is also imaginable to move the refinement with a physical discontinuity, such as a shock.

The physical position of a mesh point of an unsteady refined zone can fall on a mesh point of a steady refined zone (vehicle passing a cross-vent) or a coarse mesh point. In this case, two overlapping points would require the reduction of the mesh size by one point. This would mean that the indices of the entire mesh above the double point would have to be shifted by one index down. This procedure is computationally too expensive. A more efficient solution has been sought. The dynamic mesh generator in NUMSTA has therefore been defined in such a way as to reduce the changes of the mesh due to the movement of vehicles to a minimum.

The basic principles for mesh changes are

- to restrict changes on the mesh to the immediate proximity of the unsteady refinement zone
- to reduce all modifications to simple operations and
- to keep track of the position of the vehicles and tunnel parts in pointer arrays.

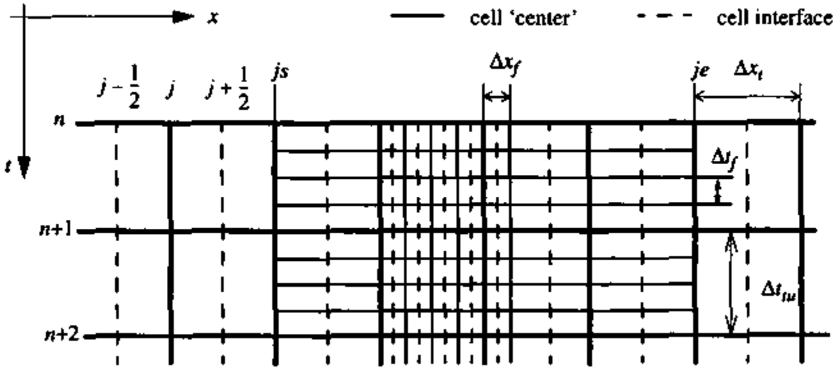

Figure 4.2 Spatial and temporal discretization of a domain with coarse and fine grid spacing and time steps

An example for the spatial and temporal discretization of the domain is given in Figure 4.2. It shows the cell centers of the coarse mesh indicated by the thick vertical lines and the cell centers of the partially refined mesh indicated with the thin vertical lines. A cell is limited by the cell interfaces to the neighboring cells, which are indicated with the dashed lines.

The thick (thin) horizontal lines indicate a coarse (fine) time step. A fine time step has to be applied in zones with cells of a width smaller than a coarse distance. For cells with a width of Δx_{tu} a small or a coarse time step can be applied without violating the CFL condition. The thick horizontal lines indicate a coarse time step. The points at the interface between refined and coarse zones, here with the indices j_s and j_e, are called transition points.

In refined zones, $n_f = \dfrac{\Delta x_f}{\Delta x_{tu}}$ intermediate time steps with Δt_f are executed during one big time step with $\Delta t_{tu} = n_f \Delta t_f$. The values at the transition points are updated for each fine time step based on the last coarse time level (see section 5.4). The vehicle movement and the associated modification in the cross-section of the computational cells is considered for discrete fine time levels. As long as the vehicle nose does not cross a position with a multiple of Δx_f, the mesh requires no adaptation. However, if this is the case, the refined zone around the vehicle nose has to be moved by Δx_f. In order to avoid that an unsteady refined zone moves out of a fine part during the execution of the intermediate time steps, at least one coarse cell is required at the end of each fine part. In order to compute the transition points based on a uniform grid, each fine part is limited with 3 coarse cells at its ends. For simplicity, only one coarse cell is represented in Figure 4.2.

After execution of all intermediate time steps, the dynamical mesh generator checks if coarse and fine parts have to be redefined, i.e. if there are no longer exactly 3 coarse cells at the end of a fine part or if, within a fine part, a coherent zone with at least 10 coarse mesh cells has been created. Particular situations occur for example if an unsteady refined zone approaches a steady refined zone. Then, the two fine parts which contain the approaching refined zones, initially separated by a coarse part, melt to one refined part. When the vehicle leaves the position of the steady refined zone, it causes the molten fine part to split and to establish again a coarse part inbetween. The actual position of coarse and fine parts is recorded in pointer arrays.

4.2 The implementation of the dynamical mesh generator

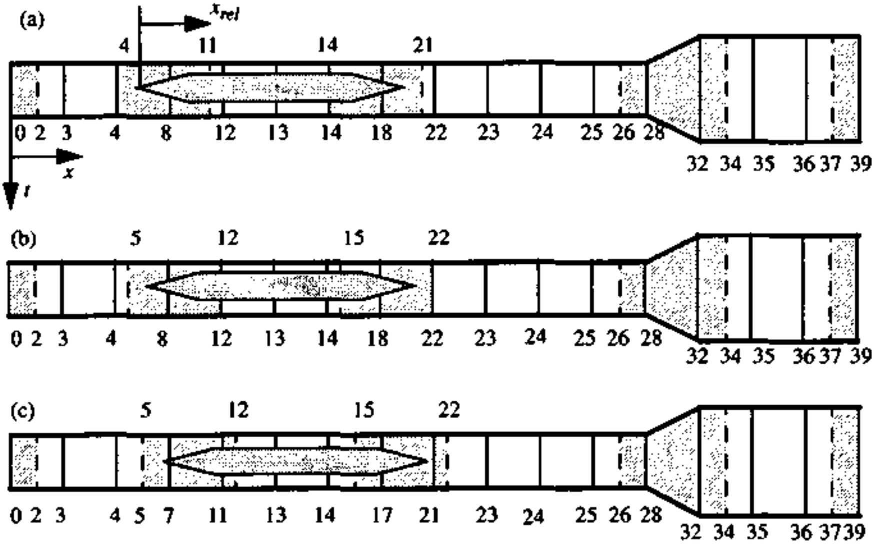

Figure 4.3 Dynamic changes on the computational mesh

The domain decomposition begins with the generation of the coarse steady mesh and the subsequent integration of steady and unsteady refined zones. An initial mesh can also be given to NUMSTA by means of input files using for example the result of a previous calculation. On the basis of this initial setting the mesh is dynamically adapted to the positions of the vehicles.

The following constraints for the dynamical mesh adaptation have been set with respect to an efficient computation:

1. The total number of mesh points is constant.
2. Each discontinuity has a minimum number of refined cells around its position.
3. If there is no overlap of two refined zones, the number of points in a refined zone is exactly the minimum number.
4. The modifications on the mesh are local and restricted to few simple operations.
5. The position of the tunnel parts, the unsteady refined zones and the corresponding array

indices are stored in pointer arrays.

6. The algorithm must be reliable also if several unsteady or steady refinement zones overlap.

An example for the action of the dynamical mesh generator is given in Figure 4.3. The tunnel has steady refined zones at its ends, around the change of the tunnel cross-section and two unsteady refined zones around the nose and the tail of the vehicle. These zones are longer than the vehicle nose or tail region itself, since a minimum refinement thickness is required around geometrical discontinuities. The vehicle moves to the right. The coarse mesh points are indicated by the solid lines, whereas the refined points are within a hatched or grey zone. In the example, the coarse mesh width is 4 times larger than the fine mesh width, thus $n_f = 4$. Time increases from (a) to (c).

The dynamic changes of the computational mesh due to the vehicle movement are indicated in Figure 4.3 (a-c). The numbers below are the array indices. The numbers on top give the indices of the unsteady refined zones. Between (a) and (b) the vehicle movement necessitates the use of the already existing point nr. 22. It is thus not necessary to generate a new mesh point. However, the indices of the unsteady refined zones increase by 1. Between (b) and (c) the movement of the refined zone at the rear requires creation of a mesh point on the right of point 12. This point does not exist yet. In this case the dynamical mesh generator searches for an existing mesh point which is no longer needed. At the position of point nr. 5 in (b) no mesh cell is needed. Thus, the points with indices between 5 and 12 can be positioned by Δx_f higher and the old x-position of point 5 is empty.

This example helps to understand more complicated changes of the mesh. The mesh changes are not trivial if an unsteady refinement zone of a vehicle overlaps with a steady refinement zone like the zone of diameter change (here between indices 26 and 34). Other complicated situations arise when two or more unsteady refinement zones interact with each other or with other steady refinement zones.

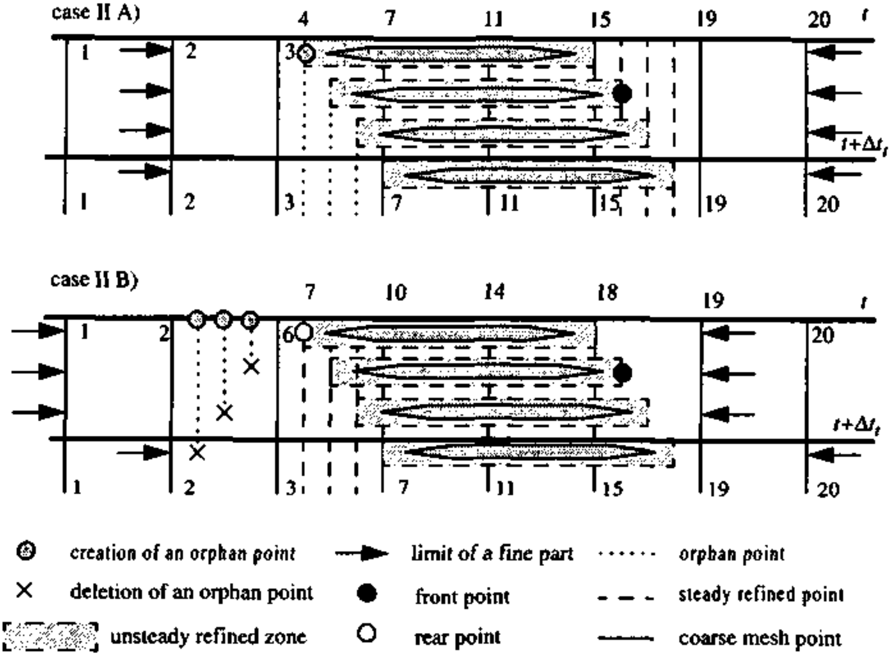

Figure 4.4 Generic cases for the dynamic adaptation of the mesh due to the movement of a vehicle (see also Table 4.1)

For the case that the mesh has to be changed, two generic situations are distinguished and illustrated in Figure 4.4. The x-location grows from left to right. For positive vehicle speed, time increases downwards. If the vehicle moves in opposite direction, similar arguments can be used. Coarse mesh points are again indicated with the thin solid lines, fine steady points are marked by dashed lines and orphan points (see remarks below Table 4.1) are associated with the dotted lines. The unsteady refined zone around the vehicle is marked by the filled rectangles. The arrows indicate the limit of the fine part, here again only with one coarse cell at its ends. The creation of an orphan point is indicated by the gray circle.

For efficient changes on the mesh, two points are of particular importance. The first point is the front position of the refined zone after the vehicle moved (filled circle), called in the sequel 'front point'. The second point of importance is the rear point which is left by the unsteady refined zone (indicated with an empty circle), called 'rear point'.

The position of the vehicle is described as in Figure 4.5. The symbols distinguish between the vehicle front (index '*fr*') and its back (index '*b*'). This notation renders the arguments independent of the direction of the vehicle movement. For the purpose of clear presentation, only a vehicle with one refined zone moving to the right is considered. For a vehicle with more refined zones, the procedure has to be performed for each refined zone separately.

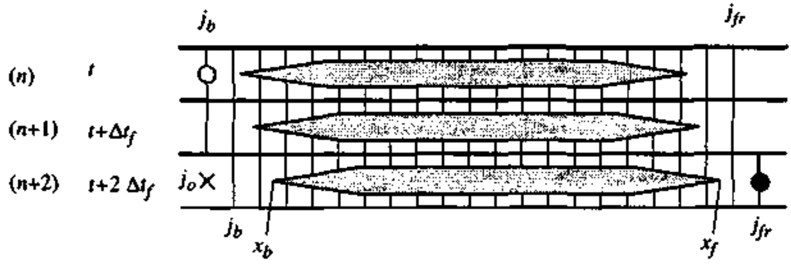

Figure 4.5 Array indices and physical coordinates in an unsteady refined zone

The vehicle movement and the associated changes of the cross-section of the cells are performed for every fine time step Δt_f. Assuming linear acceleration between two discrete time levels, the discrete step of a vehicle is

$$\Delta x_v(t) = \frac{1}{2}(sp(t) + sp(t - \Delta t_f))\Delta t_f \qquad (4.1)$$

After displacing the vehicle by Δx_v, the vehicle might remain within the old mesh points. In this case, no mesh changes are required. In case the vehicle crosses the next fine mesh point, it has to be ensured that a grid point be situated at $x_{j_f} + \Delta x_f$, since the minimum refinement thickness has to be kept. Several situations have to be distinguished (see Table 4.1).

Table 4.1 Cases to be distinguished for the algorithm of updating the mesh due to the movement of the vehicle

criteria	action
I) The vehicle front does not pass the next possible fine mesh point	- update the area function in the interval $[j_b, j_f]$ with new vehicle position - the pointer arrays for the current position of the refinement zones are unaltered
II) The vehicle front crosses the next possible fine mesh point	In order to ensure the minimum refinement thickness, a mesh point needs to be at $x_{j_f} + \Delta x_f$.
Two subcases have to be distinguished (see Figure 4.4):	
A) A mesh point in front of the point with the index j_f exists.	- update the area function in the interval $[j_b, j_f + 1]$ - update the pointer array for the current unsteady refinement zones with the new indices
B) A mesh point in front of the point with the index j_f does not yet exist	- create new mesh point at $x_{j_f} + \Delta x_f$ (see remarks) - update the area function in the interval $[j_b, j_f + 1]$ (indices based on initial mesh before creation of new mesh point) - update the pointer arrays for refinement zones - update the pointer array for the current position of the vehicles with the new indices

Remarks (see also Figure 4.4)

In the case II A), an orphan point is created at j_b. An orphan point is a point which, at the moment, is not needed, neither by a steady refined zone nor by an unsteady refined zone of a vehicle. This orphan point will be used in later phases of the vehicle movement (see II B).

In the case II B), a mesh point at the desired position in front of the vehicle has to be generated. Another point which is not needed elsewhere (orphan point) must be taken away. Such a point always exists due to the applied algorithm. The search of this orphan point and the subsequent modification of the mesh are computationally relatively costly. The algorithm searches therefore the orphan point which is closest and whose removal causes least mesh changes. An orphan point can be situated at various positions relative to the vehicle. The below described cases decrease in likelihood of appearance, thus the most likely cases are checked first in order to reduce computational effort

1. Search for an orphan point behind the vehicle in the actual fine part.
2. Search for an orphan point in front of the vehicle in the actual fine part.
3. Search for an orphan point behind the vehicle outside of the actual fine part.
4. Search for an orphan point in front of the vehicle outside of the actual fine part.

In case the orphan point has been found behind the vehicle ($j_o < j_b$) the array values in the interval $[j_o + 1, j_f]$ have to be shifted to the their new position $[j_o, j_f - 1]$. Then, the point with the index j_f is available to be positioned at $x_{j_f} + \Delta x_f$.

If an orphan point can only be found in front of the vehicle ($j_o > j_f$) the array values in the interval $[j_f + 1, j_o - 1]$ have to be shifted to the their new position $[j_f + 2, j_o]$. Then, the point with the index $j_f + 1$ is available to be positioned at $x_{j_f} + \Delta x_f$.

In both cases, mesh changes over a rather wide range are performed. It may be necessary to update the information for the pointers to vehicle positions which are within the corresponding zones.

In case the orphan point is found outside of the actual refinement zone (cases 3 and 4), pointer values of other refinement zones might have to be changed also.

The above described procedure positions mesh points with fine or coarse spacing dynamically according to the position of the vehicles. The required fine mesh points around the ends of the unsteady refined zone are dynamically generated. Changes of physical positions and array indices are restricted to the immediate environment of the actual refined zone; costly shifting of large parts of the array is avoided in most cases.

After the changes of the mesh have been realized, the pointers containing the array indices limiting the tunnel parts eventually have to be updated.

4.3 Summary of chapter 4

The necessity of an adaptive mesh for tunnel aerodynamic simulations is outlined and the method used in NUMSTA is explained. The dynamical mesh generator of NUMSTA positions zones with refined mesh where high fluid gradients are expected, i.e. around nose and tail of vehicles, at tunnel ends, at diameter changes and at positions of cross-vents. Mesh changes are required to follow the actual position of the vehicles. These mesh changes are restricted to the proximity of the moving vehicle which limits computational efforts.

5 THE MODEL ASSUMPTIONS

Friction and other purely 3D flow effects are included on the basis of empirical coefficients as additional source terms for mass, momentum and energy transfer. This method is known as the 'distributed loss model' [15, p. 81]. Its idea is to distribute the sources which apply on a control volume equally on fluid particles within, e.g. friction effects can be considered by empirical coefficients relating the average flow velocity to a friction force.

The definition of these empirical coefficients is a critical point in the construction of the numerical models. Standard coefficients to be found in text books are mostly given under simplifying assumptions, such as a generic geometry or for steady flow. Coefficients that display unsteady local 3D flow effects for a 1D computation can be obtained from a more precise local numerical simulation or from experiments.

5.1 Additional source terms

In tunnel aerodynamics, mass transfer can be due to perforated walls, cross-vents or high pressure tubes for repressurization; momentum changes are associated with friction and distortion of flow; energy exchange is due heat transfer, moving external forces and enthalpy contained in exchanged mass. Convective heat exchange occurs between the air and the tunnel or vehicle wall. Other heat sources such as the heat dissipation of electrical components, of an accidental fire in a tunnel, evaporation or condensation can also be considered.

These additional source terms can be added to the Euler equations as given in section 2.2. Surface forces due to moving system parts (vehicles, index v) have to be distinguished from surface forces induced by steady system parts (tunnel walls, index tu).

The resulting additional source term is

$$\underline{S}^a = \begin{pmatrix} \dot{m} \\ f_{ftu} + f_{fv} + f_{ex} \\ \dot{m}h_t + \dot{w}_{ex} + q \end{pmatrix} = \begin{pmatrix} S_1^a \\ S_2^a \\ S_3^a \end{pmatrix}, \tag{5.1}$$

where

$\dot{m}$ :: mass flow per unit length,

f_f :: friction force per unit length,

f_{ex} :: other external forces per unit length, e.g. due to mass exchange

$\dot{m}h_t$ :: total enthalpy flow due to mass exchange per unit length

$\dot{w}_{ex}$ :: power added by external moving forces per unit length

q :: heat flow per unit length .

The exact definition of each of these additional source terms is developed in the sequel.

5.2 Models for the system parts

NUMSTA allows to configure via user interface at execution time the following system parts:

- tunnel
- vehicle
- cross-vent
- perforated wall

The computation of each of these parts is based on particular assumptions.

5.2.1 The friction model for the tunnel walls

In order to develop a friction model for the tunnel walls, a tunnel segment with the length Δx is considered. Figure 5.1 shows a sketch of a tunnel part with a viscous velocity profile and the corresponding average velocity. The 1D simulation solves for average flow values in a computational cell. These values are taken as a basis for computing the empirical coefficients. The control volume associated with a computational cell is indicated with the dashed line.

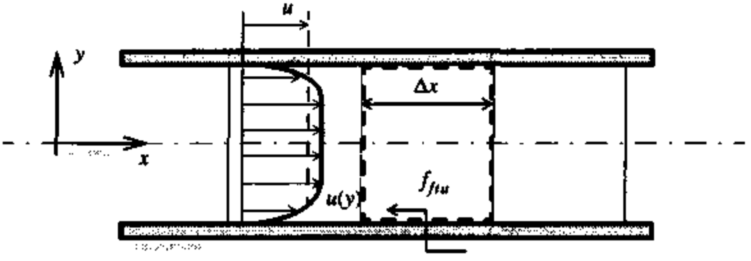

Figure 5.1 Friction force in a tunnel segment, with indication of a viscous velocity profile and average air velocity

The friction force from the walls on the fluid can be calculated with the friction factor f. For compressible flow, this value is a function of the relative wall roughness, the Reynolds number and the local flow Mach number.

The friction factor for the wall roughness k can be estimated by means of an equivalent wall roughness k_s for tubes with a uniform distribution of sand grains. A discussion of the relation between the equivalent wall roughness and the wall roughness for different flow regimes can be found in [8, p. 266].

The friction factor for incompressible flow based of the wall roughness can be found based on the Moody diagram [5, p. 473]. If the equivalent wall roughness is known, the formula of Churchill [8, p. 268] can be applied. This formula gives a good analytical approximation over the complete range of the Reynold numbers, from laminar to highly turbulent flow.

It displays also the facts that at sufficiently high Reynolds numbers the friction factor depends only on the relative wall roughness and that, if Reynolds tends to zero, the pressure loss tends to the results found analytically for the laminar Hagen-Poiseuille flow. The formula of Churchill gives the incompressible friction factor f^* in eq. (5.2).

$$f^* = 8\left[\left(\frac{8}{Re}\right)^{12} + (A+B)^{-\frac{3}{2}}\right]^{\frac{1}{12}}, \text{ where} \tag{5.2 a}$$

$$A = -2.457\ln\left[\left(\frac{7}{Re}\right)^{0.9} + \frac{0.27k_s}{d}\right] \text{ and } B = \left(\frac{37530}{Re}\right)^{16} \tag{5.2 b}$$

k_s :: equivalent sand grain wall roughness

Re :: local flow Reynolds number defined with the hydraulic diameter as for example for the tunnel: $Re_{tu} = \frac{\rho u d_{eq}}{\mu}$

The compressible friction factor can then be expressed according to [10, p. 217] with the following correction

$$f = (1 + 0.18M^2)^{-0.35} f^* \ . \tag{5.3}$$

Finally, the friction coefficient is related to the friction factor by

$$C_f = \frac{f}{4} \ . \tag{5.4}$$

Note that the notation used here follows the one applied in [5] and in [8]. Other authors, e.g. [70], denote f to be the skin-friction coefficient, which corresponds here to C_f, i.e. the symbol f is used just in an opposite way. This entanglement can be solved only by reassuring about the definition of these symbols in the corresponding context. Here, the friction factor f is used as the dimensionless pressure drop for internal flow and the friction coefficient C_f as the dimensionless surface shear stress as defined in the List of Symbols and abbreviations.

The incompressible friction coefficient computed according to eqns. (5.2) and (5.4) is visualized for the transition and the turbulent regime in Figure 5.2. The graph shows clearly the transition zone beginning at $Re \approx 2300$ and the sharp increase towards the turbulent regime. The friction coefficient diminishes then and tends to a constant value at around $Re > 10^5$. As expected, the value of the friction coefficient diminishes with the equivalent sand grain thickness. For tunnel aerodynamics, typical values for the relative equivalent wall roughness are $d/k_s = 500, 1000$ or 5000 which corresponds to wall roughnesses of k_s=10mm, 5mm or 1mm in a tunnel with a diameter of d_{tu}=5m. It can be seen that for high Reynolds numbers a typical value of the friction coefficient is $C_f^* = 0.005$. This parameter does not vary strongly with the relative wall roughness. This is an important observation, since it allows to choose a constant friction coefficient in problems related to tunnel aerodynamics, where the Reynolds number is usually very high and the equivalent sand grain roughness can be estimated only approximately.

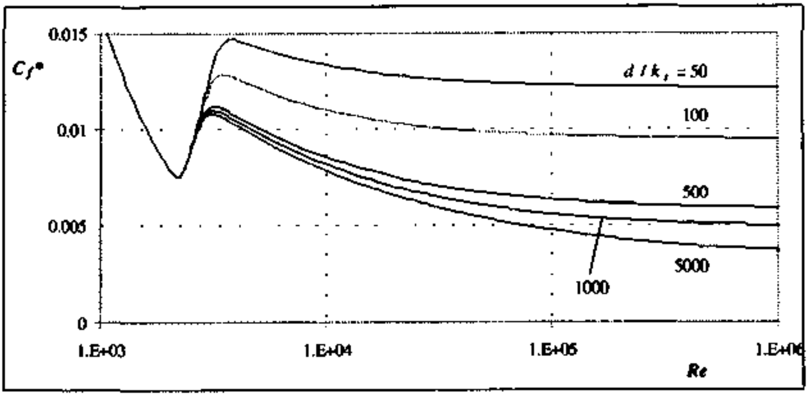

Figure 5.2 Incompressible friction coefficient C_f^* according to the formula of Churchill with relative sand grain roughness as curve parameter

The dependence of the friction coefficient on the Mach number and thus on compressibility effects is visualized in Figure 5.3, where the correction factor $g(M) = (1 + 0.18M^2)^{-0.35}$ is plotted for subsonic Mach numbers.

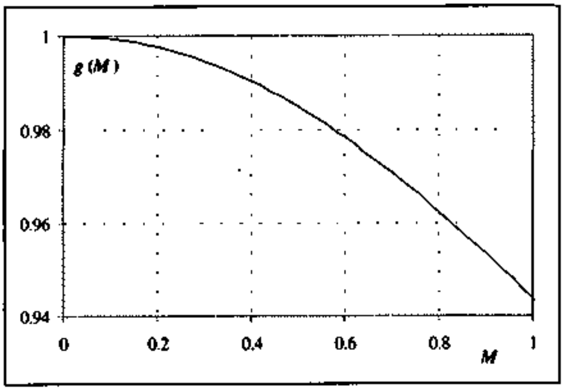

Figure 5.3 Compressible correction term for the friction factor $g(M) = (1 + 0.18M^2)^{-0.35}$

The friction force is opposed to the flow direction. Applying the definition of the friction factor, the friction force acting from the tunnel wall on the air (see Figure 5.1) can be introduced as additional source term for the momentum equation

$$S_2^a = f_{ftu} = -\mathrm{sgn}(u) C_{ftu} \frac{\rho}{2} u^2 P_{tu} . \tag{5.5}$$

The compressible correction term for the friction factor and a possible correction for an inclined tunnel wall, thus for $\frac{\partial A}{\partial x} \neq 0$, are neglected here, since other considerations have a more significant effect in this context.

5.2.2 The friction model for the vehicle

The velocity profile for the flow in the annular space between vehicle and tunnel wall depends on the pressure gradient along the vehicle and its speed. This generates a Couette-Poiseuille flow, for which an exact solution of the Navier-Stokes equations exists in the laminar and incompressible case. Figure 5.4 indicates possible velocity profiles for this flow. The graph shows that at constant relative movement of the walls, the velocity wall gradients vary with the pressure gradient, which is given here in an adimensional form.

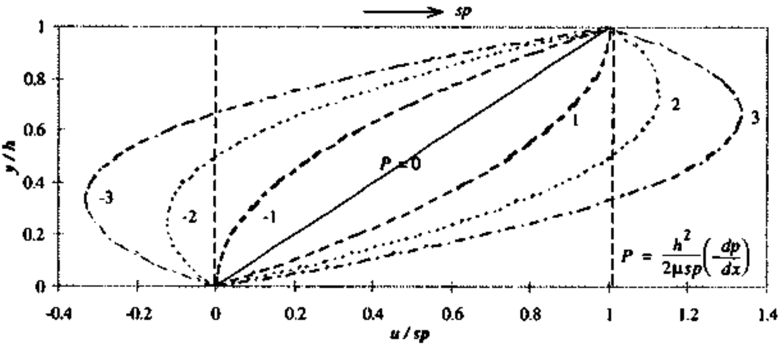

Figure 5.4 Possible laminar velocity profiles between two plates spaced *h* apart with relative movement with superposition of a pressure gradient (Couette - Poiseuille flow), according to [9, p. 78]

For the numerical simulation of the flow in the annular space, the dependence of the wall gradient and with it the wall shear stress on the pressure gradient implies a complication. Not only does the vehicle speed vary during the acceleration phase but also the pressure gradient is transient at all times. Besides, the flow around the vehicle is turbulent and compressible. The transient calculation of the local friction force acting on the fluid from the tunnel and the vehicle wall is therefore dependent on a number of parameters. This is discussed in detail in [48], where experimentally obtained laminar and turbulent velocity profiles are shown, which may have a different form than the examples given in Figure 5.4. For the present purpose, simplifications are required.

The local friction coefficients for friction between vehicle and air C_{fv} and between tunnel and air C_{ftu} are thus determined with the corresponding relative average speed in the gap and the hydraulic diameter. This means that eq. (5.2) is applied with Reynolds numbers for the flow velocity relative to the tunnel wall and to the vehicle surface, respectively. The mean air velocity relative to the vehicle v is given by

$$v = u - sp \ . \tag{5.6}$$

The additional friction force per unit length acting from the vehicle on the air (see Figure 5.5) is determined with the air velocity relative to the vehicle as

$$S_2^a = f_{fv} = -\mathrm{sgn}(v) C_{fv} \frac{\rho}{2} v^2 P_v \ . \tag{5.7}$$

The forces acting from the vehicle on the air move relative to the tunnel with the actual vehicle speed sp. Therefore, they add (consume) mechanical power if the direction of movement is equal (opposed) to the direction of the force. This has to be considered in the energy equation. The additional source term for the energy equation due to the vehicle friction force is

$$S_3^a = \dot{w}_{fv} = sp \cdot f_{fv} \ . \tag{5.8}$$

The pressure force acting from the vehicle on the air requires no special consideration here. This force is expressed in the conservation equations by the term $\underset{\sim}{S}_1$ and is considered in step 1 of the numerical algorithm. Area changes are, as before, not considered for the determination of the friction force.

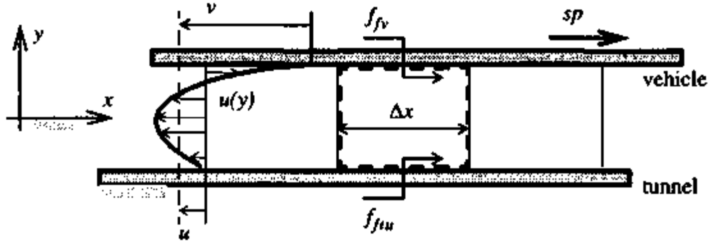

Figure 5.5 Sketch of a viscous velocity profile in the gap between tunnel and vehicle and forces acting from outside on the control volume

5.2.3 The power required to overcome aerodynamic drag

The power required by the vehicle to overcome the aerodynamic drag can be calculated by two different methods.

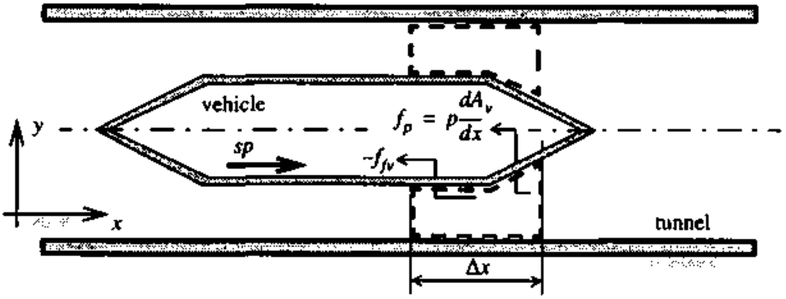

Figure 5.6 Moving forces acting from the control volume on the vehicle

method 1 (by integration of surface forces along the vehicle):

The integral of friction and pressure forces over the vehicle surface (see Figure 5.6) multiplied with the momentaneous vehicle speed determines the required power. It is defined as

$$P_v = sp\int_l\left(f_{fv} - p\frac{dA_v}{dx}\right)dx\ , \tag{5.9}$$

where, by convention, a positive sign shall indicate power added from the vehicle to the fluid and a negative sign for P_v shall indicate power transferred from the fluid to the vehicle. As shown in eq. (2.12), this expression can be transformed into

$$P_v = \int_l\left(sp\, f_{fv} - p\frac{\partial A}{\partial t}\right)dx\ , \tag{5.10}$$

where $\frac{\partial A}{\partial t}$ is the local area change of the tunnel due to the movement of the presently examined vehicle. This formula can be used to find the unsteady value of the power required. It is also valid if multiple vehicles are crossing or if the tunnel diameter varies.

method 2 (by application of control volume containing the vehicle):

Another way to determine the vehicle power required is to apply the integral form of the momentum equation on a control volume around the vehicle as shown in Figure 5.7. It is widely found in the literature with some variants [68]. Some authors prefer to look at two control volumes, one around the nose and another one for the tail of the vehicle. However, since the friction force on the tunnel along the vehicle is known, the vehicle drag is easier found if a control volume around the entire vehicle is chosen. The steady approach can be extended for unsteady phases of the vehicle movement by considering the integral momentum difference between two time levels as in

$$F_{fv} + F_p = \left(\int_0^l A \rho u dx \right)^{n+1} - \left(\int_0^l A \rho u dx \right)^n + (\rho v^2 + p)A\big|_1 - (\rho v^2 + p)A\big|_2 - F_{ftu} . \qquad (5.11)$$

where

v :: air velocity in the vehicle frame of reference

F_{fv} :: total friction force acting from the vehicle on the air

F_p :: total pressure force acting from the vehicle on the air

F_{ftu} :: total friction force acting from the tunnel on the air over the length of the control volume

The required aerodynamic power is determined by

$$P_v = sp(F_{fv} + F_p) . \qquad (5.12)$$

This method is only applicable for constant tunnel cross-sections and in absence of other vehicles. An implementation for the case of varying cross-section (vehicle crossing or tunnel diameter varies) is complex. Some authors find complicated ways to work around this [61] by treating every possible situation individually. The consideration of correction terms for unsteady phases of the vehicle movement is likewise computationally expensive.

In NUMSTA, both methods are implemented. Method 1 gives the power requirement in all situations. Drag values according to method 2 are calculated for the purpose of comparison with method 1 in quasi-steady movement.

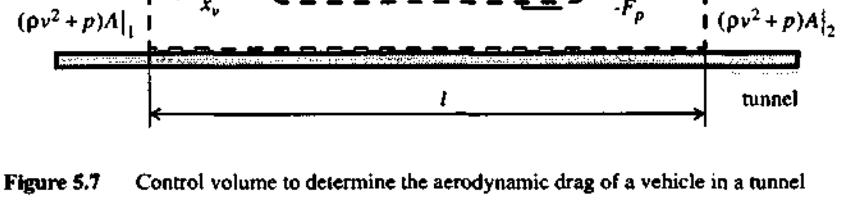

Figure 5.7 Control volume to determine the aerodynamic drag of a vehicle in a tunnel

5.2.4 The model for heat transfer

Important contributions of heat transfer are:

- convective heat transfer between tunnel walls and air and
- transfer of dissipated heat from system parts to their environment.

The problem of the convective heat transfer for flow in tunnel systems is very complex. The reason for this is that the flow under consideration is turbulent and unsteady; it may also contain discontinuities. Besides, an important parameter of the heat transfer is the tunnel wall temperature. An unsteady model for the interaction of these parameters is thus necessary if the effect of convective heat transfer is to be considered correctly in the numerical simulation.

A complete consideration of this phenomenon exceeds the focus of the present study. In early contributions to tunnel aerodynamics, pressures and air velocities have long be discussed separate from temperature effects. The flow was often assumed to be adiabatic and the energy equation was replaced by the isentropy condition. The thermal effects in railway tunnels and the importance of the temperature for the flow are discussed discussed in [26] and [53], where an empirically obtained constant heat transfer coefficient is used. A better model has been proposed already in [41] by Hammitt. He used the Reynolds analogy for a local estimate of the heat transfer coefficient.

The Reynolds analogy relates the friction coefficient with the Stanton number, out of which the convection heat transfer coefficient can be obtained. The Reynolds analogy is applicable for low pressure gradients in flow direction and fluids with $Pr \approx 1$. According to [5, p. 363], the Reynolds analogy or its modified version may also be applied for turbulent flow where $\partial p / \partial x \neq 0$. Corrective factors extend its domain of applicability to wider ranges of the Pr number. The Prandtl number of air being around $Pr \approx 0.72$ [5, A15] and the flow being mostly turbulent, the modified Reynolds analogy may be applied:

$$\frac{c_f}{2} = St \cdot Pr^{2/3} \quad , \; 0.6 < \mathrm{Pr} < 60 . \tag{5.13}$$

The computational advantage of this model is that it relates the heat transfer coefficient α to the local friction coefficient via the Stanton number defined as

$$St = \frac{\alpha}{\rho |u| c_p} . \tag{5.14}$$

For most simulations related to tunnel aerodynamics, the assumption of quasi steady heat transfer with a constant wall temperature is sufficient. This is shown in the parameter study in section 7.6, where the influence of heat transfer on the power requirement was found negligible.

The additional source term for the energy equation follows then as

$$S_3^{\alpha} = q_{tu} = \alpha (T_{wtu} - T) P_{tu} . \tag{5.15}$$

The tunnel wall temperature T_{wtu} in eq. (5.15) is yet undetermined. For a first approximation, it may be set to a constant value. However, if the local heat flux into the rock is high, e.g. during the repressurization (see section 7.10), the wall heats up. In this case, it is necessary to compute the unsteady development of the wall surface temperature. The effect not being of very high importance for the normal operation of underground trains and the computational effort being considerable, it was decided to neglect the temperature evolution in the rock.

Heat exchange with other system parts than the tunnel wall can readily be included in NUMSTA. Possible candidates are:

- convective heat exchange with between air and vehicle wall,
- heat losses from the vehicle interior to its environment,
- electrical installations in the tunnel (lamps, pumps, switches, transformers, commuters),
- losses due to eddy currents in electromagnetic tracks and
- accidental release of heat by fire or explosion.

Since their effect has to be assessed for each particular configuration individually, their effect is not discussed in more detail in the present work.

5.2.5 The model for T-branchments

In order to reduce the piston effect, cross-connections between parallel tunnels have been realized for example in the Channel tunnel [27]. Cross-vents allow the air to pass from a high pressure zone in one tunnel A into a low pressure region of a neighboring tunnel B. This reduces locally the pressure in tunnel A and with it the drag of a vehicle. Eventually, the air recirculates into a low pressure zone of A via tunnel B across another cross-vent. Cross-vents can therefore be regarded as passive flow bypasses helping to reduce the drag.

The flow in a T-branchment is 3D, unsteady and viscous. It is the philosophy of NUMSTA to simplify these complex flows so that they can be treated by 1D models with corrective terms. The model chosen here is based on the conservation equations for a control volume in the branchment as sketched in Figure 5.8.

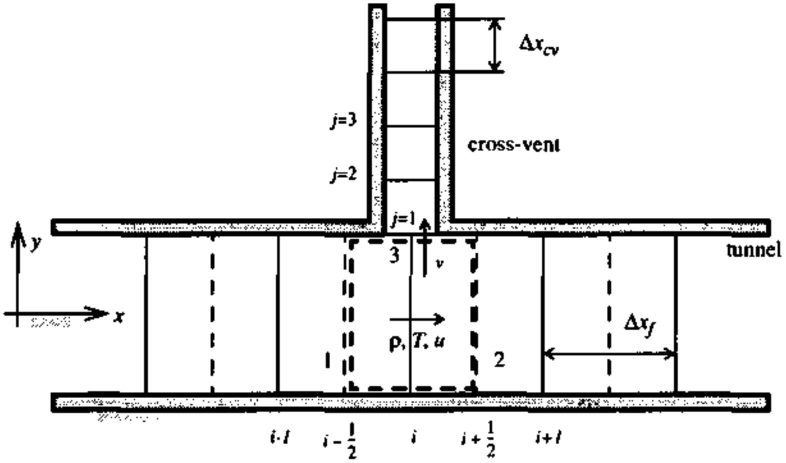

Figure 5.8 Control volume for a T-branchment with indication of cell numbering for the horizontal and the vertical 1D array

The integral form of the system of conservation equations for the dashed control volume neglegting external forces is given by

$$V\frac{\partial\rho}{\partial t} + \rho_2 u_2 A_2 - \rho_1 u_1 A_1 = \mp\rho_3 v A_3 = S_1^a \Delta x_f \qquad (5.16\text{ a})$$

$$V\frac{\partial}{\partial t}(\rho u) + (\rho_2 u_2|u_2| + p_2)A_2 - (\rho_1 u_1|u_1| + p_1)A_1 = \mp\rho_3 v u A_3 = S_2^a \Delta x_f \qquad (5.16\text{ b})$$

$$V\frac{\partial}{\partial t}(\rho e) + \rho_2 u_2 h_{t2} A_2 - \rho_1 u_1 h_{t1} A_1 = \mp\rho_3 v h_{t3} A_3 = S_3^a \Delta x_f\,, \qquad (5.16\text{ c})$$

where the negative sign is associated with the lower end of the cross-vent and the positive sign must be used at the upper end of the cross-vent, when the coordinate system as drawn in Figure 5.8 is used for orientation.

The terms on the left side of system (5.16) are already considered in the system of Euler equations for the horizontal flow. The terms on the right hand side result in additional source terms.

If the instantaneous lateral mass flow into or out of the tunnel per computational cell is $\dot{m} = \mp\rho_3 v A_3$ the source terms write

$$S_1^a = \frac{\dot{m}}{\Delta x_f} \qquad (5.17\text{ a})$$

$$S_2^a = \frac{\dot{m}}{\Delta x_f} u \qquad (5.17\text{ b})$$

$$S_3^a = \frac{\dot{m}}{\Delta x_f} h_{t3} \qquad (5.17\text{ c})$$

The flow values in the control volume, ρ, u and T are approximated with their arithmetic mean between surfaces 1 and 2 as for example the air velocity $u = \frac{1}{2}(u_1 + u_2)$. The thermodynamic values at surface 3 are estimated with the values ρ and T. The air velocity component v is obtained from the cell average of the first cell (index $j=1$) of the vertical flow. The values at the surface 3 determine the boundary conditions for the vertical array.

On the example of the passage of a vehicle at a cross-vent the advantages of an entirely tunnel fixed treatment as compared to a partially vehicle fixed treatment can be explained.

In the tunnel fixed approach, the passage of a vehicle changes the cross-section of the cells at the inlet position of the cross-vent. The effects of several vehicles on the cross-section can be superposed. The applied numerical scheme computes the source terms at the branchment after all vehicle movements and with it all source terms due to the time rate of area change have been considered.

In the vehicle fixed approach, the consideration of source terms from the cross-vent requires to determine the points in the vehicle fixed array which correspond to the position of the cross-vent. The superposition of several area changes in one array can only with difficulty be implemented.

5.2.6 The model for perforated walls

Perforated walls are installations allowing air to pass from the main tunnel to a side tunnel or to the ambient air via nearby slots in a thin wall. The following effects are imaginable:

- elimination of shock waves by diffraction across the porosities,
- smoothing of pressure variations at tunnel entries or exits and
- reduction of drag due to increased flow recirculation.

The realization of the perforated wall is imaginable as a wall on the side, on top or below the vehicle. An example is given in the wireframe sketch in Figure 5.9. The perforated wall separates the main tunnel from the side tunnel or from the ambient atmosphere.

If installed within the tunnel, the wall can be segmented and it can be assembled at the interior of the tunnel. Its principle of action is that, once the flow is in the side tunnel, it is less disturbed by the flow in the main tunnel and the passage of the vehicle. The reduced interaction between the main and the side flow may compensate the pressure loss during the passage across the perforations and the reduction in cross-section for the main tunnel.

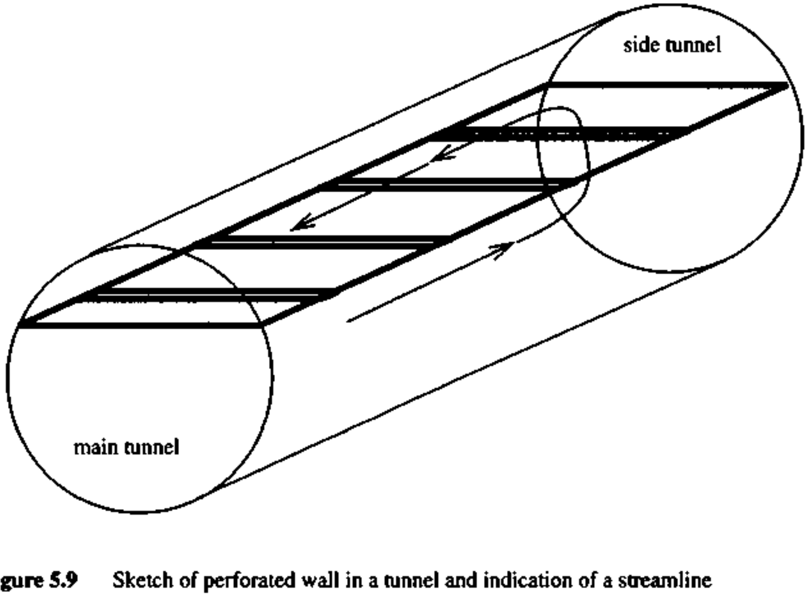

Figure 5.9 Sketch of perforated wall in a tunnel and indication of a streamline

The flow is in this case 3D and computational simulations are possible only for small scale problems (see [38] and [39]), which give interesting information for the flow patterns for such a device. Within the frame of the present 1D simulation, the perforated walls have been considered as continuous distributions of wall openings or porosities and source terms have been determined accordingly.

Figure 5.10 shows a sideview of a vertical cross-cut of a tunnel with a perforated wall placed on the top. The openings are here drawn in their generic form perpendicular to the main flow direction.

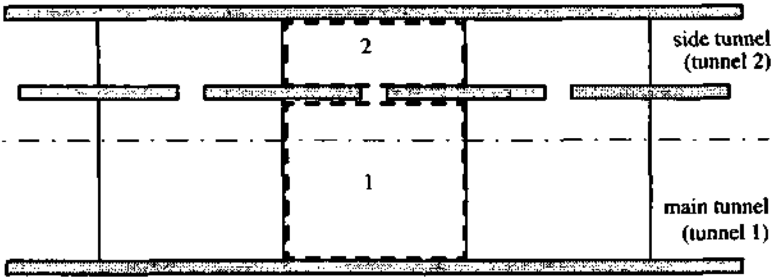

Figure 5.10 Vertical cross-cut of a tunnel with perforated wall on top, sideview

Streamlined openings are examined for their capability to force a higher flowrate to pass to the side tunnel. One option is shown in Figure 5.11, where the openings have the form of turbine blades. Their curvature at the wall surface defines the inlet angle α. It is assumed that the flow enters only in the downstream part of the opening and that it leaves the perforated wall in opposite direction and under the same angle as it entered. This assumption is discussed in the appendix A1 on the example of local 3D simulations.

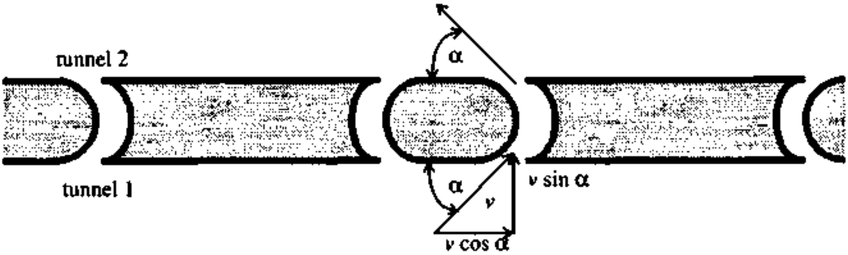

Figure 5.11 Vaned openings with indication of the inlet angle α and flow redirection

The numerical model is based on an estimate of the mass flow between main and the side tunnel due to the pressure difference on both sides of the perforated wall. For a given geometry of the opening, empirical values for the pressure loss coefficient ζ can be found in books containing empirical loss coefficient such as [4]. For simplicity and to concentrate on other parameters, a constant value of $\zeta=0.2$ has been used for all the computations presented here. This is a typical value for lateral vaned openings. It is nonetheless possible to include a model which computes the pressure loss coefficient as a function of the actual flow situation.

With the pressure difference defined as

$$\Delta p = p_1 - p_2 , \tag{5.18}$$

the transverse flow velocity from tunnel 1 into the side tunnel 2 is

$$v = \operatorname{sgn}(\Delta p)\sqrt{\frac{2|\Delta p|}{\zeta\rho}} . \tag{5.19}$$

A positive transverse velocity v indicates by convention flow from tunnel 1 (main tunnel) to tunnel 2 (side tunnel) and vice versa.

The source terms for the flow deviation are derived with the symbols introduced in Figure 5.12. The figure shows a computational cell in tunnel 1 with a lateral branchment under the inlet angle α. The control volume is limited by dotted line. It contains the computational cell of tunnel 1. Flow across the control surfaces is indicated by the arrows with the full heads. The sketch shows the mean flow velocity in the main tunnel u, which is in this case the flow velocity u_σ in the origin tunnel, the transverse flow velocity v which is inclined under the angle α to the main flow, the x-component of the force F_x acting on the control volume, the tunnel cross-section A and the surface of the lateral opening A_p.

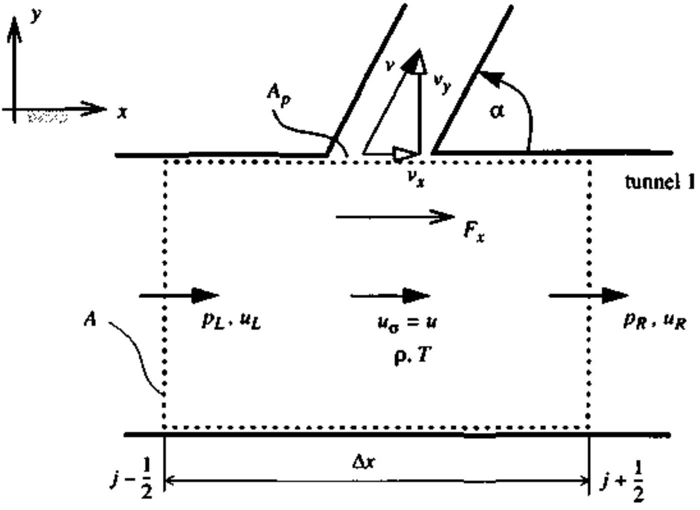

Figure 5.12 Control volume in a branchment inclined under the angle α to the main tunnel

The transverse mass flow is

$$\dot{m} = A_p \rho v \sin\alpha . \tag{5.20}$$

The additional source term for the continuity equation can then be determined to be

$$S_1^a = \frac{\dot{m}}{\Delta x} = \mp\gamma\rho v \sin\alpha \ , \tag{5.21}$$

where the upper and lower sign stands for the source terms for tunnel 1 and 2 (see Figure 5.10), respectively, and the perforation ratio is defined as

$$\gamma = \frac{A_p}{\Delta x} \ , \tag{5.22}$$

which introduces a continuous distribution of the openings.

Assuming a quasi-steady locally incompressible flow in the branchment region, the additional force on the computational cell is found by a momentum balance for the control volume, i.e.

$$F_x = -\rho A u_L^2 - p_L A + \rho A u_R^2 + p_R A + \rho v^2 A_p \sin\alpha\cos\alpha \ . \tag{5.23}$$

The pressure difference can be eliminated with Bernoulli according to

$$p_L + \frac{\rho}{2}u_L^2 = p_R + \frac{\rho}{2}u_R^2 \tag{5.24}$$

and it follows

$$F_x = \frac{\rho}{2}(u_R^2 - u_L^2)A + \rho v^2 A_p \sin\alpha\cos\alpha \ . \tag{5.25}$$

The mass conservation can be introduced by

$$\dot{m}_R = \dot{m}_L + \dot{m} \ , \tag{5.26}$$

where $\dot{m}_{L/R} = \rho u_{L/R} A$. Eq. (5.25) can then be written as

$$F_x = \frac{\dot{m}}{\rho A}\left[\dot{m}_L + \dot{m}\left(\frac{1}{2} + \frac{A}{A_p}\cot\alpha\right)\right] . \tag{5.27}$$

Since it would require an extra computational effort to determine the flow velocity at the left cell border, the term $\dot{m}_L$ is eliminated by introducing an average mass flow defined as

$$\bar{\dot{m}} = \frac{1}{2}(\dot{m}_L + \dot{m}_R) = \rho u A \ . \tag{5.28}$$

Eq. (5.27) yields then

$$F_x = \frac{\dot{m}}{\rho A}\left[\bar{\dot{m}} + \dot{m}\frac{A}{A_p}\cot\alpha\right] \text{ or } F_x = \dot{m}(u - v\cos\alpha) \tag{5.29}$$

This force has the desired properties to tend, for the case $\alpha = 90°$, to the known mixed product of u and v_y of eq. (5.16 b) and to zero for $\alpha = 0°$ as for flow remaining in the domain. Besides, the absolute value of the force is reduced with α.

Table 5.1 Redirection of flow across a perforated wall with turning vanes

	$v > 0$ ($u_\sigma = u_1$)	$v < 0$ ($u_\sigma = u_2$)
$u_\sigma > 0$		
$u_\sigma < 0$		

Considering the different flow situations as listed in Table 5.1 and deducing the corresponding signs, the additional momentum flow expressed as external force per computational cell in x-direction is given by

$$S_2^a = \frac{\dot{m}\hat{u}}{\Delta x}\,, \tag{5.30}$$

where $\hat{u} = u_{1/2} \mp \operatorname{sgn}(u_\sigma) v \cos\alpha$ and $\sigma = \begin{cases} 1 \text{ for } v > 0 \\ 2 \text{ for } v < 0 \end{cases}$. The term $\operatorname{sgn}(u_\sigma)$ gives herein the direction of the flow in the origin tunnel.

The definition of $\hat{u}$ can be interpreted as the horizontal flow velocity in the main or side tunnel from which the x-component of the transverse flow vector $\operatorname{sgn}(u_\sigma) v \cos\alpha$ at the control surface A_p is substracted. Its sign is, for the origin tunnel, equal and, for the target tunnel, opposed to the sign of the flow velocity in the origin cell. This accounts for the redirecting property of the vaned openings.

The time rate of energy transported with the transverse flow into each computational cell results in

$$S_3^a = \frac{\dot{m}h_t}{\Delta x}\,, \tag{5.31}$$

where the kinetic energy is computed with the transverse flow velocity component v.

The thermodynamic values for the transverse flow are estimated with the cell averages of the origin cell.

5.3 The boundary conditions

For a numerical domain limited by the array indices [0,N], the chosen numerical scheme updates the points in the interval [2,N-2] with 2nd order accuracy and the points 1 and N-1 with 1st order accuracy. The boundary points with the indices 0 and N are updated only with the wave contributions leaving the domain, thus the left running waves at the left end and right running waves at the right end. Additional information for the points 0,1,N-1 and N has to be supplied in order to render the calculation 2nd order accurate in the entire domain. This is the topic of the present section.

NUMSTA also allows to include via the user interface at execution time the following boundary conditions for the tunnel ends:

- closed end
- open end
- periodic
- connecting
- forced ventilation
- non reflective boundary condition

5.3.1 Closed end

A closed end of the tunnel is characterized by a zero velocity at the end. This boundary condition can be implemented using image cells mirroring the flow values within the domain. In these mirror cells, ρ and T have the same values as their brother cell and the air velocity u is opposed as is indicated with the arrows in Figure 5.13.

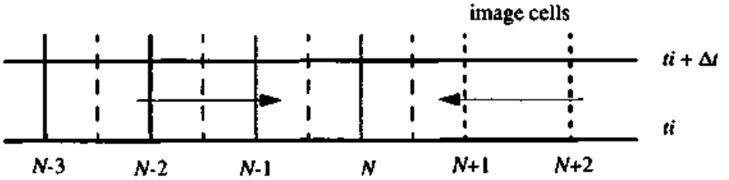

Figure 5.13 Ghost cells for the closed end boundary condition

Mathematically, this boundary condition can be formulated as

$$\rho^n_{N+k} = \rho^n_{N-k}\ ,\ u^n_{N+k} = -u^n_{N-k} \text{ and } T^n_{N+k} = T^n_{N-k} \quad \text{for } k=1,2 \tag{5.32}$$

and the numerical solver is applied until the index N+2. This updates the flow values with indices N-1 and N with 2nd order precision and enforces a zero velocity at the boundary.

5.3.2 Open end

In the case of an open end two cases have to be distinguished: inflow and outflow.

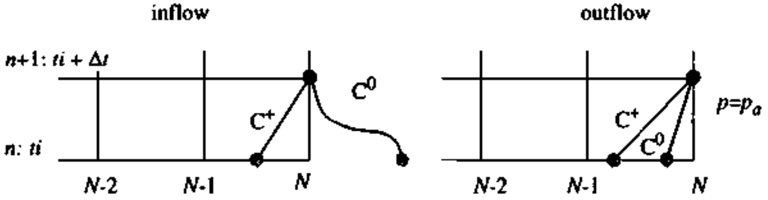

Figure 5.14 Characteristic lines and particle trajectory at a right sided open end

The directions of wave propagation for the hyperbolic problem were before defined as

$$\left(\frac{\partial x}{\partial t}\right)_{C^\pm} = \hat{u} \pm \hat{a} \text{ and } \left(\frac{\partial x}{\partial t}\right)_{C^0} = \hat{u} \ , \tag{5.33}$$

where the hat indicates an appropriate average for the flow values used to determine the directions of the characteristics and the particle trajectory. Along the characteristic lines $C^\pm$, the flow velocity and the speed of sound are related by compatibility conditions. For 1D flow in a tube with space variable cross-section and under consideration of friction the compatibility conditions are

$$\text{along } C^\pm : \frac{d}{dt}\left(u \pm \frac{2}{\kappa + 1}a\right) = \mp \frac{au}{A}\frac{dA}{dx} - \frac{f_{ftu}}{\rho A} \tag{5.34}$$

The effect of heat transfer and of friction forces in the energy equation are, without noticeable loss of precision neglected for the present purpose. Then, two conditions, isenthalpy and isentropy, can be used along the particle trajectory C^0.

$$\text{along } C^0 \text{: } h_t = \text{const. and } s = \text{const.} \tag{5.35}$$

Isentropy allows to use the relations (2.36).

The time integral of the first term on the right handed side of eq. (5.34) is, according to [33], well approximated by

$$\mp\int \frac{au}{A}\frac{dA}{dx}dt = \mp\left(\frac{a}{u \pm a}\right)_f\left(\frac{(uA)_f + uA}{2}\right)\int\frac{dA}{A^2} \tag{5.36}$$

and the second term on the right handed side of eq. (5.34) is assumed constant. Eq. (5.34) can then be written in the implicit form

$$u = u_f \pm \frac{2}{\kappa + 1}(a_f - a) + I \ , \tag{5.37}$$

where I represents the time integral of the right hand terms in the form

$$I = \mp\left(\frac{a}{u \pm a}\right)_f\left(\frac{(uA)_f + uA}{2}\right)\left(\frac{1}{A_f} - \frac{1}{A}\right) - \frac{f_{fru}}{\rho A}\Delta t \ .$$

With the friction term given, eq. (5.37) can be transformed into an explicit equation for u.

Inflow:

The particle trajectory connects point N (right end) or 0 (left end) along an arbitrary line to the ambient state, thus

$$h_{t,\,N(0)} = h_{t,\,a} \text{ and } s_{N(0)} = s_a \tag{5.38}$$

Eq. (5.38) represents 2 conditions for the 3 unknowns ρ , u and T . The third condition is given by the time integral of the compatibility condition (5.34) along the outgoing characteristic.

Outflow:

Along the particle trajectory C^0, eq. (5.35) yields the following two conditions:

$$h_{t,\,N(0)} = h_{t,\,f} \text{ and } s_{N(0)} = s_f \ . \tag{5.39}$$

The isenthalpy can not be used here since it does not provide information about the flow direction. It must therefore be replaced by the compatibility equation (5.34) along the outgoing characteristic.

The free stream condition yields the missing third condition as

$$p_{N(0)} = p_a \ . \tag{5.40}$$

Interpolation of the footvalues:

The footvalues of the characteristics are obtained by linear interpolation between two neighboring cell centers with the indices j and j-1 according to

$$\underset{\sim}{u}_f = \underset{\sim}{u}_j - \frac{\underset{\sim}{u}_j - \underset{\sim}{u}_{j-1}}{x_j - x_{j-1}}(x_j - x_f) \ . \tag{5.41}$$

Flow direction:

For the above described procedure to be consistent, a criterion is required to decide whether the boundary has to be treated with the method for inflow or outflow. Following the argumentation of [61, p. 96], a criterion for inflow is

$$(p_a \geq p_N) \wedge (u_N \leq 0) \text{ for the right end.} \tag{5.42}$$

Inflow is computationally more expensive, thus for the case of no pressure difference and zero boundary velocity none or the procedure for outflow should be used. For inflow, NUMSTA uses therefore the conditions

$$(p_a > p_N) \wedge (u_N \leq 0) \text{ for the right end} \tag{5.43 a}$$

$$(p_a > p_0) \wedge (u_0 \geq 0) \text{ for the left end} \tag{5.43 b}$$

Note on change of flow direction:

A change of the flow direction is indicated by opposite signs of u and u_f. Eventually, this will change the direction of the particle trajectory during the iteration process. In that case, the algorithm for opposed flow direction is used to compute the boundary values in the next iteration step. The temperature discontinuity caused by the change from outflow to inflow is transmitted through the grid with the precision of the numerical scheme.

Correction for inlet loss:

The total inflow pressure can be corrected to account for the Borda-Carnot loss at the opening. The initial contraction of streamlines and the subsequent non-isentropic expansion to tunnel diameter (see Figure 5.15) cause according to [61, p. 93] a loss of the total pressure of

$$\frac{p_{t1}}{p_a} = \exp\left(-\frac{\kappa}{\kappa-1}\frac{1}{c_p T_a}\zeta\frac{u_1^2}{2}\right), \tag{5.44}$$

where the pressure loss coefficient can in first approximation be obtained experimentally with incompressible fluids. The corresponding pressure loss coefficient is found by the difference of the pressure losses in a Bernoulli diffusor and a carnot diffusor as

$$\zeta = \left(1 - \frac{1}{\mu}\right)^2 \tag{5.45}$$

with the contraction ratio defined as $\mu = \frac{A_B}{A_T}$. The contraction ratio μ takes in a theoretical development the value 0.5, however, experiments [11] give values of μ=0.61 .. 0.64.

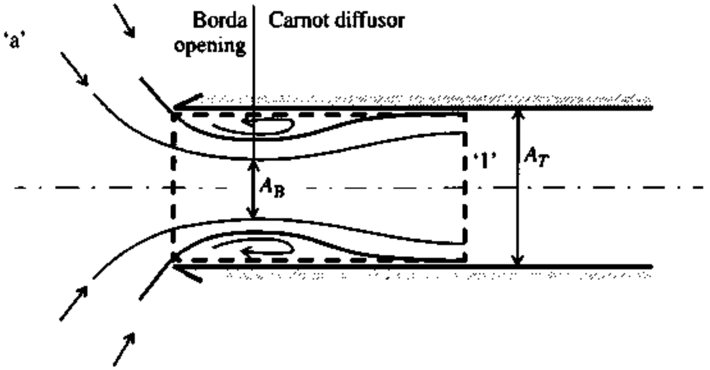

Figure 5.15 Sketch of inflow streamlines at a Borda-Carnot opening

This correction is introduced into the system assuming that the C^0 characteristic connects to the total flow values $p_{t,1}$ and $T_{t,1} = T_a$ instead of p_a and T_a as indicated in the equations for inflow in Figure 5.16.

Implementation:

Some additional assumptions have to be made concerning the effective air velocity and the speed of sound for the wave directions and the new boundary values used to determine the flow direction. These assumptions can iteratively be improved in a multi step algorithm as visualized in Figure 5.16. In the equations, the unknowns, the flow values at the boundary at time level n+1, are the variables without indices.

As first approximation, the boundary values of the previous time step determine the direction of the characteristics and the new boundary values.

In the case of inflow, the foot values of the inner characteristic are computed. With the actual estimate for the speed of sound at the boundary and the compatibility condition (5.34) a new estimate for the flow velocity at the boundary is obtained. This yields, together with the energy conservation, a new estimate for the temperature.

For outflow, the foot values of the inner characteristic and of the particle trajectory are calculated. The isentropy condition relates pressure and temperature along the particle trajectory, thus, with the pressure given by eq. (5.40), the new boundary temperature is found. A new estimate for the boundary air velocity is found with the compatibility condition along the outgoing characteristic. The density follows with the ideal gas equation.

The effective air velocity and the speed of sound for the wave directions can now be redetermined to be the average between their old foot value and their new head value. This algorithm is repeated until a consistent set of flow values has been found.

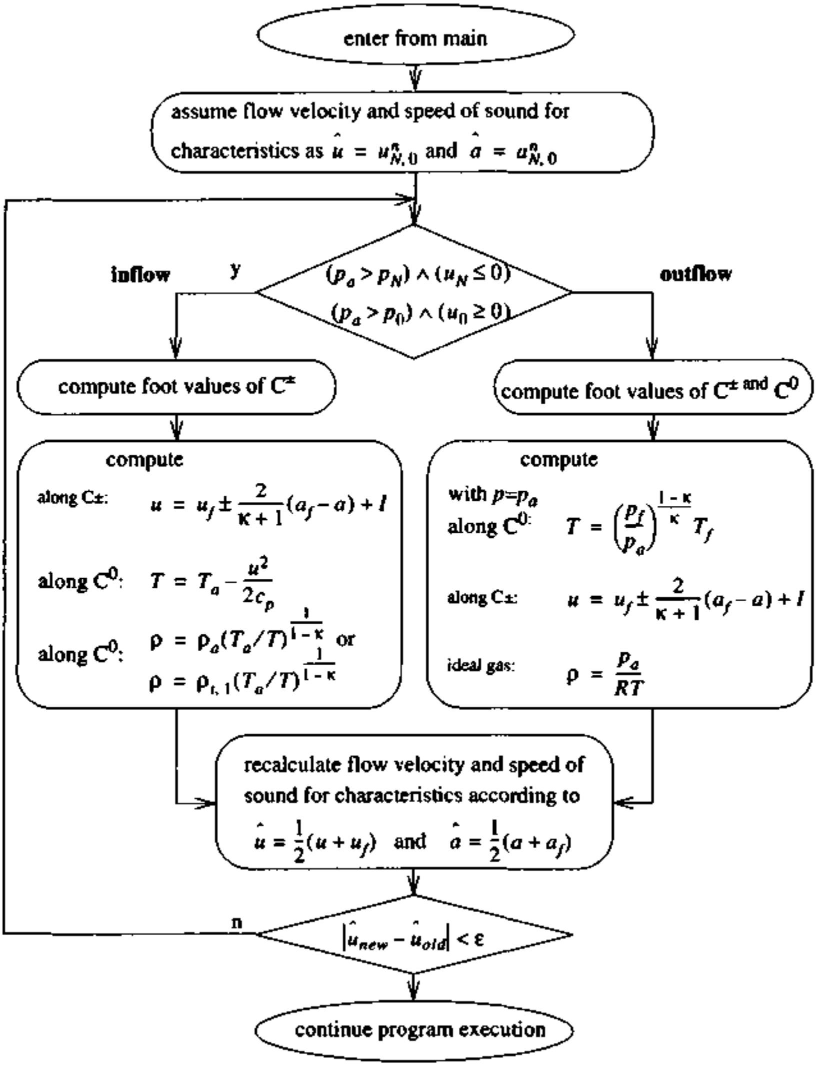

Figure 5.16 Iterative algorithm delivering the boundary conditions for an open end (right and left end, respectively)

5.3.3 Periodic boundary condition / tunnel loop

The periodic boundary condition accounts for a tunnel loop, in which the numerical solution at both ends is set equal. This type of boundary condition implies that once the vehicle reached one end of the tunnel, it has to be repositioned to the other end of the tunnel. In that case, expensive manipulation of the computational mesh is required. However, this is a rare event and allows for an infinite movement of the vehicle. Figure 5.17 illustrates the periodic boundary condition with a computational domain whose ends are connected to a loop.

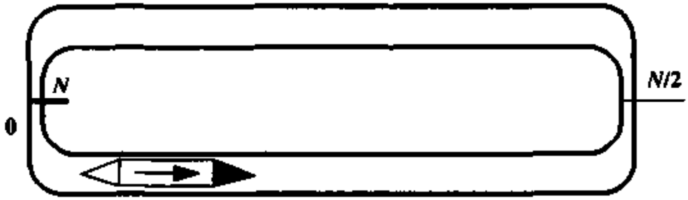

Figure 5.17 Illustration of a periodic boundary condition

Mathematically, the periodic boundary condition can be expressed as

$$\underset{\sim}{u}_0^n = \underset{\sim}{u}_N^n \,. \tag{5.46}$$

The boundary points are updated in very much the same way as the transition points (see section 5.4), where $J+j = j$ and $J-j = N-j$.

5.3.4 Connecting boundary condition

The connecting boundary condition is intended for connections between ends of different tunnels. This allows to connect for example two tunnels to a loop as shown in Figure 5.17 and additionally to connect the tunnels with cross-vents which is not possible with the periodic boundary condition. Denoting the end point of tunnel 1 to be connected with $J1$ and the corresponding point of tunnel 2 to be connected with $J2$, the connecting boundary conditions are

$$\rho_{J1}^{n} = \rho_{J2}^{n} \ , \ u_{J1}^{n} = s u_{J2}^{n} \text{ and } T_{J1}^{n} = T_{J2}^{n} \qquad (5.47)$$

where s is +1 if the two ends are opposite ends of the tunnels, e.g. the right end of tunnel 1 is connected with the left end of tunnel 2, and s takes the value -1 if the two connected ends are equal, e.g. two right ends are connected. Again, the treatment follows the same scheme as for the transition points (see section 5.4).

5.3.5 Forced Ventilation

Forced ventilation is induced by a pressure difference between both ends of the tunnel. It is therefore necessary to impose total pressure and total temperature at the high pressure end and the static pressure at the exit. If the left end is exposed to a high pressure and the right to the low pressure, thus fluid flows to the right, the boundary conditions can be written as

$$p_{t0} = \text{const.}, \ T_{t0} = \text{const. and } p_{N} = \text{const. .} \qquad (5.48)$$

5.3.6 Non reflective boundary condition

"The non reflective boundary condition expresses the physical boundary conditions as the requirement that the local perturbations propagated along incoming characteristics be made to vanish." [16, p. 370]. This boundary condition needs no special treatment, since it is in the nature of the applied scheme that it updates all the points within the domain with at least 1st order accuracy and also the boundary points with the outgoing characteristics. This boundary condition can only be used in a physically correct manner for flow without friction, where the only wave information originates from within the domain.

5.4 The numerical treatment of the transition points

The transition points are the points forming the boundary between a coarse and a fine part. As explained above, the dynamical mesh generator ensures that there are always at least 3 mesh points with coarse distance at the ends of the fine parts. Together with 3 coarse mesh points of the neighboring coarse zone, the values of 6 points spaced Δx_{tu} apart around the transition point are stored at time level *TI* (see Figure 5.18).

The solver applied in NUMSTA computes the 2^nd^ order fluxes for all points of the domain except for the 2 points at the borders (indicated by the grey lines). The flow values in these points have to be found in a separate step. The procedure stores the flow values in the points with indices [*J*-3,*J*+3] at time level *TI*. At the end of each fine time step with $TI < ti < TI + \Delta TI$, the values in the interval [*J*-1,*J*+1] are computed based on the previously stored flow values at time level *TI*. At the end of the series of small time steps, the values in [*J*-1,*J*+1] are updated for the time level *TI*+Δ*TI*. Since all the points involved are spaced by Δx_{tu}, it is possible to step in time with these points with a time step between Δt_f and Δt_{tu} without violating the CFL condition.

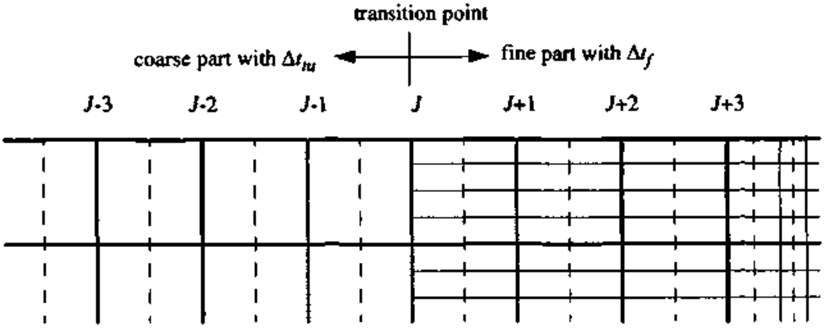

Figure 5.18 Coarse mesh points around the transition point *j* building the boundary of both neighboring zones

5.5 Summary of chapter 5

The topic of this chapter is to explain the numerical models underlying the definition of the additional source term $\underset{\sim}{S}_a$. Further, the numerical treatment of the boundary conditions and of the transition between refined and coarse mesh parts implemented in NUMSTA is explained.

The additional source term considers mass, momentum and energy exchange. Models for friction with tunnel and vehicle walls, for heat transfer, for lateral branchments and for perforated walls are discussed and their contribution to the components of the additional source term vector are defined.

Two methods for computing the forces on the vehicle have been discussed.

The physical models underlying the following boundary conditions have been discussed: the closed end, the open end (inflow and outflow), the periodic b.c., the connecting b.c., the forced ventilation and the non-reflective b.c.

6 VALIDATION

A validation can be performed by comparing NUMSTA with analytical solutions, with other computer codes which have previously been validated on experimental data or by direct comparison with experimental data. Validation is achieved if the comparison shows conformity of the data for both simple and complex cases involving the influence of many different parameters.

6.1 Stability condition

The CFL condition requires the domain of dependence of the numerical method to contain the domain of dependence of the differential equation [16, p. 288]. The scheme is thus stable for

$$|\lambda|_{max}\frac{\Delta t}{\Delta x} < 1 \ . \tag{6.1}$$

Referring to Figure 3.6, this condition can also be expressed as the condition that the waves originating at the cell interfaces must not leave the cell within one time step, since in that case it would be the wrong cell receiving the contribution of that wave.

6.2 Error analysis for numerical schemes

The higher order flux correction term in the scheme of Roe as described in subsection 3.3.3 has been found calculating the difference between the one step TVD Lax-Wendroff scheme and the 1st order Roe upwind flux (see [21] and [17, p. 182 ff]). Because the classical Lax-Wendroff scheme is of 2nd order in space and in time [16, p. 234] the resulting scheme is also of 2nd order in space and in time in smooth regions of the flow and of 1st order in regions with high gradients.

The additional terms accounting for the time dependence of the area in the discretized equation may introduce additional errors. As the subsections 3.3.4 and 3.3.6 have shown, the added terms are the result of a strict mathematical development. Except for the assumption of isentropic volume change no additional simplification has been made. There should thus be no additional error from this extension, which can be proven with a consistency analysis.

Convergence can be shown following a method given in [17, p. 102 ff]. The local error of the numerical solution $\underset{\sim}{u}_j^n$ as compared to the exact analytical solution $\widehat{\underset{\sim}{u}_j^n}$ computed at the cell centers is

$$\underset{\sim}{E}_j^n = \underset{\sim}{u}_j^n - \widehat{\underset{\sim}{u}_j^n} \ . \tag{6.2}$$

The scheme is convergent under the condition

$$\left\|\underset{\sim}{E}_j^n\right\| \to 0 \text{ for } \Delta t \to 0, \Delta x \to 0 \ , \tag{6.3}$$

e.g. that the global error, computed with some norm $\| \, . \, \|$ from the local errors tends to zero with the time step and the grid spacing.

A norm suitable to deal with a domain containing no discontinuities is the ∞-norm defined as

$$\|\varepsilon\|_\infty = max|\varepsilon(x)| \ . \tag{6.4}$$

In order to show convergence, it is thus sufficient to show that the maximal local error tends to 0 as the time step is reduced. The global error is of the same order as the local truncation error. Within the domain of stability of the applied scheme, the maximum local error behaves therefore according to the order of the scheme. For a 2nd order scheme, the global error is of the form

$$G = C_1\Delta x^2 + C_2\Delta t^2 + O(\Delta x^3, \Delta t^3) \ . \tag{6.5}$$

If, for a test case for which an analytical solution is known, the norm of the local error behaves according to eq. (6.5), it is shown that the complete scheme is of $O(\Delta x^2, \Delta t^2)$.

The error for the combined space-time discretization is determined by keeping the ratio $\frac{\Delta x}{\Delta t}$ = const. and performing computations for several Δx and Δt. If only the spatial error is to be estimated, a very low time step is chosen. This ensures that the spatial error is much bigger than the temporal error. The opposite procedure is not applicable for explicit schemes since it is not possible to choose a high time step with a dominant contribution to the error and a small Δx with negligible contribution to the error because of the stability restriction.

The order of the scheme can not be rigorously determined in the presence of discontinuities, since the definition of the truncation error is based on Taylor expansions of the discretized equations. For a domain containing discontinuities, the scheme might well converge, even though it can not be expected that the pointwise error in the neighborhood of discontinuities vanishes when the grid and the time step are refined. The method exposed above is nonetheless applied by some workers ([14] and [23]) to obtain information about the behavior of the scheme. In the presence of discontinuities, a 1st order scheme is not expected to show 1st order accuracy as discussed in [17, p. 121]. In the presence of sharp gradients a 2nd order TVD scheme is locally restricted to 1st order accuracy by the limiter function. Once a 1st order error is introduced in the computational domain, it spreads and renders the entire computation 1st order accurate. It is nonetheless of advantage to work with the 2nd order scheme rather than with the 1st order scheme, which is illustrated in the following error analysis.

The formal order of a scheme is thus not an objective criterion to judge the performance of a scheme. The only objective method to evaluate the overall performance of a numerical scheme is to determine the CPU time required to achieve results with a given precision.

The following norms can be used with advantage for rough data:

The 1-norm is defined by

$$\|\varepsilon\|_1 = \int_{-\infty}^{\infty} |\varepsilon(x)| dx \tag{6.6}$$

and the 2-norm is introduced as

$$\|\varepsilon\|_2 = \sqrt{\int_{-\infty}^{\infty} \varepsilon^2(x)dx} \quad (6.7)$$

Here, the 2-norm is not used, it has just been given for completeness. In the following, the global error will be determined with a norm applied on the relative error of the pressure according to the following definition

$$G_\infty = \left\| \frac{p - \widehat{p}}{\bar{p}} \right\|_\infty \text{ or } G_1 = \frac{1}{l} \left\| \frac{p - \widehat{p}}{\bar{p}} \right\|_1 , \quad (6.8)$$

where $\bar{p}$ is the average pressure in the entire domain. This way, G is a measure for the relative error of the scheme for the pressure. The behavior of G when reducing temporal and spatial discretization indicates the order of the scheme.

6.3 The one dimensional nozzle flow

A classical test case for one-dimensional steady state computations with space variable cross-section $A(x)$ is the nozzle flow (see Figure 6.1). It allows to test a number of flow situations: subsonic and supersonic flows without shocks, sub/supersonic transition and sub/super/subsonic flow with shock in the divergent.

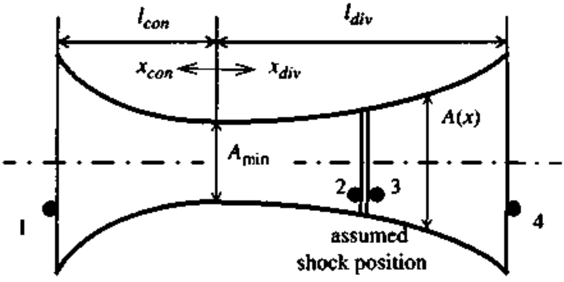

Figure 6.1 Tube with $A(x)$ as test case with indices for entry (1), assumed shock position (2, 3) and exit (4)

6.3.1 Gas dynamical functions

Elegant analytical solutions for problems in 1D gas dynamics are often obtained when using the critical Mach number or Laval number *La* instead of the Mach number *M* involving the use of the so called gas dynamical functions (GDF).

A representation of the most important relations for GDFs is given in [2]. Since they can not be found in standard text books, they shall be summarized here. GDFs are functions which depend only on the Laval number.

Mach number and Laval number are defined as

$$M = \frac{u}{a} \text{ and } La = \frac{u}{a^*}. \tag{6.9}$$

For isentropic flow, Mach number and Laval number are be related to each other by

$$La = M\sqrt{\frac{\frac{\kappa+1}{2}}{1+\frac{\kappa-1}{2}M^2}} \text{ and } M = La\sqrt{\frac{\frac{2}{\kappa+1}}{1-\frac{\kappa-1}{\kappa+1}La^2}} \tag{6.10}$$

The energy equation yields

$$\frac{a^2}{a_t^2} = \frac{T}{T_t} = 1-\frac{\kappa-1}{\kappa+1}La^2 . \tag{6.11 a}$$

For isentropic flow, the following relations are obtained when using eq. (2.36):

$$\frac{\rho}{\rho_t} = \left(1 - \frac{\kappa - 1}{\kappa + 1} La^2\right)^{\frac{1}{\kappa - 1}}, \tag{6.11 b}$$

$$\frac{p}{p_t} = \left(1 - \frac{\kappa - 1}{\kappa + 1} La^2\right)^{\frac{\kappa}{\kappa - 1}}, \tag{6.11 c}$$

where the index t designates the total state, i.e. the state the corresponding flow value would take if the flow was slowed down isentropically to rest. Note that the flow velocity follows immediately from eq. (6.9).

The critical values can be determined setting the Laval number to 1which yields

$$\frac{a^{*2}}{a_t^2} = \frac{T^*}{T_t} = \frac{2}{\kappa + 1}, \frac{\rho^*}{\rho_t} = \left(\frac{2}{\kappa + 1}\right)^{\frac{1}{\kappa - 1}} \text{ and } \frac{p^*}{p_t} = \left(\frac{2}{\kappa + 1}\right)^{\frac{\kappa}{\kappa - 1}}, \tag{6.12}$$

which for κ=1.4 take the values

$$\frac{a^{*2}}{a_t^2} = \frac{T^*}{T_t} = 0.8333, \frac{\rho^*}{\rho_t} = 0.6339 \text{ and } \frac{p^*}{p_t} = 0.5283$$

The continuity equation can be introduced by the adimensional mass flow of type 1 and 2, respectively, as

$$\theta = \frac{\dot{m}}{K_\theta\left(\frac{A p_t}{\sqrt{R T_t}}\right)} \text{ and } \chi = \frac{\dot{m}}{K_\chi\left(\frac{A p}{\sqrt{R T_t}}\right)}, \tag{6.13}$$

between which the use of the total pressure in θ and the static pressure in χ is the only difference. The coefficients K_θ and K_χ have been chosen to normalize the critical mass flows to $\theta^* = \chi^* = 1$ for La=1. They are only functions of κ.

$$K_\theta = \sqrt{\kappa}\left(\frac{\kappa + 1}{2}\right)^{-\frac{\kappa + 1}{2(\kappa - 1)}} \text{ and } K_\chi = \sqrt{\kappa\left(\frac{\kappa + 1}{2}\right)}, \tag{6.14}$$

which, for κ=1.4, take the values

$$K_\theta = 2.8624 \text{ and } K_\chi = 1.2961$$

Both types of adimensional mass flows can be expressed as gas dynamical functions yielding

$$\theta = \left(\frac{\kappa + 1}{2}\right)^{\frac{1}{\kappa - 1}}\left(1 - \frac{\kappa - 1}{\kappa + 1} La^2\right)^{\frac{1}{\kappa - 1}} La \text{ and} \tag{6.15}$$

$$\chi = \left(\frac{\kappa+1}{2}\right)^{-1}\left(1 - \frac{\kappa-1}{\kappa+1}La^2\right)^{-1} La \; . \tag{6.16}$$

Note that equations (6.11) and (6.16) can be inverted, but the zero of the inverted eq. (6.15) can only be found by approximation.

6.3.2 Analytical Solution

With this preparation, the nozzle flow can be computed. There is a multitude of ways to develop the subject. Here, the geometry of the channel $A(x)$ and the total state p_{t1} and T_t in the high pressure reservoir are given. The desired flow characteristics are then influenced by choosing the exit pressure p_4.

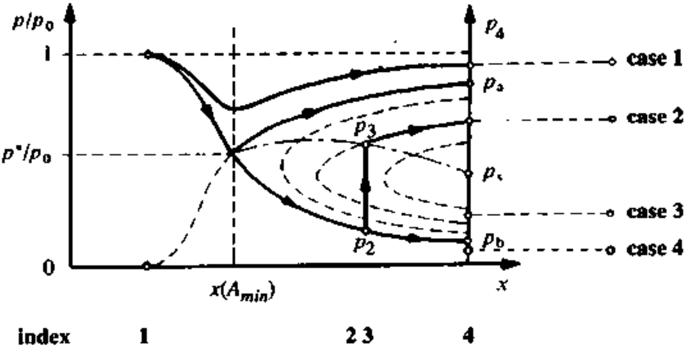

Figure 6.2 Integral pressure curves for the flow through a Laval nozzle with indices as defined in Figure 6.1

If the flow is critical in the narrowest section of the given geometry, i.e. $La(A_{min}) = 1$, the subsonic adaptation pressure p_{4a} or the supersonic adaptation pressure p_{4b} can be reached with isentropic flow. The corresponding Laval numbers at outflow are identified by La_{4a} or La_{4b}. They can be found by evaluating the expression

$$\frac{\theta_{4a}}{\theta*} = \frac{A_{min}}{A_4} \text{ or } \frac{\theta_{4ab}}{\theta*} = \left(\frac{\kappa+1}{2}\right)^{\frac{1}{\kappa-1}}\left(1 - \frac{\kappa-1}{\kappa+1}La_{4ab}^2\right)^{\frac{1}{\kappa-1}} La_{4ab} = \frac{A_{min}}{A_4} \; . \tag{6.17}$$

Since for isentropic flow the total states remain constant, the corresponding pressures at the exit p_{4ab} can be determined with

$$\frac{p_{4ab}}{p_t} = \left(1 - \frac{\kappa-1}{\kappa+1}La_{4ab}^2\right)^{\frac{\kappa}{\kappa-1}} \; . \tag{6.18}$$

Figure 6.2 shows the integral curves for the pressure in a Laval nozzle. For all $p_4 \geq p_{4a}$ (case

1), the flow will be subsonic in the divergent. If the exit pressure is reduced to values $p_4 < p_{4a}$, critical state is reached in the narrowest cross-section and the flow will enter the supersonic regime in the divergent. The flow in the divergent will be entirely supersonic if the exit pressure takes values below the supersonic adaptation pressure p_{4b} (case 4). For pressures $p_{4a} > p_4 > p_{4b}$, a shock occurs. For $p_{4a} > p_4 > p_{4s}$ (case 2), a normal shock with subsonic continuation occurs. For $p_{4s} > p_4 > p_{4b}$ (case 3), only the oblique shock with supersonic continuation leads to a feasible solution. Pressures with $p_4 < p_{4b}$ (case 4) can not be attained by continuous flow. Additional expansion at the exit occurs. Only subsonic inflow shall be considered here.

6.3.2.1 Subsonic and isentropic flow through a nozzle

If the flow is to remain entirely subsonic, one has to choose $p_4 \geq p_{4,a}$.

given: $A(x), p_{t1}, T_{t1}, p_4$

unknown: $T(x), \rho(x), p(x), u(x)$

The solution is straightforward:

1. Determine p_{4a} with eqs. (6.17) and (6.18) and choose $p_4 \geq p_{4a}$.
2. Determine La_4 from eq. (6.11 c) and θ_4 with eq. (6.15).
3. For each x, determine $A(x)$ and then $\theta(x)$ with

$$\frac{\theta(x)}{\theta_4} = \frac{A_4}{A(x)} . \qquad (6.19)$$

4. For each x, determine $La(x)$ from $\theta(x)$ with eq. (6.15).
5. For each x, determine the flow values using the GDFs in eqs. (6.9) and (6.11) from $La(x)$.

6.3.2.2 Nozzle flow with normal shock

If a normal shock is desired in the divergent, choose $p_{4a} > p_4 > p_{4s}$. Then, the flow will be critical in the narrowest section and supersonic in the divergent. The lower p_4 is chosen, the more downstream the shock appears.

Across a shock, the entropy increases, accounting for dissipative loss of the total pressure. The total temperature remains constant across a shock since the dissipated energy is not lost in an adiabatic channel. The total pressure in point 3 is lower than is point 2 since $s_3 > s_2$ and with the definition of the entropy $p_{t3} < p_{t2}$.

given: $A(x), p_{t1}, T_{t1}, p_4$

unknown: $T(x), \rho(x), p(x), u(x)$

The position of the shock can be determined with the following development.

1. Determine p_{4a} with eqs. (6.17) and (6.18) and choose $p_4 < p_{4a}$.
2. Determine La_1 from eq. (6.17) as before La_{4a} and then θ_1 with eq. (6.15), χ_1 with eq. (6.16) and p_1 with eq. (6.11 c).
3. Define the pressure ratio $\pi = \frac{p_4}{p_1}$ and the value $\varepsilon = \frac{A_4}{A_1}$ and apply the adimensional conservation equation between 1 and 4 in the form $\chi_4 = \frac{\chi_1}{\varepsilon\pi}$ in order to find χ_4.
4. Determine La_4 with χ_4 and eq. (6.16) and then θ_4 from La_4 and eq. (6.15).
5. Define the total pressure ratio as the ratio of the total pressure after and before the shock as

$$\pi_t = \frac{p_{t4}}{p_{t1}} = \frac{p_{t3}}{p_{t2}} \tag{6.20}$$

   and use the definition equation of θ, eq. (6.13). The total pressure ratio π_t can then be determined to be

$$\left(\frac{\theta_4}{\theta_1} = \frac{1}{\varepsilon\pi_t}\right) \Rightarrow \pi_t \tag{6.21}$$

6. With the Prandtl relation for a normal shock,

$$La_2 La_3 = 1 , \tag{6.22}$$

   and the fact that $A_2 = A_3$ eq. (6.15) can be used to determine La_2 from

$$\left(\frac{\theta_2}{\theta_3} = \frac{\left(1 - \frac{\kappa - 1}{\kappa + 1} La_2^2\right)^{\frac{1}{\kappa - 1}}}{\left(1 - \frac{\kappa - 1}{\kappa + 1} La_2^{-2}\right)^{\frac{1}{\kappa - 1}}} La_2^2 = \pi_t\right) \Rightarrow La_2 . \tag{6.23}$$

7. Use La_2 to compute the cross-section of the shock according to eq. (6.19) and inversely its x-position.
8. In order to prepare the computation of the flow between 3 and 4, determine

$$La_3 = \frac{1}{La_2},\ p_{t3} = \pi_t p_{t1}\ ,\ \rho_{t3} = \frac{p_{t3}}{RT_t} \text{ and } T_{t3} = T_{t2}\ . \tag{6.24}$$

Now, the procedure described in subsection 6.3.2.1 can be applied from 1 to 2 and from 3 to 4 with the corresponding total states in order to determine the flow values in the nozzle.

6.3.3 Numerical solution and definition of the parameters for the test case

In this section, the numerical boundary conditions are not examined. The correct boundary values found in the analytical solution have thus been imposed and the steady state solution was found by converging from a rather arbitrary initial condition to a steady solution applying the 2^{nd} order TVD solver by Roe as described in subsections 3.3.2 and 3.3.3 with the subroutine implemented in NUMSTA.

For the test cases, the following type of area function with the parameters given in Table 6.1 is chosen

$$A = A_{min} + (A_{max,\,con/div} - A_{min})\left(\frac{x_{con/div}}{l_{con/div}}\right)^2 \tag{6.25}$$

The dimensions for the two test cases reflect typical values occurring in tunnel aerodynamics. They are listed in Table 6.1.

Table 6.1 Parameters used in the present computations

symbol	explanation	case 1	case 2
$A_{max,con}$	max. cross-section of convergent	$16\ m^2$	
A_{min}	min. cross-section	$8\ m^2$	
$A_{max,div}$	max. cross-section of convergent	$20\ m^2$	
l_{con}	length of convergent	50 m	
l_{div}	length of divergent	100 m	
$p_{t,1}$	ambient pressure	100 kPa	
T_t	ambient temperature	288.15 K	
p_4	outlet pressure	98 kPa	70 kPa

6.3.3.1 Isentropic flow in a nozzle and order of the scheme

The first test case is concerned with entirely subsonic flow. The algorithms exposed in the subsections 6.3.2.1 and 6.3.3 are used for the analytical solution and the numerical treatment, respectively.

The very satisfying agreement between the analytical results and the numerical solution for a relatively coarse grid with Δx=5m is documented in Figure 6.3. The solution converged after approximately 600 time steps with Δt=0.005s.

Order and precision of the numerical scheme was determined according to section 6.2. Several runs were performed with different grid spacing. The time step has, within the limit imposed by the CFL condition, only little influence on the result, since a steady state solution is searched. The maximal local error, calculated on the pressure, diminishes with an exponent of 2 (see Figure 6.4). Thus, the scheme is, as expected, of 2nd order. The precision of the relative error is for Δx=5 m already as low as 10^{-5}. It can therefore be expected that sufficiently exact solutions for problems of tunnel aerodynamics can be obtained with a grid spacing in the order of several 10 m for smooth gradients.

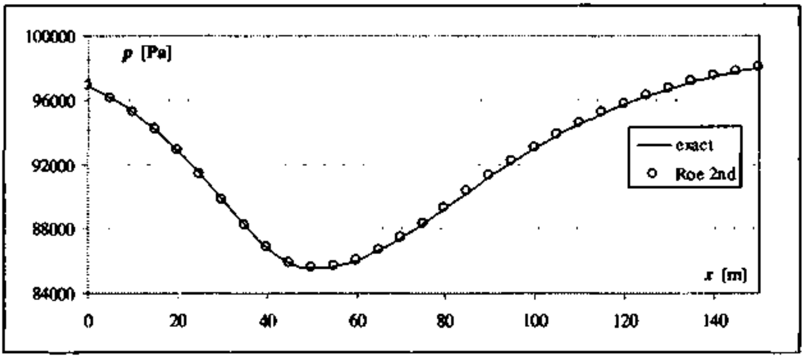

Figure 6.3 Exact analytical and numerical solution obtained with the 2nd order TVD solver of Roe for subsonic flow in the channel with space variable cross-section.

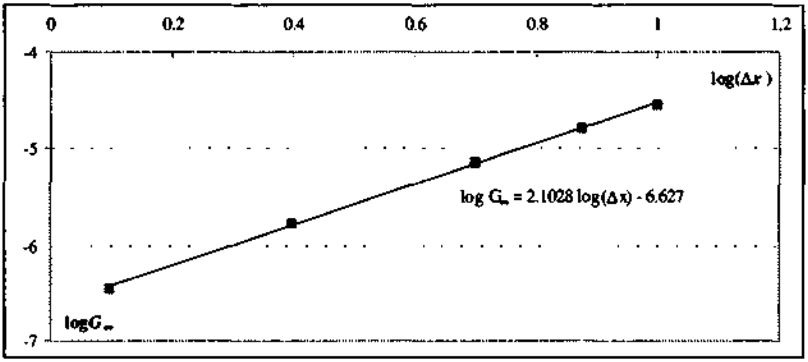

Figure 6.4 Relative error over spatial discretization in double logarithmic representation

6.3.3.2 Anisentropic flow with shock (Laval nozzle)

The second test case involves the computation of a shock. A shock is produced for the present case if an exit pressure inferior to $p_{4_b} = 96075\,\mathrm{Pa}$ is chosen. The exit pressure $p_4 = 70\,\mathrm{kPa}$ was chosen. The discretization parameters were set in the same way as before. The solution converged after approximately 600 time steps.

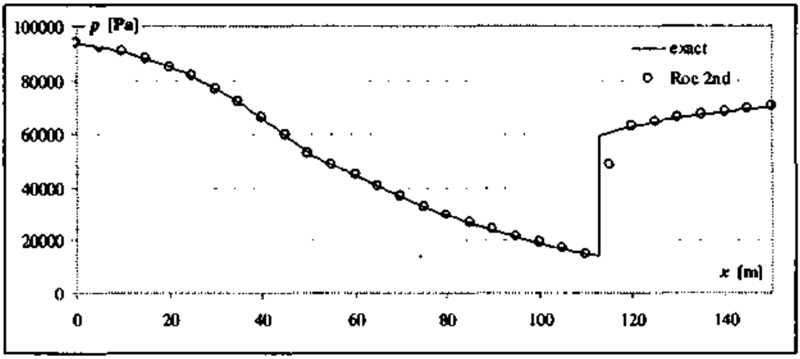

Figure 6.5 Exact analytical and numerical solution obtained with the 2nd order TVD solver of Roe for sub/super/subsonic flow in the channel with space variable cross-section

A very satisfactory fit between the analytical and the numerical solution is found. The shock position is exact and the shock is resolved over two grid points. This remains true if the mesh is refined.

A convergence analysis for discontinuous data has been performed for the flow in a shock tube (see section 6.4).

6.4 The flow in the shock tube and the order of the scheme

The third test case involves an application of the scheme of Roe on the flow in the shock tube as already discussed in section 3.2. Because of the existence of 3 discontinuities, the end of the expansion fan, the contact surface and the shock, the derivatives of the flow values are no longer continuous. Thus, the classical error analysis is, as discussed above, no longer valid. Figure 6.6 compares order and precision of the 1st order solver of Roe with the 2nd order solver of Roe for the case of the shocktube problem with a pressure ratio of 2 keeping the ratio $\Delta x / \Delta t$ = const. In Figure 6.7 the analysis is presented for a constant time step and variable spatial discretization.

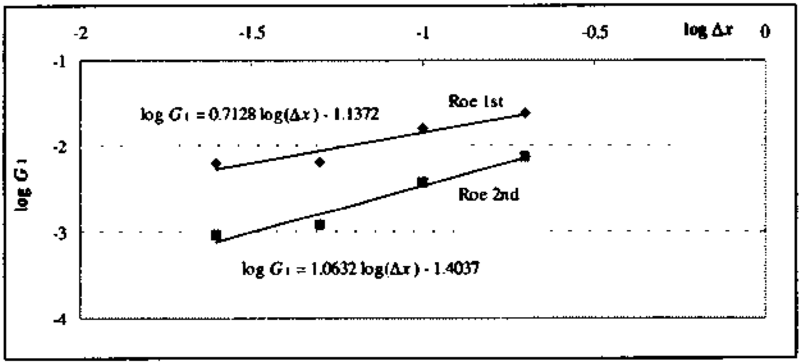

Figure 6.6 Order and precision of the scheme for $\Delta x / \Delta t$ = const.

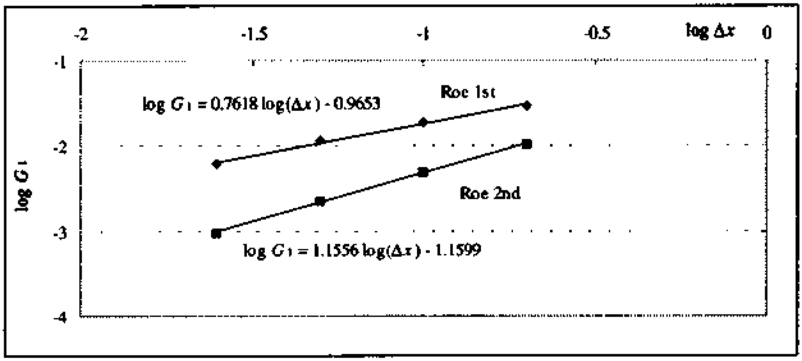

Figure 6.7 Order and precision of the scheme for Δt=0.025 ms and Δx variable

In both figures, the order of the 1st order solver of Roe is lower than 1 and the 2nd order solver of Roe shows an exponent of slightly above 1. As explained before, this behavior was expected. Even though the classical error analysis is not valid here, a useful characterization for the behavior of the schemes could be given. For the case of the low time step, the observed order is slightly higher.

6.5 Wave splitting at geometrical discontinuities

The correct treatment of geometrical discontinuities (diameter changes, tunnel ends and branchments) can be validated by comparing numerical results with analytical findings for acoustic waves [6]. The continuity and the momentum equations linearized around a certain initial state 0 are

$$\frac{\partial}{\partial t}\rho A = -\rho_0 A_0 \frac{\partial u}{\partial x} \text{ and} \tag{6.26}$$

$$\rho_0 \frac{\partial u}{\partial t} = -\frac{\partial p_e}{\partial x}, \tag{6.27}$$

where p_e symbolizes the excess pressure defined by $p_e = p - p_0$.

By taking the derivative of eq. (6.26) with respect to t and of eq. (6.27) with respect to x, the velocity u can be eliminated from the system yielding

$$\frac{\partial^2}{\partial t^2}\rho A = A_0 \frac{\partial^2 p_e}{\partial x^2}. \tag{6.28}$$

A Taylor expansion for the pressure relative to a small variation of ρA yields

$$p = p_0 + \frac{\partial p}{\partial \rho A}(\rho A - \rho_0 A_0) + \dots \tag{6.29}$$

in which the wave velocity defined by

$$c^2 = A_0 \frac{dp_e}{d(\rho A)} \tag{6.30}$$

can be introduced to yield

$$\rho A = \frac{A_0}{c^2} p_e. \tag{6.31}$$

Eq. (6.31) can then be introduced into eq. (6.28) and the excess pressure is found to satisfy the 1D wave equation

$$\frac{\partial^2 p_e}{\partial t^2} = c^2 \frac{\partial^2 p_e}{\partial x^2}. \tag{6.32}$$

with solutions of the form

$$p_e = f\left(t - \frac{x}{c}\right) + g\left(t + \frac{x}{c}\right) . \tag{6.33}$$

The test case will be concerned with the reflection and transmission of an initially right traveling incident wave at a geometrical discontinuity. The incident wave is then described by

$$p_e = f\left(t - \frac{x}{c}\right) \tag{6.34}$$

only. The function g describes the reflected wave.

By inserting eq. (6.33) into the linearized momentum equation (6.27), it is found that the velocity wave moves with the pressure wave according to

$$u = \frac{1}{c\rho_0}(f - g) . \tag{6.35}$$

Two conditions can be formulated to relate the flow values across a discontinuity surface: all domains connected to the discontinuity experience the same pressure and the volume flow has to be conserved. For the most general case of a branchment with an incident branch with index i and n side branches with indices 1...n with in general different cross-sections these conditions can be expressed as

$$p_i = p_1 = p_2 = \ldots \text{ and} \tag{6.36}$$

$$u_i A_i = \sum_n u_k A_k . \tag{6.37}$$

If the discontinuity is situated at x=0 condition (6.36) translates into

$$f(t) + g(t) = h_k(t) \text{ for } k = 1 \ldots n \tag{6.38}$$

where g stands for the wave reflected back into the incident branch and h_k stands for the transmitted waves into the side branches. Using eqs. (6.34) and (6.35) and assuming homogeneous density and speed of sound in the entire network, it follows from condition (6.37)

$$[f(t) - g(t)]A_i = \sum_n h_k A_k . \tag{6.39}$$

It follows

$$g(t) = \frac{A_i - \sum_n A_k}{A_i + \sum_n A_k} f(t) \text{ and } h_k(t) = \frac{2A_i}{A_i + \sum_n A_k} f(t) . \tag{6.40}$$

These formulae are valid for a branchment, a sudden variation of the cross-section in a tube without side branches with n=1 with $A_i \neq A_1$, for a closed end with n=1 and A_1=0 and for an open end with n=1 and $A_1 = \infty$.

A weak wave with well defined properties can be produced for the numerical experiment with an initial small pressure jump. Let the high pressure region have the index 1 and the low pressure region the index 0. According to the linear theory [12], pressure and velocity in the perturbed zone are

$$p - p_0 = \frac{1}{2}(p_1 - p_0) \text{ and } u = \frac{c}{2\kappa}\frac{p_1 - p_0}{p_0} . \tag{6.41}$$

The incident excess pressure is thus half the driving pressure difference. The following numerical experiments are based on $p_1 - p_0 = 20\ \text{Pa}$ and $p_0 = 10000\ \text{Pa}$. This corresponds to a driving relative pressure difference of 2E-03<<1 and generates an incident wave with an excess pressure of $p_e = 10\ \text{Pa}$ and a velocity of $u = 0.244\ \text{m/s}$. In order to demonstrate also the symmetry of the code, the sample configurations consist of a centered high pressure reservoir on both sides of which the geometrical discontinuity to be examined is connected.

6.5.1 The closed end

For the closed end we set A_1=0. It results

$$g(t) = f(t) \text{ and } h_1(t) = 2f(t) , \tag{6.42}$$

thus, the incident wave is totally reflected and the pressure at the end is doubled.

The test configuration consists of three tunnels, where the right end of tunnel 1 is connected to the left end of tunnel 2 and the right end of tunnel 2 is connected to the left end of tunnel 3 (see Figure 6.8). The exterior boundaries of tunnel 1 and 3 are closed. Initially, tunnel 2 has the higher pressure p_1 and the tunnels 1 and 3 have the lower pressure p_0. This configuration allows to demonstrate the correct treatment of the closed end (see subsection 5.3.1) and the connecting (see subsection 5.3.4) boundary condition.

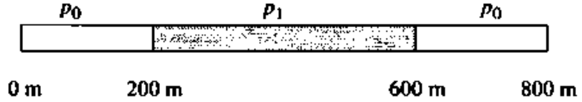

Figure 6.8 Test configuration involving a high pressure zone and two low pressure zones with closed ends

The result of the numerical experiment is given in Figure 6.9 for the instant t=0.5 s before and for t=1 s after interacting with the closed end. The primary y-axis is related to the excess pressure and the secondary y-axis scales the air velocity.

Weak shock waves move towards both ends of the configuration. The reflection at the closed ends doubles the excess pressure as predicted. The velocity distribution is parallel to the pressure waves and its amplitude corresponds to the prediction. In the high pressure segment the two rarefaction waves collide and because of the symmetry the wave behavior equals the one at a closed wall.

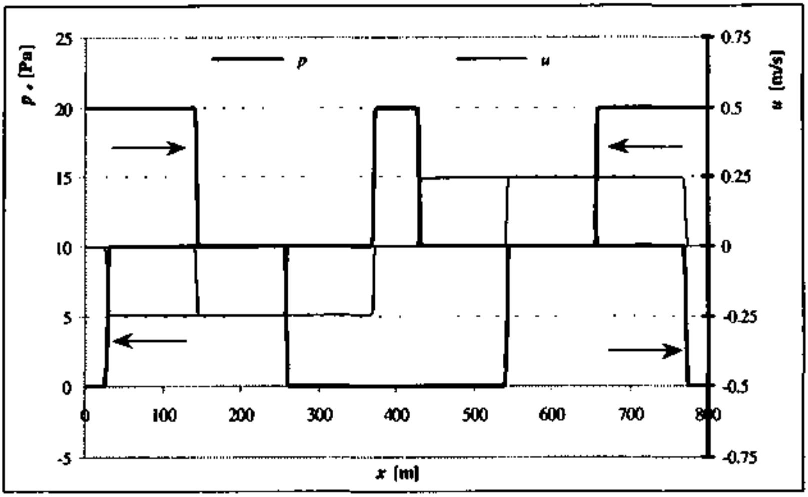

Figure 6.9 Reflection of a weak wave at closed ends (pressure and velocity distribution at t=0.5 s and t=1 s)

6.5.2 The open end

For the open end we set $A_1 = \infty$. It results

$$g(t) = -f(t) \text{ and } h_1(t) = 0 \ , \tag{6.43}$$

thus, the incident wave is canceled by the reflected wave and initial pressure is re-established at the end.

The test configuration is the same as in the previous case (see Figure 6.8) with the only difference that both ends are open to ambient conditions equal to the initial condition in the low pressure segments.

The pressure and the velocity distribution are again given for the times t=0.5 s and t=1 s. Figure 6.10 shows the pressure and velocity distribution before and after interacting with an open end. As predicted, the transmitted wave is of zero pressure amplitude and of doubled velocity amplitude. The development in the high pressure reservoir is equal to the previous case.

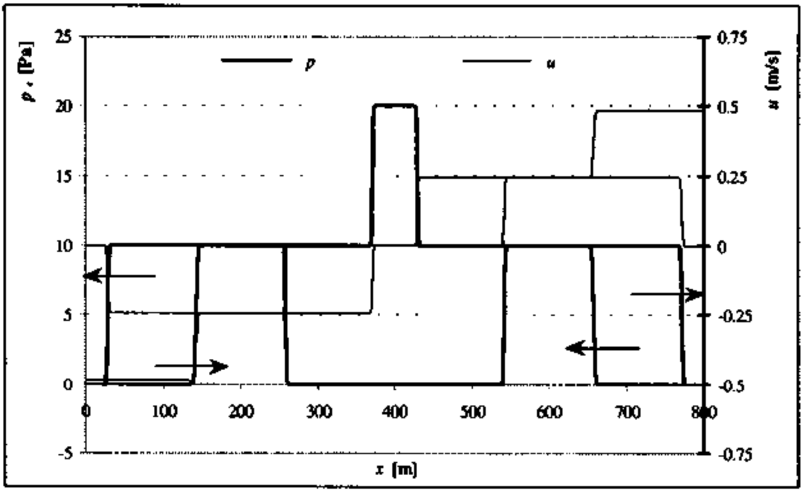

Figure 6.10 Reflection of a weak pressure wave at open ends (pressure and velocity distribution at t=0.5 s and t=1 s)

6.5.3 The sudden change of the diameter

For the sudden area variation of a duct the reflected and the transmitted waves are

$$g(t) = \frac{A_i - A_1}{A_i + A_1} f(t) \text{ and } h_1(t) = \frac{2A_i}{A_i + A_1} f(t) \,. \tag{6.44}$$

We chose a sudden increase in cross-section by a factor of 3, thus $A_1 = 3A_i$. For this case the reflected and transmitted waves take the values $g(t) = -\frac{1}{2}f(t)$ and $h_1(t) = \frac{1}{2}f(t)$.

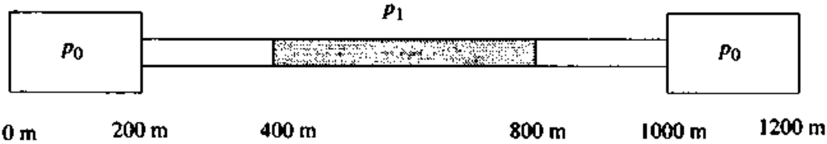

Figure 6.11 Test configuration involving a high pressure zone and two low pressure zones with variation of the cross-section

The test configuration given in Figure 6.11 consists of a high pressure reservoir connected to low pressure tubes with a sudden jump in the cross-section at x=200 m and at x=1000 m. The wave splitting is shown in Figure 6.12, where the positions of the diameter jumps are indicated with the dashed lines. The high pressure zone is, for the purpose of clear presentation, omitted in the present graph. The figure shows, as in the examples before, the pressure and the velocity distribution at t=0.5 s and t=1 s. It can be seen that the incident wave with an excess pressure of $p_e = 10$ Pa splits at the discontinuity of the cross-section in a transmitted wave with $p_e = 5$ Pa and a reflected wave of equal amplitude. The change of the absolute value of the velocity is, according to the theory $\Delta u = 0.122$ m/s which corresponds well to the numerical results.

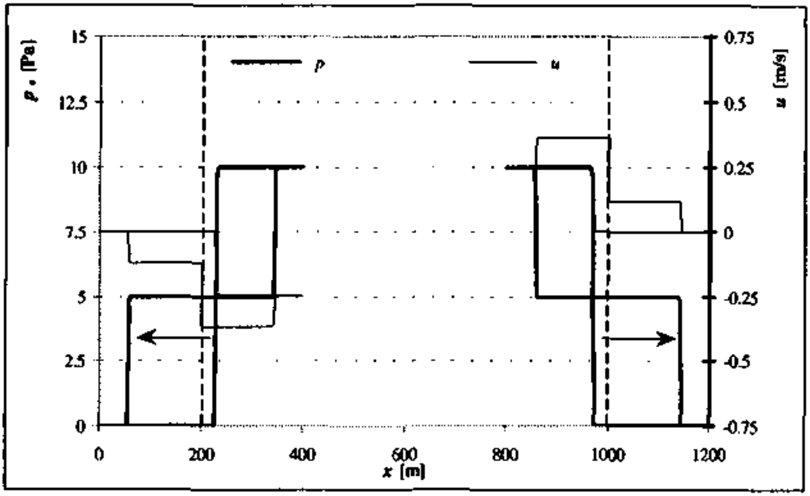

Figure 6.12 Reflection and transmission of a weak wave at an abrupt variation of the cross-section with $A_1 = 3A_i$ (pressure and velocity distribution at t=0.5 s and t=1 s, omission of the high pressure segment for the purpose of clear presentation)

6.5.4 The T-branchment

For a T-branchment with one lateral branch, eq. (6.40) reads

$$g(t) = \frac{A_i - A_1 - A_2}{A_i + A_1 + A_2} f(t) \text{ and } h_k(t) = \frac{2A_i}{A_i + A_1 + A_2} f(t) \text{ for k=1,2.} \qquad (6.45)$$

We will choose $A_i = A_1 = 2A_2$ and then reflected and transmitted waves are $g(t) = -\frac{1}{5} f(t)$ and $h_k(t) = \frac{4}{5} f(t)$.

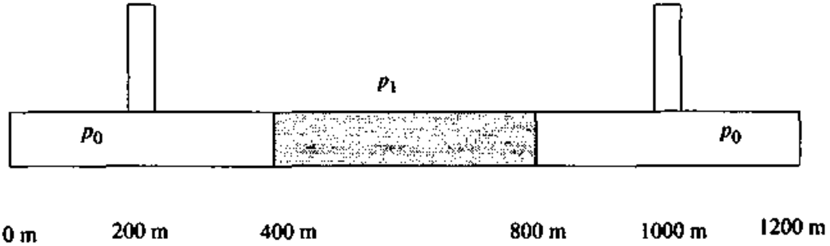

Figure 6.13 Test configuration involving a high pressure zone and two neighboring low pressure zones with laterally connected shafts at x=200 m and x=1000 m

The test configuration for this case consists again of the high pressure reservoir and the two neighboring low pressure parts. At x=200 m and x=1000 m lateral side branches are connected. These side branches are sufficiently long so that waves can travel without being reflected.

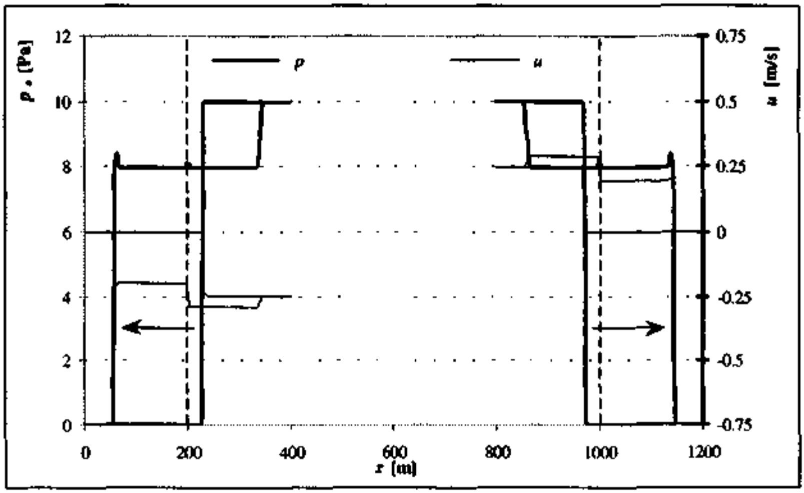

Figure 6.14 Reflection and transmission of a weak wave at a T-branchment with $A_i = A_1 = 2A_2$ (pressure and velocity distribution at t=0.5 s and t=1 s, omission of the high pressure segment for the purpose of clear presentation)

Figs. 6.14 and 6.15 give the results for the reflection and the transmission of the waves across this geometrical discontinuity. The first figure gives again the pressure and velocity distribution in the main tunnel with omission of the high pressure part. The positions of the lateral branches are indicated with the dashed lines. It can be seen that the reflected wave has the predicted amplitude of 1/5 of the incident wave. The plotted pressures and velocities correspond thus to the prediction. The transmitted wave in the lateral branch has also the predicted values which is shown in Figure 6.15.

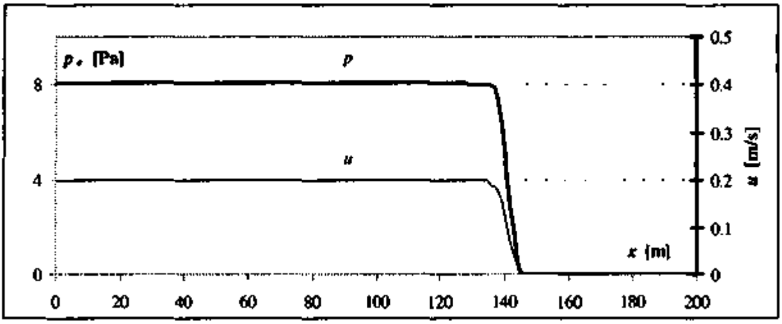

Figure 6.15 Transmitted wave in the side branch

6.6 Vehicle movement in an infinite tunnel without friction

This test case involves a vehicle in a tunnel, which is sufficiently long so that the boundary conditions do not influence the vehicle movement during the simulation time. Such a tunnel is named here 'infinite tunnel' (see Figure 6.16). Since there is no friction considered, it can also be simulated with a short tunnel and the non-reflective boundary condition.

The present comparison is restricted to the phase of quasi-steady movement. The acceleration and deceleration phases with unsteady behavior are not investigated here.

This test case is the first one where the additional terms accounting for the temporal change of the area function (see subsection 3.3.4) are considered. The numerical precision and the order of the scheme are compared with the shock tube test case.

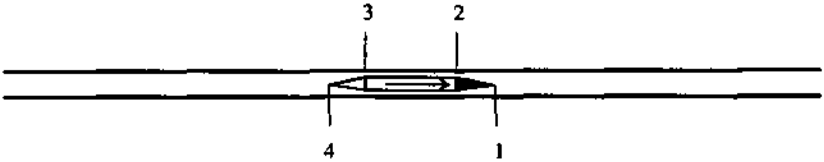

Figure 6.16 Vehicle in an infinite tunnel without influence of the boundary conditions, index convention

Table 6.2 Parameters for the present test case

l_v	vehicle length	100 m
A_{tu}	tunnel cross-section	16.08 m^2
$A_{v,max}$	max. vehicle cross-section	8.04 m^2
l_{34}	tail length	20 m
l_{12}	nose length	20 m
sp	vehicle speed	100 m/s
p_0	initial pressure	10 kPa
T_0	initial temperature	288.15 K

During the acceleration phase, the vehicle sends a compression wave to the front and an expansion wave rearwards. These waves move away from the vehicle and then the vehicle movement becomes steady with the initial flow values re-established at its front and its back. An example for a typical pressure distribution for this case is given below in Figure 6.17.

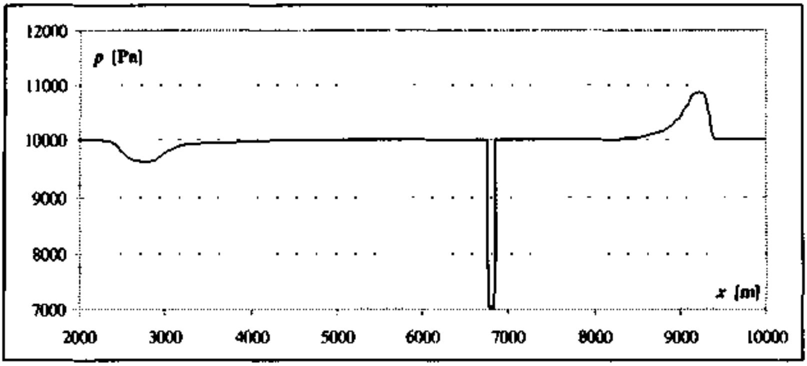

Figure 6.17 Typical pressure distribution in a frictionless tunnel after acceleration of a vehicle

The power due to aerodynamic drag has been evaluated with eq. (5.10). For steady movement, it should vanish in the present case. Figure 6.18 shows the typical curve with a steep increase during the acceleration phase, a peak at its end and then a reduction to the steady value, which is in this case slightly above 0. This is due to the somewhat uneven distribution of the pressure values for corresponding points along the nose and the tail (see Figure 3.9).

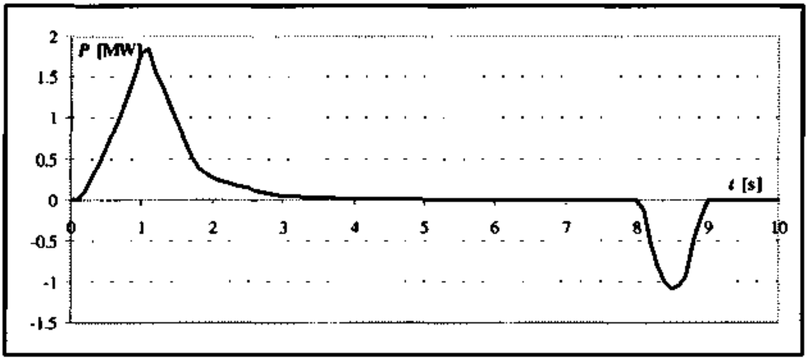

Figure 6.18 Power due to aerodynamic drag

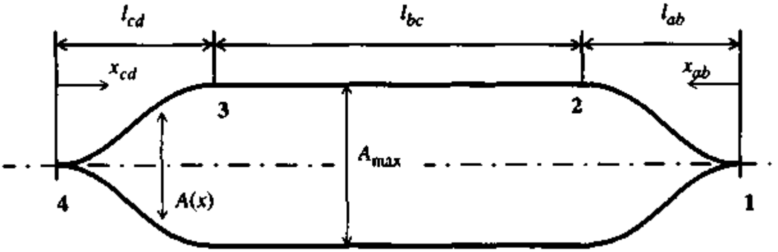

Figure 6.19 Vehicle model with indication of indices for the geometry

In order to avoid sharp gradients in proximity of the vehicle, the area function for the vehicle has been chosen with horizontal tangents at the tips and the ends of the annulus. Using the symbols introduced in Figure 6.19 the area function can be formulated as

$$A_v(x) = A_{v,\,max}\left[3\left(\frac{x_{12/34}}{l_{12/34}}\right)^2 - 2\left(\frac{x_{12/34}}{l_{12/34}}\right)^3\right] \tag{6.46}$$

where the parameters from Table 6.2 are used.

For the phase of steady movement, an analytical solution can be found using again the gas dynamical functions. In the tunnel frame of reference, the air is at rest in front of the vehicle, thus it enters the vehicle according to eq. (2.30) with the negative of the vehicle speed. The entry Laval number in the vehicle frame of reference is

$$La_1' = \frac{-sp}{a^{*\prime}}, \tag{6.47}$$

For this case, the total states relative to the vehicle frame of reference have to be determined. They are

$$T_t' = T_0 + \frac{sp^2}{2c_p} \text{ and } p_t' = p_0 + \rho_0\frac{sp^2}{2}. \tag{6.48}$$

The critical states follow with eq. (6.12). The non-dimensional mass flow at entry θ_1 can be found with eq. (6.15). This value can now be determined for each section as before for the Laval nozzle according to

$$\frac{\theta(x)}{\theta_1} = \frac{A_1}{A(x)}, \tag{6.49}$$

where $A(x) = A_{tu} - A_v(x)$ is the free tunnel cross-section around the vehicle. With the inverse function of (6.15), the Laval number in each section and subsequently the flow values can be determined by means of eq. (6.11).

Figure 3.9 gives the pressure distribution around the vehicle after the vehicle movement has become quasi steady. The exact solution is indicated with the solid line and the crosses. The solution obtained with NUMSTA is displayed with the circles. The fit is, at first sight quite satisfactory. However, the overprediction (underprediction) of the pressures in the convergent (divergent) yield a slight undesirable error in the drag curve as discussed above. This systematic error can be dealt with by manipulating the numerical scheme as discussed in subsection 3.3.5; as far as friction dominated tunnel aerodynamical problems are concerned, the slight imprecision for the inviscid test case is of no importance. It can also be observed that the numerical scheme implemented in NUMSTA slightly underpredicts the pressure levels in front of and behind the vehicle. This underprediction depends strongly on the limiter functions. It is thus due to numerical dissipation.

The same test case has been computed for different spatial and temporal discretizations keeping the ratio $\Delta x/\Delta t$ = const. An error analysis reveals convergence with an order of 0.84. This is slightly inferior to the result found in the case of the shock tube. The physical nature of the two cases is comparable since also in the case of the vehicle movement without friction a shock wave is produced. Besides, the dynamical adaptation of the mesh to the vehicle position introduces additional errors due to non uniformity of the mesh [24].

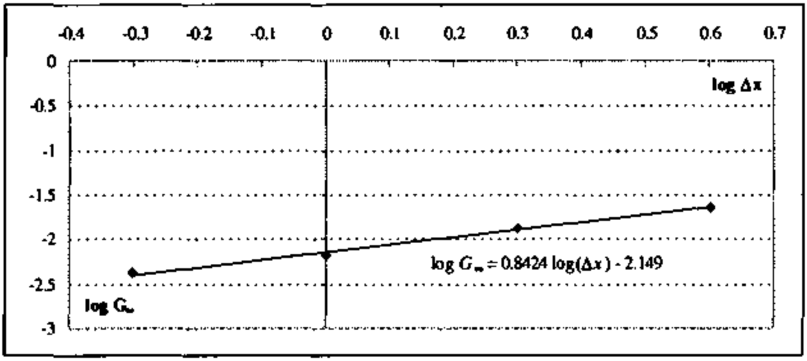

Figure 6.20 Error analysis for the test case

6.7 Steady flow with friction across a tube with varying cross-section

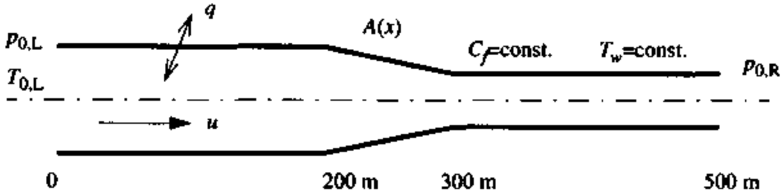

Figure 6.21 1D tube with varying cross-section with flow induced by pressure difference between both ends with friction and heat transfer

After having examined the behavior of NUMSTA for cases with no additional source terms, the following test case helps to validate the correct representation of the friction and heat transfer terms. It involves a tube with, in general space variable cross-section $A(x)$, in which flow is induced by a pressure difference between both sides. After an initial phase of repeated wave reflection steady flow is established. A sketch of the geometry for the test channel is shown in Figure 6.21 and the parameters for this test case are listed in Table 6.3. The transition zone between the two different cross-sections is modeled with a function as given in eq. (6.46). The tunnel wall temperature has been chosen unnaturally low in order to provoke a noticeable influence of heat transfer on the result.

The validation consists in comparing the results from two calculations for the entire domain. In calculation 1 the steady conservation equations are solved using a standard numerical subroutine with an entry boundary condition. Calculation 2 is the quasi-steady result obtained with NUMSTA when starting with an arbitrary initial condition. Since the entry boundary condition can not be determined analytically, it is found as a result of calculation 2 and then used as input in calculation 1.

Table 6.3 Parameters for the present test case

l_{tu}	tunnel length	500 m
A_{tu}	tunnel cross-sections	16.08 m^2, 8.04 m^2
P_t	tunnel perimeters	14.21 m, 10.05 m
C_f	friction coefficient	0.006
$p_{0,L}$	total pressure at the left end	20 kPa
$T_{0,L}$	total temperature at the left end	288.15 K
$p_{0,R}$	total pressure at the right end	10 kPa
T_w	wall temperature	228.15 K
q	heat transfer	on

For the steady case eq. (2.29) can be used to obtain the following system of first order ordinary differential equations in the tunnel frame of reference

$$\frac{d\rho}{dx} = \frac{\rho u^3 \frac{dA}{dx} + \kappa u S_2 - (\kappa - 1) S_3}{Au(a^2 - u^2)} , \tag{6.50 a}$$

$$\frac{du}{dx} = \frac{-\rho u a^2 \frac{dA}{dx} - \kappa u S_2 + (\kappa - 1) S_3}{A\rho(a^2 - u^2)} \text{ and} \tag{6.50 b}$$

$$\frac{dT}{dx} = \frac{\rho u^3 \frac{dA}{dx} + u^3 S_2 + (RT - u^2) S_3}{A\rho u(a^2 - u^2) c_v} , \tag{6.50 c}$$

where

$$S_2 = f_{ftu} + f_{fv} \text{ and } S_3 = q \ .$$

The system (6.50) can then be solved with standard mathematical subroutines. On the workstations at the IMHEF, the NAG package [19] is accessible via external program libraries. The subroutine D02BBF was used which integrates a system of first order differential equations with the Runge-Kutta-Merson method.

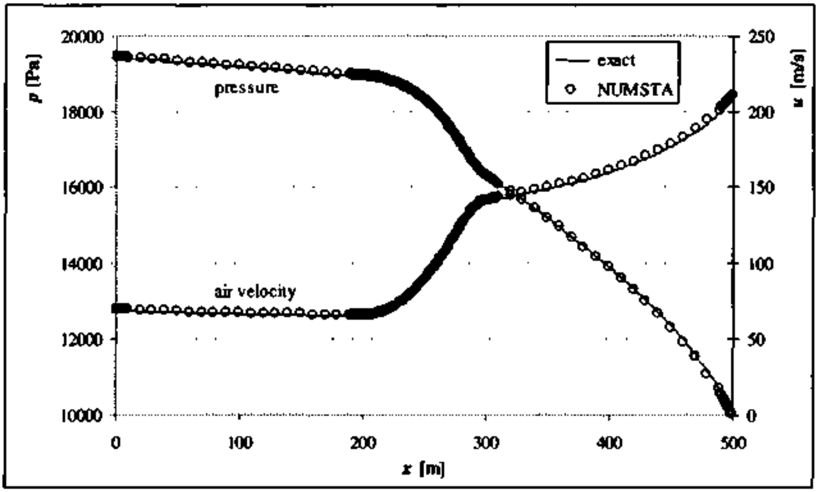

Figure 6.22 Comparison of pressure and velocity distribution for the present test case

Figure 6.22 illustrates the result by comparing the steady pressure and the air velocity distribution in the tube. The solid line corresponds to the exact solution of eq. (6.50) and the circles correspond to the quasi-steady result obtained with NUMSTA after a sufficient amount of iterations. The comparison is quite satisfactory. Towards the ends, the velocities for the exact solution are slightly lower and the pressures are slightly higher than for NUMSTA. This difference is practically of no importance, especially since the case treated here can be considered as a high-friction case with velocities of above 100 m/s. It can be explained with the discrete formulation of the additional source terms in NUMSTA, where the flow values in each cell are considered constant, whereas the continuous solution obtained with eq. (6.50) allows to account for a variation of the additional source terms within short distances which matters especially in zones with strong gradients as towards the end of the test tube.

It can therefore be concluded that the friction and heat transfer terms are correctly represented in the result, meaning that once a friction and heat transfer model is chosen, NUMSTA considers these models correctly.

6.8 Vehicle movement in an infinite tunnel without friction in the far field

An early approach to describe the flow field for the Swissmetro has been provided by Prud'homme [55] and Flatt [32]. Both examined the vehicle movement in an infinite tunnel neglegting tunnel friction in the far field flow. In this case, a steady solution for the near field flow can be found.

Prud'homme developed a quasi analytical iterative algorithm to solve the exact differential equations for the steady state case. This work has been an important contribution at the end of the preliminary study, since it gave results which have been taken as a reference during the beginning of the main study. However, the drag estimates for the steady-state are too optimimistic since they do not consider the unsteady increase of the pressure difference around the vehicle due to tunnel friction. Besides, he assumed constant total enthalpy along the vehicle. This neglects the work done by the forces moving relative to the vehicle, which was a common simplification in early tunnel aerodynamics [61, p. 7].

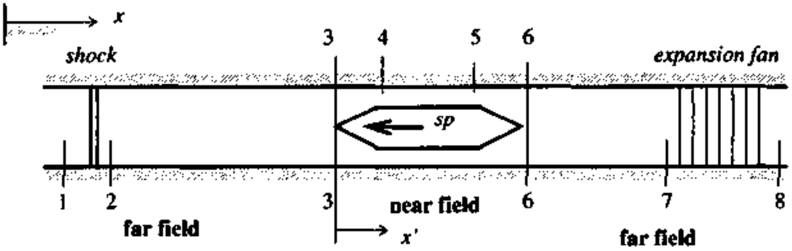

Figure 6.23 Index convention

The flow is characterized by a normal shock between 1 and 2 (see Figure 6.23). The shock limits the far field flow since the initial values are kept in zone 1. In the absence of friction, the flow values are constant between 2 and 3. From 3 to 4 the flow experiences the diameter change of the vehicle. Friction effects dominate the flow between 4 and 5 before a pressure regain in the divergent, between 5 and 6, is realized. Between 6 and 7, the beginning of the expansion fan, the flow values are again constant. Across the expansion fan the flow values vary isentropically and connect to the initial state in 8.

The figure allows also to define the near field flow and the far field flow. The near field is the immediate environment of the vehicle (here between 3 and 6) and the far field is the remainder. The near field is characterized by high gradients and also by a dominance of 3D effects. In the far field gradients are usually smaller, except around a shock or in the region of collision of pressure waves.

For the steady case eq. (2.31) can be used to obtain the following system of first order ordinary differential equations in the vehicle frame of reference

$$\frac{d\rho}{dx'} = \frac{\rho v^3 \frac{dA}{dx'} + \kappa v S_2' - (\kappa - 1) S_3'}{A v (a^2 - v^2)} , \qquad (6.51\text{ a})$$

$$\frac{dv}{dx'} = \frac{-\rho v a^2 \frac{dA}{dx'} - \kappa v S_2' + (\kappa - 1) S_3'}{A\rho(a^2 - v^2)} \text{ and} \tag{6.51 b}$$

$$\frac{dT}{dx'} = \frac{\rho v^3 \frac{dA}{dx'} + v^3 S_2' + (RT - v^2) S_3'}{A\rho v(a^2 - v^2) c_v} , \tag{6.51 c}$$

where

$$S_2' = f_{ftu} + f_{fv} \text{ and } S_3' = q - spf_{ftu} .$$

Note that eqs. (6.50) and (6.51) are very similar, the differences being the use of v instead of u, the vehicle fixed coordinate x' and the source terms. Heat transfer will be excluded for the present purpose, thus $q = 0$.

The solution algorithm requires to find the solution iteratively. We start with a certain u_2. This allows to determine the shock strength with eq. (3.18) and with it the other flow values behind the shock. With these boundary conditions, the system (6.51) can be solved as in the previous section using mathematical subroutines. A certain u_6 follows. It has to be verified if p_6 is also obtained with isentropic expansion from 8 to 7 when u_6 is given. If the pressure obtained with isentropic expansion is, measured on a convergence criterion, too low (too high) as compared to p_6, the absolute value of the air velocity in front of the vehicle $|u_2|$ has to be smaller (larger). A new iteration with a new guess for u_2 is started.

The test case from the previous section has been repeated here with the only difference that constant friction coefficients for the tunnel and the vehicle according to Table 6.4 have been chosen.

Table 6.4 Parameters used in the present computations

A_{tu}	tunnel cross-section	16.08 m^2
$A_{v,max}$	max. vehicle cross-section	8.04 m^2
P_{tu}	tunnel perimeter	14.22 m
$P_{v,max}$	max. vehicle perimeter	10.05 m
C_{fv}	vehicle friction coefficient	0.005
C_{ftu}	tunnel friction coefficient	0.006
l_v	vehicle length	100 m
β	blockage ratio	0.5
sp	vehicle speed	100 m/s

The very good agreement between the results obtained with the two methods is documented in Figure 6.24. As before, the pressure along the front (tail) is slightly overpredicted (underpredicted). This will account for a little error in the drag. An offset of the power value from the real value can be roughly estimated with the power required for the case of no friction.

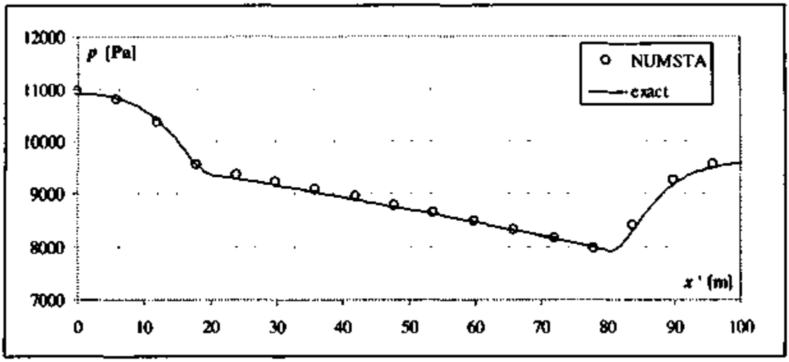

Figure 6.24 Pressure distribution along a vehicle with β=0.5 (analytical solution versus quasi steady state as obtained from NUMSTA)

6.9 Validation of the model for the perforated wall

Confidence in the correct implementation of this model can be reinforced by comparing two different ways to introduce a permeable zone as is indicated in Figure 6.25.

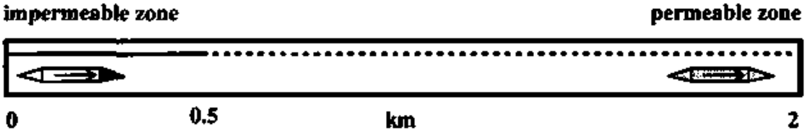

Figure 6.25 Test configuration for a validation of the perforated wall

The sketch shows an impermeable zone in the first quarter and a permeable zone along the rest of the tunnel. Simulations for the following two configurations have been performed:

1. One tunnel separated in main and side tunnel by a solid wall in the impermeable zone and a perforated wall in the permeable zone.
2. Two tunnels of equal length connected by short cross-vents spaced 20 m apart in the permeable zone.

This example tests if perforated walls can be interpreted as continuous cross-vents. This is expected because of the similar numerical models. For the comparison, the total tunnel cross-section and the perforation per unit length are in both cases equal.

Figure 6.26 shows the resulting power curves for both cases. The smooth curve corresponds to the continuous distribution of the perforations (case 1) whereas the rough curve gives the power requirement for case 2.

The two curves are parallel to each other. The continuous distribution of openings is an optimistic limit for openings with a finite distance. The result for the perforated wall is therefore at the lower limit of the result for the cross-vents, which shows a rough distribution accounting for the high frequency of the passage of the vehicle at the cross-vents.

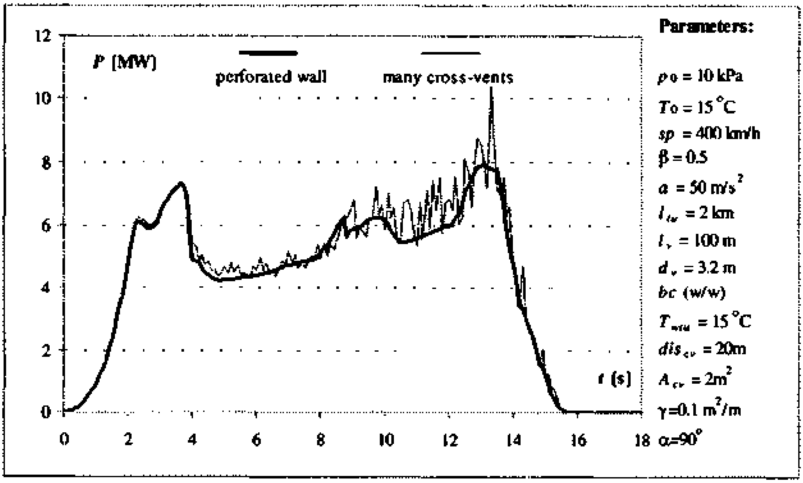

Figure 6.26 Comparison of the power curve for a configuration with perforated wall with a configuration with many cross-vents spaced only 20 m apart

This comparison shows that the models for the perforated walls and the cross-vents converge for vanishing distance of the cross-vents. A validation of the model for the perforated walls has therefore been achieved by comparison with the model for the cross-vents, which has been validated previously with acoustic waves.

6.10 Comparison with THERMOTUN/4

The computer program THERMOTUN/4 by Prof. A. Vardy has been intensively used for tunnel aerodynamic computations in the past decades (see bibliography). This code has been validated over the years on a multitude of existing technical installations. The code is based on the method of characteristics (MoC). Geometrical and flow discontinuities are modeled as discontinuity surfaces. The energy equation is replaced by the isentropy condition.

Test cases have been defined for the present validation in collaboration with the author of the code. For his collaboration to perform the thorough comparison and his permission to publish the results here I want to express my sincere gratitude at this place. The test cases are named THERMO-1, THERMO-2 and THERMO-3.

6.10.1 Vehicle in a closed tunnel without friction (THERMO-1)

The first test case comprises a vehicle in a closed tunnel with a low acceleration. In Figure 6.27 the test configuration is sketched and the history points for both the tunnel and the vehicle are indicated. For the present purpose the points T1, T5 and V3 are selected to convey a representative idea of how the far and the near field computation compare.

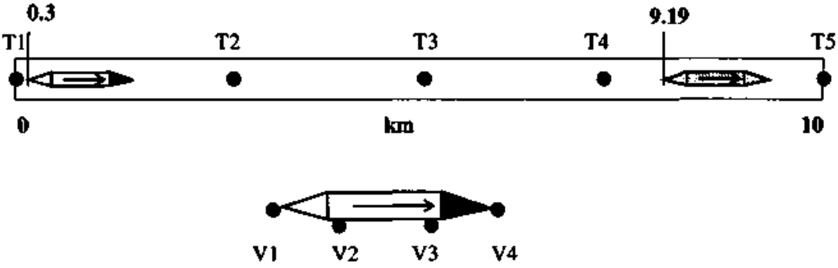

Figure 6.27 Sketch illustrating the test case THERMO-1 and the history points for tunnel and vehicle

The parameters are given in Table 6.5. Initially, the vehicle tail is positioned at x_s=300m. It accelerates in 68s to its maximum speed of sp=320 km/h. The vehicle cruises then until t=100s with constant maximum speed and decelerates then in 68 s to rest. The total simulation time has been fixed to t_e=200s in order to observe the continuing wave movement. Repeated interaction of the waves generated by the vehicle with the wall boundary conditions and entirely isentropic flow in the domain are characteristic for this test case.

Table 6.5 Parameters for THERMO-1

l_{tu}	tunnel length	10 km
l_v	vehicle length	200 m
A_{tu}	tunnel cross-section	19.50 m^2
$A_{v,max}$	max. vehicle cross-section	9 m^2
P_{tu}	tunnel perimeter	19 m
$P_{v,max}$	max. vehicle perimeter	10.5 m
sp	max. vehicle speed	320 km/h
a	acceleration	1.3072 m/s^2
x_s	start position	300 m
x_e	end position	9188.88 m
p_0	initial pressure	15 kPa
T_0	initial temperature	288.15 K
q	heat transfer	off
t_e	total simulation time	200 s

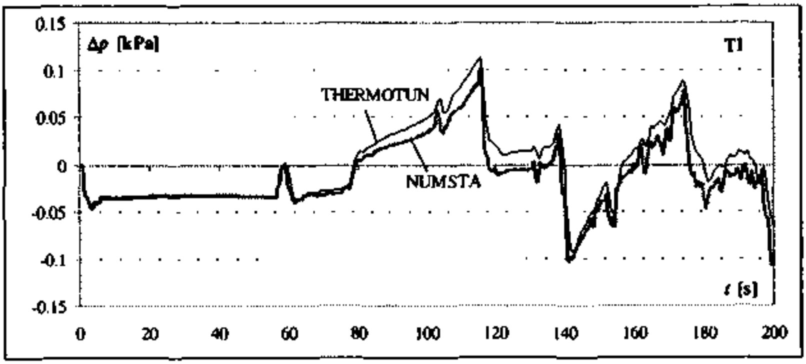

Figure 6.28 Pressure history for THERMO-1 in point T1 (left end of the tunnel)

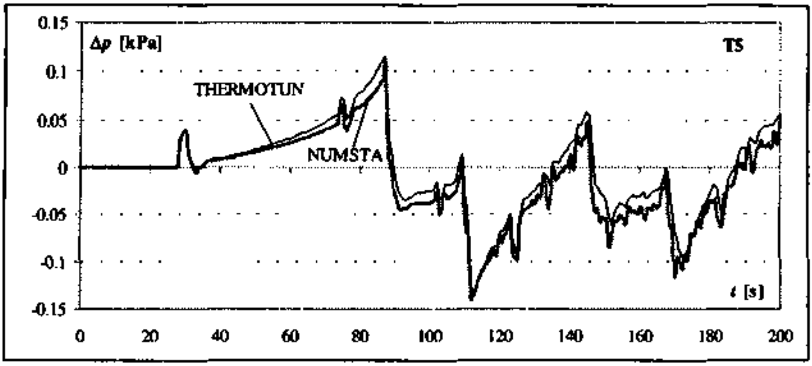

Figure 6.29 Pressure history for THERMO-1 in point T5 (right end of the tunnel)

The first comparison shows the history of the pressure perturbation at the points T1 (Figure 6.28) and T5 (Figure 6.29), the left and the right tunnel end, respectively. The agreement during the acceleration phase (t=0 - 68 s) is very good. The pressure curves remain in the sequel parallel with more details given by NUMSTA. As soon as reflected waves from the right tunnel end interact with the vehicle, NUMSTA predicts a slightly lower pressure than THERMOTUN. The effect of lowering the pressure has been described above and is due to numerical dissipation which is only noticeable in the inviscid case. The wiggles in the lower curve may be due to the conceptual difference that the nose and the tail represent discontinuity surfaces in the characteristic based model, whereas in NUMSTA the vehicle shape is modeled explicitly. An oncoming wave is therefore reflected as time delayed waves of varying strength, damped only by numerical dissipation. The wave timing and the main peaks are quite close in both cases. The maximum pressure difference for both cases amounts to some 20 Pa which is a very small value if compared to the pressure drop around the vehicle which amounts to some 2300 Pa or if compared to the typical pressures perturbations if friction effects are considered.

This argument is backed by looking at the history of the pressure perturbation alongside the vehicle close to the nose in Figure 6.30 or the air velocity history at the same point in Figure 6.31. On this scale, the two programs are in good agreement.

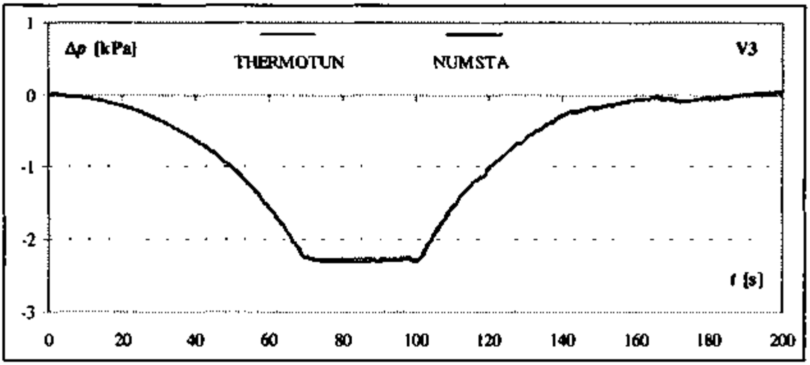

Figure 6.30 Pressure perturbation for THERMO-1 alongside vehicle in point V3

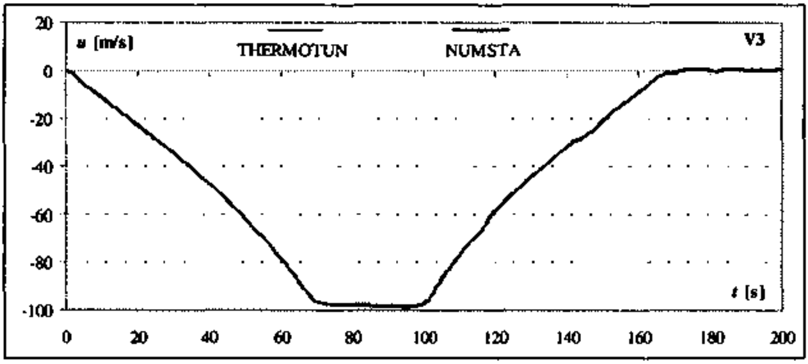

Figure 6.31 Velocity history for THERMO-1 alongside vehicle in point V3

6.10.2 Vehicle in an open tunnel with friction (THERMO-2)

The test case THERMO-2 comprises a vehicle entering a tunnel and crossing it with constant speed (see Figure 6.32). The history points are, as before at the tunnel ends and at tunnel quarter points as well as at both ends of the vehicle and alongside. It is the first test case involving friction in the entire tunnel system. The open end boundary condition is tested here as well. The parameters for this test case are listed in Table 6.6.

For this case data obtained with a simulation program developed at the TU Vienna are also available. This will allow to compare NUMSTA with two different codes on the same configuration.

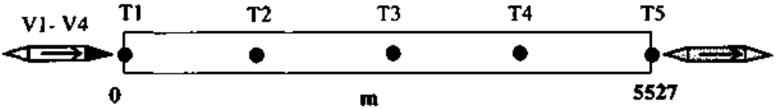

Figure 6.32 Configuration for the test case THERMO-2 with indication of history points

Table 6.6 Parameters for the present test case

l_{tu}	tunnel length	5527 m
l_v	total vehicle length	114 m
A_{tu}	tunnel cross-section	82 m^2
$A_{v,max}$	max. vehicle cross-section	10.3 m^2
P_{tu}	tunnel perimeter	32.1 m
P_v	max vehicle perimeter	10.3 m
C_{fv}	vehicle friction factor	0.005
C_{ftu}	tunnel friction factor	0.00625
sp	max. vehicle speed	305 km/h
p_0	initial pressure	100 kPa
T_0	initial temperature	288.15 K
q	heat transfer	off
t_e	total simulation time	70 s

Friction effects are, for this case, less dominant than if friction was turned on in THERMO-1, since the blockage ratio is much smaller and also the speed is inferior. It will be interesting to discuss how NUMSTA compares to THERMOTUN/4 for a case where friction effects are small and then for a case where friction effects become more dominant.

This test case confirms the above mentioned assumption that the pressure loss due to numerical dissipation in THERMO-1 has no influence on a test case where physical dissipation is significant. NUMSTA no longer underpredicts systematically the reference values. The Figs. 6.33 - 6.35 show a very good match between the two curves. The wave shape is slightly sharper resolved and the wave amplitude is smaller with the 2^{nd} order flow solver than with the MoC. NUMSTA predicts the wave amplitudes and the air velocities sensibly lower, especially at larger times. This accounts for the more pronounced consideration of friction terms as compared to THERMOTUN/4. This can be confirmed by the high friction test case THERMO-3.

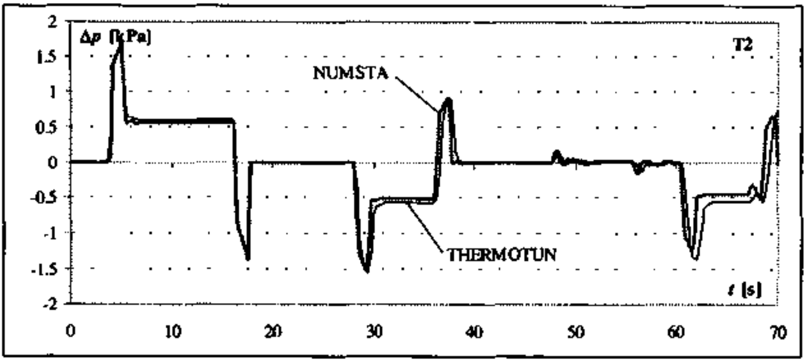

Figure 6.33 Pressure history for THERMO-2 for the point T2 (first tunnel quarter point)

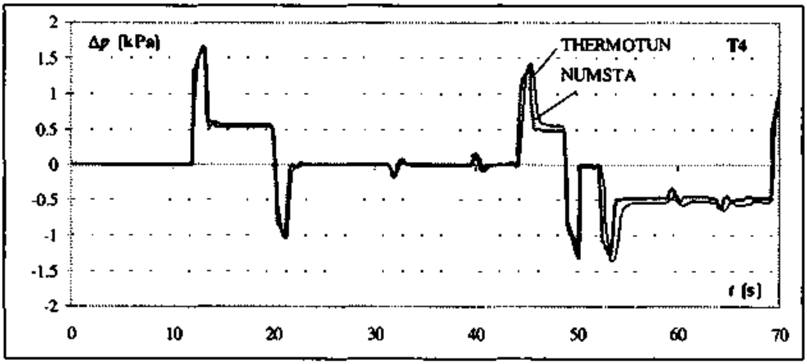

Figure 6.34 Pressure history for THERMO-2 for the point T4 (third tunnel quarter point)

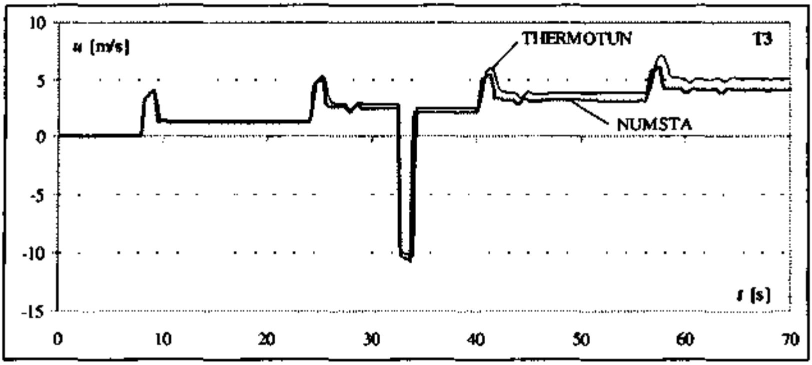

Figure 6.35 Air velocity history for THERMO-2 for the point T3 (tunnel center)

6.10.3 Vehicle in a closed tunnel with friction (THERMO-3)

The third comparison with the name THERMO-3 shows the main differences between the two programs.

The test case THERMO-3 corresponds to the same configuration as THERMO-1. The only difference is that friction is now considered. The test case is thus described by Figure 6.27 with the parameters from Table 6.5 and the friction coefficients from Table 6.7.

Table 6.7 Friction coefficients for the test case THERMO-3

C_{ftu}	tunnel friction coefficient	0.005
C_{fv}	vehicle friction coefficient	0.003

This test case is discussed on the example of the pressure histories in the tunnel end points. As opposed to the previous comparisons, Figure 6.36 and Figure 6.37 show significant differences between the two curves. This concerns mainly the amplitude of the pressure curves, whereas the form of the curves is similar since sharp changes of the slope occur at about the same times. This indicates that the generating waves are similar in both cases and that only the wave attenuation mechanism is different. The pressure history for the point T1 shows that the expansion wave as computed with NUMSTA is initially stronger. During the phase of movement with constant speed, air flows to the back and 'fills' up the low pressure zone created behind the vehicle. In the meantime, dissipated energy causes the temperature to increase in the zone influenced by the vehicle. Both phenomena cause pressure perturbation in point T1 to increase again, eventually to positive values. Again, it can be observed that the pressure evolution of NUMSTA is more pronounced than with the MoC code.

The pressure history in point T5 shows a similar behavior, i.e. that the initial pressure wave is stronger and also the increase with time is steeper with NUMSTA than with THERMOTUN/4. This was expected since more dominant dissipation causes a stronger pressure loss along the vehicle. Pressure balancing through bypassing causes in the sequel the reduction of the pressure level in front of the vehicle and also the difference between the two curves.

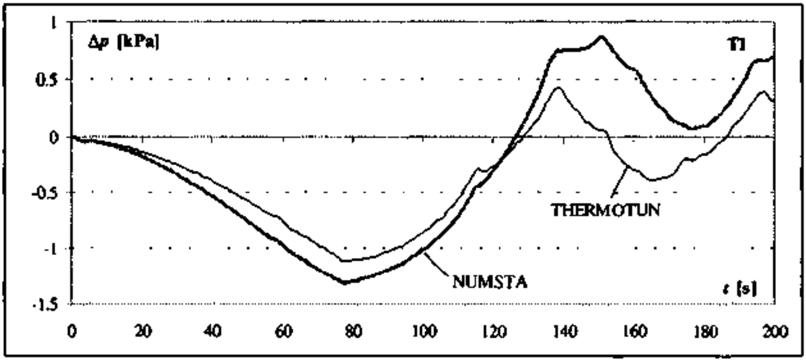

Figure 6.36 Pressure history for THERMO-3 in the point T1

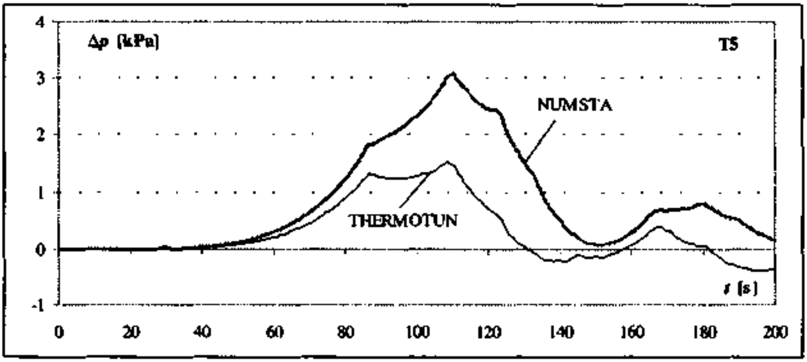

Figure 6.37 Pressure history for THERMO-3 in the point T5

This example is particularly interesting because it demonstrates that for flows with high blockage ratios and vehicle speeds involving high flow velocities, where friction effects become dominant, the two codes give different results. The explanation of the origin of these differences is the subject of the following subsection.

6.10.4 Analysis of the disagreement between NUMSTA and THERMOTUN/4 for high-friction cases

The significant disagreement between NUMSTA and THERMOTUN/4 for high-friction cases could be explained by two differences of the codes:

1. The energy equation, i.e. the assumption of isentropic flow in THERMOTUN/4 and the complete energy equation used in NUMSTA.
2. The different discretization methods, i.e. the MoC in THERMOTUN and the finite volume approach in NUMSTA.

influence of the energy equation

The first option can be tested by discussing the influence of the source term in the energy equation.

In a first step, the influence of convective heat transfer is examined. In Figure 6.38 the pressure history for the point T5 in THERMO-3 with heat transfer as computed with NUMSTA (label 'q on') with the result found by THERMOTUN/4 is compared. As expected, heat transfer helps to reduce the distance between the two curves. However, the difference remains considerable.

In a second step, an artificial heat transfer term rendering the flow isentropic is introduced. It can be found by transforming the conservation equations (2.25) as follows. If the momentum equation is written with derivatives of one variable only, the continuity equation can be inserted to find on the LHS the differential form of the Euler equation

$$\frac{\partial u}{\partial t} + u\frac{\partial u}{\partial x} + \frac{1}{\rho}\frac{\partial p}{\partial x} = \frac{S_2^q}{\rho A}\ . \tag{6.52}$$

with the additional source terms considered on the RHS. The energy equation can be transformed to derivatives of one variable only using merely the continuity with the result

$$\frac{de}{dt} - \frac{p}{\rho^2}\frac{d\rho}{dt} + u\left(\frac{\partial u}{\partial t} + u\frac{\partial u}{\partial x} + \frac{1}{\rho}\frac{\partial p}{\partial x}\right) = \frac{S_3^q}{\rho A}\ . \tag{6.53}$$

With the definition of the entropy in the form $Tds = de + pd\frac{1}{\rho}$ and with eq. (6.52), the energy equation can be transformed into

$$\frac{ds}{dt} + u\frac{S_2^q}{\rho A} = \frac{S_3^q}{\rho A}\ . \tag{6.54}$$

In absence of friction forces and heat transfer eq. (6.54) yields simply $\frac{ds}{dt} = 0$, thus the flow is isentropic. However, if friction forces in the momentum equation are considered, the flow is no longer isentropic unless an artificial heat transfer term is added. For flow with friction, the source terms are $S_2^q = f_{ftu} + f_{fv}$ and $S_3^q = sp \cdot f_{fv} + \hat{q}$, where only an artificial heat transfer $\hat{q}$ has been added, then eq. (6.54) can be forced to yield isentropy by choosing $\hat{q} = u(f_{ftu} + f_{fv}) - sp \cdot f_{fv}$. NUMSTA was programmed to account for this term and the simulation THERMO-3 was repeated.

The result of this approach is shown in Figure 6.38. It allows to compare the forced isentropic result as found with NUMSTA (label 's=const.') with the result from THERMOTUN/4. Forced isentropy helps even more than heat transfer to reduce the difference between the two programs. However, the two curves are still not close to each other. Thus, the origin of the differences are not only due to the difference in the energy equation.

influence of the discretization method

The above mentioned second option, i.e. differences of the discretization methods, is now considered.

In sections 6.7 and 6.8 it was shown that NUMSTA accounts correctly for additional source terms in steady cases. Besides, the numerical scheme implemented in NUMSTA is based on the conservation form of the equations and therefore inherently ensures conservation.

On the other hand, the MoC does not provide conservation with increasing consequences for increasing values of the RHS of the conservation equations as discussed for example in [47], [70] and [78]. Sources of errors in the MoC are

- the location of the wave paths,
- the interpolation of the foot values,
- the integration of the source terms and
- the treatment of discontinuity surfaces.

These systematic problems lead to repeated small errors. A relatively simple method to detect them is to find an error in the mass conservation.

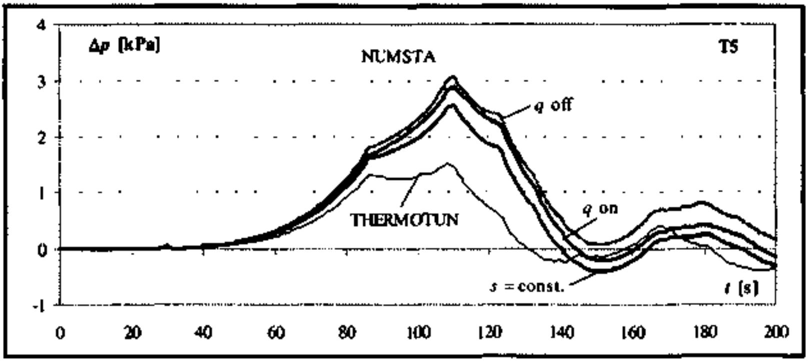

Figure 6.38 Comparison of the pressure history for THERMO-3 in point T5 with, without heat transfer and for isentropic flow as computed with NUMSTA with the result from THERMOTUN/4

Evidence has been gathered to determine which simulation program satsfies mass conservation better.

- evidence 1

In the time interval $t \approx [85s, 110s]$, Figure 6.38 displays the influence of the vehicle while moving with constant speed on the pressure at the right tunnel end (point T5).

In this time interval, a slight pressure decrease is shown. A slight pressure decrease in front of a vehicle and the associated temporary reduction of the power requirement can be observed and is due to a reduction of inertia forces at the end of the acceleration phase. Several examples in chapter 7 confirm this (see subsection 7.1.1). However, this effect is only a very short term effect after which the pressure in front of the vehicle and the associated power requirement increase again due to friction. For low accelerations and high friction, the inertia effect is even overridden by the friction effect and not noticeable. The well noticeable pressure decrease shown by THERMOTUN/4 at around t=85s is thus unlikely since the acceleration chosen is quite low and friction effects are important; a pressure increase, as obtained with NUMSTA is expected instead.

- evidence 2

Vardy [71] pointed out that the violation of the conservation property of the MoC should be noticeable by a clear difference of the mass flow in different points along the vehicle. Particularly in the phase of movement with constant speed (t = [68s, 100s]), but also during phases with a small acceleration, the flow around the vehicle is expected to be practically steady; unsteady effects due to friction and the boundary conditions are expected to be small.

Since THERMOTUN/4 uses the isentropic flow assumption, the density can be obtained with equation (2.36) from the pressure and the initial conditions. Vardy used the fluid properties R = 287 kJ/(kg K) and $\kappa = 1.401$. It is thus possible to plot the mass flow relative to the vehicle at different points around the vehicle from the available data. For steady flow, the mass flow must be equal at all points along the vehicle. Time histories in the points V1, V2, V3 and V4 (see Figure 6.27) have been recorded during the runs of both programs.

The Figure 6.39 a) shows the evolution of the mass flow relative to the vehicle in all 4 points obtained with NUMSTA. The two vertical lines indicate the phase of movement with constant speed. All curves are practically congruent. This displays the expected behavior.

On the contrary, the corresponding graph obtained from THERMOTUN/4, Figure 6.39 b) shows clear differences between the curves. These differences are particularly large while moving with high speeds. This is in clear contradiction of the expected mass conservation.

The figure allows to see that mass is lost between point V4 and V3 and also between V3 and V2 (remark: air flows relative to the vehicle from V4 to V1). Between V2 and V1 the absolute value of the mass flow increases again, i.e. mass is produced.

It is interesting that the curves for V1 and V3 of THERMOTUN/4 are not only practically congruent but match also the result obtained from NUMSTA until deceleration begins (see Figure 6.39 c)). At this moment, the flow velocity at the front of the vehicle changes sign from positive to negative. This possible explanation can be seen on the history graph for the flow velocity in point V4, not displayed here. The correspondence between THERMOTUN/4 and NUMSTA at V1 and V3 ist not explained and may be accidental. At any rate, the curves for the points V2 and V4 from THERMOTUN/4 are for most of the simulation time considerably different from NUMSTA.

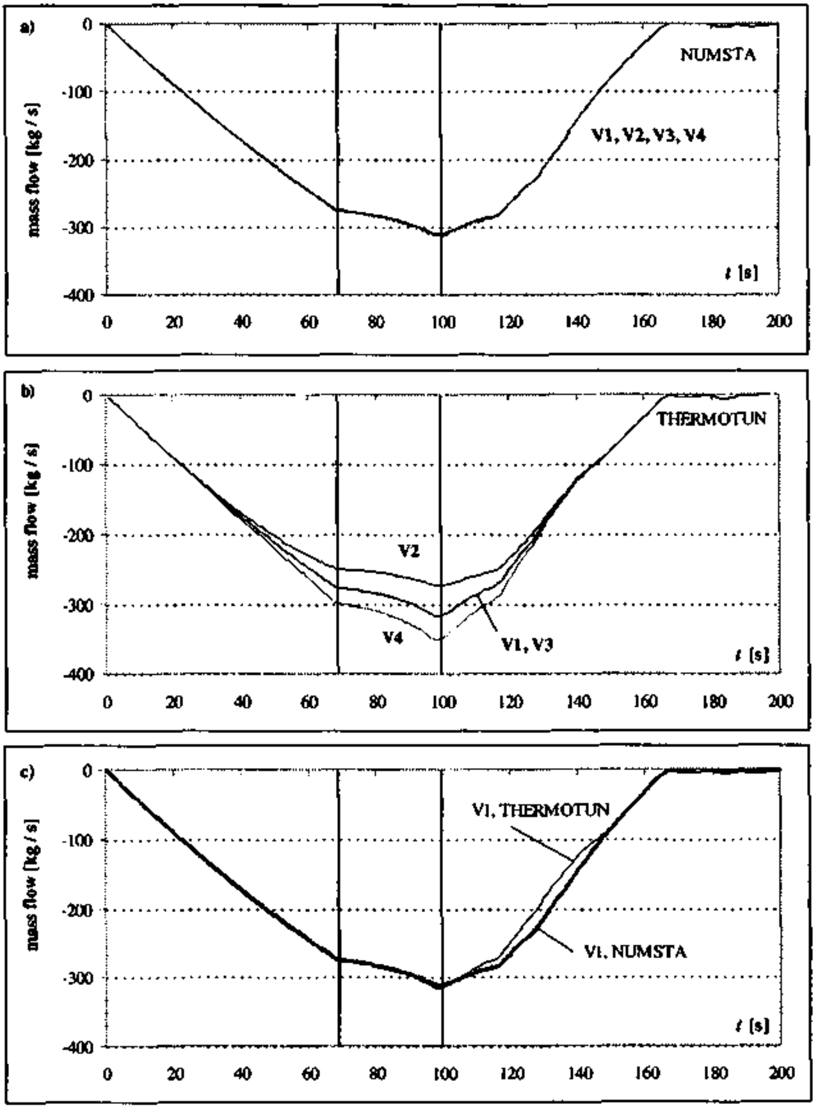

Figure 6.39 Comparison of the mass flow relative to vehicle at different points along the vehicle during the simulation time obtained with NUMSTA and with THERMOTUN/4 for the test case THERMO-3

- evidence 3

The picture can be completed by investigating the mass flow for the no friction case.

Just as in Figure 6.39, Figure 6.40 shows the time history of the mass flow in the vehicle frame of reference for four points traveling with the vehicle. The upper graph is the result from NUMSTA, the middle one displays the finding of THERMOTUN/4 and the graph at the bottom compares the results of both programs for points V1.

The curves obtained with NUMSTA are again congruent. For THERMOTUN/4 only pairs of curves, i.e. V1 and V4 as well as V2 and V3, match. The curves in these pairs are related to points of equal cross-section. After around $t \approx 40s$, i.e. when the vehicle speed is above ca. 200 km/h (the blockage ratio for this case is β=0.46), the two pairs separate and rejoin at around $t \approx 130s$, i.e. when the vehicle speed is again below ca. 200km/h.

This shows that at high flow velocities, but in absence of friction, there is a loss of mass flow between point V4 and V3 and a regain of the same magnitude between V2 and V1. Mass flow is conserved between V3 and V2. The conservation of mass flow between V1 and V4 is intriguing since two discontinuity surfaces are in between.

The pressure differences for the test case THERMO-1 highlighted above are therefore most likely due to an erroneous treatment of singularities by the MoC, which appears to become prominent at high flow velocities.

Figure 6.40 c) shows a good match between the two codes for the points V1 (and V4) except for slight differences during the phase of movement with constant speed.

The conservation problem for the MoC was recognized and improvements were published (for example in [70]) or are about to be published (for example in [72]).

The observations from evidence 3 allow to conclude that in absence of friction THERMOTUN/4 produces a mass flow error at discontinuity surfaces. However, between two points without discontinuities in between, mass conservation is achieved. As was shown in evidence 2, between two points without discontinuities in between, mass conservation is no longer achieved once friction is turned on.

Thus, in the MoC, the treatment of the discontinuities and of the friction terms seems therefore critical. A significant error due to the determination of wave paths and interpolation errors can not clearly be identified.

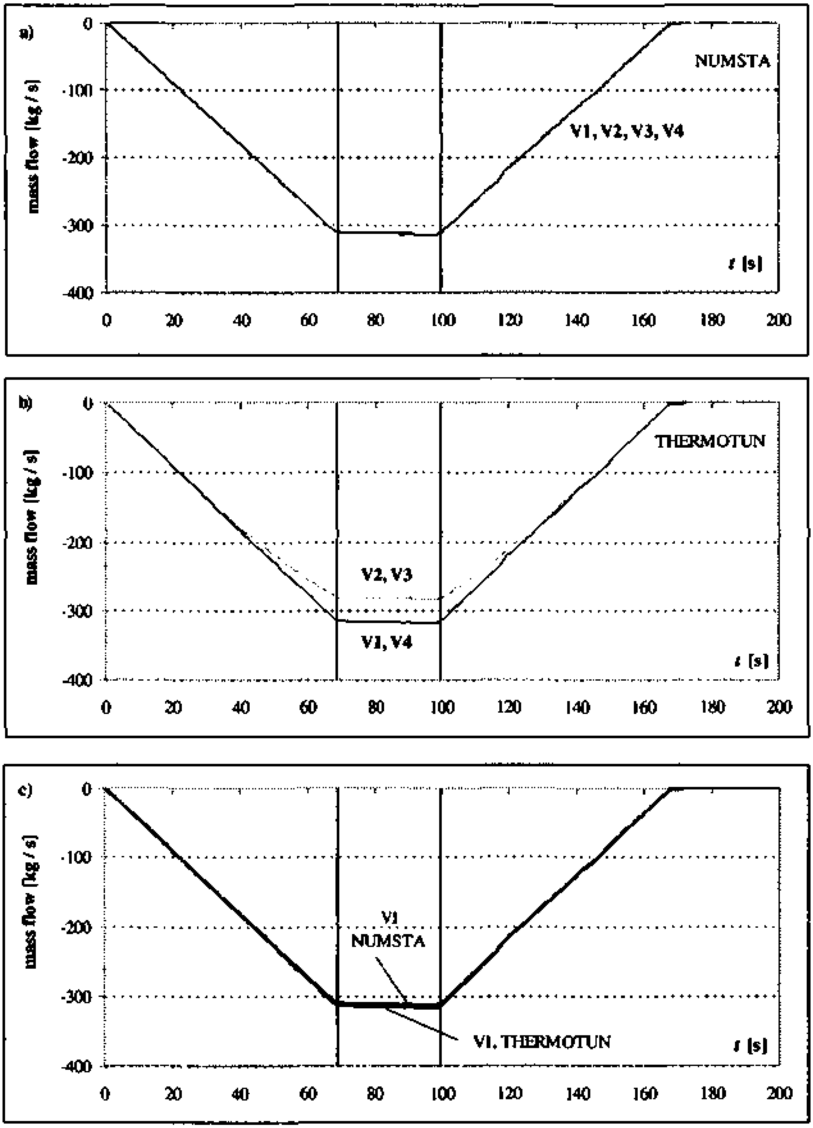

Figure 6.40 Comparison of the mass flow relative to vehicle at different points along the vehicle during the simulation time obtained with NUMSTA and with THERMOTUN/4 for the test case THERMO-1

6.11 Comparison with a computer program developed at the TU Wien

At the Technical University of Vienna (TU Wien) computer codes for the quasi 1D modeling of fluid flow through a tunnel have been developed by several workers around Prof. Sockel.

According to [61] a first version of the computer code was developed by Waclawiczek [73] based on a fluid model by Harwarth [42]. Steinrück [61] continued to develop the code for the DB research project TG311. Ottitsch [50] worked along the same line. Following the explanations in [61], the code developed at the TU Wien is based on the MoC with explicit modeling of discontinuity surfaces. Variations of the train shape can also be simulated as reported in [57].

The present test case is distributed in a report with restricted access [60] and permission for the present validation was granted by the institute of Prof. Sockel whom I would like to thank for the collaboration.

This comparison is based on the test case THERMO-2 (see Table 6.6) with the only difference that the history points made available to us are different than those given before. The history points are indicated in Figure 6.41. The point V1 is situated 64 m from the vehicle tail and the point T1 is 345 m away from the left tunnel end.

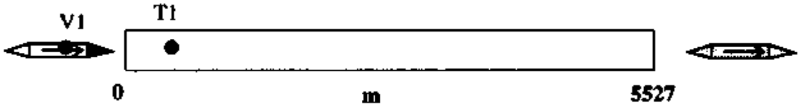

Figure 6.41 Positions of history points for the comparison with the code from the TU Wien

The comparisons in Figure 6.42 show the two pressure histories for the points T1 and V1. The values for the code from Wien have been digitized from a graph.

The wave attenuation in NUMSTA is inferior and the reflected waves are observed earlier than in the reference code. The latter may be due to the correcting model at the exit implemented in the code from Vienna which causes that waves are reflected with a short delay to the incident wave. Another possible explanation is based on the observation that the wave traveling speed is lower for the code of Vienna. This may be due to different temperatures.

With NUMSTA, the waves keep their angular form. They appear rounder with the other code. A possible explanation is that in the code from Vienna unsteady friction is considered which accounts for the higher dissipation behind strong pressure waves. However, detailed information about the models used for the present computation are not available to the author.

In phases of constant pressure in V1, e.g. in the time interval $t \approx [30s, 40s]$, NUMSTA shows a slightly higher pressure. The reason for this can be found in the different ways the two codes model the vehicle form. In NUMSTA, the vehicle is modeled with a certain shape which is reduced to discontinuity surfaces in the case of the code from Vienna. This causes points of equal pressure to be shifted by the nose length to the rear.

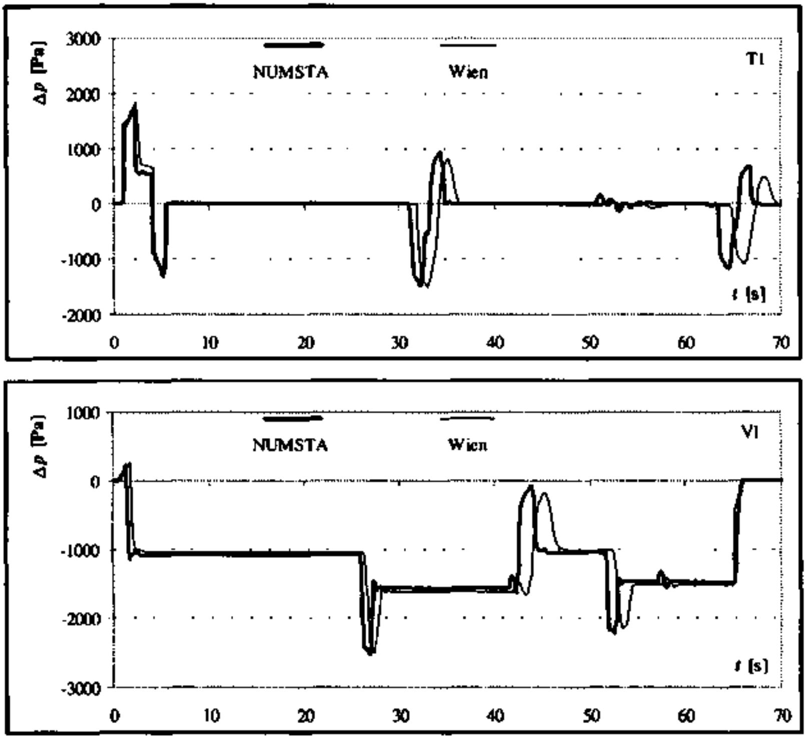

Figure 6.42 Comparison of the pressure history in the points T1 and V1 for the case THERMO-2

6.12 Comparison with experimental data

According to publications at the 'International Symposium for Aerodynamics and Ventilation in Vehicle Tunnels' the 'Deutsche Bahn' disposes of a set of experimental data (see [34], [35], [36], [65]).

Experimentally obtained pressure histories for a number of tunnel and vehicle fixed points are published in [35] and compared with THERMOTUN/2, a previous version of the MoC based code. These data were obtained in field tests for the passage of trains through the Mühlbergtunnel (l_t=5527m) and the Einmalbergtunnel (l_t=1140m) in 1988.

The above defined test case THERMO-2 corresponds in fact to the crossing of the Mühlbergtunnel (see Table 6.6). Since NUMSTA agrees well with both referenced codes for this case, the comparison between experimental findings and THERMOTUN/2 can be used to convey a first impression about how NUMSTA would compare to experimental findings.

A direct comparison with NUMSTA is not possible in all cases because some of the graphs are plotted in a very small scale and the data has not been made available to us. However, the graphs showing the damping of the entrance pressure wave for the crossing of the Mühlbergtunnel in [35] are sufficiently large in scale so that data points could be digitized.

Figure 6.43 compares the experimental finding of the pressure histories for the first 25 s in three points, situated at x=345m, x=1727m and x=5182m from the tunnel entrance. The graphs allow a direct comparison of the experimentally obtained wave speeds, the damping of the initial pressure wave traveling along the tunnel and other flow details with the numerical result from NUMSTA.

In the two upper graphs, the entrance pressure wave and the vehicle passage with a period of constant pressure in between are clearly visible. The entrance pressure wave is slightly stronger in NUMSTA. In the first graph, the pressure profiles of the vehicle passage correspond well. The train passage at the second observation point is slightly delayed in the experiment, which indicates a speed which is in reality lower than the declared value. This could explain the stronger entrance pressure wave in NUMSTA. After the passage of the entrance pressure wave the experimentally recorded pressure differs slightly from the numerical result. This can be explained with secondary pressure waves due to diameter changes. A discussion of this aspect and an account of the correct vehicle position over time and the correct tunnel geometry can be found in [49]. After the passage of the vehicle, initial pressure is in both cases nearly re-established.

The pressure history in the point x=5182m shows the initial pressure wave and the reflected wave shortly before both interact. There is no trace of the vehicle passage since the vehicle passes at this point after the observation period. This graph also shows the stronger damping of the entrance pressure wave in the experiment which causes the difference between numerical and experimental result to increase as the wave travels downstream. The reflected wave behaves accordingly with a negative pressure difference. It can also be observed on the third graph that the pressure waves obtained numerically with NUMSTA have a sharper form than in reality. This indicates that real waves are more damped and 'flatter' than the ones obtained numerically with a high resolution scheme. This has been discussed in connection with the effect of unsteady friction (see for example [56], [67] and [69]).

When a certain amount of experimental data is available, an improved model for friction can readily be implemented in NUMSTA to yield data closer to experimental findings.

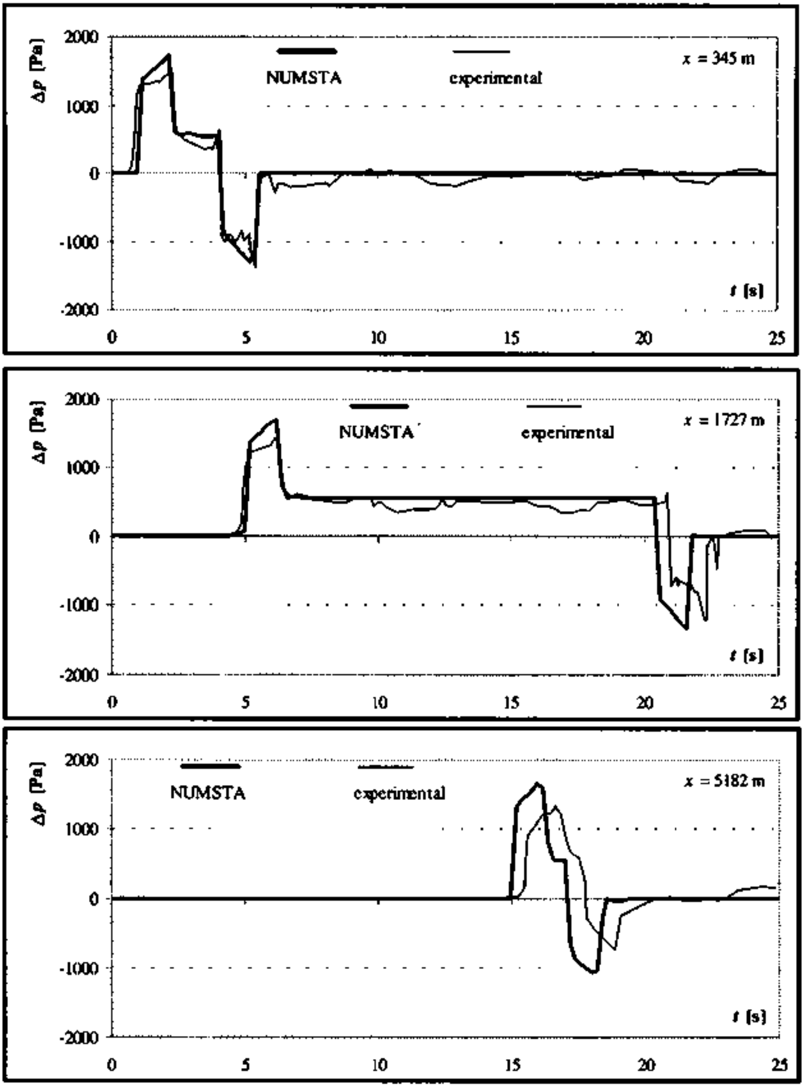

Figure 6.43 Comparison of NUMSTA with the pressure history at x=345 m from the left tunnel portal until t=25 s as determined experimentally for the passage of an ICE/V train through the Mühlbergtunnel

6.13 Summary of chapter 6

The purpose of this chapter is to develop confidence in NUMSTA as a new method for tunnel aerodynamic simulations. The numerical models are validated by analytical solutions, comparison with other numerical solutions and with experimental data.

Validation of the numerical solver is achieved for the steady subsonic and supersonic flow through a Laval nozzle and the shock tube. The precision and the behavior of the solver relative to a change of Δx and Δt are assessed in an error analysis.

The boundary conditions, sudden area changes and lateral branchments are validated for acoustic waves.

After these tests, cases including the vehicle are considered. The vehicle movement in an infinite tunnel without friction serves to demonstrate successfully that initial conditions are, after the acceleration phase, re-established in front and behind the vehicle and that Bernoulli flow is established around the vehicle.

Additional source terms for friction and heat transfer are tested with the steady flow through a tube with spatially varying cross-section. The numerical and the steady state solution shows a good fit. Also for the case of the vehicle movement in an infinite tunnel with friction only in the near field, agreement between NUMSTA and the steady state solution is achieved.

The model for the perforated walls is validated by comparison with a configuration with many short cross-vents instead of a perforated wall.

NUMSTA is compared with a code from the TU Vienna and with THERMOTUN/4, a code which has been widely used in the last decades for tunnel aerodynamic simulations. It is found that NUMSTA and THERMOTUN/4 compare well for the isentropic case with no friction (THERMO-1) and for cases with relatively low flow velocities and friction (THERMO-2). Important differences have been identified for cases with high flow velocities, the so called high-friction cases.

One example (THERMO-3) for a high-friction case is discussed in detail. Error sources for the MoC are outlined and evidence is discussed which links the differences between both NUMSTA and THERMOTUN/4 to the different formulation of the energy equation and to the discretization method. As most important error sources are the treatment of discontinuities and the integration of the source terms identified. Other reasons can not be excluded.

It is an important result of this chapter that classical codes based on the MoC are found to be not applicable to high-friction cases because mass conservation errors become too large. These cases can only be computed with a finite volume method as implemented in NUMSTA. However, improvements on the MoC for these critical cases have been developed or are about to be developed and are referenced under [70] and [72].

Thus, NUMSTA's domain of applicability covers the complete range of classical train/tunnel configurations up to high speed and high blockage ratio cases.

The comparison with experimental data is, within the limits of availability and of experimental uncertainty, satisfactory.

7 EXAMPLES

This chapter illustrates the range of applicability of NUMSTA on classical train / tunnel configurations as well as on special cases involving a high blockage ratio and high vehicle speeds as for example the Swissmetro system.

This chapter starts by discussing typical flow patterns and their influence on the vehicle movement for different configurations, i.e. the single open or closed tunnel, the tunnel with caverns, the tunnel system with air shafts and the tunnel system with cross-vents. In section 7.6, the previously given results are compared and the influence of several parameters is discussed. The last 3 subsections are concerned with the perforated wall, the capability of NUMSTA to compute a complex configuration with several vehicles and with problems related to the repressurization of a tunnel segment.

In order to simplify the discussion, all the examples presented here are variations of a reference configuration with parameters given in Table 7.1. For all closed configurations, the initial pressure chosen is p_0=10 kPa, the vehicle circulates in the interval x=[100 m, 1900m] and the total simulation time is t_e=20 s; the open configurations are calculated with an initial pressure of p_0=100 kPa, the vehicle enters and leaves the tunnel with the maximum speed and the total simulation time is t_e=25 s. The vehicle and the tunnel dimensions chosen here correspond to a blockage ratio of β=0.5 and the reference vehicle speed is sp=400 km/h. For the reference case the friction coefficients are set constant. Heat transfer is turned on. The reference configuration corresponds to a possible configuration for Swissmetro. Variations of the parameters relative to the reference configuration are discussed in a parameter study.

Table 7.1 Parameters for the reference case with β=0.5 and sp=400 km/h

l_{tu}	tunnel length	2000 m
l_v	total vehicle length	100 m
l_n l_{tl}	length of vehicle tail and nose	10 m
A_{tu}	tunnel cross-section	16.08 m^2
$A_{v,max}$	max. vehicle cross-section	8.04 m^2
P_{tu}	tunnel perimeter	14.21 m
P_v	max vehicle perimeter	10.05 m
C_{ftu}, C_{fv}	tunnel, vehicle friction factor	0.005, 0.006
sp	max. vehicle speed	400 km/h
a	acceleration	50 m/s^2
p_0	initial pressure	10 kPa, 100 kPa
T_0	initial temperature	288.15 K
T_{wtu}	tunnel wall temperature	288.15 K
q	heat transfer	on

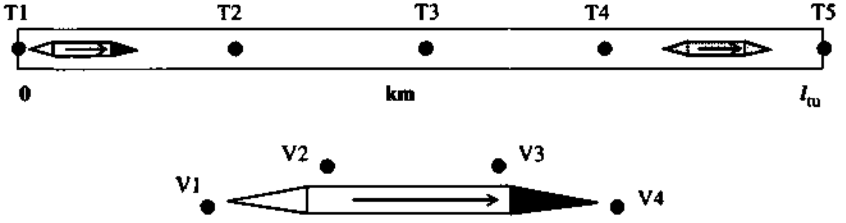

Figure 7.1 Position of history points in tunnel (top) and along vehicle (bottom) used in the subsequent examples

The calculations have been performed for varying blockage ratio β. For the given vehicle dimension, the corresponding tunnel dimensions can be found in Table 7.2.

The observed tunnel length was chosen as 2 km which is relatively short and the acceleration is set to a=50 m/s^2. This is an unnaturally high value, but the acceleration barely influences the typical flow phenomena. They can better be demonstrated with a short acceleration phase and a short tunnel. NUMSTA can also be used for realistic tunnel lengths and train accelerations as was the case for the intensive simulation campaigns during the Swissmetro main study. The results can be found in several technical reports (see bibliography).

Results are given in several formats in order to demonstrate standard output as implemented in NUMSTA. History points are either tunnel or vehicle fixed. Tunnel fixed history points used in the sequel are the tunnel end points (T1 and T5) and the 3 tunnel quarter points (T2, T3, T4). Vehicle fixed history points are the points positioned at both ends of the vehicle (V1 and V4) as well as 2 points alongside the vehicle (V2 and V3).

Table 7.2 Blockage ratio and corresponding tunnel area and tunnel perimeter for a cylindric vehicle with d_v=3.2 m

β	d_{tu} [m]	A_{tu} [m^2]	P_{tu} [m]
0.2	7.16	40.21	22.48
0.3	5.84	26.81	18.35
0.4	5.06	20.11	15.90
0.5	4.53	16.08	14.22
0.6	4.13	13.40	12.98

7.1 Vehicle movement in a single tunnel

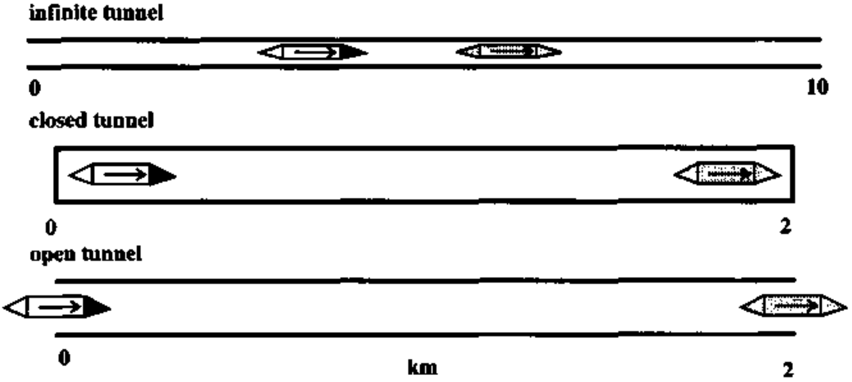

Figure 7.2 Configurations involving the vehicle movement in a single tunnel

The simplest case reported here is the vehicle movement in a closed or open tunnel with constant cross-section. If a vehicle accelerates in a tunnel with air initially being at rest, the air starts to move with the vehicle, a pressure wave is sent to the front and an expansion wave moves downstream. The pressure difference between the vehicle front and its back generates air flow around the vehicle with velocities increasing with the blockage ratio and the vehicle speed. Increasing air velocity with friction causes a higher pressure drop along the vehicle and the drag increases. The maximum air velocity allowed in the annular gap between vehicle and tunnel is sonic speed, in which case the flow is said to be choked. Choked flow does no longer allow to increase the mass flow around the vehicle to compensate for the increasing pressure difference. It is thus required to push all the excess air to the front. In consequence, the vehicle drag increases more strongly with the vehicle speed. Besides, in the choked case supersonic speed may be attained in the vehicle tail which eventually adapts to the pressure behind the vehicle by a normal shock. This results in reduced pressure recovery in the tail and thus an increased drag as well as likely unsteady forces on the tail region with associated noise. It should therefore be avoided to cruise under choked conditions.

The impact of these cases on the vehicle movement are best described with the power required to overcome aerodynamic drag because it represents an integral of the forces acting on the vehicle. A pressure decrease in front of or a pressure decrease behind the vehicle translates into an increase of the power required. The graphs presented in this section compare the vehicle movement in an infinite tunnel, in a closed tunnel and finally in an open tunnel.

7.1.1 Infinite tunnel

In the case of an infinite tunnel, wave reflections at the tunnel ends are excluded. The pressure and the expansion waves, originating at the vehicle, move, only influenced by friction and heat transfer, away from the vehicle. This causes the pressure difference between both ends of the vehicle to increase and accelerates the flow around it. Unless choking occurs, the power curves are smooth curves with a steady increase. The case of the vehicle movement in an infinite tunnel represents an academic reference case describing the vehicle movement with friction in absence of boundary conditions.

The power requirement is given here for *sp*=400 km/h (Figure 7.3) and for *sp*=500 km/h (Figure 7.4). The increase of the speed by 100 km/h roughly doubles corresponding values of both graphs. The little overshot at the end of the acceleration phase is due to a sudden reduction of inertia forces. The graphs show a strong dependence of the power requirement on the blockage ratio. For each step of β by 0.1 the power requirement increases by a factor of 1.5 to 2. For low blockage ratios, the power requirement remains relatively constant, whereas for higher blockage ratio it increases visibly with time.

A typical distribution of flow values around a vehicle is displayed in Figure 7.5. It is the reference vehicle with β=0.5 and *sp*=400 km/h at *t*=5 s. The pressure in front of the vehicle (right end) is increased as compared to the initial pressure. It falls steeply along the vehicle nose due to the diameter change. Along the annular space of the vehicle, where the available cross-section remains constant, friction causes pressure loss. Expansion of the flow follows and with it an increase of the absolute flow velocity. The temperature reduction is due to the acceleration of the flow, which explains also the progressive form of the curves displaying the compressible nature of the flow.

The absolute flow velocity relative to the vehicle reaches 125 m/s and the temperature ranges between 0 and 25 °C. These values become more extreme for higher blockage ratios and speeds and also under the influence of reflected waves. The pressure recovery in the tail region amounts to around 2'500 Pa. This is a high value and indicates the importance of the vehicle shape on the total drag. Note that the 1D computations assume the flow tube to be defined by the vehicle form. In reality and for the Reynolds numbers considered, separation and a turbulent wake region are likely. This reduces the pressure recovery and increases the drag.

The vehicle shape, in particular in the tail region, should therefore be optimized with respect to the pressure recovery. The vehicle structure must be designed to support the occasionally occurring extreme values for flow velocity and temperature.

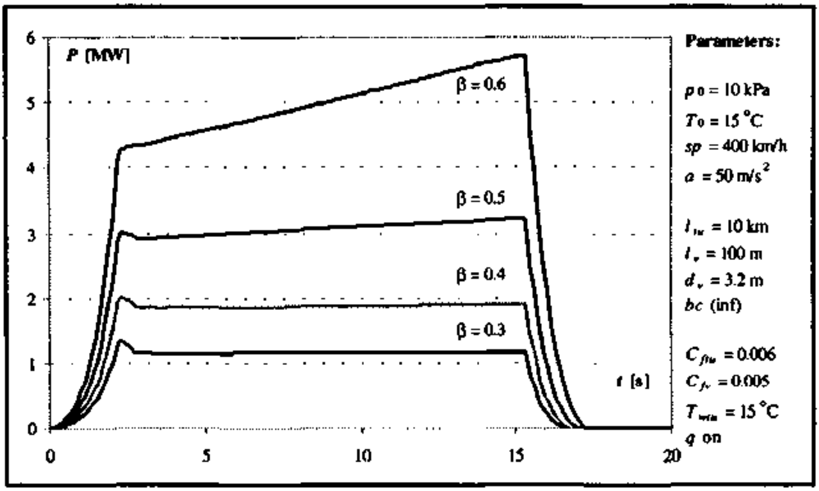

Figure 7.3 Power required to overcome aerodynamic drag for varying blockage ratio in an infinite tunnel (*sp*=400 km/h)

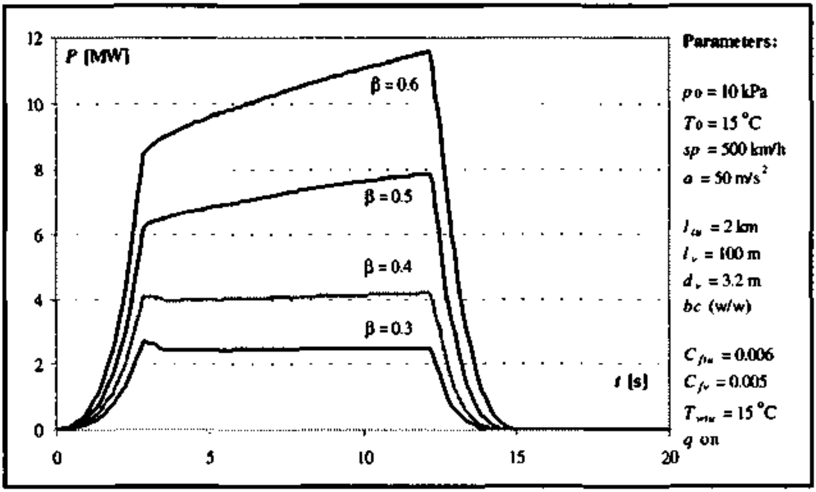

Figure 7.4 Power required to overcome aerodynamic drag for varying blockage ratio in an infinite tunnel (*sp*=500 km/h)

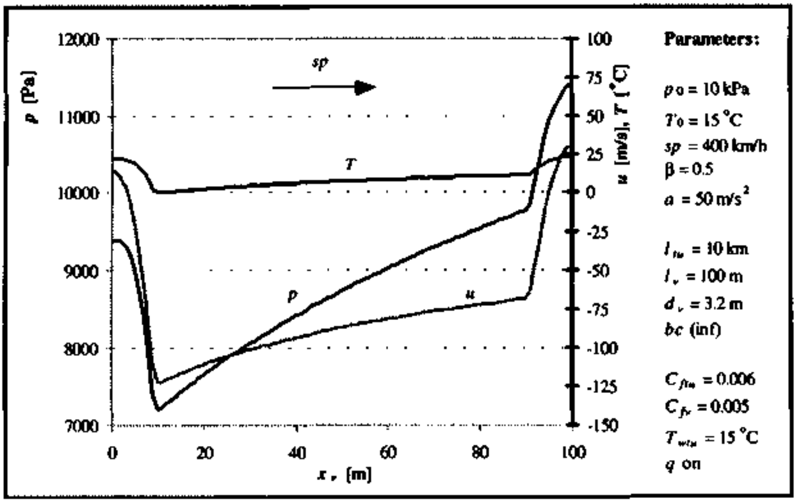

Figure 7.5 Distribution of flow values along the vehicle at t=5 s for the circulation in an infinite tunnel (β=0.5, sp=400 km/h)

The steep gradients shown in Figure 7.5 allow also to discuss qualitatively the flow around the vehicle for longer vehicles. A vehicle with a length of 200 m experiences a very steep pressure drop along the annular space and a high pressure difference between both ends results. The drag is therefore dependent on the vehicle length. A longer vehicle is also more prone to operate under choked condition.

From a purely 1D consideration, the lengths of the vehicle nose and tail have little influence on the forces on the vehicle. However, this is only true if there is no separation in the tail region. Experiments showed that the half angle of a cone exposed to flow shall be below 3° in order to avoid separation. Therefore, the 1D model should consider a reasonable length for nose and tail or to model the separation at a given position along the vehicle tail. The drag value increases then considerably as compared to the case without separation.

This discussion is concluded by pointing out that the useful length of a vehicle is the determining value. This is because it is mainly the pressure drop along the annular space of the vehicle which is responsible for the pressure difference between both ends of the vehicle. The useful length is the total vehicle length reduced by the lengths for nose and tail, thus the part with constant maximum diameter. If a vehicle is considered as a blunt body, i.e. a cylinder without nose and tail, corrective models for the wake are required.

7.1.2 Closed tunnel

In a closed tunnel, the waves are reflected at the ends with an increased amplitude (see subsection 6.5.1). The reflected waves collide with the vehicle and split in a reflected and transmitted wave just as in the case of a diameter change (see subsection 6.5.3). Continued reflection and transmission of waves between tunnel ends and vehicle occurs. This phenomenon can well be observed on the power curve of a vehicle circulating in a closed tunnel as given in Figure 7.6. The arrival of a reflected wave translates into the stepwise increase of power requirement while moving with constant speed. In the case examined here, a third reflected wave arrives when the vehicle starts to decelerate which causes the peak. The distance of the steps diminishes since the vehicle changes its position and approaches the right end. As can be seen, the power requirement increases considerably under the influence of the boundary conditions. In fact, the vehicle movement in a short tunnel can be compared to the movement of a piston in a pump with closed outlet. As the piston approaches the end, the air becomes more and more compressed, the temperature increases and the resistance against moving the piston increases. In the case of the vehicle, there is still a gap between vehicle and tunnel wall allowing some air to pass. However, the pressure loss along the vehicle and sonic blockage limit the speed when a maximum power is imposed.

The important influence of the vehicle movement in a closed tunnel on the temperature in the tunnel is displayed in Figure 7.7, which shows the histories at both ends and in the middle of the tunnel. First, the temperature in point T1 sinks accounting for the expansion of air initially at rest. Point T5 experiences with the arrival of the first pressure wave a steep increase of the temperature of 20 K and the following pressure waves act in the same way until finally a temperature level of 75 °C is reached.

The temperature history in point T3 allows to discuss how a tunnel fixed observer would experience the passage of a vehicle. First, an increase of the temperature would be experienced. The temperature reduces then slightly because of heat transfer effects. When the vehicle arrives, a sudden drop of the temperature to values below 0 °C could be measured due to expansion along the vehicle. The recompression along the tail results in a temperature increase to a value above the one measured during the passage of the vehicle nose. At first sight this is astonishing. But unsteady flow effects have to be considered. During the passage of the vehicle at point T3 the reflected wave hit the vehicle; this caused a rise in the temperature level around the vehicle.

An example for an instantaneous distribution of flow values in a closed tunnel is given for the time t=7.5 s in Figure 7.8. It shows the typical distribution of flow values around the actual vehicle position. The expansion wave has, at the instant shown, already reached the left end. The pressure is almost constant behind the vehicle. The temperature is slightly increased only within the region of vehicle movement. The strong dissipation around the vehicle leaves a trace in the temperature distribution. The air velocity behind the vehicle takes small positive values compensating the low pressure zone behind the vehicle. The pressure wave in front of the vehicle has reached the right end shortly before. It has just been reflected. A reflected wave with higher pressure than the incoming one is on its way back to the vehicle. Its impact can be seen on the power graph at $t \approx 9$ s. The positive air velocity in front of the vehicle indicates a deposit of mass between vehicle nose and right tunnel end, thus an increase of density. This effect is amplified by the continuous wave reflections in that zone and the impact on the vehicle movement can be seen on the power curve.

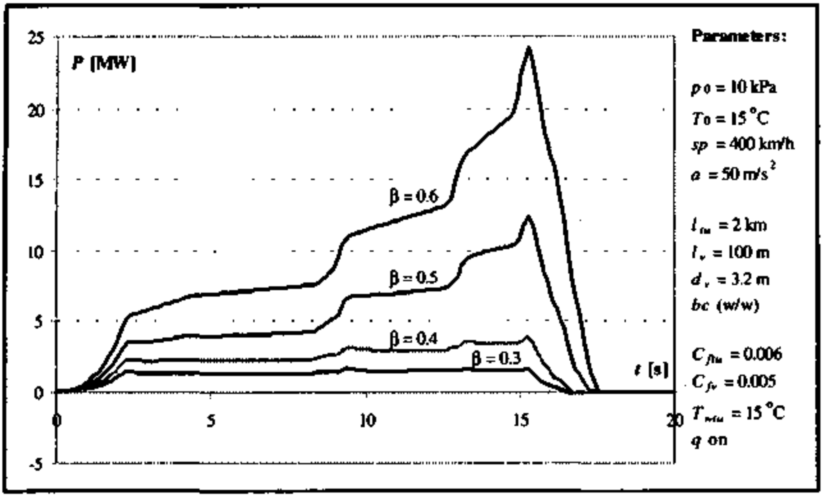

Figure 7.6 Power required to overcome aerodynamic drag for varying blockage ratio in a closed tunnel (*sp*=400 km/h)

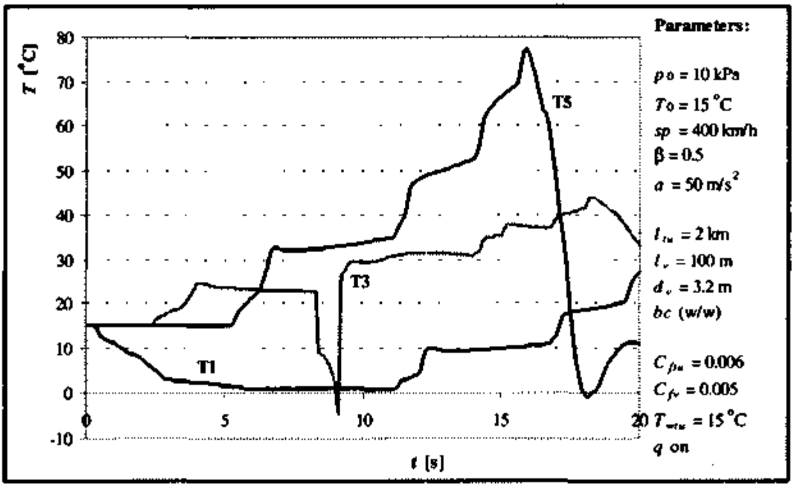

Figure 7.7 History of the temperature in the tunnel end points and the tunnel center in a closed tunnel (β=0.5, *sp*=400 km/h)

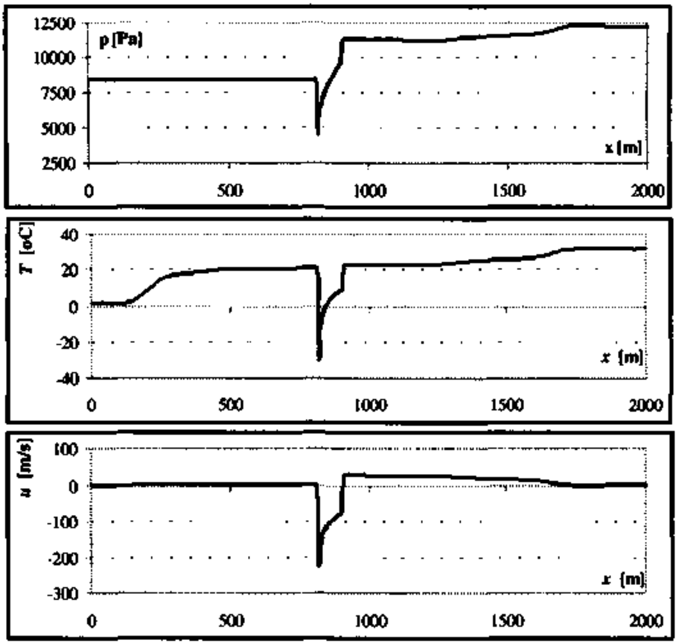

Parameters:

p_0 = 10 kPa
T_0 = 15 °C
sp = 400 km/h
β = 0.5
a = 50 m/s^2

l_{tu} = 2 km
l_v = 100 m
d_v = 3.2 m
bc (w/w)

C_{ftu} = 0.006
C_{fv} = 0.005
T_{wtu} = 15 °C
q on

Figure 7.8 Pressure, temperature and air velocity distribution in a closed tunnel at t=7.5 s

7.1.3 Open tunnel end

At an open end reflected waves carry the information of low pressure back to the origin of the incident wave (see subsection 6.5.2).

Figure 7.9 shows the power requirement of a vehicle which starts, as indicated in Figure 7.2, outside of the tunnel and enters into it with maximum speed. The vehicle then cruises with constant speed and leaves the tunnel before it decelerates. Acceleration and deceleration can be identified at both ends of the power curve. Following the acceleration there is a short phase of movement at open air, where the only contribution to the drag is the friction drag accounting for a constant power requirement of P=3.7 MW. The moment the vehicle enters the tunnel, the power requirement increases fast to a value 3 to 10 times higher than the value at open air, depending on the blockage ratio. The first peak is reached when the vehicle is entirely in the tunnel and when it has to work against the inertia forces of the air. Once the first wave leaves the vehicle, the power requirement decreases and then shows a gradual increase due to friction with a slope depending on the blockage ratio. The vehicle movement is then relatively steady before the interaction with the first wave reflected at the right hand open end which causes a sudden fall of the power curve followed by a continuous decrease because of depressurization. The second wave stops this decrease and increases the power curve slightly since it reduces the flow velocity ahead of the vehicle. As the vehicle approaches the right end, the initial pressure peak is more and more reduced and the pressure distribution homogenized. The power requirement reduces.

The power curve shows also for this case a rather unsteady behavior. In the case of the open tunnel, the influence of the reflected waves reduces the power requirement which is the opposite effect as compared with the closed end. Note that the power values can not readily be compared to the closed configurations because the pressure level in the open configuration is 10 times higher accounting for the increase in the power requirement by the same factor.

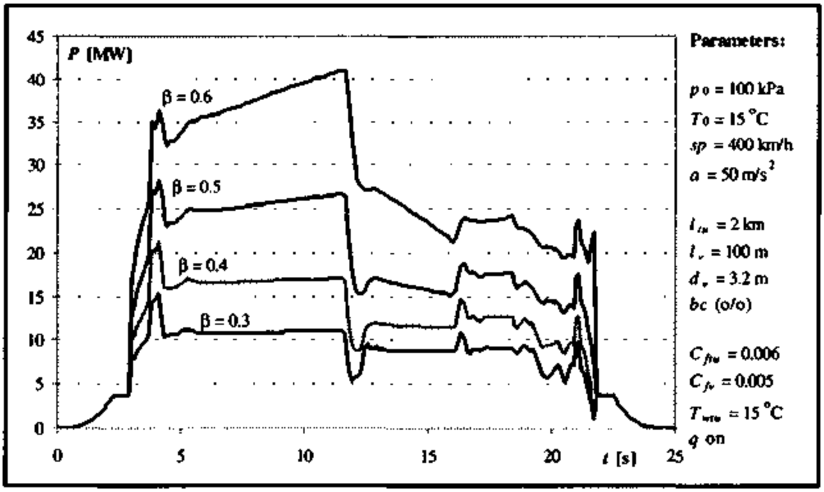

Figure 7.9 Power required to overcome aerodynamic drag for varying blockage ratio for a vehicle crossing an open tunnel (sp=400 km/h)

7.2 Vehicle movement in a tunnel loop

If a vehicle moves in a tunnel loop, the compression and the expansion wave meet and balancing pressure waves are sent back to the vehicle (see subsection 5.3.3). The reflected waves have the tendency to decrease the power requirement. The numerical model of the tunnel loop assumes a connection between both ends of the tunnel. Wave reflections at the tunnel ends are here not possible as might be suggested by the sketch in Figure 7.10.

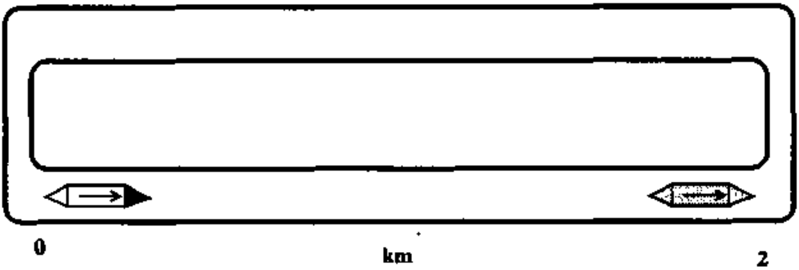

Figure 7.10 Schematic drawing of the tunnel loop

Figure 7.11 shows the required power for the movement in this case. After the acceleration phase, the power requirement behaves exactly as in the case of the infinite tunnel until the reflected waves interact with the vehicle. For low blockage ratios the waves help to reduce the power requirement. This happens also for the higher blockage ratios but this effect is counteracted by friction effects. After some time, the power requirement reduces also in this case resulting from the pressure reduction because of heat transfer. If the vehicle did several loops, the curve would become constant. In this case, the temperature level and with it the pressure level would increase due to the dissipation around the vehicle until heat transfer stabilizes both. The continuous movement in a tunnel can be compared with the stirring of a coffee pot with a spoon. If the coffee is stirred long enough, it adapts to the movement of the spoon.

The vehicle movement in a tunnel loop is thus very stable and the effect of reflected waves comparably small. The power curves vary only little also for higher blockage ratios.

The tunnel loop can be used for a first description of the effect of passive installations for flow bypassing. However, it represents a very optimistic limit of the effect of cross-vents, i.e. a tunnel loop with 4 km length shows a better performance than two parallel tunnels with 2 km length connected by cross-vents close to the ends or a configuration with several cross-vents spaced 2 km apart. This is due to the only partial flow deviation provided by the cross-vents as compared to the total flow recirculation modeled by the tunnel loop boundary condition (see also section 7.5).

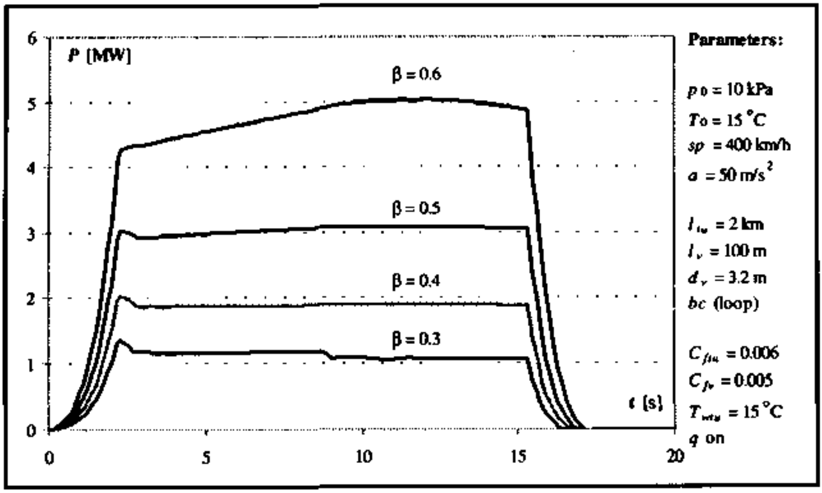

Figure 7.11 Power required to overcome aerodynamic drag for varying blockage ratio in a tunnel loop (*sp*=400 km/h)

7.3 Local variations of the tunnel cross-section

As the first example for flow bypassing measures, local enlargements of the tunnel cross-section or caverns as sketched in Figure 7.12 are discussed. The idea is that air can, in distances defined by the vehicle speed, pass the vehicle and thus contribute to keep the power requirement within a relatively narrow margin. The effect of reflected waves at the sudden diameter changes add unwelcome unsteady effects to the vehicle movement. Smooth diameter changes reduce reflected waves.

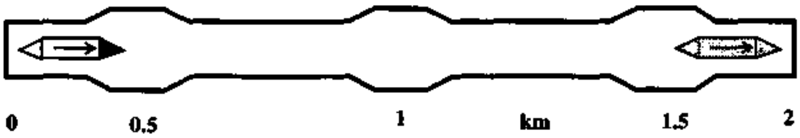

Figure 7.12 Schematic drawing of the tunnel with local variations of the cross-section (caverns)

In this example, cases with blockage ratios of the main tunnel from $\beta=0.3$ to $\beta=0.6$ are considered. The local enlargements are twice as long as the vehicle and are centered at the three tunnel quarter points. Their cross-sections corresponds to a reduction of the blockage ratio by 0.1.

Figure 7.13 gives the power requirement for this case. The vertical rectangles indicate the time period beginning with the entry of the train nose into the caverns and ending with the exit of the tail from the caverns. It can be seen that for the low blockage ratios the power requirement can be held within a narrow band but for the higher blockage ratios the reflected waves increase the power requirement in a qualitatively similar manner as in the case of a closed tunnel. The unsteady wave behavior causes, other than in the previous cases, an important variation of the power requirement during the entire simulation time.

If the power curve during the passage of the vehicle at the cavern is studied, a slight increase in a first phase can be noticed which is caused by inertia forces of the air, which moves in a cavern slower than in the narrower tunnel. Once the vehicle is in the center of the cavern and has accelerated the air to flow around it, it experiences a drop of the power curve accounting for the locally reduced blockage ratio. As it leaves the cavern, the drag increases again before it reduces when approaching a zone with higher cross-section. These effects can be read out of the power curve when the effects of the boundaries are neglected.

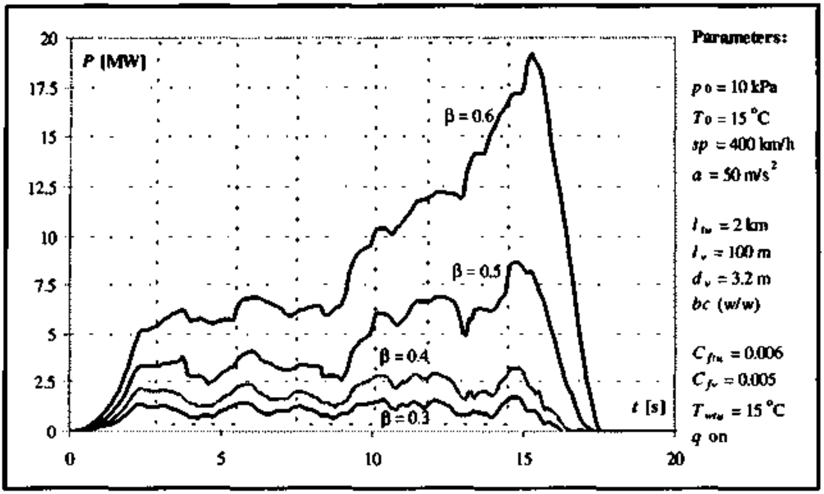

Figure 7.13 Power required to overcome aerodynamic drag for varying blockage ratio in a tunnel with local enlargements (*sp*=400 km/h)

7.4 Air shafts in closed and open systems

A second configuration enabling flow bypassing are air shafts (see Figure 7.14). It is the idea of the closed system that air is stored by compression when a vehicle approaches and released by expansion when the vehicle leaves the shaft position. In an open system air can be evacuated from the tunnel by the compression wave of the vehicle and sucked from the ambient into the tunnel by the low pressure zone behind the vehicle. Technically, these air shafts may be realized with existing excavation pits or are introduced afterwards where the tunnel is only little below ground. The air shafts considered here are cylindric and have a diameter of d_{sh}=2 m.

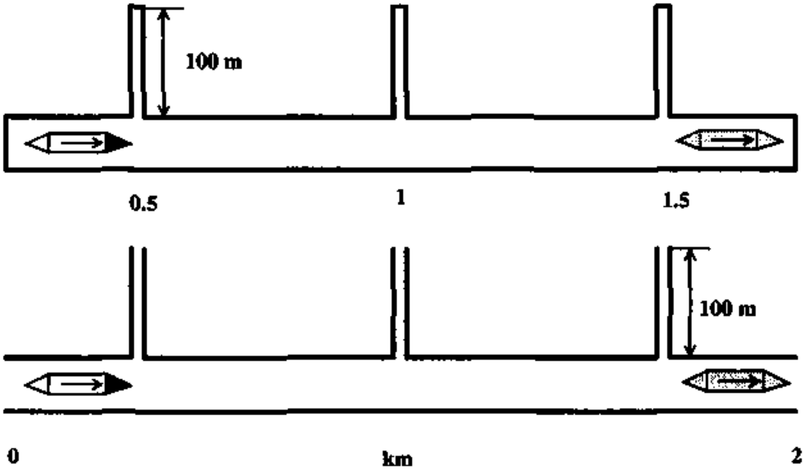

Figure 7.14 Schematic drawing of a closed and an open tunnel with air shafts

Figure 7.15 shows the power required during a passage of a vehicle through a closed system. Again, the passage of the vehicle at the shaft position is indicated by the vertical rectangles. Qualitatively, the curve resembles the one of the closed tunnel except that the vehicle power is more unsteady. The curve shows a trend to increase during the passage at such a shaft, which is expected since the damping effect of the shaft is not available at that moment. Only while passing the first shafts a slight power reduction can be noticed when the vehicle leaves the shaft. This effect was expected to be more dominant since the high pressure accumulated in the shaft while the vehicle approaches can now be expanded and help to propel the vehicle.

Figure 7.16 refers to the open configuration as drafted in the lower part of Figure 7.14. For this configuration the vehicle was started from within the tunnel in order to avoid the entry peak. Typically for open configurations opposed to closed configurations, the power requirement is highest in the beginning and then reduces under the influence of the boundaries. For this case, a general trend can be described. While approaching the first shaft the power requirement reduces, during the passage at the shaft it increases, because the shaft is blocked by the vehicle. If only the general trend is considered and the complex wave reflection pattern is neglected, the above described behavior of the power curve repeats with each passage at an air shaft.

An overall evaluation of these methods of flow-bypassing can be done only by comparing the present power curves with the ones related to the tunnels without shafts (see section 7.6).

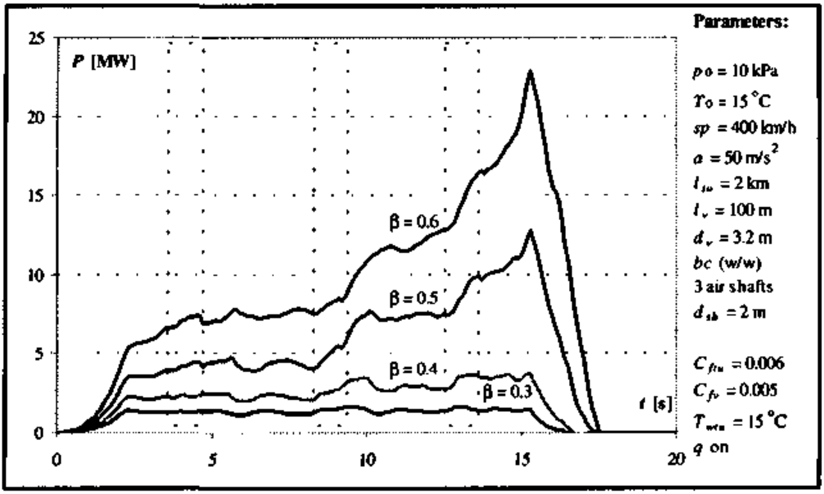

Figure 7.15 Power required to overcome aerodynamic drag for varying blockage ratio in a closed tunnel system with air shafts (*sp*=400 km/h)

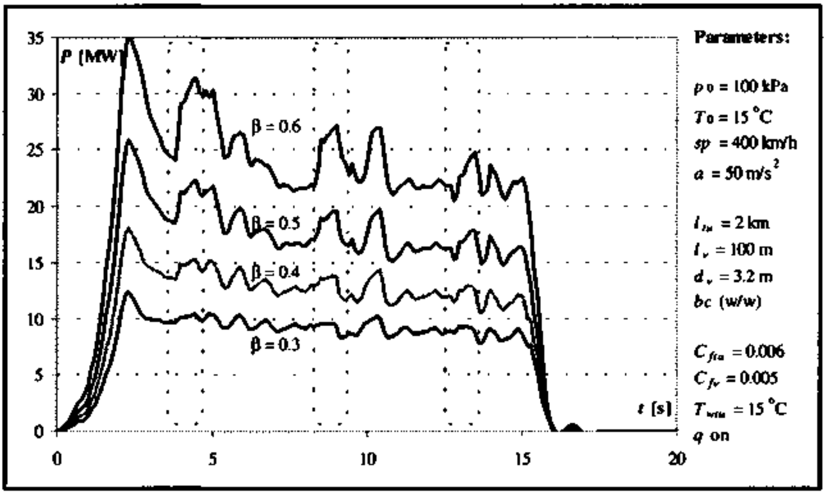

Figure 7.16 Power required to overcome aerodynamic drag for varying blockage ratio in an open tunnel system with air shafts (*sp*=400 km/h)

7.5 Vehicle movement in a twin tunnel with cross-vents

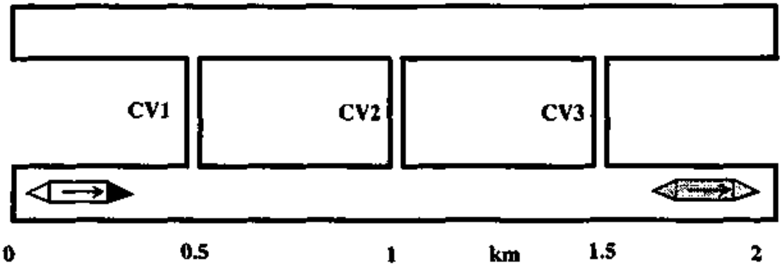

Figure 7.17 Schematic drawing of the twin tunnel with cross-vents

An installation for drag reduction are cross-connections between parallel tunnels, which have been realized in the Channel tunnel [27].

At a cross-vent, an incoming pressure wave is split at the branchment into a reflected and a transmitted wave (see subsection 6.5.4). For typical cross-sections of the lateral branch inferior to the main tunnel, only a small fraction of the air is deviated. Several cross-vents are required to achieve a reduction of the incoming pressure wave. The effect of cross-vents can therefore only very roughly be compared to the tunnel loop, where the entire incoming wave is deviated into the parallel tunnel.

The cross-vents couple both tunnels aerodynamically rendering vehicle movement particularly unsteady if several vehicles are present. The form of the power curve shown in Figure 7.18 is similarly unsteady as in the previous case.

If only the power curve around the passage of a vehicle at a cross-vent is looked at, a typical behavior can be noticed. The power requirement reduces as the vehicle approaches a cross-vent and reaches a local minimum just before the nose enters the branchment. During the passage, the power curve increases and reduces then again as the vehicle moves away from the branchment. This behavior can be explained with the flow in the cross-vents illustrated by Figure 7.19. It shows the history curves of the air velocity in the three cross-vents. During the passage of a vehicle at a cross-vent, the air velocity changes sign. The pressure wave pumps air into the branchment and once the vehicle moves away, air is sucked back into the tunnel.

The velocities are quite remarkable. They reach absolute values of up to 150 m/s for the relatively small shaft diameter of 2 m. The force of a laterally impinging air jet on a passing train is destabilizing. This is the reason why dampers and reflectors were introduced subsequent to commissioning the Channel tunnel. These installations helped to meet a certain force criteria with maximum air velocities in the cross-vents limited to max. 30 m/s [27].

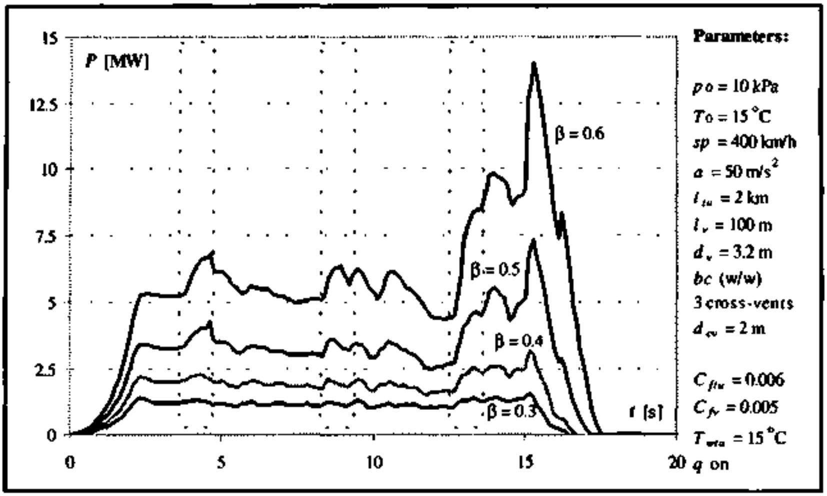

Figure 7.18 Power required to overcome aerodynamic drag for varying blockage ratio in a closed tunnel system with cross-vents (*sp*=400 km/h)

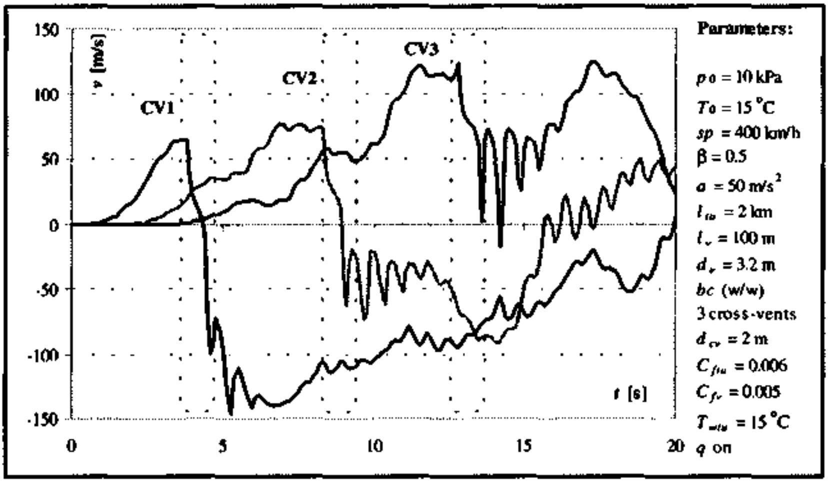

Figure 7.19 History curve for the air velocity in the cross-vents (β=0.5, *sp*=400 km/h)

7.6 Parametric study

In this section the influence of a variation of individual parameters on the power curve of the reference configuration as defined in Table 7.1 is examined. The study thereby is restrained to the configurations discussed so far.

Comparison of the power requirement for different configurations

The similar geometries employed in all examples so far allow to discuss the impact of a particular configuration on the power curve. It is obvious that each configuration represents different implications on various fields, such as feasibility, economic viability, security, electromechanical or comfort aspects. To discuss these questions is not the subject of the present text, but the importance of aerodynamics with respect to an optimum configuration shall be demonstrated on basic aspects.

Figure 7.20 shows the power curves of 6 different configurations for β=0.5 and sp=400 km/h. The different configurations are indicated with self-explanatory symbols. The graph shows the characteristic differences between the cases and allows a first assessment of their impact on the train operation.

The curve with the lowest power requirement corresponds to the tunnel loop, followed closely by the curve related to the infinite tunnel. Both these curves show a smooth and almost constant time evolution, which indicates the absence of strong reflected pressure waves.

This is different for the other 4 cases, which should be compared to the case of the closed tunnel. This case shows a very typical step-like power curve influenced by the wave reflections at the ends. For the parameters used here, the additional introduction of lateral shafts adversely affects the power requirement. This suggests that it is probably better to compress the air in front of the vehicle over a long distance than in lateral shafts, since the gain by depression is negligible but the additional power requirement for the compression is not. An optimization of the shaft length in a way that the reflection of the pressure peak from the front of the vehicle interacts with the tail region favorably may improve the situation, but seems only little promising.

The two other configurations, caverns and cross-vents, improve the system performance. The curve related to the local enlargements of the cross-section follows approximately the case of the closed tunnel with stronger variations around a certain average value. Overall, it shows a by approximately 10-20% improved performance. The configuration with the cross-vents is even capable of annihilating the effect of the first reflected wave (at $t = 9$ s), but the second wave reflection causes nonetheless a sudden increase of the power requirement. Until $t \approx 13$ s the cross-vents allow to keep the power requirement within a range of 1.5 MW around the almost constant curve related to the tunnel loop. This also confirms that simulations of the tunnel loop can be used for a first rough estimate of the power required in a tunnel system with cross-vents. The power requirement can be reduced by 25-60% as compared to the closed tunnel, which indicates that the use of cross-vents represents an interesting means for flow-bypassing.

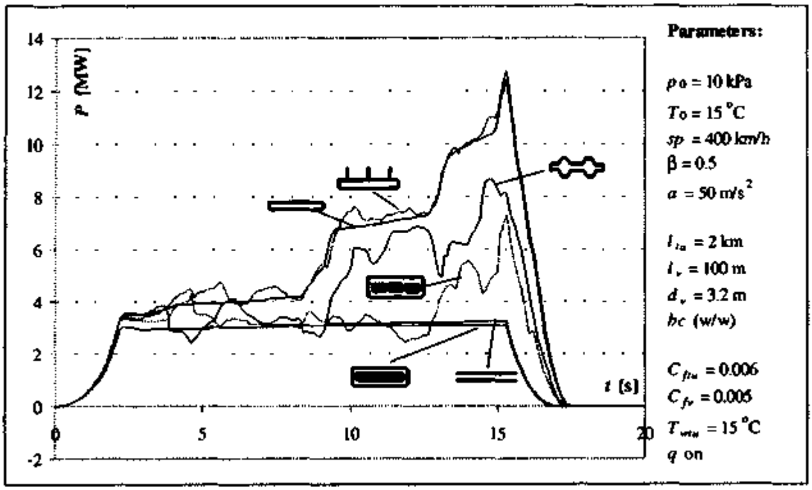

Figure 7.20 Comparison of the power requirement of different closed configurations for β=0.5 and *sp*=400 km/h

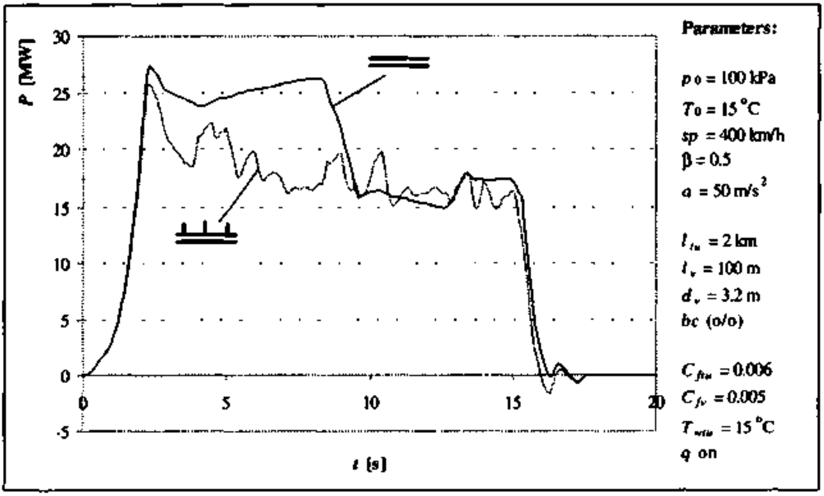

Figure 7.21 Comparison of the power requirement of different open configurations for β=0.5 and *sp*=400 km/h

Influence of heat transfer

As can be seen on Figure 7.22, heat transfer influences the result only little. The reference curve and the curve without heat transfer are practically the same. Differences can only be detected for oncoming pressure peaks. In these situations, heat transfer helps to reduce the pressure peak and has therefore a slight smoothening effect on the power curve. In other simulations, it was observed that the tunnel wall temperature has an important influence on the power curve. If the tunnel wall temperature can be held low, the power peak while approaching the tunnel end can be cut off.

Influence of the friction coefficient

In NUMSTA, the friction coefficient can either be given as a constant or calculated locally as a function of the wall roughness and the local Reynolds number. Calculations for constant friction coefficients are computationally cheaper than if the friction coefficients are computed locally. Note that this has also an influence on the heat transfer coefficient since this value is related to the friction coefficient by the Reynolds analogy.

For the parameter study in Figure 7.22, two variations of the reference configuration are displayed. One calculation was performed with wall roughnesses given and a second variation was done for increased constant friction coefficients. In both cases, the power requirement is higher than in the reference case and the curves are still parallel. Thus, the choice of the method has a high influence on the magnitude of the power requirement but not so much on the form of the curve. It seems therefore justifiable to use constant friction coefficients. Their value can be found by field experiments, if available. It this is not the case, a parametric study including the best / worst case scenario gives a range for the power requirement.

Influence of the vehicle length

The vehicle length and with it the amount of passengers per train is an important economic parameter. However, it is also an important aerodynamic parameter, since the vehicle length has a strong influence on the vehicle drag as discussed in subsection 7.1.1.

The gradients along the vehicle are considerable. The vehicle length not only influences the pressure difference between both ends of the vehicle, but also the critical speed at which, for a given configuration, sonic blockage appears. The reference configuration is compared with total vehicle lengths of 50 m and 150 m. Nose and tail are, as before, 10 m long. Thus, vehicles with a usable length of 30 m, 80 m and 130 m are compared.

Figure 7.23 shows a strong influence on the power curve for a variation of this parameter. It is interesting that the peak for the last wave impact for the case of the shortest vehicle is less significant than in the other cases. This indicates that the short vehicle can handle the increased mass flow induced by the oncoming high pressure wave, whereas in the other two cases sonic blockage is limiting the increase of the mass flow which is expressed by the steep power increase. The longest vehicle requires roughly twice the power of the shortest examined vehicle with a usable length more than four times as large. The power requirement increases thus degressively with the vehicle length.

Influence of the vehicle speed

The vehicle speed has a high influence on the strength of the generated pressure waves and with it on the power requirement. For open air and, in first approximation, also for unchoked vehicles in an infinite tunnel, the power required is proportional to the third power of the speed. For choked flows and flows influenced by the action of the boundary conditions only instantaneous power requirements can be given.

Influence of the vehicle acceleration

The vehicle acceleration influences the time history of the flow but not so much its nature. This is the reason why a high acceleration could be chosen for this chapter, which was of advantage for the presentation and the discussion. However, if an analysis for a defined configuration is the scope, the simulation should be performed with a realistic acceleration.

Influence of the initial pressure

In all simulations performed so far, it was found that the initial pressure level p_0 influences the power requirement in a linear way. Thus, an increase of p_0 by a factor f also increases the power requirement by the same factor. This makes it possible to perform simulations only for one service pressure level and allows to easily deduce the power requirements for other pressures. It was further found that the observed temperatures and flow velocities do not change with the initial pressure; only the density follows the initial pressure.

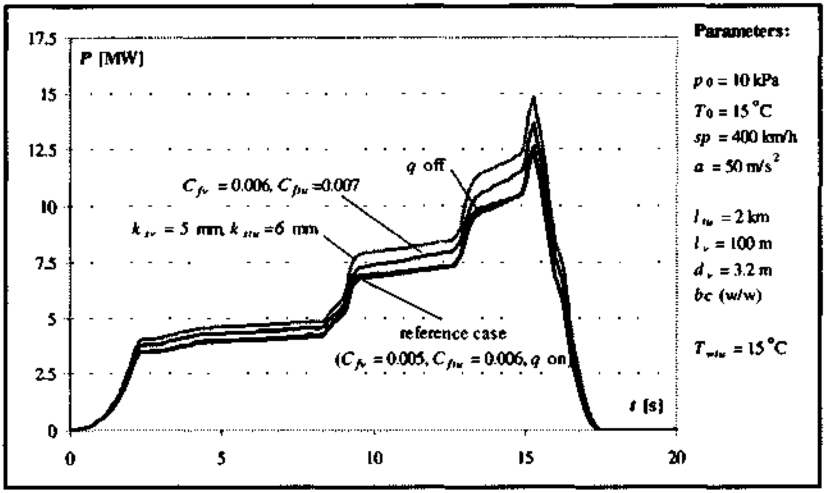

Figure 7.22 Sensitivity of the power requirement to a variation of heat transfer and friction coefficient

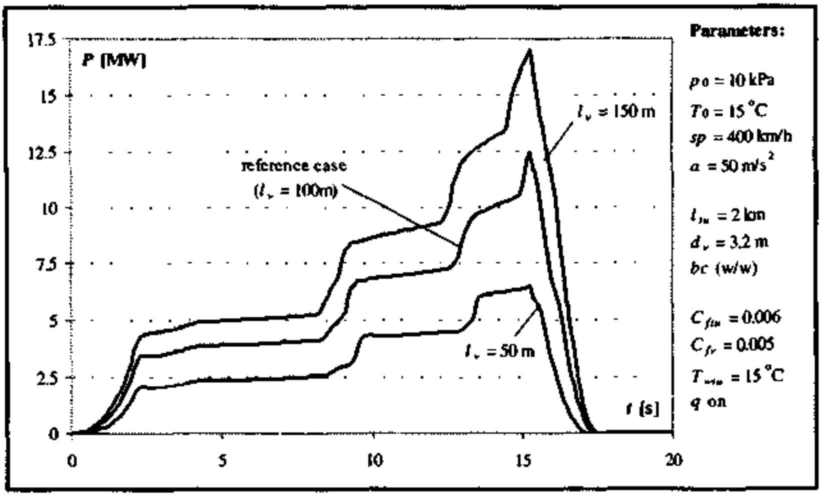

Figure 7.23 Sensitivity of the power requirement to a variation of the total vehicle length (tail and nose length each 10 m)

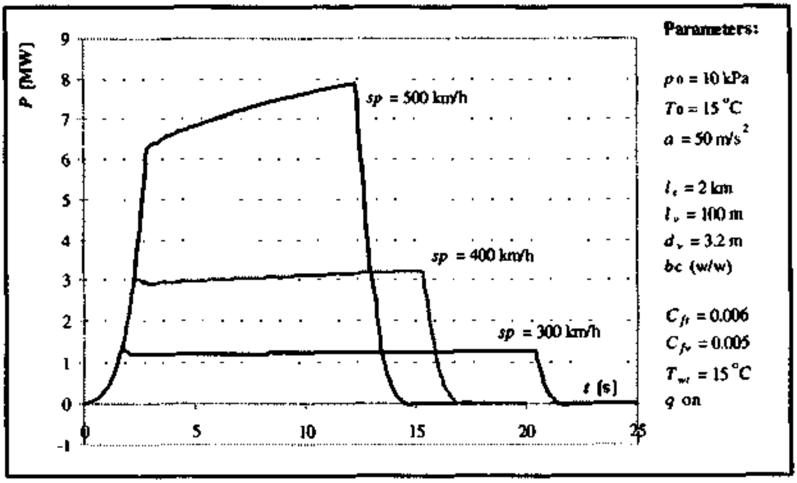

Figure 7.24 Sensitivity of the power requirement to a variation of the vehicle speed in an infinite tunnel

7.7 The perforated wall

Perforated walls may be included in a tunnel system in two ways as sketched in Figure 7.25:

1. alongside the tunnel as a wall with perforations separating the tunnel in a main tunnel and a side gallery and
2. at the tunnel ends to smoothen transition between circulation at open air and in the tunnel.

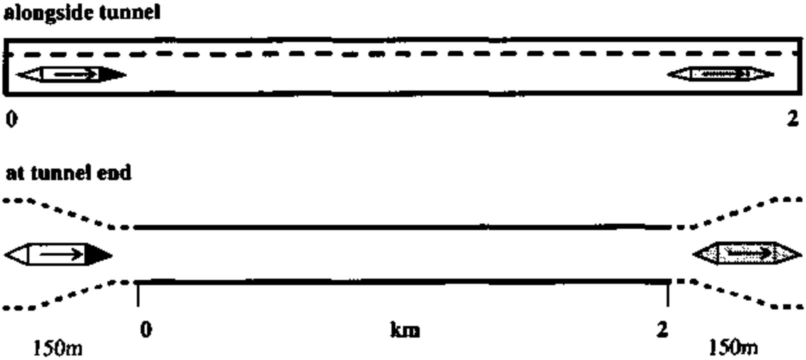

Figure 7.25 Schematic representation of the use of perforated walls

In case 1, the perforated wall allows air exchange between the main and the side tunnel. Air in the side tunnel is not subjected to the friction force exerted by the moving vehicle surface. Flow resistance for the bypassing air is therefore lower than without the perforated wall. The question is whether the energy loss by crossing the narrow perforations is outbalanced by the reduced friction in which case a drag reduction is expected.

In case 2, the perforated wall smoothens entrance or exit pressure profiles. It may therefore contribute to reduce the entrance peak of the power requirement and to improve travel comfort.

Results of simulations for both cases are presented in the sequel. In all cases, the total tunnel cross-section for different blockage ratios has been calculated as before, then the tunnel has been divided into a main tunnel with 2/3 of the total available cross-section for the vehicle and a side gallery with 1/3 of the total available cross-section. The resulting values for the cross-sections, perimeters and diameters are given in Table 7.3. No simulations for β=0.6 have been performed, since the resulting available cross-section in the main tunnel would be unrealistically close to the vehicle cross-section.

Table 7.3 Cross-sections, perimeters and diameters of the tunnel and the side gallery for the simulations with perforated wall

β	A_{tu} [m^2]	P_{tu} [m]	d_{tu} [m]	A_{ga} [m^2]	P_{ga} [m]	d_{ga} [m]
0.3	17.87	14.99	4.77	8.94	10.60	3.37
0.4	13.40	12.98	4.13	6.70	9.18	2.92
0.5	10.72	11.61	3.69	5.36	8.21	2.61

perforated wall alongside a closed tunnel:

Figure 7.26 shows the power requirement for the circulation of a vehicle in the closed tunnel for the vehicle speed sp=400 km/h, a perforation of γ=0.1m^2/m and an inlet angle of α=90°. The form of the curve resembles qualitatively the case without the perforated wall (see Figure 7.6). In between the impacts of the reflected waves, the vehicle movement is slightly rougher. The effect of the reflected waves is less dominant. An interesting result is that the power peak for the case β=0.5 is below 10 MW, which is clearly below the corresponding value in Figure 7.6. This allows the assumption that the introduction of a perforated wall in an existing tunnel alone allows to reduce the power requirement in certain cases. This observation will be examined more closely in section 7.8.

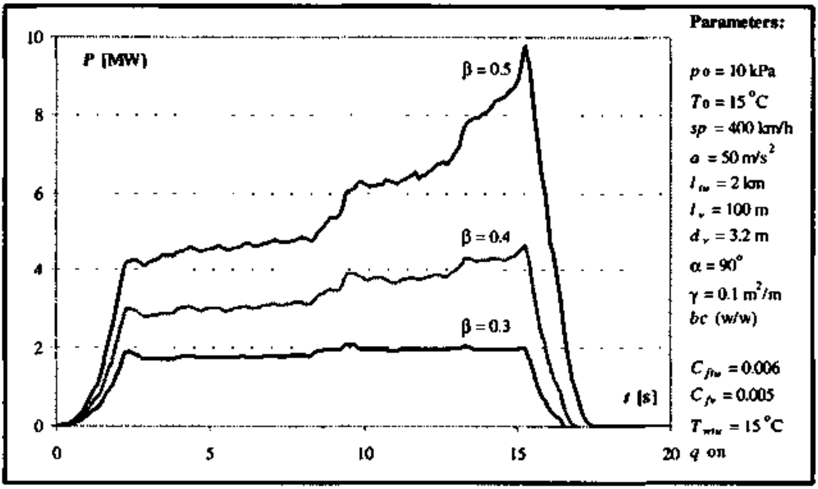

Figure 7.26 Power requirement in a closed tunnel separated in a main tunnel and a side gallery by a perforated wall for sp=400 km/h

perforated wall at the tunnel ends:

Figure 7.27 shows the power requirement for the passage of a vehicle through an open tunnel with conical ends. The vehicle speed is *sp*=400 km/h, the perforation is of γ=0.1m^2/m and an inlet angle of α=90° was chosen. The maximum cross-section of the conical end is twice as large as the corresponding value of the main tunnel. The perforated region is separated in 3 sections as indicated in Figure 7.25. The total length of this region is twice as long as the vehicle and the diameter change extends over one vehicle length. The smaller vertical rectangle in Figure 7.27 indicates the passage of the vehicle nose and the larger one indicates the passage of the vehicle tail at the perforated region at the entrance.

A period of constant power requirement for the movement at open air can be seen. As the vehicle enters the perforated region, the curve increases in two steps accounting for the passage of the vehicle nose and tail. When the vehicle nose leaves the perforated entrance region and enters into the narrow main tunnel, the power requirement increases steeply followed by a gradual increase with a maximum at the moment when also the tail enters the main tunnel. Then, just as in the reference case of the open tunnel without perforated ends (see Figure 7.9) the power requirement decreases shortly before the flow around the vehicle is mainly dominated by friction effects. The first reflected wave transports information of low pressure at the right end and causes the sudden reduction of the power requirement at $t \approx 13.5s$. This has also been observed in the reference case. But the behavior of the vehicle after the interaction with the first reflected wave is then characteristically different. In the presence of perforated ends, the entrance wave is weaker and so is the reflected wave. The pressure reduction on the vehicle front is therefore smaller and subsequently the power requirement increases for the case with perforated walls and the opposite behavior was noticed for the reference case. This is a remarkable difference which is caused by the perforated ends.

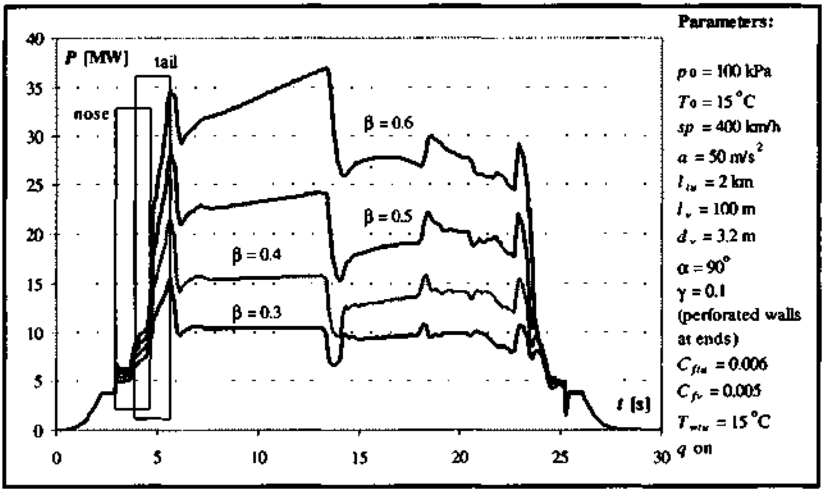

Figure 7.27 Power requirement for the crossing of an open tunnel with conical openings with *sp*=400 km/h

A comparison in Figure 7.28 shows best the differences between the two cases. As before, the case with sp=400 km/h and β=0.5 has been chosen for the comparison. The time scales for both cases have been adjusted so that the vehicles enter the main tunnel at the same moment. The two curves show interesting differences. The entrance peak is almost equal in both cases but the initial reduction after the vehicle is entirely in the main tunnel is stronger for the case with perforated walls. This curve remains below the reference case until the impact of the first reflected wave. From there on the case without perforations yields the better performance. This behavior can be explained with the damping of the initial pressure wave whose reflected wave transports less pressure reduction from the right end back to the vehicle. For explanation, the reader is referred back to subsection 6.5.2, where the reflected wave at an open end has been shown to be the inverted incident wave; thus a smaller incident wave results in a less negative reflected wave.

It can be concluded that the perforated ends help to reduce the power requirement in a first phase of the movement in an open tunnel, but that the reduction of the power requirement after interaction with the first reflected wave is less than in the reference case. The fluctuation of the required vehicle power for the passage through an open tunnel with perforated ends is therefore reduced. This renders the vehicle movement more steady.

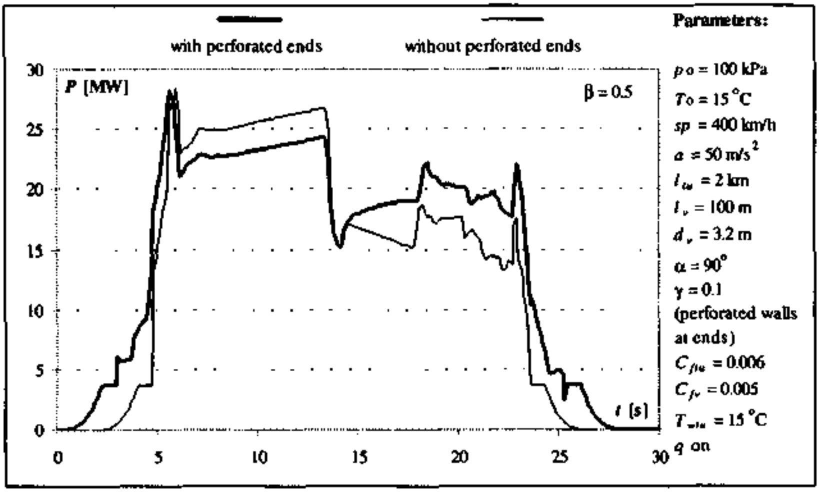

Figure 7.28 Comparison of the power requirement with and without perforated wall for sp=400 km/h and β=0.5

7.8 Parametric study with perforated wall alongside a tunnel

In this section the influence of a variation of several parameters on the power curve of the reference configuration involving the perforated wall in a closed tunnel is examined.

The power requirement for closed tunnels with and without perforated walls is compared for different blockage ratios and vehicle speeds. The thicker lines in Figure 7.30 and Figure 7.29 correspond to the reference case of the closed tunnel without perforated walls as discussed in section 7.1. The thinner lines correspond to the same configuration with perforated walls. Intentionally, the results for three blockage ratios and vehicle speeds are shown, because both parameters contribute to modify the wave strength, which seems to have an important influence on the performance of the perforated walls.

If the vehicle speed is 400 km/h (Figure 7.30) the performance of the configuration with the perforated walls is inferior for the low blockage ratios. For β=0.5 an interesting observation can be made. As soon as the first reflected wave interacts with the vehicle, the thin line crosses the thick one and remains below it. This evokes the idea that in the presence of strong waves, the perforated walls improve the performance. This idea is strengthened by looking at the corresponding graph for *sp*=500 km/h (Figure 7.29). Here, even for low blockage ratios, the thin lines are below the thick ones. The power curve with β=0.5 with perforated wall even touches the one with β=0.4 without this device.

This allows the astonishing conclusion: the stronger the involved waves are, the more perforated walls are of advantage and for weak waves, these walls deteriorate the performance.

A closer look at the distribution of flow values in the main and the side tunnel helps to describe the bypassing mechanism in more detail. The air velocity distribution in Figure 7.31 shows best the principle of action of the perforated walls. In the main tunnel the air velocity behind the vehicle has a high positive value with a peak at the vehicle tail. In the side tunnel the air velocity is negative from the left end until a bit in front of the vehicle nose. This shows that air is transported from the front of the vehicle to its rear and furthermore to the entire zone behind it. This behavior is intended as flow bypassing mechanism. A graph with the pressure distribution in both tunnels is not displayed here since it shows two congruent curves with the typical shape for the vehicle movement in a closed tunnel (see Figure 7.8).

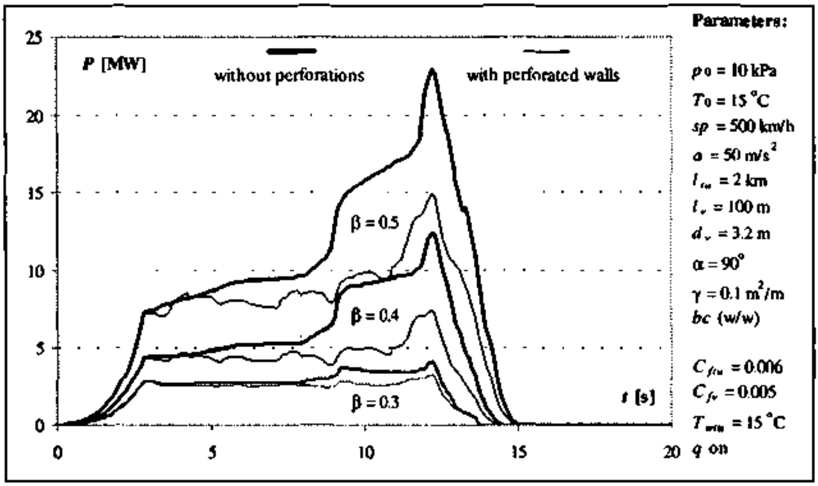

Figure 7.29 Comparison of the power curve for the closed tunnel with and without perforations (sp=500 km/h)

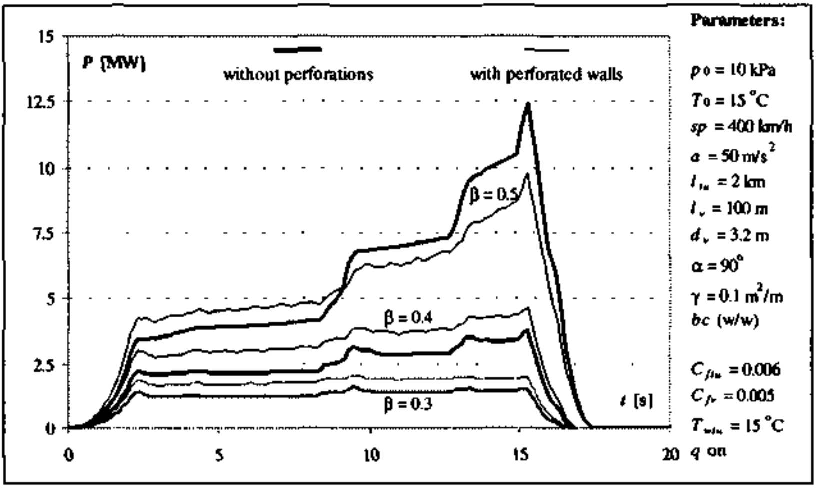

Figure 7.30 Comparison of the power curve for the closed tunnel with and without perforations (sp=400 km/h)

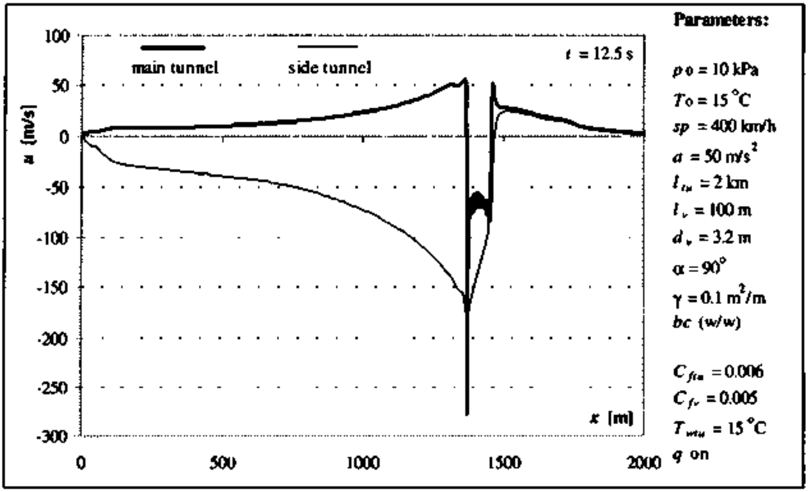

Figure 7.31 Air velocity distribution in main and side tunnel at t=12.5 s for β=0.5 and sp=400 km/h

The improved vehicle performance calls for a further examination of perforated walls. The influence of important parameters of the perforated wall, i.e. the perforation and the inlet angle, on the power curve is therefore examined. The configuration with β=0.5 and sp=400 km/h is again used as reference.

Figure 7.32 shows the influence of the perforation on the power requirement for an inlet angle of α=90°. In an early phase, the power value has the tendency to increase with perforation, whereas shortly after interaction with the first reflected wave, a reduction of the power value can be noticed. It is due to the fact that the reflected wave in the side tunnel passes the vehicle and then helps to 'fill up' the expansion wave. During interaction with the following reflected waves, the power value increases because of the already relatively homogeneous pressure distribution.

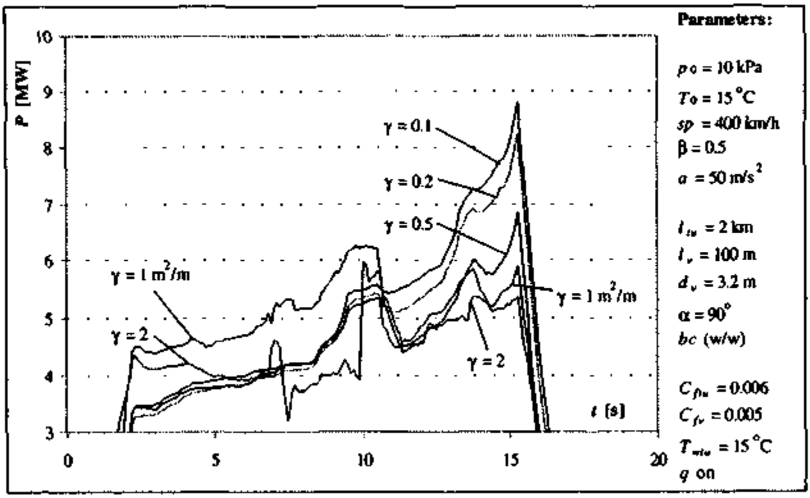

Figure 7.32 Influence of perforation on the power curve for β=0.5 and sp=400 km/h

The effect of a reduction of the inlet angle in a closed tunnel for a perforation of γ=0.1m²/m is shown in Figure 7.33. In absence of reflected waves, the perforated wall with α=90° shows no improvement as compared to the case without perforated wall, whereas the configurations with low inlet angle give slightly improved performance. This situation is inversed once reflected waves interact with the vehicle. A possible explanation is that the bypassing effect is reduced by fluid which re-enters the main tunnel in front of the vehicle; an effect which is favored by reducing the inlet angle.

Figure 7.34 refers to a case of a long tunnel, where the vehicle moves until interaction with the wave reflection at the left end ($t \approx 10$s) in absence of the effect of the boundary conditions. This allows to study the effect of the local flow field generated by the perforated walls with variation of the inlet angle. It is interesting to observe that for α=90° the performance is during the entire simulation time worse than without perforated walls, whereas a reduction of the inlet angle influences the flow field with advantage until the vehicle interacts with the wave reflection at the right end ($t \approx 14$s). This allows the hypothesis that the recirculation is, in absence of superposed waves, improved by the streamlined openings.

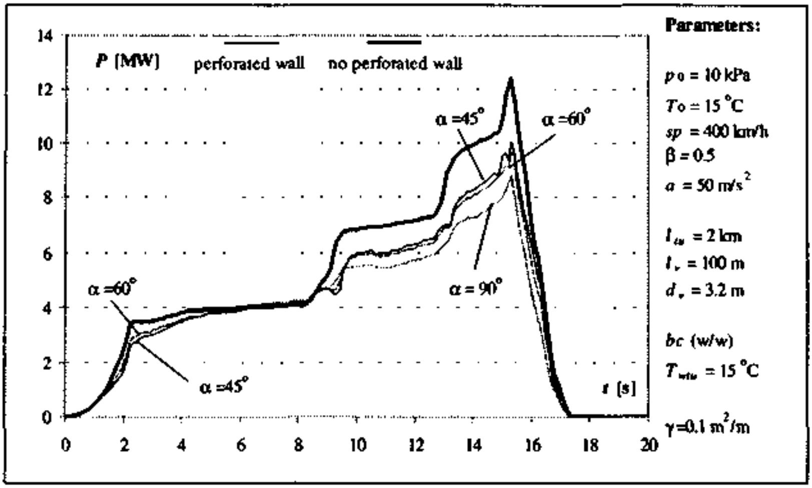

Figure 7.33 Influence of the inlet angle on the power curve for $\beta=0.5$ and $sp=400$ km/h in a closed tunnel

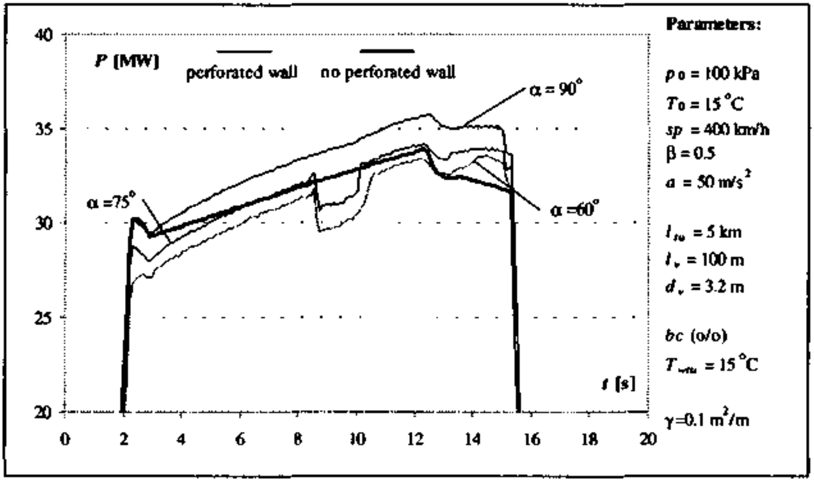

Figure 7.34 Influence of the inlet angle on the power curve for $\beta=0.5$ and $sp=400$ km/h in an open tunnel

7.9 Vehicle movement in a complex system

The following example demonstrates NUMSTA's capability to compute complex systems involving several vehicles, cross-vents, perforated walls and air shafts. It allows to convey an idea of the vehicle movement when the above individually examined system parts are superposed.

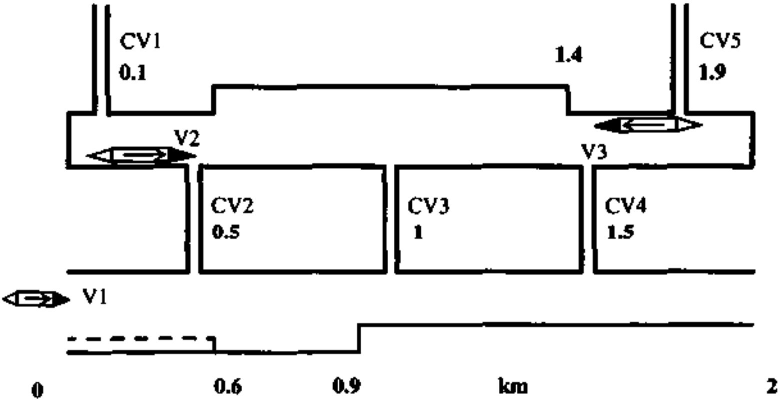

Figure 7.35 Complex system with several vehicles, cross-vents, air-shafts and a perforated entrance region

Table 7.4 Important parameters for the example of a complex system

$A_{tu,lrg}$	large cross-sections	32.17 m^2
$A_{tu,red}$	reduced cross-sections	16.08 m^2
A_v	vehicle cross-section	8.04 m^2
l_v	total vehicle length for V1, V2, V3	50, 100, 100 m
sp	vehicle speed for V1, V2, V3	500, 360, 400 km/h
C_{ftu}	tunnel friction coefficient	0.006
C_{fv}	vehicle friction coefficient	0.005
p_0	initial pressure	100 kPa
T_0	initial temperature	288.15 K
T_{wtu}	tunnel wall temperature	288.15 K
q	heat transfer	on

The geometry of the configuration can be concluded from Figure 7.35. The tunnel cross-sections have been chosen as to yield a blockage ratio of $\beta = 0.5$ for the narrow segments with one vehicle and $\beta = 0.25$ for the local enlargements. In the region with the perforated wall, the side tunnel has 1/3 of the total cross-section. Table 7.4 lists the most important parameters for the present example.

For illustration of the very complex results, the power requirement of the 3 vehicles and their positions are plotted over time in Figure 7.36. The power requirement fluctuates considerably under the mutual interaction of the vehicles. Remarkable are the power decrease of V1 during passage at the perforated wall and the subsequent slightly higher power when circulating in a tunnel with the same total cross-section and the power peak of V1 shortly before passing at CV4. The power peak of V2 when approaching the right end of the tunnel is interesting when compared with the corresponding behavior of V3 when approaching the left end. In this case the peak is considerable lower even though the vehicle speed is higher.

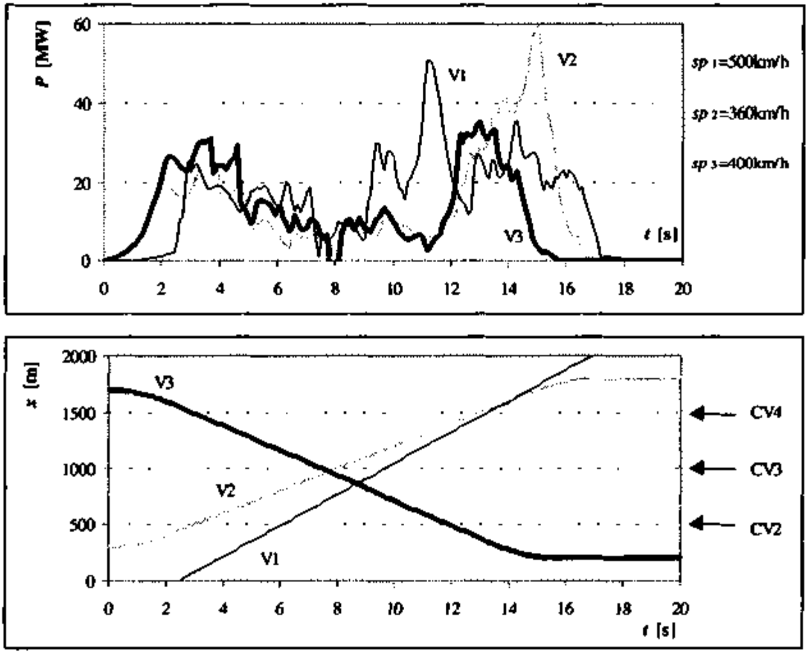

Figure 7.36 Power requirement of the 3 involved vehicles and their nose position over time

Figure 7.37 shows the pressure and air velocity fluctuations in the cross-vents during the simulation time. The diagonal lines indicate the position of the vehicle nose if the abscissa of each graph is interpreted as the position of the corresponding cross-vent.

Influences of individual vehicles are distinguishable only with difficulty. However, the passage of V1 at the 3 cross-vents causes in all three graphs an important pressure fluctuation inducing an inversion of the flow direction. The same is visible for V2 in the graphs for CV2 and CV3, where the flow direction changes from negative values to positive values. Since V1 and V2 pass CV4 at approximately the same instant, both effect are superposed here. For the passage of V3 at the cross-vents an inversion from negative to positive values can again be observed.

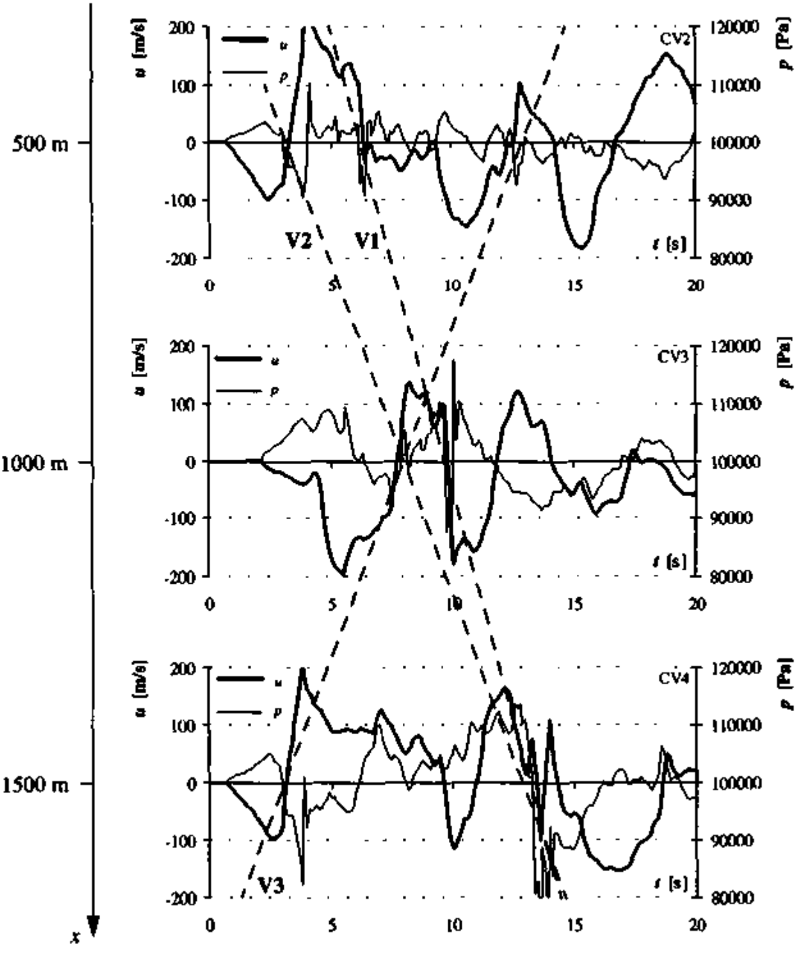

Figure 7.37 Pressure and air velocity fluctuation in the 3 cross vents with indication of the pathlines of the noses of the vehicles

7.10 Repressurization

In case of emergency, the tunnel, being under partial vacuum, has to be pressurized [89]. Conditions for the repressurization process are imposed by biomedical constraints. In this chapter it is discussed whether these constraints can be met and the associated aerodynamical and thermodynamical phenomena are described.

If a vehicle has an accident, it cannot be ensured that it can be towed to a predefined position. Therefore the tunnel segments have to be separated by heavy pressure locks. Because these doors are costly, they will be spaced several kilometers apart. The repressurization of a tunnel part can be realized by air shafts connecting to the atmosphere.

The high pressure difference between the ambient state and partial vacuum result in high flow velocities. Pressure waves originate at the air inlet positions. They propagate away from the air shafts and interact with air locks and blocked vehicles. For dimensioning, the forces applied on both have to be known.

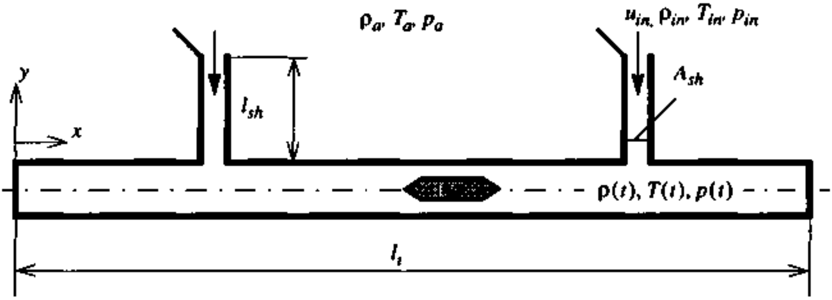

Figure 7.38 Sketch of the repressurization of the tunnel in case of an emergency

One of the configurations examined here is the one shown in Figure 7.38. It represents a tunnel segment with an accidented vehicle in the middle. In this sketch, two shafts supply fresh air. Other configurations, especially unsymmetrical ones, are imaginable.

The relation between the pressure and the temperature of two equilibrium states can be given in a closed expression. This does not yet give any information about the time dependence of the problem and the influence of the geometry. Until the critical pressure in the reservoir is reached, the inflow is at a constant sonic state, which depends only on the ambient conditions. If the internal pressure is above critical pressure, the inflow values vary with time. Critical and subcritical repressurization can be described analytically. The solution for the time dependent problem is influenced by the system geometry. The analytical solution can only provide information about the time dependence of equilibrium states and not about the distribution of flow values.

The numerical solution with NUMSTA allows furthermore to determine the time dependent distribution of the flow values in and the forces applied on the system. Friction and heat transfer are considered in the numerical model. As will be shown in the sequel, heat transfer considerably influences the process of repressurization even within the relative short times involved.

An analytical solution for the repressurization of a reservoir is a good example for 1D gas dynamics. Thermodynamics can give the relation between equilibrium states. Gasdynamics allows furthermore to predict the time dependence of the process for equilibrium states.

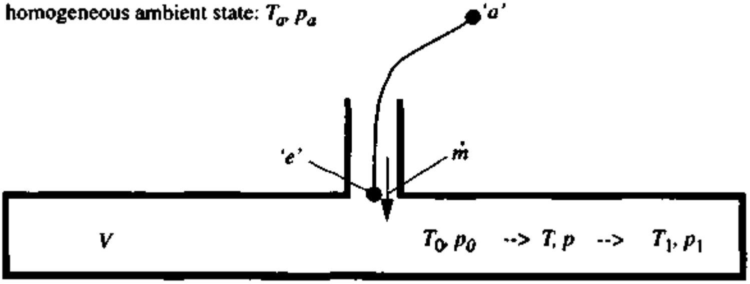

Figure 7.39 Sketch for indices used in the analytical formulation of the problem

7.10.1 Relation between the states of equilibrium

For an adiabatic process, the energy equation for an open control volume reads

$$\frac{\partial}{\partial t}(me) = \dot{m}\left(h_e + \frac{u_e^2}{2}\right) = \dot{m}h_a \quad , \tag{7.1}$$

where isenthalpy along a streamline allows the second equality. Two equilibrium states can be related by integrating the energy conservation over time for an open control volume and it follows with h_a=const.

$$m_1 e_1 - m_0 e_0 = (m_1 - m_0)h_a \quad . \tag{7.2}$$

The final mass m_1 and the initial mass m_0 can be expressed using the thermodynamic equation of state according to:

$$m_0 = \frac{p_0 V}{RT_0} \quad \text{and} \quad m_1 = \frac{p_1 V}{RT_1} \quad . \tag{7.3}$$

Replacing the corresponding terms in eq. (7.2), a closed expression for the final temperature T_1 can be given:

$$\frac{T_1}{T_0} = \left[1 + \left(\kappa\frac{T_a}{T_0} - 1\right)\frac{p_0}{p_1}\right]^{-1}\left(\kappa\frac{T_a}{T_0}\right) . \tag{7.4}$$

Remarks on eq. (7.4):

1. The final temperature increases also if initial and ambient temperature are equal. This is due to the latent heat contained in the inflow (see explanation to Figure 7.45).
2. The result is not dependent on the volume of the reservoir.
3. Thermodynamics does not deliver information about the time dependence of the problem. This can be examined with classical gas dynamics.

7.10.2 Time dependence for a series of equilibrium states

In addition to the assumption of isenthalpy, gas dynamics requires information about the way the state is changed. Isentropy will be assumed in the sequel.

The energy equation (7.1) can be written in the form

$$c_v \frac{\partial}{\partial t}(mT) = \dot{m}(t) c_p T_a \quad . \tag{7.5}$$

As the values are only dependent on time, it follows

$$m\frac{dT}{dt} = \dot{m}(t)(\kappa T_a - T) \quad . \tag{7.6}$$

The energy increase of the system can be related to the pressure increase using the equation of state in the form

$$mT = \frac{V}{R}p \quad \Rightarrow d(mT) = \frac{V}{R}dp \ . \tag{7.7}$$

Substituting the term $d(mT)$ in eq. (7.5) it follows

$$\frac{dp}{dt} = \dot{m}(t)\frac{R}{V}\kappa T_a \quad . \tag{7.8}$$

The entry values T_e, ρ_e and p_e can be expressed as a function of the Laval number and the ambient values with the gas dynamical functions (see subsection 6.3.1).

For the purpose of clear presentation, these relations are repeated here.

$$\frac{T_e}{T_a} = 1 - \frac{\kappa - 1}{\kappa + 1} La_e^{\ 2} , \tag{7.9}$$

$$\frac{\rho_e}{\rho_a} = \left(1 - \frac{\kappa - 1}{\kappa + 1} La_e^{\ 2}\right)^{\frac{1}{\kappa - 1}} \text{ and} \tag{7.10}$$

$$\frac{p_e}{p_a} = \left(1 - \frac{\kappa - 1}{\kappa + 1} La_e^2\right)^{\frac{\kappa}{\kappa - 1}} . \tag{7.11}$$

Integration of (7.6) and (7.8) give a relation for the time dependence of the temperature and the pressure inside the tunnel, respectively. The integration over time is simplified if the mass flow is constant. This is the case as long as the pressure in the tunnel is below the critical value. During subcritical inflow, the mass flow itself is time dependent.

Inflow with critical state:

If a low pressure reservoir with p_0 is filled up from an infinitely large high pressure reservoir with p_a=const., the inflow is sonic as long as the critical pressure relation is fulfilled:

$$\frac{p}{p_a} \le \frac{p^*}{p_a} = \left(\frac{2}{\kappa+1}\right)^{\frac{\kappa}{\kappa-1}} = 0.528 \text{ for air} \tag{7.12}$$

The Laval number (and also the Mach number) at the entry is then $La_e(= M_e) = 1$ and the inflow is choked with the critical mass flow given by $\dot{m}^* = \rho^* a^* A_{sh}$. It is only dependent on the ambient state and is constant over time. Integration of (7.6) and (7.8) between initial state 0 and the time dependent value T and p gives closed expressions for temperature and pressure, respectively, over time for a sequence of equilibrium states

$$\frac{T}{T_0} = \kappa\frac{T_a}{T_0} - \left(\frac{m_0}{m_0 + \dot{m}^* t}\right)\left(\kappa\frac{T_a}{T_0} - 1\right) \ . \tag{7.13}$$

$$p - p_0 = \dot{m}^* \frac{R}{V} \kappa T_a t \ . \tag{7.14}$$

The pressure increase during critical repressurization is mathematically linear.

Solving (7.14) for time, the period of critical repressurization is

$$t_c = \frac{p^* - p_0}{\dot{m}^* \frac{R}{V} \kappa T_a} \ . \tag{7.15}$$

Subcritical Repressurization:

After the average pressure in the tunnel has reached critical value, inflow occurs with Laval numbers below 1. The mass flow is no longer constant.

During subcritical repressurization, the coupling condition relates the actual pressure inside the tunnel p and the pressure at the bottom of the air shaft p_e by

$$p = p_e \ . \tag{7.16}$$

With relation (7.9), the mass flow can be expressed as a function of the Laval number as

$$\dot{m} = A_{sh}\frac{p_e}{RT_e}La_e a^* = \sqrt{\frac{2\kappa}{\kappa+1}}\frac{A_{sh}p_e}{\sqrt{RT_a}}\left(\frac{La_e}{1-\frac{\kappa-1}{\kappa+1}La_e^2}\right) \quad . \tag{7.17}$$

Using (7.16) and (7.17), equation (7.8) can be reformulated to a differential equation for p_e over t as a function of La_e yielding

$$\frac{dp_e}{dt} = \sqrt{\frac{2\kappa}{\kappa+1}}\frac{A_{sh}p_e}{\sqrt{RT_a}}\left(\frac{La_e}{1-\frac{\kappa-1}{\kappa+1}La_e^2}\right)\frac{R}{V}\kappa T_a \quad . \tag{7.18}$$

The value for p_e can be eliminated using (7.11) in its logarithmically differentiated form:

$$\frac{dp_e}{p_e} = -\frac{2\kappa}{\kappa+1}\left(\frac{La_e}{1-\frac{\kappa-1}{\kappa+1}La_e^2}\right)dLa_e \tag{7.19}$$

yielding

$$dLa_e = -\sqrt{\frac{\kappa+1}{2\kappa}}\frac{A_{sh}}{\sqrt{RT_a}}\left(\frac{R}{V}\kappa T_a\right)dt \quad . \tag{7.20}$$

All coefficients being constant, the Laval number at the entry is a linear function. A surprising consequence is that the process is finite. The Laval number during subcritical repressurization follows as

$$La_e(t) - 1 = -\frac{A_{sh}}{V}\sqrt{\frac{\kappa(\kappa+1)}{2}RT_a}(t-t_c) \quad . \tag{7.21}$$

The time dependent flow values are found with the Laval number by means of the gas dynamical functions. The tunnel pressure p equals according to (7.16) the inflow pressure p_e. The corresponding tunnel temperature can be obtained using (7.4).

The repressurization process ends with La_e=0. The total repressurization time is therefore

$$t_t = t_c + \frac{1}{\frac{A_{sh}}{V}\sqrt{\frac{\kappa(\kappa+1)}{2}RT_a}} \tag{7.22}$$

Note that this value depends only on the ambient temperature and the geometry parameters. The final pressure influences the result only in so far as the total repressurization time was defined to be the time it takes to achieve ambient pressure.

7.10.3 Analytical solution for an example

A configuration corresponding to a typical Swissmetro case has been chosen as an example. The parameters used for the analytical development and the numerical solution are given in Table 7.5.

Table 7.5 Parameters for the analytical and numerical solution

symbol	explanation	analytical	numerical
p_0	tunnel service pressure	10, 20, 30 kPa	10 kPa
T_0	initial tunnel temperature	20 °C	
p_a	atmospheric pressure	100 kPa	
T_a	ambient temperature	20 °C	
l_{tu}	length of tunnel	10 km	
n_{sh}	number of shafts	2	
d_{sh}	diameter of shaft	2, 3 m	2 m
A_{tu}	tunnel cross-section	20.1 m^2	
P_{tu}	tunnel perimeter	15.9 m	
C_{ftu}	tunnel friction coefficient	0	0.006
q	heat transfer (on/off)	off	on
p_e	final pressure level		60 kPa
t_e	end of the simulation time		200 s

Figure 7.40 show results for the time dependence for the pressure increase in the tunnel for different shaft cross-sections.

The interface between critical and subcritical repressurization is indicated with a little interruption in the curve. The pressure increase is almost linear also in the subcritical region, except close to the final pressure, where the driving force, the difference between ambient and tunnel pressure, tends to zero.

The graphs show that, in absence of heat transfer, pressure levels of around 60 kPa can be reached within 60s with only 2 small air shafts.

The total time for repressurization is reciprocal to the shaft cross-section A_{sh}. Figure 7.41 demonstrates the importance of a high ventilation surface and the low influence of the initial pressure on the repressurization time.

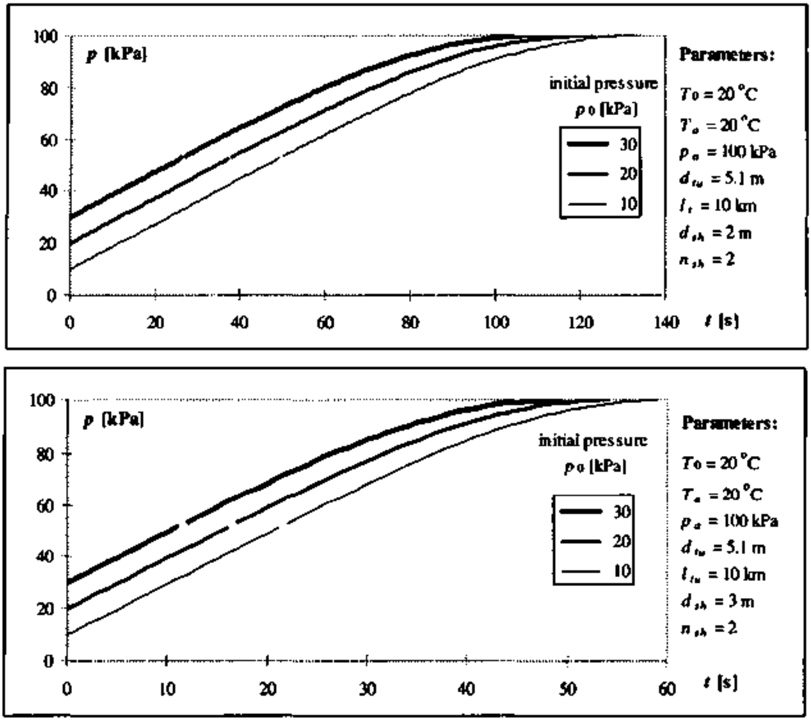

Figure 7.40 Time dependence of p for 2 shafts with d_{sh}= 2 m and with d_{sh}=3 m

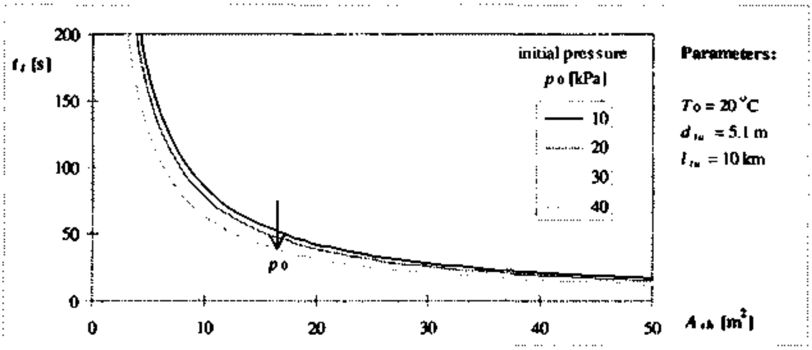

Figure 7.41 Total repressurization time t_t over sum of all inlet cross-sections A_{sh} with the parameter initial pressure p_0

7.10.4 Numerical solution

A numerical simulation for a case similar to the analytical development has been performed (see Table 7.5). Friction and heat transfer are included here. The repressurization has been interrupted as soon as the pressure in the center reached for the first time p_e=60 kPa by closing the ventilation shafts; the simulation was nonetheless continued until t_e=200s.

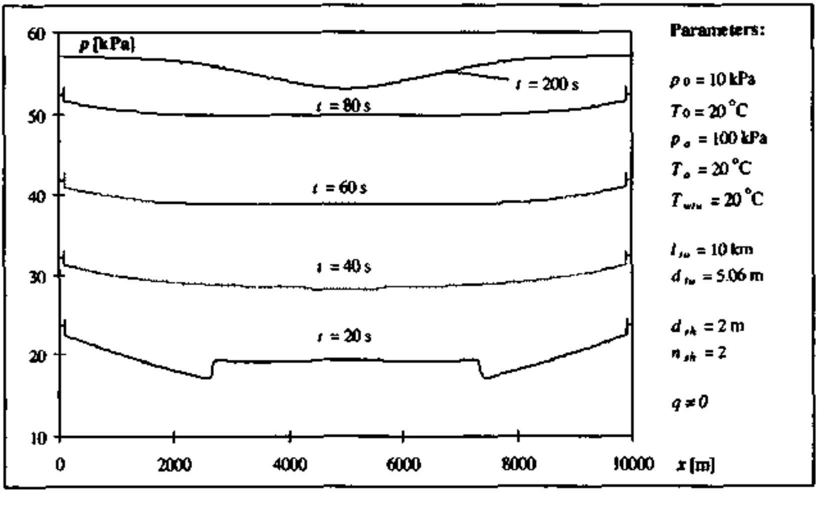

Figure 7.42 Pressure distribution at different times during the repressurization process

Additional to the findings obtained with the analytical development, the numerical simulation allows to visualize the distribution of the flow values in the system at different times. Figure 7.42 shows the pressure distribution in the examined tunnel segment at 5 different instants. The initial sharp pressure waves are smoothened by friction and heat transfer, so that the pressure distribution becomes already quasi homogeneous after ca. 30 s. Heat transfer has the effect to reduce the air temperature and with it the pressure in the tunnel. It is for this reason that the pressure increase is slower in the numerical simulation than analytically predicted.

Figure 7.43 gives the information concerning the air velocity. The graph shows the typical triangular distribution with peaks at the ends reaching 100 m/s. This exceeds extreme natural wind speeds of 88 m/s (for comparison, 12 on the Beaufort scale corresponds to ca. 33 m/s). Even after 80 s, the wind speed around the inlet is still 50 m/s but air movement degenerates after the closing of the inlet valve to weak waves moving back and forth between the tunnel ends.

Figure 7.44 shows the air velocity in an inlet shaft. As expected, the air velocity at the bottom reaches critical value, the lower absolute value at the top accounts for the acceleration due to the pressure and density loss by friction. The absolute value of the inflow velocity is then reduced by the diminishing driving pressure difference.

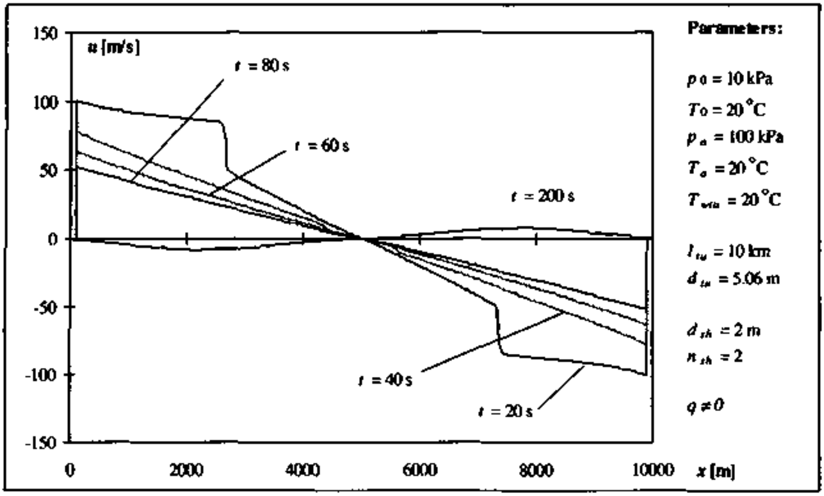

Figure 7.43 Air velocity distribution at different times during the repressurization process

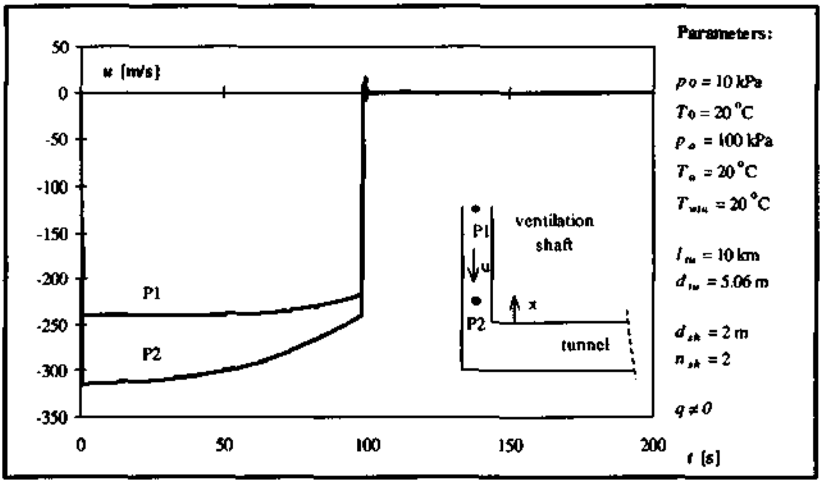

Figure 7.44 History of the air velocity in an inlet shaft recorded at points at the top and at the bottom

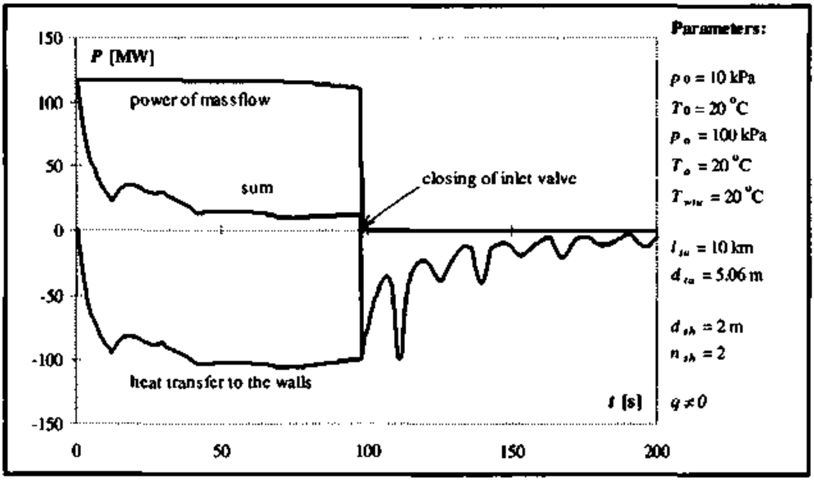

Figure 7.45 Comparison of the power of the mass flow with the heat transfer during the repressurization process

In the present simulation, convective heat transfer and the latent heat in the inflow were recorded. The expression latent heat is here used for that part of the enthalpy of the inflow which can contribute to heating up the reservoir if initial temperature and ambient temperature are equal. The specific latent heat of the inflow is given by the term p/ρ in the definition equation of enthalpy $h = e + p/\rho$.

Figure 7.45 shows that the convective heat transfer to the wall reaches already after some seconds a level comparable to the one of the latent heat in the inflow. It can be concluded that heat transfer considerably influences the repressurization process, even during the relatively short time of repressurization. Note that in this simulation the effect of heat transfer is overestimated because the tunnel wall temperature has been set constant. In reality, the important energy flow into the wall increases the wall temperature and reduces heat transfer.

In several simulations, it has been found that the presence of a vehicle has a negligible influence on the distribution of the flow values.

7.11 Summary of chapter 7

The purpose of this chapter is to demonstrate the range of applicability of NUMSTA on problems related to tunnel aerodynamics. A reference configuration with the following parameters is defined to facilitate the comparison of results: sp=400km/h, β=0.5, l_v=100m, constant friction coefficients (C_{ftu}=0.006 and C_{fv}=0.005), heat transfer on.

In section 7.1, the vehicle movement in a single infinite, closed or open tunnel is investigated. Power-time curves, instantaneous distributions of flow values along the vehicle and in the tunnel as well as history curves for selected tunnel fixed points are discussed.

In the sections 7.2 - 7.5, the vehicle movement in a tunnel loop, a tunnel with local variations of the cross-section, a tunnel with air shafts (open and closed system) and a tunnel system with cross-vents are examined.

The parametric study in sections 7.6 discusses the influence of the following variations on the power requirement: configuration, heat transfer, friction coefficient, vehicle length, vehicle speed, vehicle acceleration and initial pressure p_0.

In sections 7.7 and 7.8 configurations including a perforated wall are explored in detail. Perforated walls alongside the tunnel reduce the power requirement for high vehicle speeds and blockage ratios. Perforated ends help to smoothen the power curve.

Section 7.9 shows the capability of NUMSTA to compute complex configurations. In section 7.10 high air velocities, increased temperatures and eventually the duration of the process were pointed out as security aspects of the repressurization of a tunnel system under partial vacuum.

8 THE TURBO SWISSMETRO

The TurboSwissmetro (TSM) deals with the fundamental problem of flow bypassing by compressing the air in front of the vehicle and forcing it around. The TSM can therefore be considered an active installation for flow bypassing (see also [88]).

Several advantages as compared to the classical concept of the Swissmetro (CSM) are associated with this concept. If the system is dimensioned so that inflow and outflow velocities are the negative of the vehicle speed, the flow is limited to the proximity of the vehicle. Then, the flow is steady in the vehicle frame of reference. The vehicles no longer influence each other. All energy transfer to the fluid is concentrated at the vehicle. This allows to concentrate expensive elements of the system rather than to distribute them over the entire tunnel length.

The sketch below illustrates the concept of the TSM showing a vehicle moving from the right to the left. A compressor is placed in the front and a turbine is indicated in the tail region.

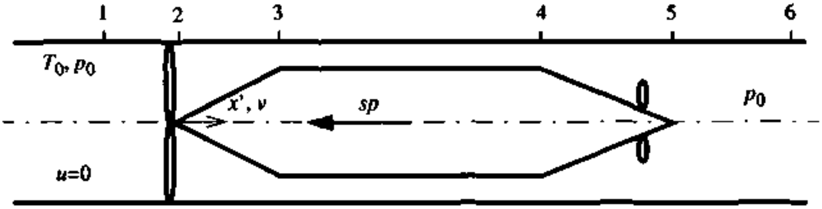

Figure 8.1 Sketch of the Turbo Swissmetro

According to Figure 8.1 the flow around the TSM is separated into three parts:

- the flow through the compressor (1 --> 2),
- the flow along the vehicle (2 --> 5) and
- the flow behind the vehicle (5 --> 6).

The flow behind the vehicle does not need a special treatment. The pressure p_5 was imposed leaving v_5 and T_5 open. This allows for a non zero exit flow velocity. Its value will be given in the results. The superfluous kinetic energy in point 5 can be used by a small turbine producing some of the energy needed on board.

8.1 The computational algorithm

The computational algorithm is defined by the physics of the problem. When the TSM moves in steady state, the air approaches with the negative of the vehicle speed seen in the vehicle frame of reference, which will be the relative system used in the sequel. The flow values in point 1 are the same as in 0 (rest).

The initial compressor power P_{c0} is chosen to be high. The higher the compressor power, the higher the maximal possible speed for a given tunnel diameter. From point 1 to 2 (see Figure 8.1) the compressor increases the density ρ and for continuity reasons slows down the air. Since the train speed is subsonic, the air velocity until 2 is so, too. In the convergent from 2 to 3 the air velocity increases. This is the case also in the annular space, from 3 to 4, because of friction effects. If it becomes sonic before 4 the system is overdetermined and the entry flow values have to be redefined. The vehicle speed must therefore be smaller.

If sonic speed is reached in 4 (M_4=1), the divergent acts like a laval nozzle. Supersonic expansion and a shock may appear. This case is excluded since for technical reasons there is no interest in constructing a vehicle with shock in the divergent. First, the energy requirement would be increased by supersonic expansion and secondly a shock produces important unsteady forces on the vehicle structure, which has to be avoided with respect to fatigue and passenger comfort.

The problem can therefore be studied with non-conservative first order ordinary differential equations, which do not allow sonic speed. Nonetheless, M_4 may be very close to the critical value. In this case the mass flow and with it the vehicle speed reach their maximal possible values for the given tunnel diameter. The flow in the divergent is then a subsonic recompression. The program verifies if p_5 is sufficiently close to p_t, which is the boundary condition chosen. Another possibility is to set u_5=u_0=0. The compressor power is adjusted accordingly.

Once all the above mentioned conditions are fulfilled, the calculation is finished for one value of the tunnel diameter and the vehicle speed. The results are stored in the output file.

The free power is due to the fact that there is a resulting force on the vehicle. This force is always propelling since the compressor has to overcome not only the friction on the vehicle but also on the tunnel wall. The vehicle has thus to be slowed down in order to remain in steady movement. This can be realized by the means of a little turbine fixed on the tail of the TSM. A positive side effect is that energy transfer to the vehicle is possible this way. The total power is thus the compressor power diminished by the free power.

If initial compressor power and speed, P_{c0} and sp_0, were chosen high enough, the resulting speed is the maximal possible speed for the examined tunnel diameter. Lower speeds are possible and the corresponding power requirement determined. The procedure is repeated for different tunnel diameters. Figure 8.2 shows a flow diagram of the above described procedure.

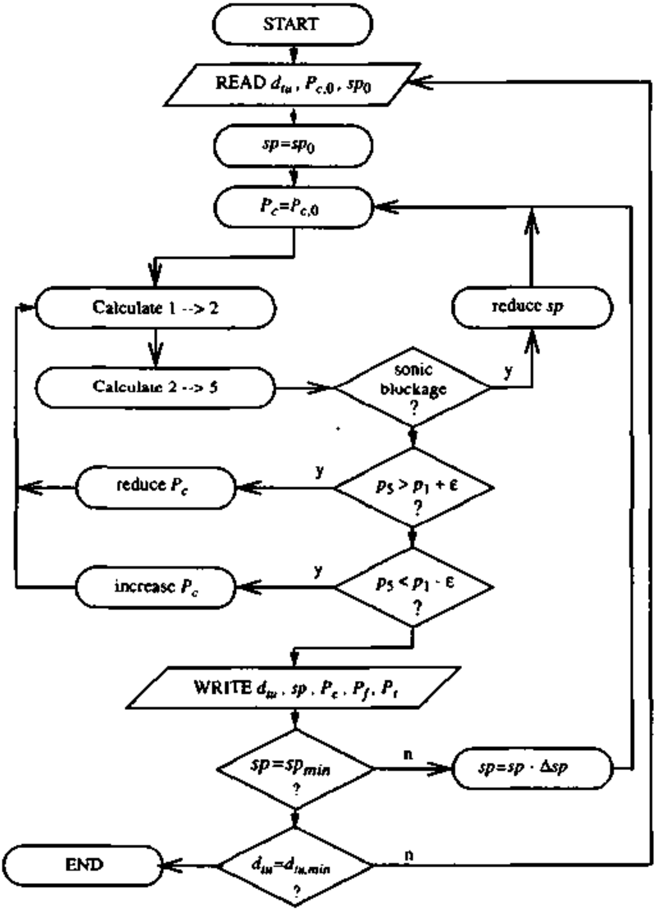

Figure 8.2 Flow chart for the computation of the TurboSwissmetro

The flow through the compressor (1 - 2):

The compression is modeled as 1D, steady and isentropic. Mass, energy conservation and the definition of the entropy give the system (8.1 a) - (8.1 c):

$$\rho_2 v_2 = \rho_1 v_1 \tag{8.1 a}$$

$$c_p T_2 + \frac{v_2^2}{2} - \left(c_p T_1 + \frac{v_1^2}{2}\right) = \frac{P_c}{\dot{m}} \tag{8.1 b}$$

$$T_2 \rho_2^{1-\kappa} = T_1 \rho_1^{1-\kappa} \tag{8.1 c}$$

with

P_c :: compressor power

$\dot{m}$ :: mass flow through the compressor.

The flow along the vehicle (2 - 5):

The flow around the TSM in the vehicle frame of reference is 1D, steady, compressible. Friction and heat transfer have to be considered. Flow discontinuities are conceptually excluded. The problem can thus be described using the conservation equations in the vehicle frame of reference (2.31) in first order ordinary differential form as given in system (6.50) for the quasi steady vehicle movement.

The forces on the vehicle:

The vehicle experiences the forces due to the distribution of the static pressure and the vehicle friction force as well as the forces acting from the compressor and the turbine on the vehicle nose and tail, respectively. The pressure force and the friction force are opposed to the direction of movement. The compressor force pulls the vehicle like an airplane propeller.

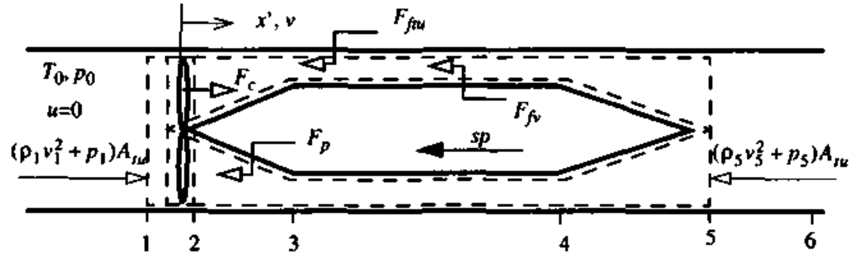

Figure 8.3 Forces acting on the air in a vehicle fixed control volume covering all moving system parts

The resulting force exerted by the vehicle on the surrounding air is calculated as the sum of the forces crossing the control volume from the vehicle, i.e.

$$F_v = F_c + F_p + F_{fv} \,. \tag{8.2}$$

Using eq. (8.2), the momentum balance for the control volume covering all moving system parts reads

$$(\rho_1 v_1^2 + p_1)A_{tu} - (\rho_5 v_5^2 + p_5)A_{tu} + F_{ftu} + F_v = 0 . \tag{8.3}$$

The resulting force acting from the air on the vehicle is given by $F_v' = -F_v$ can be found in two ways:

1. By calculating F_c by means of a momentum balance for a control volume between 1 and 2 and integrating F_p and F_{fv} over the entire vehicle length, F_v is found by means of eq. (8.2).
2. Eq. (8.3) requires the flow values in 1 and in 5 as well as the integral tunnel friction force F_{ft}.

The second method is preferred since it involves less numerical approximation.

As will be found, the compressor force is always superior to the sum of the pressure and the friction forces acting on the vehicle. This result was anticipated because in a vehicle fixed control volume with the idealized assumption that the exit flow values equal the entry flow values, the compressor force has to overcome the pressure and the friction forces acting on the vehicle plus the tunnel friction force. A propelling force results. It is therefore necessary to expose the vehicle to a retarding force in order to keep the speed constant. This force can at least partially be established by the tail turbine with the side effect to produce required electrical energy needed on board. The turbine can produce at most as much electrical power as the technical exergy contained in the flow in point 5.

The present examination shall be limited to the energetic aspect of such a tunnel vehicle. Technical feasibility and economic aspects are not discussed here.

8.2 Sample results for the TSM

The representation for the power requirement needs explanation. As discussed above, a maximum speed can be determined for each blockage ratio so that sonic blockage is just avoided. A vehicle movement with inferior speeds is possible. The results display therefore the power requirement as a function of the vehicle speed. For each blockage ratio, these curves end at the maximum speed.

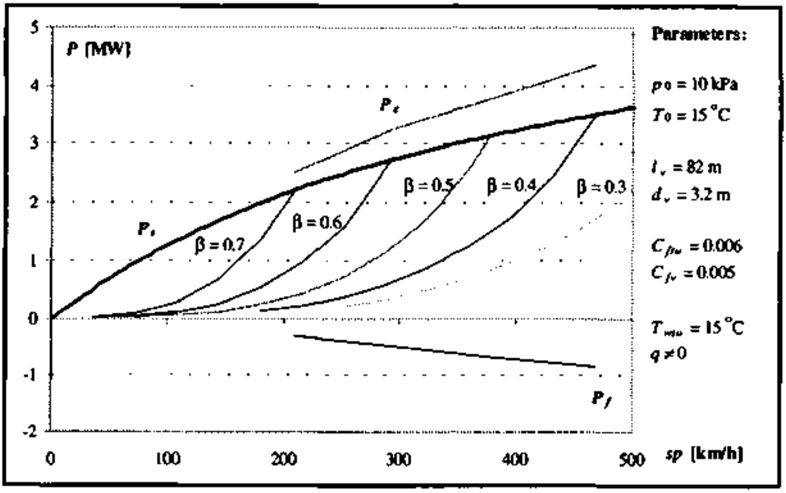

Figure 8.4 Power requirement for the TSM for different blockage ratios with indication of compressor power (P_c), free power (P_f) and total power (P_t). Heat transfer was considered and the friction coefficients were held constant.

Three different values for the power can be distinguished: the compressor power which is the power required to compress the air given by eq. (8.1 b), the free power which results from the integral of forces acting on the vehicle and the total power which is the sum of both. The free power expresses that the resulting force acting on the vehicle is propelling. It can be regained by means of a turbine producing energy needed on the vehicle, which has the positive side effect to provide equlibrium of forces. Compressor power, free power and total power are plotted in Figure 8.4. The power value for β=0.5 and *sp*=105 m/s amounts to P_t=3.1MW, a value which is near the power required for the CSM (see [92]). It is thus interesting to examine the technical characteristics and feasibility of the TSM further.

Interesting are also the distribution of flow values along the vehicle. A case similar to the projected configuration of the CSM with β=0.5 at the maximum speed (*sp*=-105 m/s) for that configuration has been chosen. Figure 8.5 shows the distribution of the Mach number and the temperature along the vehicle. The graph corresponds to the zone between the points 2 and 5 according to the index convention on Figure 8.1. As intended, the Mach number is close to 1 at the end of the annulus. The temperature is increased by the compression between 1 and 2 and is then reduced by expansion until 4. The recompression between 4 and 5 increases the temperature again to a value above the initial temperature.

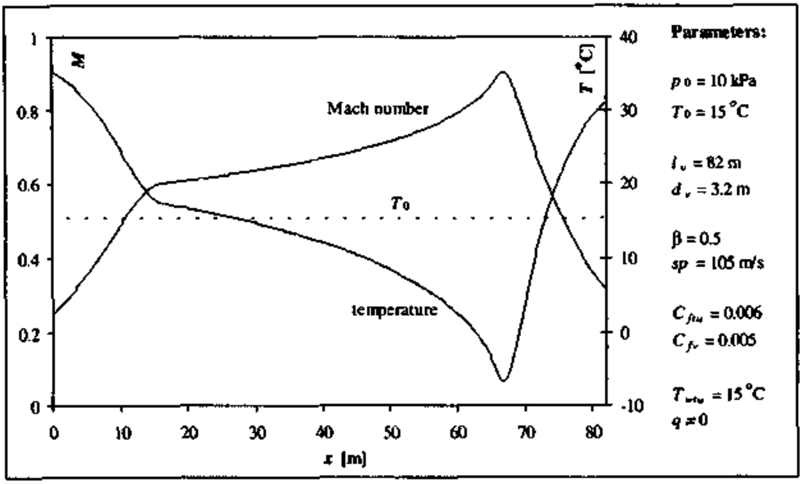

Figure 8.5 Mach number and temperature distribution along a TSM with β=0.5 and *sp*=-105 m/s with indication of initial temperature T_0

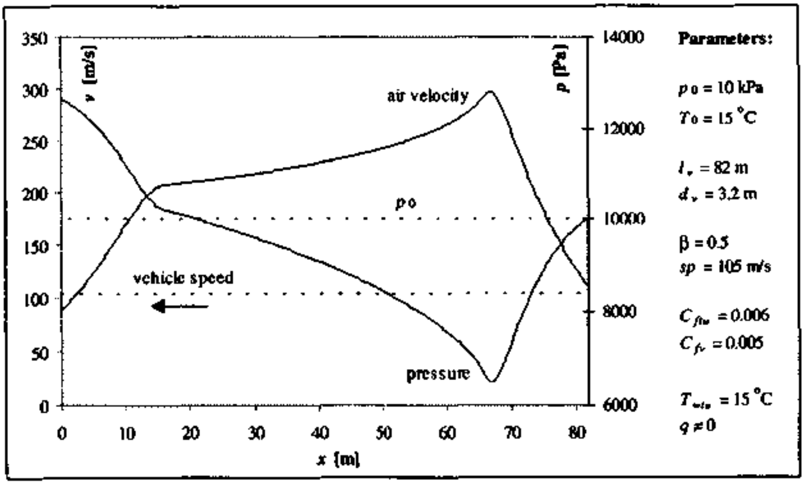

Figure 8.6 Air velocity and pressure distribution along a TSM with β=0.5 and *sp*=-105 m/s with indication of the vehicle speed *sp* and the initial pressure p_0

The distribution of the air velocity in the vehicle frame of reference and the pressure is plotted in Figure 8.6. Following continuity, the compression reduces the air velocity between 1 and 2. It then increases until point 4 due to expansion effects. Between 4 and 5 the air velocity reaches almost initial value. The superfluous kinetic energy could be used by a turbine. The pressure distribution is as qualitatively expected opposite to the velocity distribution. The compressor has to reach p_2=12'600 Pa in order to ensure that all air is forced around the vehicle.

The final pressure has been imposed to be the initial pressure. It is not possible to impose all exit values to be initial values, because this would overdetermine the system. A little perturbation propagating into the tunnel therefore always remains. However, it dissipates fast due to friction effects.

8.3 Summary of chapter 8

In this chapter some ideas concerning an alternative to the classical Swissmetro, the TurboSwissmetro (TSM), are presented. The TSM is a vehicle with a compressor forcing all the air to pass the vehicle. The flow around the vehicle is steady. High air velocities dependent on the vehicle speed result. A natural limit for the air velocity in the annular gap is given by sonic blockage, which also limits the vehicle speed for a given blockage ratio.

The power graph shows 5 curves for the power requirement over the vehicle speed for each blockage ratio which end at the maximal speed. Besides, it displays 3 curves corresponding to the power requirement at maximal speed for the compressor power P_c, the free power P_f (which corresponds to the kinetic energy of the outflow) and the total power P_t (which is the sum of compressor and free power).

The power requirement for the TSM is for equal vehicle speeds and blockage ratios slightly higher but comparable to the CSM. Besides, the TSM generates practically no flow and pressure waves far from the vehicle. It is therefore recommended to study the feasibility of the TSM in more detail.

CONCLUSIONS

The present work describes, validates and applies the program NUMSTA for the NUMerical Simulation of Tunnel Aerodynamics. New for a simulation program in this domain are:

- the numerical method

Classical simulation programs for train / tunnel systems are based on the method of characteristics (MoC). NUMSTA is based on the conservative form of the Euler equations for flow in a tube with spatio-temporally varying cross-section. Mass, momentum and energy exchange are considered by an additional source term. An explicit finite volume method based on the 2nd order TVD scheme of Roe discretizes the equations.

- the dynamical mesh generator and the two-time step method

The dynamical mesh generator adapts the position of the local mesh refinements to the actual position of the vehicles and ensures a minimum number of fine mesh points around geometrical discontinuities. Necessary mesh changes are restricted to the immediate environment of the moving vehicle. Refined parts are computed with a small time step and parts with coarse mesh spacing allow a coarse time step. The dynamical mesh generator and the 2 time step method contribute to CPU time efficient computations.

- the domain of applicability

It has been shown that the MoC is not suited to produce accurate data for cases with high air velocities and important source term contributions (high-friction cases). The numerical method chosen for NUMSTA allows to simulate classical low-speed as well as modern high-speed train/tunnel configurations.

- its extensibility to new problems

The consideration of numerical models in additional source terms and the modular program structure allows to refine or coarsen existing numerical models easily in order to adapt the program to new requirements (precision or speed). Besides, new models, e.g. for the propagation of pollutants or heat release by fire, can readily be included.

With NUMSTA, so far unexplored train/tunnel configurations have been simulated. In particular, numerical simulations have been carried out for the a future high-speed underground train in a partially evacuated tunnel system with the name 'Swissmetro', where aerodynamic phenomena had to be related to energy, feasibility and security aspects.

In this work, typical compressible flow phenomena have been discussed for various configurations with high vehicle speeds and high blockage ratios. The influence of different parameters (heat transfer, friction coefficient, vehicle length, vehicle speed a.o.) on the vehicle power requirement in a tunnel has been investigated .

The effect of perforated walls alongside the tunnel and at the tunnel ends has been examined. It was found that perforated walls alongside the tunnel help to reduce the power requirement for sufficiently high vehicle speeds and blockage ratios. Perforated tunnel ends reduce the entrance pressure wave and have the tendency to smooth the power curve.

The repressurization of a tunnel part has been discussed and high flow velocities, air temperature rise and the duration of the process before a certain survival pressure can be established were identified as security problems.

In addition to the classic Swissmetro (CSM), the TurboSwissmetro (TSM) has been investigated. The TSM forces air with a compressor around the vehicle. Far field effects are practically avoided and the power requirement was found to be close to the CSM.

FUTURE WORK

improvement of the scientific value of NUMSTA

One of the main limitations of the 1D approach for the simulation of tunnel aerodynamics is the realistic modeling of 3D effects, such as friction, heat transfer, pressure losses at branchments or perforated walls and flow separation.

It is desirable to obtain more accurate empirical coefficients for individual configurations from small or large scale experiments. In the future, quasi 1D models should be assessed and calibrated by means of local 3D simulations with boundary conditions given by global 1D calculations. This could avoid expensive experiments. Besides, the availability of experimental data and the permission to use them for publication are frequent problems.

The perforated walls show, in the first evaluation given here, an interesting performance. A further examination of the aerodynamic characteristics of this device with in depth investigation of the validity of the 1D model is promising. The question of momentum transfer between main and side tunnel needs to be investigated. The flow angles in and out of the perforations in particular remain an open question which can for example be resolved with detailed 2D and 3D simulations.

A focus of the existing rich literature about tunnel aerodynamics is corrective models, e.g. for unsteady friction, empirical train shapes, time delay of wave reflections, influence of ballast on wave propagation, velocity profiles for the flow in the annular gap, temperature development in the sourrounding rock a.o. It would be interesting to include some of these models for the more detailed study of flow phenomena with NUMSTA.

The simulation of a fire and the smoke propagation could in principle be implemented. The concept of the moving refined zones may be extended to refinements around physical discontinuities traveling with their actual speed. The code could also be extended to allow for the passage of a train from one tunnel into another and to allow for Y-type tunnel connections.

application of NUMSTA

The present version of NUMSTA is now ready to be used to optimize actual train/tunnel systems with parameters not widely considered so far. It allows for example to establish a train schedule making use of the aerodynamic interaction of vehicles, to propose cross-vents, air shafts or a speed function as to avoid undue power or pressure peaks, to optimize the process of repressurization or to examine the mixed use of passive and active means of flow bypassing. A final evaluation of the results of an aerodynamic analysis has of course to be followed by a detailed analysis of feasibility and economic aspects.

improvement of the user-friendliness of NUMSTA

Until now, NUMSTA has been used for scientific computations. Only little attention was paid to the user interface. First steps were undertaken using Visual Basic macros for existing standard applications. This concerns the management of the input files as well as the animated display of the results. Additional efforts in this direction could render the code marketable.

BIBLIOGRAPHY

Texts related to theoretical or experimental fluid dynamics

[1] Baehr, H.D. *Thermodynamik: eine Einführung in die Grundlagen und ihre technischen Anwendungen.* 8. Aufl. Berlin [a.o.]: Springer, 1992.

[2] Flatt, R. "Résolution sans itérations de problèmes d'écoulements unidimensionels en Dynamique des Gaz." in Entropie **170**, 1992: 43-49.

[3] Försching, H.W. Grundlagen der Aeroelastik. Berlin (u.a.): Springer-Verlag, 1976.

[4] Idel'cik, I.E. *Memento des pertes de charge.* Traduit du russe. Paris: Eyrolles, 1960.

[5] Incropera, F. and David P. de Witt. *Fundamentals of Heat and Mass Transfer.* 3rd ed. New York [a.o.]: John Wiley&Sons, 1990.

[6] Lighthill, J. *Waves in Fluids.* Cambridge, UK [a.o.]: University Press, 1978.

[7] Panton, Ronald L. *Incompressible Flow.* New York [a.o.]: John Wiley & Sons, 1984.

[8] Ryhming, Inge L. *Dynamique des Fluides.* Lausanne: Presses polytechniques romandes, 1985.

[9] Schlichting, H. *Boundary Layer Theory.* 6th ed. Karlsruhe [a.o.]: G. Braun, 1968.

[10] Sédille, Marcel. *Turbo-Machines Hydrauliques et Thermiques.* Tôme IV. "Mécanique des fluides compressibles". Paris: Masson et C^{ie}, 1970.

[11] Zierep, J. *Grundzüge der Strömungslehre.* 3. überarb. Aufl. Karlsruhe: G. Braun, 1987.

[12] Zierep, J. *Theoretische Gasdynamik.* Karlsruhe: G. Braun, 1976.

Texts on numerical methods

[13] Fletcher, C.A.J. *Computational Techniques for Fluid Dynamics.* Vol. I+II. Berlin [a.o.]: Springer, 1988.

[14] Gustafsson, B. *High order methods on structured grids.* Seminar held at the IMHEF on 13 Nov 1997.

[15] Hirsch, C. *Numerical Computation of Internal and External Flows.* Vol. I. Chichester [a.o.]: John Wiley&Sons, 1988.

[16] Hirsch, C. *Numerical Computation of Internal and External Flows.* Vol. II. Chichester [a.o.]: John Wiley&Sons, 1988.

[17] LeVeque, Randall. *Numerical Methods for Conservation laws.* Basel [a.o.]: Birkhäuser, 1992.

[18] Lister, M. "The numerical solution of hyperbolic partial differential equations by the method of characteristics" in *Mathematical Methods for Digital Computers.* A. Wolf and H.S. Ralston (eds.). New York: Wiley, 1960.

[19] *NAG Mark16. The Fortran Library.* Downers Grove (IL): Numerical Algorithms Ltd., 1990.

[20] Roe, P.L. and J. Pike. "Approximate Riemann Solvers, Parameter Vectors, and Difference Schemes" in *Journal of computational Physics* **43**, 1981: 357-372.

[21] Roe, P.L. "Characteristic-based Schemes for the Euler equations" in *Ann. Rev. Fluid Mech.* 18, 1986: 337-65.

[22] Roe, P.L. "Modern numerical methods applicable to stellar pulsation" in *The Numerical Modeling of Nonlinear Stellar Pulsations: problems and prospects* ed. by R. Buchler. NATO ASI series, Vol. 302. Dordrecht (NL): Kluwer Academic Publishers, 1990: 183-213.

[23] Roe, P.L. Personal Conversation at EPFL on 05 Dec 1997 about Hancocks Method.

[24] Turkel, E. and S. Yaniv, U. Landau. *Accuracy of schemes for the Euler equations with non-uniform meshes.* ICASE Report No. 85-59. Langley: NASA, 1985.

Texts on tunnel aerodynamics

[25] Baron, A. and P. Losi. *Simulazione numerica dei fenomeni aerodinamici prodotti da treni ad alta velocità in tunnel di forma complessa.* Internal report. Milano: Politecnico, 1994 (?).

[26] Barrow, H. and C.W. Pope. "Aspects of flow and heat transfer in railway tunnels" in *Proc. 6th Intl. Symp. on Aerodynamics and Ventilation of Vehicle Tunnels.* (Durham, UK: 27-29 Sep 1988). Cranfield, UK: BHRA Fluid Engineering, 1988: paper B1.

[27] Bradbury, W.M.S., and T.A. Pope. "Channel Tunnel: The performance rationalization" in *Proc. 8th Intl. Symp. on Aerodynamics and Ventilation of Vehicle Tunnels* (Liverpool, UK). Bury St. Edmonds, London: Mech. Eng. Publications Ltd., 1994.

[28] Bourquin, V. and P. Monkewitz. *The need for the construction of a multipurpose high-speed train aerodynamic testing rig (HISTAR) at the EPFL within the Swissmetro project.* Swissmetro report EPFL 1.0018/1.6210/a. Lausanne: EPFL, 1995.

[29] Burry, J. and F. Zumsteg. "Airshafts for the alleviation of pressure waves in tunnels of the new Swiss Rail 2000" in *Proc. 9th Intl. Symp. on Aerodynamics and Ventilation of Vehicle Tunnels* (Aosta, Italy: 06-08 Oct 1997). BHR Group Conference Series. Bury St. Edmonds, London: Mech. Eng. Publications Ltd., 1997.

[30] Dayman, B. and D.W. Kurtz. "Experimental studies relating to the aerodynamics of trains travelling in tunnels at low speeds" in *Proc. 1st Intl. Symp. on Aerodynamics and Ventilation of Vehicle Tunnels* (Canterbury, UK: 10-12 Apr 1973). Cranfield: BHRA Fluid Engineering, 1973, paper G2.

[31] Daymann, B. and A. Vardy. "TRUNNEL - A gun fired 0.5% scale facility for pressure transients tests of very high speed trains in tunnels" in *Proc. 7th Intl. Symp. on Aerodynamics and Ventilation of Vehicle Tunnels* (Brighton, UK: 27-29 Nov 1991). Essex: Elsevier Publishers Ltd., 1991: 757-787.

[32] Flatt, R. "Traînée aérodynamique d'un métro à grande vitesse dans un tunnel étroit" in *Ingénieurs et Architectes Suisses* 9, 1994.

[33] Fox, J.A. and A.E. Vardy. "The generation and alleviation of air pressure transients caused by the high speed passage of vehicles through tunnels" in *Proc. 1st Intl. Symp. on Aerodynamics and Ventilation of Vehicle Tunnels* (Canterbury, UK: 10-12 Apr 1973). Cranfield [a.o.]: BHRA Fluid Engineering, 1973: paper G3.

[34] Gaillard, M.A. "Aerodynamic measurements with high-speed trains (250 km/h) in the Heitersberg tunnel. Comparison theory and experiment" in *Proc. 3rd Intl. Symp. on Aerodynamics and Ventilation of Vehicle Tunnels* (Sheffield, UK: 19-21 Mar 1979). Cranfield [a.o.]: BHRA Fluid Engineering, 1973: paper G2.

[35] Glöckle, H. and P. Pfretzschner. "High speed tests with ICE/V passing through tunnels and the effect of sealed coaches on passenger comfort" in *Proc. 6th Intl. Symp. on Aerodynamics and Ventilation of Vehicle Tunnels.* (Durham, UK: 27-29 Sep 1988). Cranfield, UK: BHRA Fluid Engineering, 1988: paper A2.

[36] Glöckle, H. "Comfort investigations for tunnel runs on the new line Würzburg-Fulda" in *Proc. 7th Intl. Symp. on Aerodynamics and Ventilation of Vehicle Tunnels* (Brighton, UK: 27-29 Nov 1991). Essex: Elsevier Publishers Ltd., 1991: 155-171.

[37] Grégoire, R., J.M. Réty, F. Masbernat [a.o.]. "Experimental study (scale 1/70th) and numerical simulation of pressure waves and micro-pressure waves due to high-speed train-tunnel entry" in *Proc. 9th Intl. Symp. on Aerodynamics and Ventilation of Vehicle Tunnels* (Aosta, Italy: 6-8 Oct 1997). BHR Group Conference Series. Bury St. Edmonds, London: Mech. Eng. Publications Ltd., 1997: 877-904.

[38] Guignard, O. *Simulation numérique de l'écoulement incompressible autour d'une paroi perméable*. Travail pratique de 4ième année: EPFL-DGM, 1996.

[39] Guignard, O. *Etude de l'évacuation de l'écoulement engendré par un véhicule à haute vitesse dans un tunnel.* Projet de diplôme. EPFL-DGM, 1997.

[40] Hammitt, A.G. *The Aerodynamics of High Speed Ground Transportation.* Hollywood: Western Periodicals Company, 1973.

[41] Hamitt, A.G. "Aerodynamic Analysis of Tube Vehicle Systems" in *AIAA Journal* **10** (3), 1972.

[42] Harwath, F. *Instationäre Strömungsvorgänge bei Zugfahrten im Tunnel.* Dissertation. Wien: TU, 1974.

[43] Henson, D.A. *Pressure transients in tunnels.* Ph.D. thesis. Leeds, UK: University, 1969.

[44] Henson. D.A., W.M.S. Bradbury. "The aerodynamics of the Channel tunnel trains" in *Proc. 7th Intl. Symp. on Aerodynamics and Ventilation of Vehicle Tunnels* (Brighton, UK: 27-29 Nov 1991). Essex: Elsevier Publishers Ltd., 1991: 927-956.

[45] Jufer, M. *Zusammenfassung der Vorstudie.* Lausanne: EPFL - Swissmetro, 1993.

[46] Matsuo, K., T. Aoki, H. Kashimura [a.o.] "Attenuation of compression waves in a high-speed railway tunnel simulator" in *Proc. 7th Intl. Symp. on Aerodynamics and Ventilation of Vehicle Tunnels* (Brighton, UK: 27-29 Nov 1991). Essex: Elsevier Publishers Ltd., 1991: 239-252.

[47] Murray, S.J. "Transient analysis of partially full pipe flow" in *Proceedings of the International Conference on Unsteady Flow and Fluid Transients,* (Durham, UK: 29 Sep - 01 Oct 1992). Amsterdam: Balkema, 1992: 143-157.

[48] Nayak, U.S.L., Z.A. Gralewski and S.J. Stevens. "The Aerodynamic drag of tube vehicles travelling at low subsonic speeds" in *Proc. 2nd Intl. Symp. on Aerodynamics and Ventilation of Vehicle Tunnels* (Cambridge, UK: 23-25 Mar 1976). Cranfield [a.o.]: BHRA Fluid Engineering, 1976: paper E1.

[49] Ottitsch F., H. Sockel and A. Peiffer. "The influence of aprupt changes in the cross-sectinal area of a railway tunnel on the propagation of pressure waves caused by passing trains" in *Proc. 8th Intl. Symp. on Aerodynamics and Ventilation of Vehicle Tunnels* (Liverpool, UK: 6-8 Jul 1994). BHR Group Conference Series. Bury St. Edmonds, London: Mech. Eng. Publications Ltd., 1994: 135-149.

[50] Ottitsch, F. *Schwache mehrdimensionale Druckwellen in Rohrleitungen zufolge unstetiger Querschnittsveränderungen am Beispiel der Eisenbahnaerodynamik.* Dissertation. Wien: TU, 1995.

[51] Ozawa, S. a.o. "Reduction of micro-pressure wave radiated from tunnel exit by hood at tunnel entrance" in *Quart. Rep. of RTRI*, JNR, **19**, 1978: 2.

[52] Peiffer, A., F. Ottitsch, H. Sockel. "Experimental and theoretical investigation of two- and threedimensional pressure waves propagating inside a tunnel due to a train passage" in *Proc. 8th Intl. Symp. on Aerodynamics and Ventilation of Vehicle Tunnels* (Liverpool, UK: 6-8 Jul 1994). BHR Group Conference Series. Bury St. Edmonds, London: Mech. Eng. Publications Ltd., 1994: 151-173.

[53] Pope, C.W. and W.A. Woods. "The prediction of thermal effects in railway tunnels" in *Proc. 5th Intl. Symp. on Aerodynamics and Ventilation of Vehicle Tunnels*. (Lille, France: 20-22 Mai 1985). Cranfield, UK: BHRA Fluid Engineering, 1985: paper E3.

[54] Pope, C.W. "The simulation of flows in railway tunnel using a 1/25th scale moving model facility" in *Proc. 7th Intl. Symp. on Aerodynamics and Ventilation of Vehicle Tunnels* (Brighton, UK: 27-29 Nov 1991). Essex: Elsevier Publishers Ltd., 1991: 709-737.

[55] Prud'homme, O. *Etude de l'écoulement autour du nez d'un train a grande vitesse dans un tunnel sous vide partiel.* Travail de diplôme. Lausanne: EPFL-DGM-IMHEF, 1994.

[56] Schultz, M. and H. Sockel. "The influence of unsteady friction on the propagation of pressure waves in tunnels" in *Proc. 6th Intl. Symp. on Aerodynamics and Ventilation of Vehicle Tunnels*. (Durham, UK: 27-29 Sep 1988). Cranfield, UK: BHRA Fluid Engineering, 1988: 123-135.

[57] Schultz, M. and H. Sockel. "Pressure transients in short tunnels" in *Proc. 7th Intl. Symp. on Aerodynamics and Ventilation of Vehicle Tunnels* (Brighton, UK: 27-29 Nov 1991). Essex: Elsevier Publishers Ltd., 1991: 221-237.

[58] Sockel, H. *The tunnel entrance problem.* VKI Lecture Series on High speed ground vehicles. Bruxelles: VKI, 1972.

[59] Sockel, H. and F. Harwarth. "Unsteady flow due to trains passing a tunnel." in *Proc. 3rd Intl. Symp. on Aerodynamics and Ventilation of Vehicle Tunnels*. (Sheffield, UK: 19-21 Mar 1979). Cranfield, UK: BHRA Fluid Engineering, 1979: 151-160.

[60] Sockel, H. und F. Ottitsch. *PC-Rechenprogramm für die aerodynamische Berechnung der Durchfahrt mehrerer Züge durch einen Tunnel.* Wien: TU, 1992.

[61] Steinrück, P. *Ein Verfahren zur Berechnung instationärer Strömungsvorgänge bei Fahrten von mehreren Zügen durch Tunnels mit und ohne Portalvorbauten.* Dissertation. TU-Wien: Fakultät für Maschinenbau, 1984.

[62] Strom, C.R. "Aerodynamic analysis of vehicles in tunnels" in *Proc. 1st Intl. Symp. on Aerodynamics and Ventilation of Vehicle Tunnels* (Canterbury, UK: 10-12 Apr 1973). Cranfield: BHRA Fluid Engineering, 1973, paper C2.

[63] Swissmetro SA. *Etude principale 1994-1998 - Financement.* Swissmetro report SMS 1.0002/1.0000 a. Genève: Swissmetro SA, 1996.

[64] Tollmien, W. "Luftwiderstand und Druckverlauf bei der Fahrt von Zügen in einem Tunnel" in *Zeitschrift des Vereins dt. Ingenieure*. Bd. **71** (6), 1927: 199-203.

[65] Triebstein, H. "Transient pressure measurements at the top of the engine 103 during the passage through the Heitersberg tunnel" in *Proc. 3rd Intl. Symp. on Aerodynamics and Ventilation of Vehicle Tunnels* (Sheffield, UK: 19-21 Mar 1979). Cranfield [a.o.]: BHRA Fluid Engineering, 1973: paper G3.

[66] Vardy, A. "On the use of the method of characteristics for the solution of unsteady flows in networks" in *Proc. 2nd Intl. Conf. on pressure surges* (London, UK, Sept 22-24 1976) Cranfield, UK: BHRA Fluid Engineering, 1976: 15-30.

[67] Vardy, A. "Unsteady flows: fact and friction" in *Proc. 3rd Intl. Conf. on Pressure Surges* (Canterbury, England: 25-27 Mar 1980). Cranfield, UK: BHRA Fluid Engineering, 1980: 15-26.

[68] Vardy, A. "Unsteady Airflows in rapid transit systems" in *Proc. Instn. Mech. Engrs.* Vol. **194** (32), 1980: 341-356.

[69] Vardy, A. and K. Hwang. "A characteristic model of transient friction in pipes" in J. of Hydraulic Research **29**, 1991: 669-684.

[70] Vardy, A. and Zhiqiu Pan. "Quasi-steady friction in transient polytropic flow" in *Computers & Fluids* **26** (8), 1997: 793-809.

[71] Vardy, A. personal conversation on 27 Apr 1998 and various other occasions.

[72] Vardy, A. and Zhiqiu Pan. "Interpolation in transient polytropic flow" in *Computers & Fluids* (to appear).

[73] Waclawiczek, M. *Druckschwankungen und aerodynamische Leistung bei Zugfahrten im eingleisigen Tunnel mit maximal zwei Luftschächten.* Dissertation. Wien: TU, 1984.

[74] Wolf, W.B. de and E. Demmenie. "A new test facility for the study of interacting pressure waves and their reduction for high-speed trains" in *Proc. 9th Intl. Symp. on Aerodynamics and Ventilation of Vehicle Tunnels* (Aosta, Italy: 6-8 Oct 1997). BHR Group Conference Series. Bury St. Edmonds, London: Mech. Eng. Publications Ltd., 1997: 301-318.

[75] Woods, W.A. and R.G. Gawthorpe. "The train and tunnel - a large scale unsteady flow machine" in *Proc. 2nd Intl. JSME Symp. on Fluid Machinery.* 1972.

[76] Woods, W.A. and C.W. Pope. "Wave action associated with a train entering a tunnel" in *Proc. 1st Intl. Symp. on Aerodynamics and Ventilation of Vehicle Tunnels* (Canterbury, UK: 10-12 Apr 1973). Cranfield: BHRA Fluid Engineering, 1973, paper G4.

[77] Woods, W.A. and C.W. Pope. "On the range of validity of simplified one dimensional theories for calculating unsteady flows in railway tunnels" in *Proc. 3rd Intl. Conf. on Aerodynamics and Ventilation of Vehicle Tunnels* (Sheffield, UK: 19-21 Mar 1979). Cranfield, UK: BHRA Fluid Engineering, 1979: 115-150.

[78] Wylie, E.B. "Unsteady internal flows - dimensionless numbers & time constants" in *Proc. 7th Intl. Conf. on Pressure Surges and Fluid Transients* (Harrogate, UK: 16-18 Apr 1996). Cranfield, UK: BHRA Fluid Engineering, 1996: 283 - 288.

General texts on railway technology

[79] Uden, Marco von. *The european railway server.* Internet address: "http://mercurio.iet.unipi.it/". last updated: 27 Oct 1997.

[80] Hartung, Karlheinz. *1835-1985 Daten und Fakten aus 150 Jahren Eisenbahngeschichte.* Düsseldorf: Alba, 1985.

Technical reports and publications on NUMSTA by the author

[81] Rudolf, A. *Numerical simulation of fluid flow through a system of tunnel induced by trains traveling at high speed.* Swissmetro report EPFL 1.0012 / 1.6210/a. Lausanne: EPFL, 1995.

[82] Rudolf, A. *Proposal for a shock tube for the experimental examination of the tunnel aerodynamics of the Swissmetro train.* Swissmetro report EPFL 1.0015/1.6210/a. Lausanne: EPFL, 1995.

[83] Rudolf, A. *The TurboSwissmetro - an alternative concept.* Swissmetro report EPFL 1.0019/1.6210/a. Lausanne: EPFL, 1995.

[84] Rudolf, A. *Tunnel Aerodynamics of the Swissmetro.* Swissmetro report EPFL 1.0032/ 1.6210/a. Lausanne: EPFL, 1995.

[85] Rudolf, A. *Aerodynamic drag of a vehicle in a tunnel.* Swissmetro report EPFL 1.0034/ 1.6210/a. Lausanne: EPFL, 1995.

[86] Rudolf, A. *Vehicle movement in a tunnel II.* Swissmetro report EPFL 1.0043 / 1.6210/a. Lausanne: EPFL, 1996.

[87] Rudolf, A., F. Losi, M. Mossi. *Comparison of Results obtained with the code by Losi and with NUMSTA.* Swissmetro report EPFL 1.0029 / 1.6210/a. Lausanne: EPFL, 1996.

[88] Rudolf, A. *Comparison of systems for active and passive flow bypassing.* Travail de Diplôme d'Etudes Approfondies. Lyon, Lausanne: ECL, EPFL, 1996.

[89] Rudolf, A. *Repressurization in case of emergency.* Swissmetro report EPFL 1.0050 / 1.6210/b. Lausanne: EPFL, 1996.

[90] Rudolf, A. *Pressure, temperature and air velocity ranges for the Swissmetro.* Swissmetro report EPFL 1.0063 / 1.6210/b. Lausanne: EPFL, 1996.

[91] Rudolf, A. *Numerical simulation of fluid flow through a system of tunnel induced by trains traveling at high speed.* Swissmetro report EPFL 1.0012 / 1.6210/d. Lausanne: EPFL, 1997.

[92] Rudolf, A. *Aerodynamic reference values for the Swissmetro system.* Swissmetro report EPFL 1.0087 / 1.6210/a. Lausanne: EPFL, 1997.

[93] Rudolf, A. "Compressible flow phenomena in the Swissmetro tunnel network" in *Proc. 9th Intl. Symp. on Aerodynamics and Ventilation of Vehicle Tunnels* (Aosta, Italy: 6-8 Oct 1997). BHR Group Conference Series. Bury St. Edmonds, London: Mech. Eng. Publications Ltd., 1997: 263-288.

CURRICULUM VITAE

14 / 03 / 1968	birth in Hof / Saale (Germany), son of Gertraud Rudolf (nurse) and Herbert Rudolf (University Assistant)
1974 - 1978	primary school in Alfter next to Bonn
1978 - 1987	high school 'Helmholtz - Gymnasium', Bonn-Duisdorf
10 / 87 - 12 / 88	compulsory military service as morse code radio receiver in Daun, Eifel
10 / 88 - 3 / 94	studies in theoretical mechanical engineering at the 'Universität (TH) Karlsruhe' during that time: • teaching assistant at several institutes • internships at Wolfferts GmbH&Co KG, Bosch GmbH and BMW AG • 5 / 93 - 12/93 stay for studies at the University of Massachusetts at Amherst, USA • majors are thermodynamics and fluid dynamics
1990 - 1995	scholarshipholder of the Friedrich-Naumann Foundation
since 05 / 94	intern, assistant and then Ph.D. student at the 'Institut de Machines Hydrauliques et de Mécanique des Fluides' (IMHEF) at the Swiss Federal Institute of Technology in Lausanne (EPFL) collaboration at the project Swissmetro
10 / 95 - 09 / 96	'DEA' of the 'Ecole Centrale de Lyon (ECL)' and 'certificat de 3^e cycle en dynamique des fluides' of the EPFL
10 / 05 / 1997	marriage with Christina Wai Ying Chang

A1 3D FLOW ACROSS THE PERFORATED WALLS

2D and 3D numerical studies for the flow across the perforated walls in proximity of the vehicle have been performed for Swissmetro in the frame of a semester project [38] and a diploma work [39]. 1D results obtained with NUMSTA have been used to define the boundary conditions for the local multidimensional studies whose results have then been used to refine the 1D model.

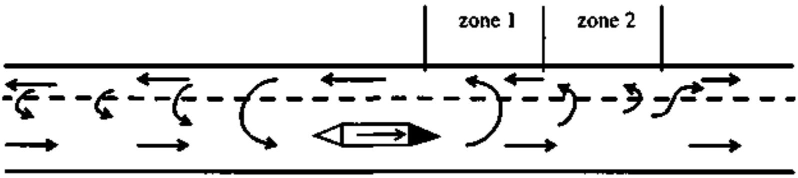

Figure A1.1 Intended flow pattern in proximity of a train in presence of a perforated wall in the upper part of the tunnel

In absence of the influence of boundary conditions, zones with characteristic flow patterns can be identified. These zones move with the vehicle (see Figure A1.1). Local 3D studies for zone 1 and zone 2 have been performed for steady state across a perforated wall with streamlined openings and some sample results are discussed in the sequel with the aim to explain the choice of the 1D model for the perforated walls.

Figure A1.2 shows the flow velocities (grey scale) and the streamlines for the flow across a perforated wall in zone 1, close to the vehicle. In the upstream opening flow enters and leaves quasi perpendicular to the main flow direction and in the downstream opening, the flow follows better the advantageous shape of the streamlined opening. Recirculation zones establish behind and in the concave part of both openings. The numerical model neglects the flow across the upstream part of the opening.

The streamlines across the perforated wall situated in zone 2 are displayed in Figure A1.3. They show a similar pattern except that the inlet and outlet angle are quite different. The inlet angle of the flow in the main tunnel follows well the shape of the openings whereas the outlet angle for the flow in the side gallery is much flatter than in Figure A1.2. The cross-flow in zone 2 is much slower than in zone 1 and the change of the flow direction is therefore easier.

The two examples are given to assess the fit of the 1D model for the perforated walls on the numerically simulated 3D flow patterns. It can be concluded that in the zone close to the vehicle, the flow follows relatively well the form of the openings. In the zones further away from the vehicle, the flow deviates from this idealized assumption. However, since the perforated walls act more importantly in proximity of the vehicle and their action is reduced far away from the vehicle, the chosen 1D model displays the 3D flow patterns in a first approximation.

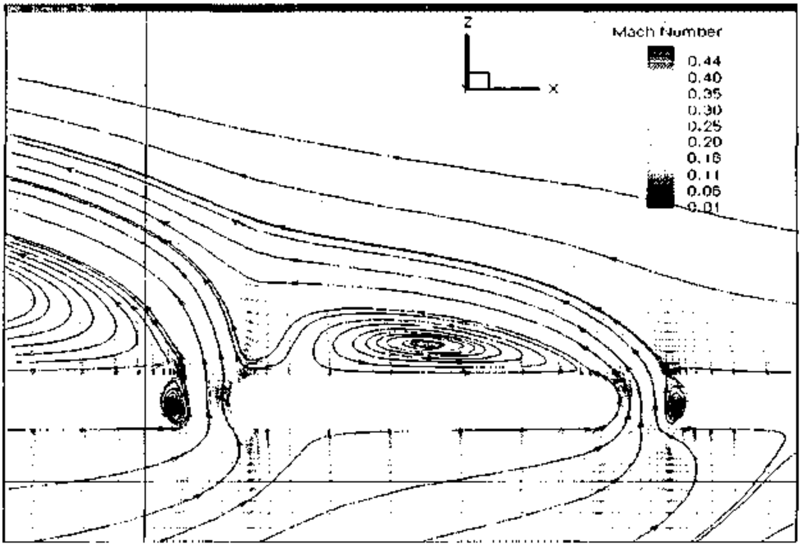

Figure A1.2 Flow velocities and streamlines close to the vehicle (zone 1) in a vertical cut across a tunnel with a horizontal perforated wall in the upper part

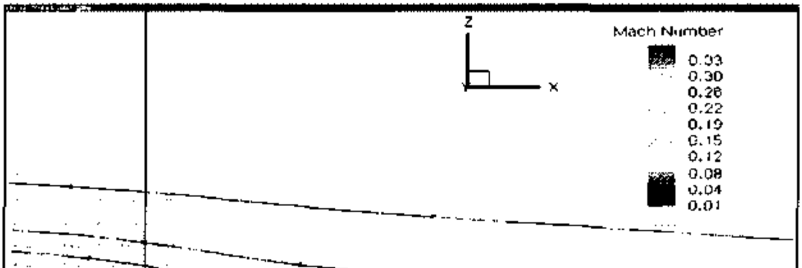

Figure A1.3 Flow velocities and streamlines further away from the vehicle (zone 2) in a vertical cut across a tunnel with a horizontal perforated wall in the upper part

A2 VALIDATION OF THE DYNAMICAL MESH GENERATOR

The mesh generator can be validated by showing that it performs standard and complex operations on the array of flow values and the according pointer arrays correctly. The results of the action of this tool is demonstrated for the following situations with increasing complexity:

- mesh generation for a tunnel with only one part
- mesh generation for a tunnel with several parts of different cross-sectional area
- inclusion of the refinement zones needed by the cross-vents
- inclusion of the refinement zones of a vehicle
- movement of this vehicle in a zone of coarse mesh points
- movement of a vehicle across a steady refinement zone
- interaction of several vehicles
- interaction of several vehicles and steady refinement zones.

The mesh generator has to ensure in all situations:

- the correct position of the mesh points according to the minimum refinement width around all geometrical discontinuities,
- the correct modification of the information concerning the cross-sectional area and
- the correct modification of the information in the pointer arrays.

In the validation the following parameter configuration will be used.

Table A2.1 Parameters used for the validation

symbol	explanation	values
l_t	length of tunnel	400 m
n_p	number of tunnel parts (initially)	1, 2
n_v	number of vehicles	1, 2
lv	length of vehicles	20 m
sp	speed of vehicles	100, -100 m/s
dx_{tu}	coarse grid spacing	10 m
dt_{tu}	coarse time step	0.01 s
dx_f	fine grid spacing	1 m
dt_f	fine time step	0.001s
n_f	refinement thickness in Δx_f	5

The mesh generator updates information about flow values and refinement zones in arrays. The usage of these arrays is explained here in order to enable the reader to follow the subsequent validation. The mesh, the flow values and the geometry information are stored in the array uT(k,j,i). The actual position of coarse and fine zones and the corresponding pointers are stored in the array tunp(k,ip,i). The array vehs(k,iv) stores the pointers to the current positions of the vehicles.

The indices of the array uT(k,j,i) and their ranges are defined as:

k [0:9] :: index for flow and geometry values according to Table A2.2.

j [0:n] :: index for mesh point,
where the total number of points *n* is typically between 1000 and 10000

i [1:10] :: index for tunnel nr.

Table A2.2 Usage of the values with the *k*-index in the uT - array

k	symbol	explanation
0	x	x - position
1	ρ	1st conservative variable
2	ρu	2nd conservative variable
3	$\rho u e_t$	3rd conservative variable
4	$A(x,t)$	actual cross-section with vehicles
5	$P(x,t)$	actual perimeter with vehicles
6	$A(x)$	tunnel cross-section without vehicles
7	$P(x)$	tunnel perimeter without vehicles

The indices of the array tunp(k,ip,i) and their ranges are defined as:

k [1:5] :: index for value according to Table A2.3

ip [0:100] :: index for tunnel part

i [1:10] :: index for tunnel number

Table A2.3 Usage of the values with the *k*-index in the tunp - array

k	symbol	explanation
1	x_s	start x - position
2	x_e	end x - position
3	j_s	start j - index
4	j_e	end j - index
5	Δt	time step in zone [js,je]

The indices of the array vehs(k,iv) and their ranges are defined as:

k [1:9] :: index for value according to Table A2.4

iv [1:10] :: vehicle number

Table A2.4 Usage of the values with the k-index in the vehs - array

k	symbol	explanation
1	vit	vehicle in tunnel nr. vit
2	x_t	x-position of tail
3	x_n	x-position of nose
4	j_4	j-index of point 4
5	j_3	j-index of point 3
6	j_2	j-index of point 2
7	j_1	j-index of point 1
8	sp	actual speed
9	npv	number of refinement parts (1/2)

The validation is based on the computation of different configurations without physical solution for the flow field. Concentration is on the demonstration that the values in the arrays uT, tunp and vehs are altered correctly.

In the first graphs, the array indices of the mesh points are plotted over their physical coordinates. The slope of the dotted line corresponds to the point density.

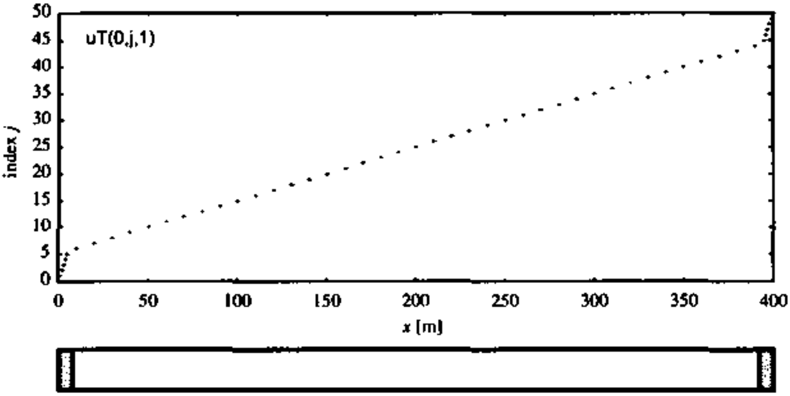

Figure A2.1 Mesh of a tunnel with steady refinement zones at the ends

The simplest configuration is a tunnel only. Figure A2.1 shows the high density of points at both ends and the constant mesh spacing in the center. The next step is to add a refinement zone in the middle of the tunnel where a diameter change has been imposed. Figure A2.2 shows the 3 refinement zones and 2 zones with coarse mesh spacing.

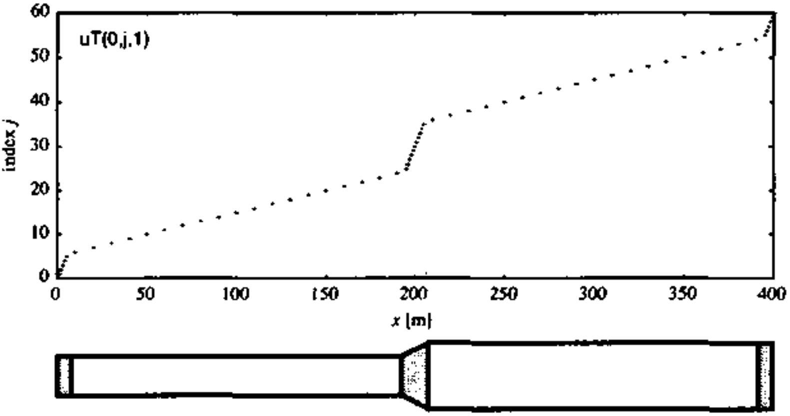

Figure A2.2 Mesh of a tunnel with diameter variation in its center

A very similar graph results if the refinement zone in the center is formed by a vehicle. However, this time, the refinement zone being unsteady, can move and the distribution of the fine mesh points changes. Figure A2.3 shows this effect by plotting the index number over the position at two different times.

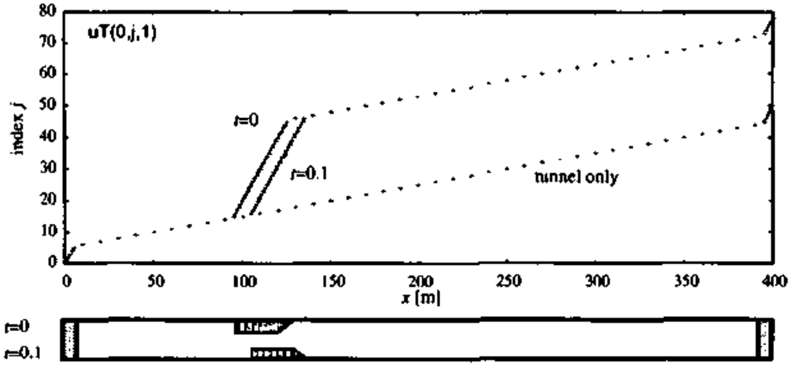

Figure A2.3 Mesh of a tunnel with one vehicle (shown at t=0 and after 10 time steps)

This situation has been made more complex by including 2 vehicles in a tunnel with a diameter change. This results in the appearance of 2 unsteady refinement zones and 3 steady refinement zones. Figure A2.4 shows this result.

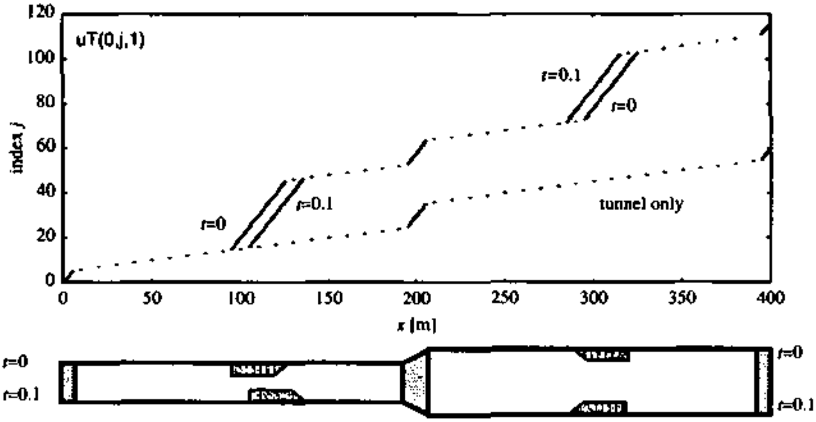

Figure A2.4 Mesh of a tunnel with diameter variation and two vehicles moving in opposite direction (shown at t=0 and after 10 time steps)

The presentation for the following graphs has been changed. They show the physical coordinates of the mesh points at different times. Refined zones can be distinguished by the increased point density along the horizontal line.

Figure A2.5 shows the movement of a vehicle across the steady refinement zone in the center over 200 time steps. The experiment performed here included melting of an unsteady with a steady refinement zone and the subsequent splitting of the mixed refinement zone behind the vehicle after it had produced enough coarse mesh distances to form an independent coarse zone.

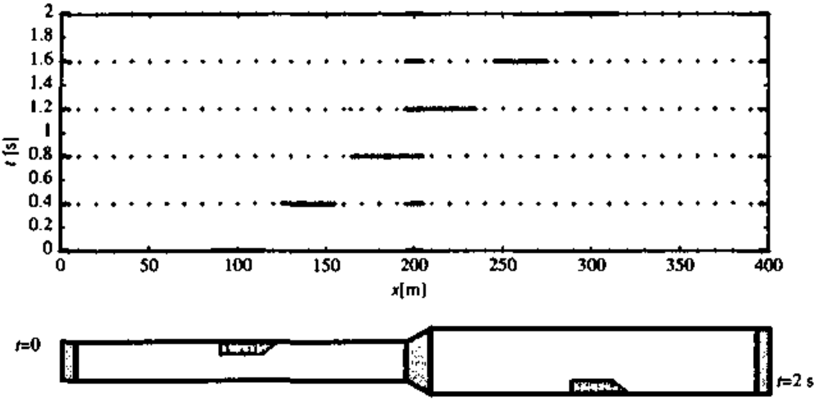

Figure A2.5 Tunnel with diameter variation and one vehicle crossing the steady refinement zone (shown at t=0 and every 40 time steps, final position at t=2 s)

The experiment in Figure A2.6 shows the melting of 2 unsteady refinement zones. Two vehicles in a symmetric configuration pass each other, the refinement zones melt and separate again.

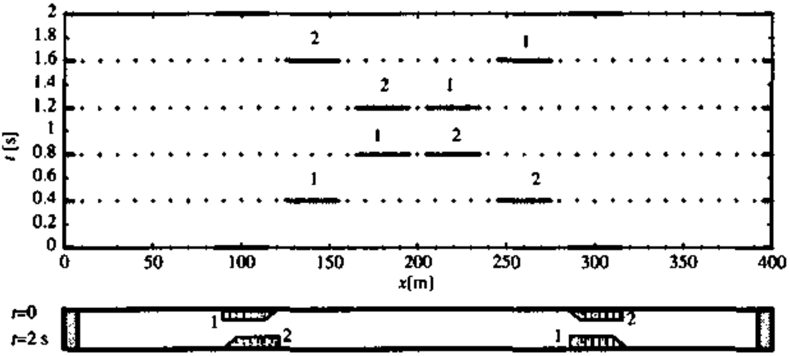

Figure A2.6 Tunnel with two vehicles crossing (shown at t=0 and every 40 time steps, final position at t=2 s)

All the effects explained so far are combined in the next experiment: 2 vehicles meet at the position of a steady refinement zone, melt with it and leave it behind after having left the big refinement zone (see Figure A2.7).

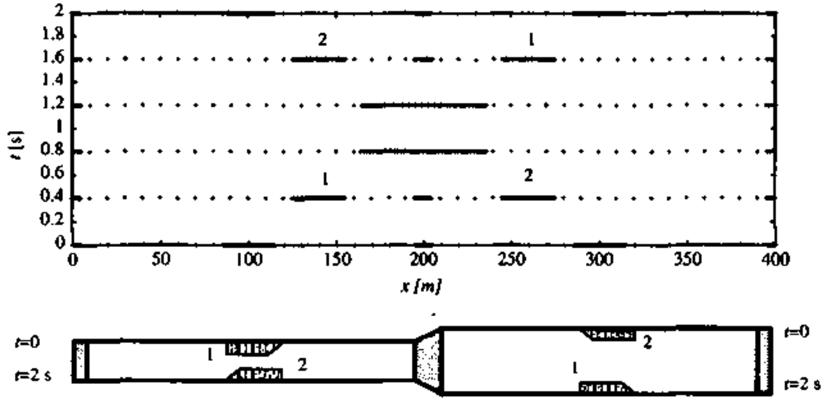

Figure A2.7 Tunnel with diameter variation and two vehicles moving in opposite direction crossing the steady refinement zone (shown at t=0 and each 40 time steps, final position at t=2s)

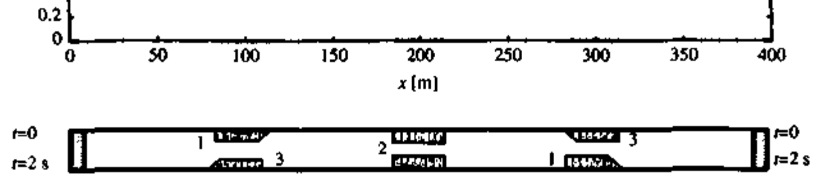

Figure A2.8 Tunnel with three vehicles, among which one is remaining at its initial position where the others cross (shown at t=0 and each 40 time steps, final position at t=2 s)

A very similar experiment is the case where the steady refinement zone in Figure A2.7 is replaced by a vehicle which remains at its initial position. Two more vehicles cross each other at the position of the standing vehicle. Thus, the mesh generator can treat the melting and the correct splitting of 3 unsteady refinement zones.

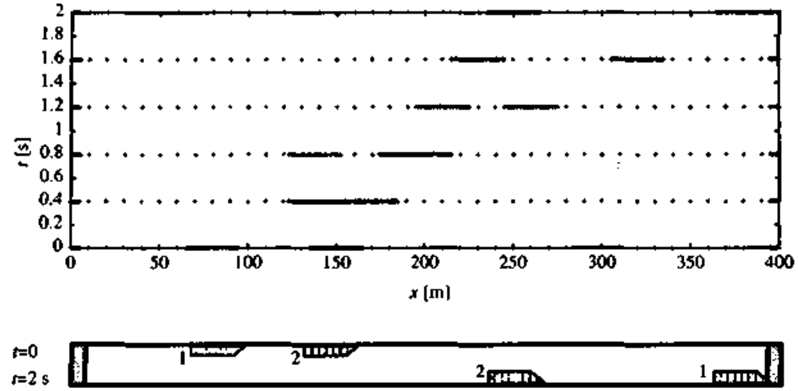

Figure A2.9 Tunnel with two vehicles cruising at different speed from left to right; vehicle 1 passes vehicle 2 (shown at t=0 and each 40 time steps, final position at t=2 s)

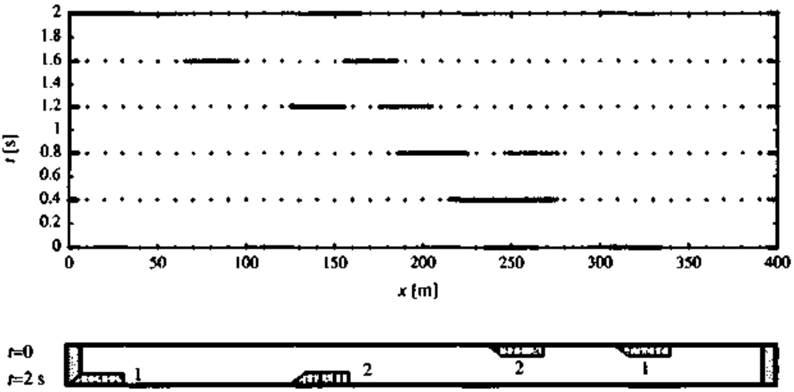

Figure A2.10 Tunnel with two vehicles cruising at different speed from right to left; vehicle 1 passes vehicle 2 (shown at t=0 and each 40 time steps, final position at t=2 s)

Vehicles may overtake each other if they have different speeds. This case is demonstrated for positive and negative speed in Figure A2.9 and Figure A2.10. During the process of overtaking (at t=0.8 s), the mesh spacing in the tunnel part with the two vehicles is not completely regular. This is solved when the faster vehicle, vehicle 1, is ahead of vehicle 2. At the end of the simulation time, the integrity of the refinement zones is reestablished and the zone between the two vehicles is again large enough to be treated as an independent tunnel part with large time step.

This series of graphs shall be concluded with a graph demonstrating the capability of the dynamic mesh generator to deal with very complex situations. Figure A2.11 shows that the coherence of steady and unsteady refinement zones is kept even if vehicles meet in an arbitrarily chosen situation. Here, two vehicles, vehicle 1 and 2, move to the right and vehicle 3 moves opposite. Vehicle 1 is faster than nr. 2 and overtakes it. During this process (t=0.4 s, 0.8 s), vehicle 3 joins vehicles 1 and 2 at the position of the steady refinement zone. At later times (t > 0.8 s), the separation of the 3 vehicles can be observed. This process regenerates again the initial steady refinement zone and zones with coarse mesh spacing.

As described above, the pointer arrays `tunp(k,ip,1)` and `vehs(k,iv)` account for the dynamic mesh modifications. As an example, they are displayed here for the complex case of two vehicles in a tunnel with one steady refinement zone (see Figure A2.7).

The contents of the array `tunp(k,ip,1)` is given in Table A2.5 and the array `vehs(k,iv)` is given in Table A2.6 with the values for both vehicles. The values are given at the end of the simulation for t=2 s after 200 time steps. Both tables show the expected values. The problem being symmetric, the final pointer values are expected to be the initial pointer values. This is the case. Even though the array values for intermediate time steps are not displayed here, the fact that Figure A2.11 shows clearly the process of melting the 3 refinement zones and the subsequent splitting as the vehicles dislodge and the observation that the final values of the pointers are correct allows to conclude that the arrays were set correctly during the entire simulation.

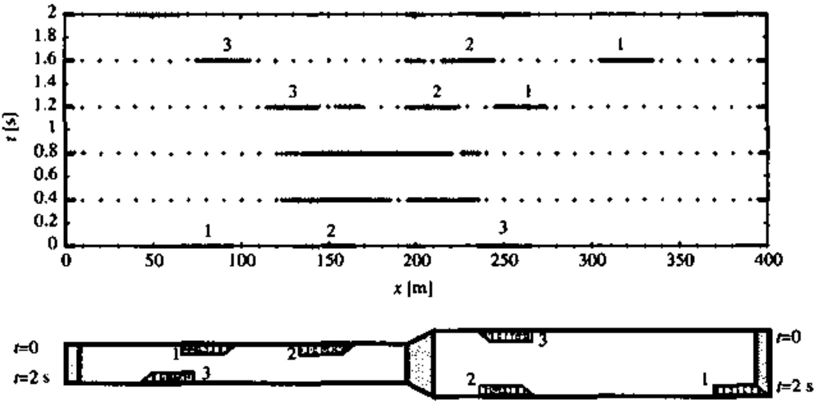

Figure A2.11 Tunnel with diameter variation and 3 vehicles moving with different speed and in different directions; vehicle 1 passes vehicle 2, vehicle 3 moves from right to left (shown at t=0 and each 100 time steps, final position at t=4 s)

Table A2.5 Values in the tunp(k,ip,1) - array for the case of 2 vehicles crossing a steady refinement zone (at t=2s)

	k				
ip	1	2	3	4	5
	np	*bcl*	*bcr*		
0	9.	1.	1.		
	xa	*xe*	*js*	*je*	*dt*
1	0.	20.	0	7	0.001
2	20.	70.	7	12	0.010
3	70.	130.	12	46	0.001
4	130.	180.	46	51	0.010
5	180.	240.	51	85	0.001
6	240.	270.	85	88	0.010
7	270.	330.	88	122	0.001
8	330.	380.	122	127	0.010
9	380.	400.	127	134	0.001

Table A2.6 Values in the vehs(k,iv) - array for the case of 2 vehicles crossing a steady refinement zone (at t=2s)

iv	*vit*	*xd*	*xa*	*j4*	*j3*	*j2*	*j1*	*spd*	*npv*
1	1	290.	310.	90	120	0	0	100.	1
2	1	90.	110.	14	44	0	0	-100.	1

A3 THE UTILIZATION OF NUMSTA

This chapter gives practical information about the use of NUMSTA by explaining the flow diagram, the input and output files. As a side effect, this manual gives an idea of the multitude of parameters which can be chosen at run-time by the user and serves for a base of discussion.

A3.1 The flow diagram

NUMSTA has been developed with a dynamic mesh generation tool (see section 4) which enables the user in a preprocessing step to define the computational mesh and the pointer files on the basis of the input files as indicated in the right upper corner of Figure A3.1. However, the user can also give computational meshes and pointer files from NUMSTA to the program and continue previous calculations as sketched in the left upper corner. Given the time constraints per job on modern mainframes, this feature makes high simulation times possible.

The separation of the computational domain into fine and coarse zones allows to apply different time steps, small and big. It is characteristic for NUMSTA to perform the time integration with two different time steps, the computation being synchronized by the big time step. The flow chart displays that feature by an outer loop for a big time step in *TI* and an inner loop with a small time step in *ti*.

The outer loop solves for the coarse zones and imposes the boundary conditions if the tunnel ends are coarse zones. In the inner loop, the numerical scheme as explained in subsections 3.3.4 and 3.3.6 is applied. This means, that first all the source terms due to the vehicle movement are computed: the change of the cell width, the change of the area function and the power due to the change of the area function. These source terms are immediately added to the array of flow values yielding the flow values at the intermediate time level *n*1 as discussed in subsection 3.3.4. The additional source terms are evaluated based on that intermediate time level and are stored. Then, the source terms due to the perforated walls are added to the array and the Roe flow solver is applied on all refined zones. The values at the time level *ti* at the transition positions between coarse and refined zones are found using a 2nd order scheme on the basis of the previously saves values at time *TI*. The boundary conditions at the tunnel ends are set if the ends are refined zones.

At the end of a series of fine time steps, the mesh is checked if the refined zones have to redefined. This is the case if at the ends of each refined zone there is less than two or more than three coarse mesh points. If refined zones approach each other so that the coarse zone inbetween has less than 4 mesh points the three zones melt to one. Inversely, if a 'hole' of 8 coarse mesh points is built within a refined zone the refined zone is split into three zones. The pointer arrays are corrected accordingly. The flow values are saved in defined intervals.

The code's structure is modular, allowing for an independent computation of additional source terms for different system parts. Additional source terms are added to the conservative variables at the corresponding space positions. The superposition of effects of separate parts, e.g. friction of multiple vehicles at one space position, is thus possible. The modular structure of the code allows to adapt physical models for single system parts to new requirements or to implement new models easily.

The input files allow the user to define a multitude of parameters at run-time. The input files contain general and individual data for a specific system part. General data contains general information for a particular system part (e.g. number of cross-vents) whereas specific data describes the characteristics of an individual of a system part (e.g. length of cross-vent nr. 4).

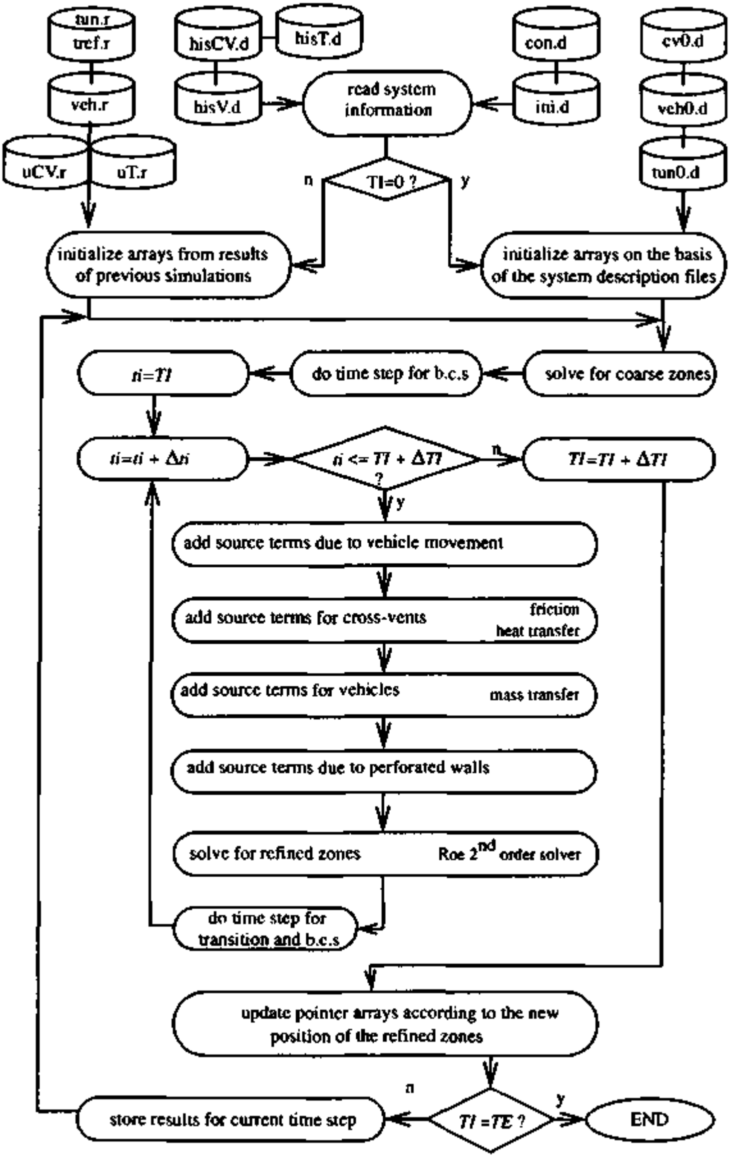

Figure A3.1 Flow diagram for NUMSTA

Results are stored in data files with a well defined data sequence. Those files can be used for input into NUMSTA. This allows to continue previously interrupted calculations or to perform simulations with meshes generated externally.

Graphical visualization of the results is possible during execution or in a postprocessing step with external graphics packages.

A3.2 The input files

The input files are read in the beginning of the simulation and are available during program execution to all subroutines via arrays defined in COMMON blocks.

If a new simulation is started, the configuration is defined via initial system description files containing the characteristics of the tunnels ('tun0.d'), the vehicles ('veh0.d') and the cross-vents ('cv0.d'). Program control parameters are stored in 'control.d' and initialization information is given in 'ini.d'. Other input files contain information about history points which are to be stored during program execution, i.e. 'hisT.d' contains information about the tunnel points to be stored, 'hisV.d' contains history points of the vehicles and 'hisCV.d' contains information about the history points in the cross-vents.

If a previously performed calculation is to be continued, its final results are used for input. This requires that all actual system description files are available with the final values e.g. for the vehicle positions or the definition of the refinement zones. For continuation of an old calculation, the following files are required: 'tun.r', 'tref.r', 'veh.r', 'uT.r', 'uCV.r' (if applicable) and all of the initial system description files (see above).

Comment lines explain the data. They are indicated with the character 'C' (like in FORTRAN 77). The input subroutines ignores these lines.

A3.2.1 The file 'ini.d'

The file 'ini.d' contains the initial flow values in the tunnel network. The values are again given sequentially with the format:

`C p0 [Pa]` `10000.`	initial pressure, ($p_0 < 0$: individually varying pressure in each tunnel)
`C u0 [m/s]` `0.`	initial air velocity
`C T0 [K]` `288.`	initial temperature
`C pa [Pa]` `100000.`	ambient pressure
`C Ta [K]` `288.`	ambient temperature
`C u forcing [m/s]` `0.`	forcing air velocity
`C p final [Pa]` `60000.`	final pressure level for repressurization

A3.2.2 The file 'control.d'

The file 'control.d' contains important control parameters for the program execution. The values are given sequentially with the following format:

'control.d'	explanation
`C dxtu` `10.`	coarse mesh width
`C dttu` `0.01`	coarse time step
`C dxf` `1.`	fine mesh width
`C dtf` `0.001`	fine time step
`C ts` `0.`	start time (*ts* > 0: continuation of previous calculation)
`C te` `10.`	end time
`C nf_dis` `10.`	number of refinement points around geometrical discontinuity
`C nf_cv` `5.`	number of refinement points around cross-vent inlet
`C nit for porous walls` `2.`	number of intermediate time steps for porous walls
`C entirely refined grid(0/1)` `0.`	mesh generation with entirely refined grid

A3.2.3 The file 'tun0.d'

The file 'tun0.d' describes the properties of the tunnels involved in the simulation. It has the following format:

```
C...1....2....3....4....5....6....7....8....9...10...11...12
C information for all tunnels
C   n dtst dtsH dtsQ
   2.   1.  0.1  0.1
C
C tunnel nr. 1
C general data
C np0  bcl  bcr   cl   cr    f   q C/ks  Twt   p0   u0   T0
   2.   1.   1.   0.   0.    0   0 0.005 288.1000.   0. 288.
C data for parts
C  xs   xe    A    P  gal  gam   al
C tp11
   0.1000.  10.  11.   0.   0.   0.
C tp12
 1000.2000.  20.  25.   0.   0.   0.
C
C tunnel nr. 2
C general data
C np0  bcl  bcr   cl   cr   Cf   q C/ks  Twt   p0   u0   T0
   1.   1.   1.   0.   0.    0   0 0.005 288.1000.   0. 288.
C data for parts
C  xs   xe    A    P  gal  gam   al
C tp21
   0.2000.  10.  11.   0.   0.   0.
```

The first line of valid data refers to all tunnels, i.e.

n	number of tunnels
dtst	interval for saving the complete distribution of all flow values in all tunnels
dtsH	storage interval for tunnel history points
dtsQ	storage interval for the actual heat transfer situation

Now, the input subroutine expects information for n tunnels. Data describing general data for the first tunnel are in the second valid line, i.e.

np0	initial number of tunnel parts
bcl	left handed boundary condition
bcr	right handed boundary condition
cl	connection left
cr	connection right
f	0: C_f=const.; 1: $C_f=f(Re,ks)$
q	0: heat transfer on; 1: heat transfer off

C/k_s	value for friction coefficient or equivalent sand grain roughness
T_{wtu}	tunnel wall temperature
p_0	initial pressure (applies only if $p_0<0$ in 'ini.d')
u_0	initial air velocity (applies only if $p_0<0$ in 'ini.d')
T_0	initial temperature (applies only if $p_0<0$ in 'ini.d')

After this line the input subroutine expects np0 lines with information for the tunnel parts of the actual tunnel, i.e.

x_s	starting x-value
x_e	end x-value
A	cross-section (if $A<0$ this tunnel part is considered open air)
P	perimeter
gal	0: no gallery; 1: with gallery
gam	porosity γ
al	deflection angle α

The input subroutine continues until information for all the tunnels and tunnel parts is loaded.

A3.2.4 The file 'hisT.d'

The file 'hisT.d' contains information about tunnel fixed points in which the history of flow values shall be recorded. History data files have the format

'hisT.d'	explanation
`C tunnel 1`	
`3`	number of history points for tunnel 1
`0. 1000. 2000.`	position of history points
`C tunnel 2`	
`3`	number of history points for tunnel 2
`0. 1000. 2000.`	position of history points

A3.2.5 The file 'veh0.d'

The file 'veh0.d' describes the initial properties of the vehicles involved in the simulation. It has the following format:

```
C  1    2   3    4  5   6   7   8   9   10    11    12  13  14   15
C information for all vehicles
C nv dtsv dtsF dtsH
  2.   1.  0.1  0.1
C vehicle nr. 1
C iv   xs   xe  sp  a  lv  Av  Pv  ll   lr  C/ks    Tw   p   f   q
   1   10  900  10  5 100   8  10   5   5. 0.005   288   1   0   0
C vehicle nr. 2
C iv   xs   xe  sp  a  lv  Av  Pv  ll   lr  C/ks   Twv   p   f   q
   1  900   10  10  5 100   8  10   5   5. 0.005   288   1   0   0
```

The first valid data line initializes some values common to all vehicles, i.e.

nv	number of vehicles
dtsv	interval for saving the complete distribution of all flow values around all vehicles
dtsF	interval for storing the forces on the vehicles
dtsH	storage interval for tunnel history points

Now, the input subroutine expects information for *nv* vehicles. Individual vehicles are characterized by the following data

iv	initial tunnel number of vehicle
x_s	start position of vehicle tail
x_e	final position of vehicle tail
sp	maximum speed
a	acceleration and deceleration
l_v	vehicle length
Av	maximum vehicle cross-section
Pv	maximum vehicle perimeter
l_l	length of left end
l_r	length of right end
C_f	vehicle friction coefficient
T_{wv}	vehicle wall temperature
p	separate discretization for left and right end
f	0: *Cf*=const.; 1: *Cf*=*f*(*Re*,*ks*)

q	0: no heat transfer considered; 1: heat transfer considered

A3.2.6 The file 'hisV.d'

The file 'hisV.d' contains information about vehicle fixed points in which the history of flow values shall be recorded. History data files have the format

'hisV.d'	explanation
`C vehicle 1`	
`4`	number of history points for vehicle 1
`-10. 10. 90. 110.`	position of history points
`C vehicle 2`	
`4`	number of history points for vehicle 2
`-10. 10. 90. 110.`	position of history points

A3.2.7 The file 'cv0.d'

The file 'cv0.d' contains initial information for the cross-vents with the format

```
C...1 ...2 ... 3....4 ...5....6 ...7 ... 8....9 ..10 .. 11...12
C information for all tunnels
C ncv dtscv dtsH  dis   xe    f    q   Tw   p0   T0   v0
    2     1  0.1    0    0    0    0  288 1000  288    0
C
C cross-vent nr. 1
C   x   lcv    A     P    dx C/ks   cl   ch   xh
  100    20 3.14  6.28   1. 0.006    1    2  100
C cross-vent nr. 2
C   x   lcv    A     P    dx C/ks   cl   ch   xh
 1900    20 3.14  6.28   1. 0.006    1    2 1900
```

The first valid data line initializes some values common to all cross-vents, i.e.

ncv	number of cross-vents
dtscv	interval for saving the complete distribution of all flow values in all cross-vents
dtsH	storage interval for tunnel history points
dis	distance of cross-vents
x_e	position of rightmost cross-vent (applies only if dis > 0)
f	0: C_f=const.; 1: $C_f=f(Re,ks)$
q	0: heat transfer off; 1: heat transfer on
T_w	wall temperature
p_0	initial pressure (applies only if $p_0<0$ in 'ini.d')

v_0	initial vertical air velocity (applies only if p_0<0 in 'ini.d')
T_0	initial temperature (applies only if p_0<0 in 'ini.d')

Now, the input subroutine expects information for ncv cross-vents. Individual cross-vents are characterized by the following data

x	position of the cross-vent
l_{cv}	length of the cross-vent
A	cross-section of the cross-vent
P	perimeter of the cross-vent
dx	spatial discretization in the cross-vent
C/k_s	friction coefficient or sand grain roughness
c_l	lower connection to tunnel nr.
c_h	upper connection to tunnel nr.
x_h	upper connection to position xh in tunnel number ch

A3.2.8 The file 'hisCV.d'

The file 'hisCV.d' contains information about cross-vent fixed points in which the history of flow values shall be recorded. History data files have the format

`'hisCV.d'`	explanation
`C cross-vent 1`	
`2`	number of history points for cross-vent 1
`2. 18`	position of history points
`C cross-vent 2`	
`2`	number of history points for cross-vent 2
`2. 18.`	position of history points

A3.3 The output files

The results obtained with NUMSTA are stored in actual system description files and in files containing history values in certain points.

The actual state of the system is described with the files 'tref.r', 'tun.r', 'veh.r', 'uT.r' and 'uCV.r' (if applicable). Given these files and the corresponding initial system description files, a previously interrupted computation can be continued.

Histories for flow values in certain tunnel fixed points are stored in the files with the names 'PT*ij*.r', where *i* indicates the tunnel number and *j* indicates the index of the history point. Histories for flow values in certain vehicle fixed points are given in the files with the names 'PV*ij*.r', where *i* indicates the vehicle number and *j* indicates the index of the history point. The forces on the vehicle are recorded in the file 'F*i*.r', where *i* indicates the number of the vehicle. There is an additional history file with the name 'QT*i*.r' recording the history of the heat transfer situation in tunnel nr. *i*.

A3.3.1 The file 'tref.r'

The file 'tref.r' stores the position of coherent stationary refinement zones. It allows to distinguish between unsteady and steady refinement zones.

```
          'tref.r'                          explanation

C time
   10.                       time level corresponding to following information

C tunnel nr. 1
C    i    nr                 tunnel nr., number of refinement zones
     1     3
C
C   ir    xs    xe           refinement zone nr., start, end
     1     0    10
     2   990  1010
     3  1990  2000

C tunnel nr. 2
C    i    nr                 tunnel nr., number of refinement zones
     1     3
C
C   ir    xs    xe           refinement zone nr., start, end
     1     0    10
     2   990  1010
     3  1990  2000
```

A3.3.2 The file 'tun.r'

The file 'tun.r' stores information about the actual zones of the tunnels. Here, it is no longer distinguished between stationary and temporary refinement zones. This file merely describes the actual state of the computational mesh. It has the following format.

`'tun.r'`

```
C time
   10.

C tunnel nr. 1
C    i    np   bcl   bcr
     1     3    1.    1.
C
C   xs    xe    js    je      dt
     0    10     0    10   0.001
    10   990    10   108    0.01
   990  1000   108   118   0.001
```

Refined zones can be distinguished from coarse zones by the time step. The first valid line contains the time level to which the following information belongs. The second line contains information about the index of the tunnel (*i*), the total number of parts (*np*), the left handed boundary condition (bcl) and the right sided boundary condition (bcr). The *np* following lines define the actual physical position and the corresponding indices of the existing tunnel parts as well as the time step applied in each part.

A3.3.3 The file 'veh.r'

The file 'veh.r' contains actual information for the position of unsteady refinement zones. It has the following format

`'veh.r'`

```
C time
   10.

C vehicle nr. 1
C    i    xd    xa    j4    j3    j2    j1    sp   npv
     1   300   400    30    40     0     0   100     1

C vehicle nr. 2
C    i    xd    xa    j4    j3    j2    j1    sp   npv
     1   700   800    70    80     0     0   100     1
```

As before, the first valid line gives the corresponding time level. The then following valid lines give each the complete information for the actual vehicle position, the corresponding indices and its speed.

A3.3.4 The data files 'uT.r' and uCV.r'

The files 'uT.r' and 'uCV.r' contain the complete actual distribution of flow values in the tunnels and the cross-vents. In order to reduce storage requirements, they are written unformatted.

The generating FORTRAN procedures are

for 'uT.r'

```
OPEN (10,FILE='uT.r', STATUS='UNKNOWN', ACCESS='UNFORMATTED')
WRITE(10) ti
DO i=1,n
DO j=0,je
WRITE(10) (uT(k,j,i),k=0,8)
ENDDO
ENDDO
CLOSE (10)
```

and for 'uCV.r'

```
OPEN (10,FILE='uCV.r', STATUS='UNKNOWN', ACCESS='UNFORMATTED')
WRITE(10) ti
DO i=1,n
DO j=0,je
WRITE(10) (uCV(k,j,i),k=0,3)
ENDDO
ENDDO
CLOSE (10)
```

A3.3.5 The history files 'PT*ij*.r', 'PV*ij*.r' and 'PCV*ij*.r'

History files for tunnel points have the name 'PT*ij*.r' where *i* indicates the tunnel number and *j* the point number as specified in 'hisT.d'. Vehicle and cross-vent history files follow the same nomenclature. The files contain lines corresponding to different instances and the associated flow values in the colums in the following order:

```
ti          ρ          u          T          p          x
```

(time, density, air velocity, temperature, pressure and position)

A3.3.6 The history file 'F*i*.r'

The file 'Fi.r' contains the forces acting on the vehicle nr. *i* at different moments. The values are in the following order:

```
ti          sp          Ffv          Fp          Pt          xv
```

(time, speed, total friction force, total pressure force, total power required, position of vehicle)

A3.3.7 The history file 'QT*i*.r'

In NUMSTA, it is possible to store the total amount of heat transfer in every moment. It contains a line for each instant and the colums contain the following data:

```
ti          qt          qcv          mRT
```

(time, heat transfer in tunnel walls, heat transfer in cross-vents, latent heat in mass flow)